HEINRICH HEINE
UNIVERSITÄT DÜSSELDORF

Synthese mono – und intermetallischer Nanopartikel in Ionischen Flüssigkeiten

Kumulative Dissertation

zur

Erlangung des Doktorgrades *Dr. rer. nat.*

der Mathematisch-Naturwissenschaftlichen Fakultät

der Heinrich-Heine-Universität Düsseldorf

vorgelegt von

Susann Wegner

aus Dresden

Düsseldorf, August 2017

aus dem Institut für Anorganische Chemie und Strukturchemie I

der Heinrich-Heine-Universität Düsseldorf

Gedruckt mit der Genehmigung der

Mathematisch-Naturwissenschaftlichen Fakultät der

Heinrich-Heine-Universität Düsseldorf

1. Berichterstatter: Prof. Dr. Christoph Janiak

2. Berichterstatter: Prof. Dr. Christian Ganter

Tag der mündlichen Prüfung:

Eidesstattliche Erklärung

Ich versichere an Eides statt, dass die vorliegende Dissertation von mir selbstständig, ohne unzulässige fremde Hilfe und unter Beachtung der „Grundsätze zur Sicherung guter wissenschaftlicher Praxis“ an der Heinrich-Heine-Universität Düsseldorf erstellt worden ist. Die aus fremden Quellen direkt oder indirekt übernommenen Gedanken sowie Ergebnisse sind als solche kenntlich gemacht. Die Arbeit wurde bisher weder im Inland noch im Ausland in gleicher oder ähnlicher Form einer anderen Prüfungsbehörde vorgelegt. Es wurden keine früheren erfolglosen Promotionsversuche unternommen.

Ort, Datum

____

Unterschrift

____

Für meine Familie

„Deo volente nobis viventibus.“

Jakobus 4, 15

Danksagung

Im Folgenden möchte ich meinen Dank all denjenigen aussprechen, die zum Gelingen dieser Dissertation beigetragen haben.

Ich danke meinem Doktorvater Prof. Dr. Christoph Janiak für die Betreuung dieser Arbeit und die Förderung der Kooperationen, mit deren Hilfe viele interessante Aspekte für diese Arbeit zusammengetragen wurden.

Herrn Prof. Dr. Christan Ganter danke ich für die Übernahme des Zweitgutachtens, die vielen interessanten Diskussionen rund um meine Arbeit und die Hilfestellung und Begleitung als Mentor.

Ein großer Dank gilt auch Herrn Dr. Juri Barthel, der stets seine Hilfe und sein Wissen für alle Fragen rund um die Mikrokopie zur Verfügung stellte. Von ihm konnte ich für die Untersuchung an der Nanopartikelchemie sehr viel lernen.

Bedanken möchte ich mich auch bei meinen Bürokollegen Bea Melara, Alexa Schmitz, Karsten Klauke, Marcell Demandt, Anna Kautz und Janina Dechnik für die tollen, teils lustigen, manchmal auch ernsthaften Gespräche und den regen Gedankenaustausch rund um die Chemie. Ferner gilt mein Dank allen Mitarbeitern der Anorganischen Chemie I für die gute Zusammenarbeit und die angenehme Arbeitsatmosphäre.

Ein sehr großer Dank gilt Marvin Siebels. Danke für Deine Hilfe bei allen Fragen, die vielen guten Gespräche und Deine Freundschaft.

Mein allergrößter Dank gilt meinen Eltern. Für ihre Liebe, ihre Geduld und das sie mich immer unterstützt haben. Ich danke Euch!

Die vorliegende Arbeit wurde in der Zeit von Juli 2014 bis August 2017 an der Heinrich-Heine-Universität Düsseldorf im Institut für Anorganische Chemie und Strukturchemie I im Arbeitskreis von Prof. Dr. Christoph Janiak angefertigt.

Publikationsliste

Susann Wegner, Masaichi Saito, Juri Barthel, Christoph Janiak: Soft wet-chemical synthesis of Ru-Sn nanoparticles from single-source ruthenocene-stannole precursors in an ionic liquid
J. Organomet. Chem., **2016**, 821, 192-196.

Susann Wegner, Christina Rutz, Kai Schütte, Juri Barthel, Alexey Bushmelev, Annette Schmidt, Katharina Dilchert, Roland A. Fischer, Christoph Janiak: Soft, wet-chemical synthesis of metastable superparamagnetic hexagonal close-packed nickel nanoparticles in different ionic liquids
Chem. Eur. J., **2017**, 23, 6330-6340.

Susann Wegner, Christoph Janiak: Metal nanoparticles in ionic liquids
Top. Curr. Chem., **2017**, 375:65.

Kurzzusammenfassung

Das Interesse an Metallnanopartikeln (M-NPs) ist in den letzten Jahrzehnten stetig gestiegen. Vor allem durch die vielfältigen Möglichkeiten, sie in ihrer Morphologie, Größe und Größenverteilung beeinflussen zu können, lassen sie sich im Bereich der Optik, Katalyse, Medizin, Lumineszenz und Elektronik sehr gut einsetzen. Hierbei haben sehr kleine Nanopartikel < 5 nm einen Vorteil gegenüber großen Nanopartikeln, da die Oberfläche der Partikel mit immer kleiner werdenden Durchmesser zunimmt. Die große Oberfläche, die vor allem auch in der Katalyse von Nutzen ist, hat aber auch den Nachteil, dass es während des Partikelwachstums zur Agglomeration der Partikel kommt. Um dies zu verhindern, werden verschiedene Stabilisatoren, wie z.B. Koordinationsliganden, Surfactants oder verschiedene Polymere eingesetzt. Durch diese sterischen und elektrostatischen Möglichkeiten der Stabilisierung wird die Agglomeration der M-NPs zwar weitgehend verhindert, allerdings haben diese auch Einfluss auf die Oberflächeneigenschaften der M-NPs und können diese einschränken bzw. verändern. Um M-NPs stabilisieren zu können, die Eigenschaften derselben jedoch nicht zu verändern, stellt die Verwendung von Ionischen Flüssigkeiten (ILs) eine gute Alternative dar. Mit Hilfe dieser < 100 °C flüssig vorliegenden Salze lassen sich M-NPs ebenfalls in ihrer Morphologie und Größe variieren, die Oberflächeneigenschaften bleiben hierbei jedoch weitgehend erhalten. Durch die Stabilität der ILs bis zu 200 °C und höher, der niedrigen Viskosität und dem kaum vorhandenen Dampfdruck, lassen sich Nanopartikelsynthesen auch bei höheren Temperaturen nasschemisch mittels Mikrowellenstrahlung durchführen.

Der Schwerpunkt der vorliegenden Arbeit liegt zum einen auf der Synthese und Stabilisierung von monometallischen Nanopartikeln in ILs mit Hinblick darauf, wie z.B. eine Veränderung der Kationen, Anionen und der Seitenkettenlänge der IL Einfluss auf die Morphologie und Größe der Partikel nehmen kann und zum anderen darauf, wie sich aus Single-Source Precursoren intermetallische Nanopartikel in den bereits gut untersuchten ILs 1-Butyl-3-Methyl-imidazolium Tetrafluoroborat [BMIm][BF_4] und 1-Butyl-3-Methyl-imidazolium Triflatimid [BMIm][NTf_2] synthetisieren lassen.

Abstract

The interest in metal nanoparticles (M-NPs) has risen steadily during the last decades. Most of all because of the various possibilities to influence their morphology, size and particle size distribution lets them be implemented in the fields of optics, catalysis, medicine, luminescence and electronics. Extremely small nanoparticles < 5 nm have advantages compared to large nanoparticles, because of the growing surface with smaller becoming diameter. The large surface, which is particularly useful in catalysis, has the disadvantage of agglomerating particles during particle growth. To avoid this, different stabilizers like coordinating ligands, surfactants or different polymers are used. Because of those steric and electrostatic possibilities of stabilizing such agglomeration of M-NPs is mostly prevented, however they also influence the M-NPs' surface properties and can either restrict or modify them. To stabilize M-NPs without modifying their properties, a good alternative is the use of ionic liquids (ILs). With the help of those < 100 °C liquidly available salts M-NPs can be varied in their morphology and size whereby the surface properties can mainly be preserved. Because of the ILs' stability of 200°C and above, their low-viscosity and the barely existing vapour pressure, nanoparticle synthesis can be conducted wet-chemically through microwave irradiation at higher temperatures.

The focus of the present thesis lies on the synthesis and stabilization of monometallic nanoparticles in ILs with respect to how a modification of cations, anions and alkyl chain length of those ILs influences the morphology and size of the particles and on the other hand on how single-source precursors can be synthesized to intermetallic nanoparticles and those already well examined ILs 1-butyl-3-methyl-imidazolium tetrafluoroborate [BMIm][BF_4] and 1-butyl-3-methyl-imidazolium triflatimide [BMIm][NTf_2].

Abkürzungsverzeichnis

°C	Grad Celsius
% d. Th.	Prozent der theoretischen Ausbeute
Å	Ångström
Abb.	Abbildung
EDX	Energiedispersive Röntgenspektroskopie
eV	Elektronen Volt
GC	Gaschromatographie
Gew% bzw. wt%	Gewichtsprozent bzw. weight percent
h	Stunde(n)
HV	Hochvakuum
Hz	Hertz
IC	Ionenchromatographie
IL(s)	Ionic Liquid(s)
KFT	Karl-Fischer-Titration
kV	Kilo Volt
LM	Lösemittel
(M)-NPs	(Metall)-Nanopartikel
MHz	Mega Hertz
min.	Minute(n)
mL	Milliliter
mol	Mol
MWI	Microwave Induction
nm	Nanometer
PXRD	Röntgenpulverdiffraktometrie
RT	Raumtemperatur
SAED	Selected Area Electron Diffraction
STEM	Scanning Transmission Electron Microscope
Tab.	Tabelle
TEM	Transmissionselektronenmikroskopie
W	Watt

Inhaltsverzeichnis

1. Einleitung

Abschnitt 1.1 beinhaltet die Einleitung dieser Dissertation in Form eines Reviews, welches in einem internationalen Journal publiziert wurde und wird in kumulativer Form dargestellt. Die Einleitung steht für sich und beinhaltet ein separates Quellenverzeichnis.

1.1 Metal Nanoparticles in Ionic Liquids

Susann Wegner, Christoph Janiak

Top. Curr. Chem. **2017**, *375*, 65.

DOI: 10.1007/s41061-017-0148-1, Quelle [1]

In den letzten Jahren wurden ionische Flüssigkeiten (ILs) zunehmend als Reaktionsmedien, Wasserstoffquellen, Katalysatoren, Templatmittel und Stabilisatoren für die Synthese von (monometallischen und bimetallischen) Metallnanopartikeln genutzt und erforscht. Besonders ILs mit 1,3-Dialkyl-imidazolium-Kationen eigneten sich bei der Bildung und Stabilisierung von M-NPs hervorragend. Dieses Kapitel fasst Studien zusammen, die sich auf die Interdependenzen der IL mit dem Metallnanopartikel fokussieren und versucht z.B. den Einfluss der IL-Kation, -Anion und Alkylkettenlänge zu erläutern. Qualitativ wurde festgestellt, dass die Größe der M-NPs mit der Größe des IL-Anions ansteigt, wohingegen der Einfluss des IL-Kations weniger klar ist. Es wurde festgestellt, dass die M-NP-Größe mit zunehmenden Kettenlängen des 1,3-Dialkyl-imidazolium-Kations sowohl zu- als auch abnimmt. Aus diesen Berichten über Kationen- und Anioneneffekte der ILs geht hervor, dass die Wechselwirkung zwischen einer IL und einem (wachsenden) M-NP wenig verstanden ist. Faktoren wie die IL-Viskosität, Wasserstoff-Bindungsfähigkeit und das relative Verhältnis von polaren und nicht-polaren Domänen von ILs können ebenfalls einen Einfluss auf die Stabilität von M-NPs in ILs haben und ein besseres Verständnis für die IL-Nanopartikel Wechselwirkung wäre für ein rationelleres Design von Nanomaterialien in ILs erforderlich. Darüber hinaus tragen Thiol-, Ether-, Carbonsäure-, Amino-, und Hydroxylfunktionalisierte ILs zur Komplexität bei, indem sie auch als koordinierende Capping-Liganden wirken. Des weiteren sind Imidazolium-Kationen Vorläufer für N-heterocyclische Carbene, NHCs, die sich aus imidazoliumbasierten ionischen Flüssigkeiten durch in situ-Deprotonierung an der sauren H_2-Ringposition als Zwischenspezies während des Nanopartikelbildungs-, und Wachstumsprozesses oder als oberflächenkoordinierender Ligand für die Stabilisierung der Metallnanopartikel bilden.

Anteil an der Veröffentlichung:

- Literaturrecherche und Konzipierung des Reviews, Schreiben der Kapitel und Bearbeitung des Manuskripts nach Revision. Korrekturen des Reviews wurden durch Herrn Prof. Dr. Christoph Janiak vorgenommen.

Top Curr Chem (Z) (2017)375:65
DOI 10.1007/s41061-017-0148-1

REVIEW

Metal Nanoparticles in Ionic Liquids

Susann Wegner[1] · **Christoph Janiak**[1]

Received: 16 January 2017 / Accepted: 9 May 2017

Abstract During the last years ionic liquids (ILs) were increasingly used and investigated as reaction media, hydrogen sources, catalysts, templating agents and stabilizers for the synthesis of (monometallic and bimetallic) metal nanoparticles (M-NPs). Especially ILs with 1,3-dialkyl-imidazolium cations featured prominently in the formation and stabilization of M-NPs. This chapter summarizes studies which focused on the interdependencies of the IL with the metal nanoparticle and tried to elucidate, for example, influences of the IL-cation, -anion and alkyl chain length. Qualitatively, the size of M-NPs was found to increase with the size of the IL-anion. The influence of the size of imidazolium-cation is less clear. The M-NP size was both found to increase and to decrease with increasing chain lengths of the 1,3-dialkyl-imidazolium cation. It is evident from such reports on cation and anion effects of ILs that the interaction between an IL and a (growing) metal nanoparticle is far from understood. Factors like IL-viscosity, hydrogen-bonding capability and the relative ratio of polar and non-polar domains of ILs may also influence the stability of nanoparticles in ionic liquids and an improved understanding of the IL-nanoparticle interaction would be needed for a more rational design of nanomaterials in ILs. Furthermore, thiol-, ether-, carboxylic acid-, amino- and hydroxyl-functionalized ILs add to the complexity by acting also as coordinating capping ligands. In addition imidazolium cations are precursors to *N*-heterocyclic carbenes, NHCs which form from imidazolium-based ionic liquids by in situ deprotonation at the acidic C2-H ring position as intermediate species during the nanoparticle

---

This article is part of the Topical Collection "Ionic Liquids II"; edited by Barbara Kirchner, Eva Perlt.

✉ Christoph Janiak
janiak@uni-duesseldorf.de

[1] Institut für Anorganische Chemie und Strukturchemie, Heinrich-Heine Universität Düsseldorf,
Universitätsstr. 1, 40225 Düsseldorf, Germany

seeding and growth process or as surface coordinating ligand for the stabilization of the metal nanoparticle.

Keywords Ionic liquids · Metal nanoparticles · Cation and anion effects · Alkyl chain effects · Stabilization

1 Introduction

Already in the nineteenth century the first research efforts were seen on the synthesis of nanoparticles and the study of their properties [1–6]. Michael Faraday found in 1857 that nano-alloys can be synthesized by chemical reduction of noble-metal compounds and placed solutions of metal salt precursors with Au, Pt and Ag in a reducing atmosphere of “sulphured hydrogen” [7]. Over the last decades the evolvement of imaging methods like electron and scanning microscopies together with the application oriented interest in their properties has led to an exponential growth of metal nanoparticle (M-NP) research [8–10]. M-NPs have become significant for applications in medicine [11, 12], optics [13, 14], electronics [15], luminescence [16] and catalysis [17–19].

The synthesis of metal nanoparticles can be commonly carried out by chemical reduction [20–22], electrochemical reduction [23] and thermal decomposition [24] also induced by microwave heating [25–27]. Through the synthetic methodology, it is possible to vary the morphology, size and size distribution of M-NPs. Strong reducing agents such as sodium hydride seldom control the size and shape of M-NPs but mild reducing agents such as sodium citrate and ascorbic acid [28] which simultaneously act as coordinating capping ligands can control the size and shape of metal NPs. The size of metal nanoparticles could also be controlled by varying the concentration of metal salt precursors, reducing agents, pH, and temperature [28].

Depending on the application, e.g., in catalysis a small nanoparticle size of for example less than 5 nm may be desirable. At the same time, agglomeration of such small nanoparticles in the process of Ostwald-ripening needs to be avoided (Fig. 1).

To avoid agglomeration the nanoparticles have to be stabilized sterically or electrostatically (see also Sect. 4). For this, M-NPs are typically surrounded by coordinating (capping) ligands, by surfactants (electrostatic stabilization) or organic polymers (steric stabilization) (Fig. 2) [30]. Examples for common capping ligands are thiols, organic acids, alcohols or amines. Protic ligands like thiols and organic acids become deprotonated upon surface coordination and bind to the surface metal atoms as thiolates and carboxylates. In turn, the metal surface layer can be assumed to become cationic [31, 32]. The mean size of dodecanethiolate-stabilized Au nanoclusters can be finely adjusted by the Au:dodecanethiolate ratio and the temperature and rate at which the reduction is conducted to vary between diameters of 1.5 and 5.2 nm ($\sim$110–4800 Au atoms/core) [31]. Phosphine-stabilized gold nanoparticles can be easily prepared from $HAuCl_4$ trihydrate and sodium borohydride in the presence of triphenylphosphine in a water/toluene mixture where tetraoctylammonium bromide transferred the reactants into the organic phase. The biphasic synthesis can be carried out quickly under ambient conditions, permits

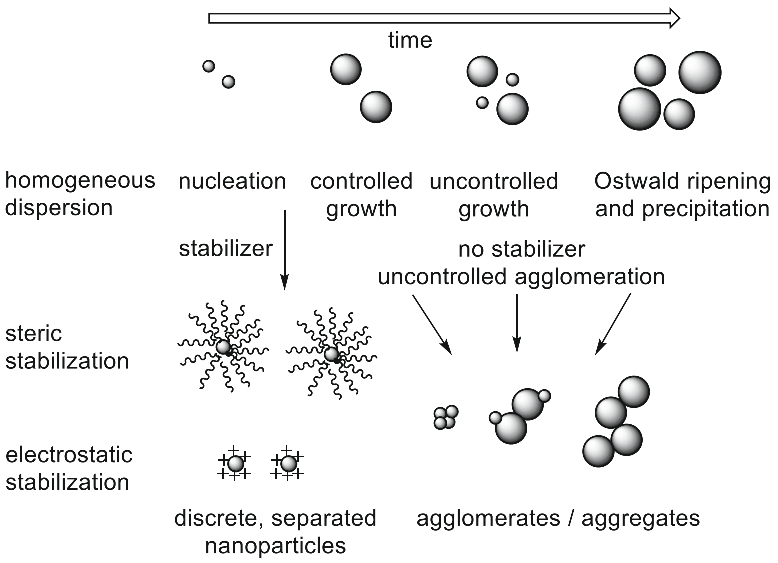

Fig. 1 Schematic presentation of (metal) nanoparticle growth and stabilization [29]

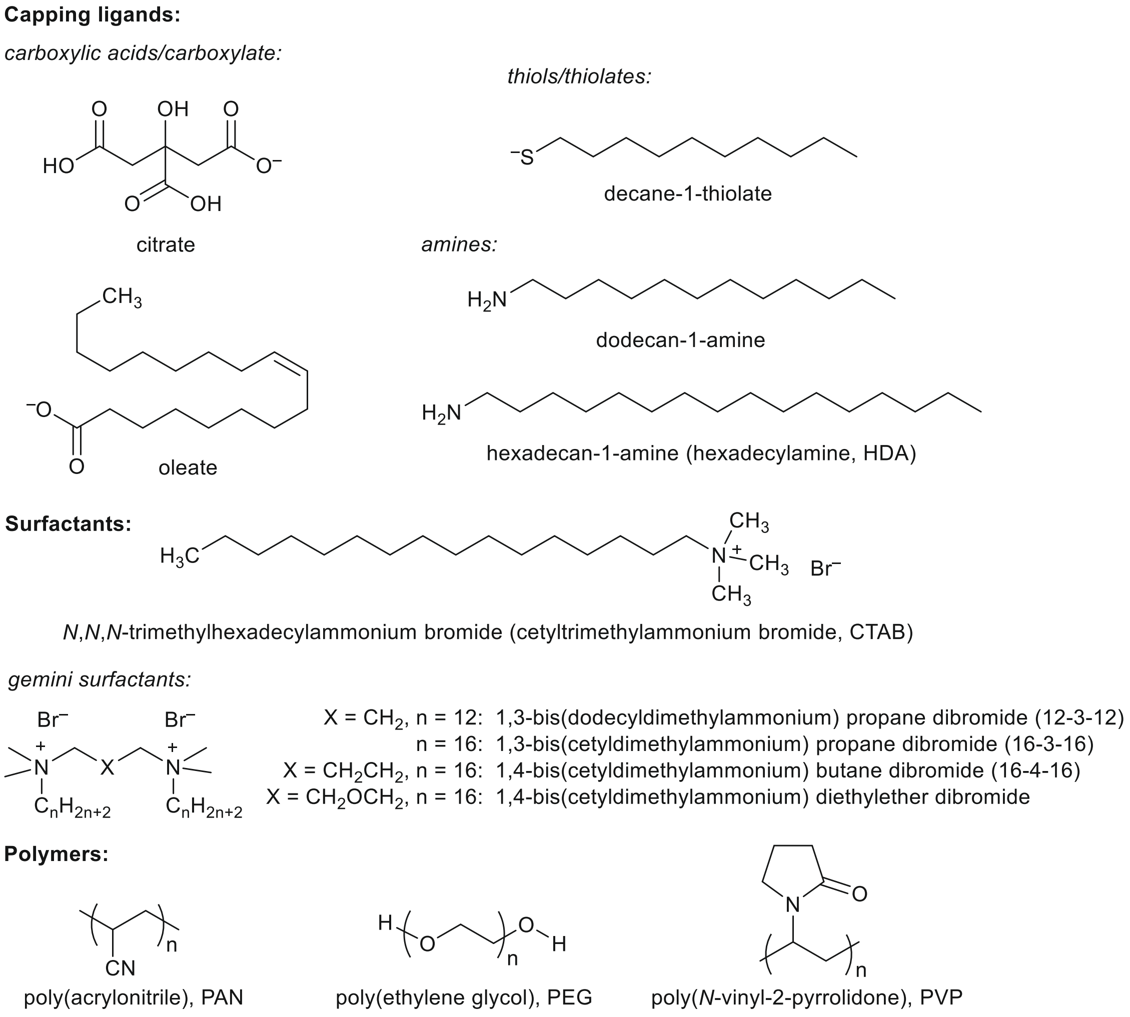

Fig. 2 Examples of typical classic stabilizers for metal nanoparticles

the use of a variety of phosphines as passivating ligands, and provides control over particle core size to produce 1.5-nm nanoparticles [33]. Phosphine-stabilized nanoparticles are precursors to other functionalized nanoparticle building blocks where nearly any functional group can be introduced into the ligand shell, and the metal core size can be tuned from 1.4 to 10 nm in diameter through ligand exchange reactions [34]. Further, non-agglomerated Ru- and Pt-NPs with a diameter of 2 ± 1 nm were prepared in ethylene glycol with acetate as coordination and stabilizing ligand [35], small Ru-NPs with a diameter of 2–3 nm were stabilized with alkylamines and alkylthiols [36].

Examples for surfactants used in the stabilization of metal nanoparticles are sodium dodecylsulfate (SDS) for Pd-NPs [37], gemini surfactants (cf. Figure 2) for Au-NPs, Ag-NPs, Au/Ag-alloy-NPs, Pd-NPs and Pt-NPs [38–42] or cetyltrimethylammonium bromide (CTAB) [42].

Examples for stabilizing polymers (cf. Figure 2) are poly(ethylene glycol), poly(acrylonitrile) and poly(vinylpyrrolidone). Poly(ethylene glycol) (PEG) can be used to control the formation and stability of Ag-NPs [43]. With poly(acrylonitrile) (PAN) it is possible to stabilize Pd-NPs with a nanoparticle diameter of 10–60 nm [44] and poly(vinylpyrrolidone) (PVP) can be used as stabilizer for Ag-NP in hybrid latex mini-emulsion at higher temperatures above 150 °C [45]. Gold and silver nanoparticles can be prepared from $HAuCl_4$ and $AgNO_3$, respectively, by using polysaccharides as reducing/stabilizing agents to obtain positively charged chitosan-stabilized gold nanoparticles and negatively charged heparin-stabilized silver nanoparticles inside the nanoscopic polysaccharide templates. The morphology and size distribution of prepared gold and silver nanoparticles varied with the concentration of both the polysaccharides and the precursor metal salts [46].

At the same time, the stabilization of M-NPs by the aforementioned coordinating capping ligands, surfactants or polymers results in a change of the surface properties and the surface accessibility of the nanoparticles particularly with regard to applications in catalysis [47].

2 Ionic Liquids

An alternative way for stabilizing metal nanoparticles can be the use of ionic liquids (ILs). By definition ionic liquids are molten organic or inorganic salts with a melting point below 100 °C [48–51], for practical purposes ILs are preferably already liquid at room temperature (RTILs). The low melting point of the ionic liquids is due to their low lattice energy, which in turn is a consequence of having weakly coordinating cations and anions. The weakly coordinating ion character derives from having large and mostly only single-charged ions so that the charge is delocalized over a large surface area. Consequently, the Coulomb attraction between ions with an effectively low surface charge density is weak. Examples of typical non-functionalized IL cations and anions are shown in Fig. 3. ILs have a very low vapor pressure which makes them easy to handle solvents [52], albeit problematic to recycle and purify by distillation. The thermal stability of typical ILs usually extends to 200 °C and even above [53–57]. Further, their physical properties

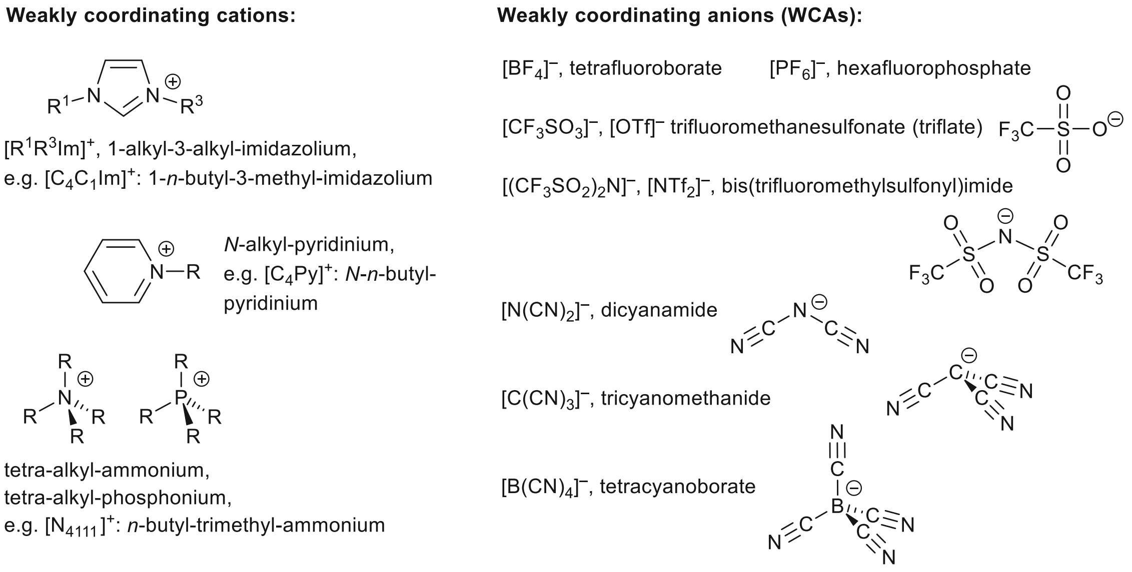

Fig. 3 Typical cations and anions of common non-functionalized ILs

like high polarity, high charge density and high dielectric constant [58] together with the formation of supramolecular mesoscopic networks [59] sets them apart from conventional organic solvents.

The well-established and probably most studied ILs contain an imidazolium cation (e.g. 1-ethyl-3-methylimidazolium $[C_2C_1Im]^+$ or 1-butyl-3-methylimidazolium $[C_4C_1Im]^+$) [60] and weakly-coordinating anions (WCAs) such as tetrafluoroborate $[BF_4]^-$, hexafluorophosphate $[PF_6]^-$ and trifluoromethylsulfonate (triflate) $[CF_3SO_3]^-$ ($[OTf]^-$) or bis(trifluoromethylsulfonyl)imide (triflimide) $[(CF_3SO_2)_2N]^-$ ($[NTf_2]^-$) [61, 62]. ILs with the 1-*n*-butyl-3-methylimidazolium $[C_4C_1Im]^+$ cation and the relatively weakly coordinating anions tetrafluoroborate, hexafluorophosphate and trifluoromethanesulfonate, are liquids over a large range of temperatures (down to −80 °C), possess high thermal and chemical stability, a large electrochemical window, high ion density, relatively low viscosity, and negligible vapor pressure [63].

Variation of the side chain R, R^1, R^3 (cf. Figure 3) of the cation or variation of the anion results in a change of the physicochemical properties of the IL like thermal behavior, viscosity and density. The viscosity increases with the length of the side chain of the imidazolium cation from $[C_2C_1Im][(CF_3SO_2)_2N]$ to $[C_8C_1Im][(CF_3SO_2)_2N]$ whereas the ionic conductivity decreases [64].

3 Metal Nanoparticles in Ionic Liquids

In the last years many different M-NPs (monometallic and bimetallic) in ILs were obtained. The activities in this field have already been summarized in reviews which provide an overview of available metal nanoparticles in ionic liquids with their precursor, size and size dispersion. “A short review on stable metal nanoparticles using ionic liquids, supported ionic liquids and poly(ionic liquids)” focused on supported IL-like phases and on different types of poly(ionic liquids) [P(ILs)] and polyelectrolytes as stabilizing agents for the synthesis of M-NPs. P(ILs) are an emerging class of cationic polymers with a poly(vinyl) backbone, e.g., from the polymerization of 1-vinyl-3-alkyl-imidazolium salts. P(ILs) possess properties of polymers as well as ILs with tunable properties through the anion and varying imidazolium alkyl chain length [8]. The main focus of the review “On the structural and surface properties of transition-metal nanoparticles in ionic liquids” [65] is on the different synthesis methods of transition-metal nanoparticles in ILs, the polar and non-polar regions in the M-NP/IL dispersion and steric and electronic protective layer formation against aggregation or agglomeration of the M-NPs. Further this review discusses the use of stable transition-metal NPs in ILs as green catalysts for several reactions and also as novel materials for chemical sensors. Particular attention is also paid to the stabilization models proposed to explain the stability and properties of the M-NP/IL dispersion [65]. The reviews entitled “naked metal nanoparticles from metal carbonyls in ionic liquids: Easy synthesis and stabilization” [47] and “synthesis and application of metal nanoparticle catalysts in ionic liquid media using metal carbonyl complexes as precursors” [66] *inter alia* summarize work on the synthesis of metal nanoparticles in ionic liquids from metal carbonyls. Commercially available binary metal carbonyls $M_x(CO)_y$ are unique precursors as they contain the metal atoms already in the zero-valent oxidation state needed for M-NPs. Thus, no reduction process is necessary and the only side-product CO is easily given off to the gas phase and removed from the reaction mixture. The microwave induced thermal decomposition of metal carbonyls in ILs provides an especially rapid and energy-saving procedure because of the ILs significant absorption efficiency for microwave energy. Examples for the direct use of M-NP/IL dispersions in hydrogenation catalysis of cyclohexene and benzene, Fischer–Tropsch reaction, and dehydration catalysis are also given in these reviews [47, 66]. The synthesis of metal nanoparticles from bulk metals, metal salts, metal complexes and metal carbonyls in ILs was reviewed in [30, 67, 68]. The synthesis of M-NPs in ILs can be carried out by chemical or electroreduction, thermolysis and photochemical methods including decomposition by microwave or sono-/ultrasound irradiation. Gas-phase syntheses can use sputtering, plasma/glow-discharge electrolysis and physical vapor deposition or electron beam and γ-irradiation. The in situ deposition of the M-NPs on supports, such as graphene-type materials was also addressed as was the use of M-NP/IL dispersions or on supports as catalysts for C–C coupling or hydrogenation catalysis [30, 67, 68]. The minireview “ionic liquids for the convenient synthesis of functional nanoparticles and other inorganic nanostructures” focusses on ionic liquids in the synthesis of crystalline nanoparticles at ambient temperatures and self-assembled, highly organized hybrid nanostructures [69].

The scope of this review here is the stabilization of metal nanoparticles in ionic liquids and the elucidation of the different factors which play a role in the stabilization and control the metal nanoparticle formation.

Briefly, metal nanoparticles of Rh, Pd, Pt, Ir, Fe, Ru, Co, Au, Ag, Cu and Ni were obtained from $RhCl_3 \cdot 3H_2O$, $PdCl_2$, $Pt_2(dba)_3$ (dba = dibenzylidene acetone), $[Ir(COD)Cl]_2$, $Fe_2(CO)_9$, Ru(COD)(COT), $Co_2(CO)_8$, $KAuCl_4$, $AgBF_4$, $Cu(NO_3)_2$ and $Ni(COD)_2$. Metal nanoparticles have been synthesized mostly in the ionic liquids $[C_4C_1Im][PF_6]$, $[C_4C_1Im][BF_4]$, $[C_4C_1Im][CF_3SO_3]$, $[C_{10}C_1Im][NTf_2]$, $[C_4C_1Im][NTf_2]$ by hydrogenation, chemical reduction and thermal decomposition. Sizes of M-NPs in ILs were found from 2.3 nm (Rh) [70], 4.2 ± 0.8 nm (Pd) [71], 2.8–3.3 nm (Pt) [116], 2–3 nm (Ir) [76], 5.2 nm (Fe) [72], 2.6 ± 0.4 nm (Ru) [73], 14 nm (Co) [164], 2.6-200 nm (Au) [74], 3–5 nm (Ag) [75], 3.5–9.5 nm (Cu) [76] and 5.1–5.9 nm for Ni [137]. Imidazolium ILs feature prominently in the formation and stabilization of M-NPs [77]. Imidazolium ILs are air, water and electrochemically stable with a wide liquidus range.

1-Alkyl-3-alkyl'-imidazolium ILs simultaneously act as reaction media, hydrogen sources, catalysts, templating agents and stabilizers for the synthesis of metal nanoparticles. It should be clear, however, that there are ILs which (i) have a strong influence on particle formation, (ii) which are good nucleation aids, but poor stabilizers, (iii) which are good nucleation aids and good stabilizers, and (iv) are none of this [78].

Examples of recent M-NP syntheses are given in Table 1. The examples show that metal nanoparticle synthesis occurs often by reduction of metal salts with added reducing agents such as H_2 or $NaBH_4$. Alternatively, the IL imidazolium cation with its protic C2-H or salt anions such as acetate, acetylacetonate, 1-(dimethylamino)propan-2-olate ($^{-}OCH(Me)CH_2NMe_2$) or amidinate ($MeC(N^iPr)_2^-$) act as internal or intramolecular reductants. The entries in Table 1 also show that microwave induced heating features prominently because of the very high absorption efficiency of ILs for microwave energy.

4 Stabilization of Metal Nanoparticles

Generally, the stabilization of M-NPs occurs through (I) electrostatic or (II) steric stabilization or (III) a combination of both electrostatic and steric stabilization [91]. The effect of stabilizing agents for nanoparticles is to build up a repulsive force between the particles [92], or at least to decrease any attractive van der Waals forces. Stabilizing agents surround NPs to prevent the agglomeration. The mechanism of stabilization has first been described in the Derjaguin–Landau–Verwey–Overbeek theory [93, 94].

4.1 Derjaguin-Landau-Verwey-Overbeek theory (DLVO theory)—Electrostatic Stabilization and Van Der Waals Interactions

The classic and most commonly used theory of a "mechanism of stabilization" was put forward by Derjaguin and Landau in 1940 as a quantitative theory [95] and later by Verwey and Overbeek in 1948 [96]. Both descriptions referred to colloidal materials. This basic theory combines repulsive Coulomb and attractive van der Waals (vdW) forces through the sum of an effective electrostatic term and a van der Waals term for the stabilization of these materials. Van der Waals forces originate from correlations between electron motions leading to non-spherical electron distributions in two adjacent particles or molecules. VdW forces are short-range, unidirectional and relatively weak compared to other intermolecular interactions.

Table 1 Recent mono and bimetallic NP synthesis in imidazolium ILs

Ionic liquid	Precursor	Conditions, reducing agent	NP with particle diameter	References
			Monometallic M-NPs	
$[C_4C_1Im][PF_6]$	$RhCl_3 \cdot 3H_2O$	H_2	Rh	[79]
			3.5 nm	
$[C_4C_1Im][BF_4]$	$CoCl_2 \cdot 6H_2O$	$NaBH_4$	Co	[80]
		Ultrasound	30 ± 5 nm	
	$Cu[OCH(Me)CH_2NMe_2]_2$	Microwave heating, intramolecular red. or IL	Cu	[81]
			3.3 ± 0.9 m	
	$Cu(OAc)_2 \cdot H_2O$		Cu_2O nanocubes	
			43 ± 15 nm	
	Cu(I)-amidinate	Microwave heating, intramolecular red. or IL	Cu	[82]
	Zn(II)-amidinate		11 ± 6 nm	
	$[Cu\{MeC(N^iPr)_2\}]_2$		Zn	
	$[Zn\{MeC(NiPr)_2\}]$		3 ± 1 nm	
	$Ir_4(CO)_{12}$	Microwave heating,	Ir	[83]
			1.0 ± 0.4 m	
		electron beam	2.7 ± 0.7 nm	
$[C_4C_1Im][NTf_2]$	$(NH_4)_6Mo_7O_{24} \cdot 4H_2O$	$NaBH_4$	Mo	[84]
			10–50 nm	
			Bimetallic M-NPs	
$[C_4C_1Im][BF_4]$	$Fe_2(CO)_9$	Thermal decomposition	FeRu	[85]
	$Ru_3(CO)_{12}$		1.65 ± 0.3 nm	
	Cu(I)-amidinate	Microwave heating, intramolecular red. or IL	β-CuZn	[82]
	Zn(II)-amidinate		51 ± 29 nm	
	$[Cu\{MeC(N^iPr)_2\}]_2$		γ-Cu_3Zn	
	$[Zn\{MeC(NiPr)_2\}]$		48 ± 12 nm	
	$Ni(COD)_2$	H_2	NiGa	[86]
	$Ga(C_5Me_5)$		14 ± 5 nm	
	Triple-decker ruthenocene,	Microwave heating, intramolecular red. or IL	RuSn	[87]
			4.3 ± 1.5 nm	
	Anionic ruthenocene			
$[C_4C_1Im][NTf_2]$	$Co(acac)_3$	Thermal decomposition, intramolecular red. or IL	CoPt-nanorods	[88]
	$Pt(acac)_2$		8 nm	
	[Ru(COD)(COT)]	H_2	RuCu	[89]
	[CuMes]		1.9–2.8 nm	
$[C_4C_1Im][PF_6]$	$HAuCl_4$	$NaHB_4$	PdAu	[90]
	K_2PdCl_4	H_2	5.3 ± 3.0 nm	

Electrostatic and van der Waals interactions are present in nearly all colloidal and nanoparticular systems [97]. DLVO theory assumes flat surfaces of the particles and a homogeneous charge density, even upon approach of the particles. The concentration of the counter-ions, which cause the electric potential, is taken as constant. DLVO theory treats anions as ideal point charges. The influence of the solvent is considered only through its dielectric constant. DLVO theory is fundamental for colloids and predicts very well the stability of lyophobic colloids [98].

Ionic components as in surfactants or ionic liquids will generate an ionic double or Debye layer around the NPs (Fig. 3) resulting in electrostatic repulsion between equally surrounded NPs which will prevent the aggregation of the NPs in the dispersion. The effectiveness of such an electrostatic stabilization depends on parameters like pH, temperature, and concentration [92, 99]. Electrostatic repulsion is an important contribution for the stabilization of NPs using ionic compounds. The outer part of the ionic double layer may be formed by the bulky and less surface-coordinating alkyl ammonium, sulfonium, phosphonium, and imidazolium moieties which then add a steric stabilization (see below) [8].

For metal nanoparticles the anion of an original metal salt precursor has to be taken into account as electrostatic stabilizer. Small halide anions come closest to the “DLVO-type” point charge electrostatic stabilizers. DLVO theory predicts that the anion charges should be the primary source of stabilization for the unsaturated, electrophilic and possibly positively charged metal nanoparticles [100, 101]. The metal nanoparticles and their anion layer on the surface form then an overall negatively charged particle and are subject to Coulomb repulsion within the DLVO theory [47].

The stability of a colloid increases with the thickness of the Debye layer, which is the sum of the layers of counter-ions surrounding the particle. A thicker Debye layer stabilizes the particles by increasing the distance between them and reducing their van der Waals attraction. Also, the stability of colloids increases with the dielectric constant of the medium [102].

Limits of the DLVO theory are that it can only be applied to dilute systems ($<5 \times 10^{-2}$ mol/L) and cannot be applied to multiply charged ions or to sterically stabilized systems [103]. DLVO theory needs to be extended for effects such as hydrogen bonding, the hydrophobicity and steric interactions.

4.2 Steric Stabilization

Another important contribution in preventing aggregation of metal NPs is steric stabilization. Coordinating capping ligands like thiols, carboxylates, alcohols, long-alkyl-chain surfactants or polymers/oligomers act more or less through this type of stabilization [8].

When two nanoparticles enclosed by polymers or surrounded by long alkyl chains of ligands adsorbed on their surface approach each other, the polymer or alkyl chain layers will be compressed which results in a strong repulsion which is termed steric stabilization [104]. Steric repulsion derives from combination of entropic and osmotic contributions. The entropic part stems from a volume restriction effect that decreases the number of possible configurations in the compressed region. The osmotic effect is due to an increase in concentration of the adsorbed polymers or ligand in the region between the two nanoparticles surfaces as they approach closer. Steric interactions in colloidal dispersions in molecular solvents have been extensively studied [104–108].

4.3 Combination of Both Electrostatic and Steric Stabilization

Compounds which stabilize both through electrostatic and steric effects are, for example, surfactants with long alkyl chains, such as cetyltrimethylammonium bromide (CTAB) or its gemini derivatives (cf. Fig. 2) [38–42], polymers containing ionic charges such as carboxyl-terminated poly(ethylene glycol) [93] or ionic liquids (see below). From theoretical and experimental studies, it became evident that the effectiveness of electrostatic stabilization increases with increasing particle size, whereas the effectiveness of steric stabilization increases with decreasing particle size [109]. The combination of electrostatic and steric stabilization is also referred to as *electrosteric* stabilization.

5 Stabilization of Metal Nanoparticles in Ionic Liquids

5.1 Electrostatic and Steric = Electrosteric Stabilization

ILs offer an interesting potential for stabilizing materials in the synthetic process. Their low interface energy is favorable for stabilizing small particles. ILs consist of cations and anions, which can act as electrostatic stabilizing agents. The IL ions or ion clusters are attracted to the nanoparticle surface by electrostatic forces [110]. The nature of the immediate ion layer around metal nanoparticles in ILs is still a matter of debate. DLVO theory predicts that the anion charges should be the primary source of stabilization for the unsaturated, electrophilic and probably positively charged metal nanoparticles [100, 101]. The metal nanoparticles and their anion layer on the surface would then form an overall negatively charged particle and are subject to Coulomb repulsion within the DLVO theory [47]. On the other hand, there are statements that the ionic liquid cations are attracted to the surface of a negatively charged nanoparticle to form a positive ion layer, and then counter-anions form a second layer on the nanoparticle surface by electrostatic attraction [111–113].

Palladium nanoparticles, which were grown onto multiwalled carbon nanotubes modified with imidazolium groups were claimed to be stabilized by the electrostatic interaction occurring between the imidazolium cations and the nanoparticle surface due to a coordination involving the imidazolium cation [114]. Upon exchange of the imidazolium counter-anion from Br^- and $[SbF_6]^-$ to $[NTf_2]^-$ no change in the material structure was noticed, i.e. no separation of the nanoparticles from the multiwalled carbon nanotubes [114]. Also, results from an X-ray photoelectron spectroscopy (XPS) investigation of functionalized imidazolium ILs with gold or platinum nanoparticles were seen to support this cationic coordination mode. Three

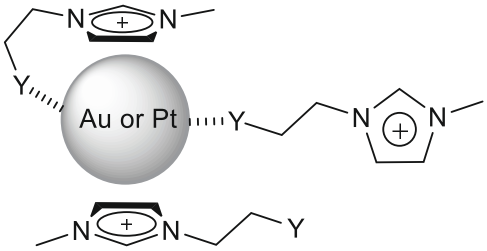

Fig. 4 Schematic proposed stabilization possibilities between metal nanoparticles and functionalized imidazolium cations [115]

possible interactions, involving either the functional group and/or the imidazolium ring were proposed (Fig. 4) [115].

On the other hand, an XPS and an extended X-ray fine structure spectroscopy study (EXAFS) of iridium or platinum nanoparticles in the imidazolium ILs $[C_4C_1Im][BF_4]$, $[C_4C_1Im][PF_6]$ and $[C_4C_1Im][OTf]$ showed interactions of the ionic liquid with the metal surface and the formation of an ionic liquid protective layer surrounding the metal particles [116, 117]. With small-angle X-ray scattering (SAXS) a variation in the protective layer length, from 2.8 to 4 nm, was evidenced depending on the type of anion. Moreover, the XPS analyses proved that the interaction between the metal surface and the IL occurs through F^-, when the anion is $[BF_4]^-$ of $[PF_6]^-$ or through O with the triflate, $[CF_3SO_3]^-$ anion [116, 117]. Consequently, one would assume that the ionic multilayer is composed of anions located immediately adjacent to the nanoparticle surface (Fig. 5) [166].

Density functional theory (DFT) binding energy (BE) calculations in a gas phase model favor interactions of Au_n clusters ($n = 1, 2, 3, 6, 19, 20$) between IL anions, such as $[BF_4]^-$, instead of imidazolium cations. This suggests an Au···F interaction and anionic Au_n stabilization in fluorous IL-anions [119]. Free imidazole bases (*e.g.* 1-methylimidazole) show similar binding energies. The Cl^- anions have the highest binding energy and can therefore be expected to bind to the NP if present in the solution. At the same time no significant binding of the $[C_4C_1Im]^+$ or $[HC_1Im]^+$ imidazolium cations was found. These findings support the model of preferred interaction between anions and Au-NPs, but also confirm the importance to consider a possible presence of Cl^- anions in the ionic liquid solution [74, 119].

The DFT study used the binding energy (BE) of different IL-ions, free bases and the Cl^- anion to gold clusters of various sizes as a relative measure for the interaction strength. The BE is defined as the difference of the relaxed energies of the gas phase anions and the Au_n clusters to the energy of their adduct (Eq. 1) [74, 119].

$$\begin{aligned}\mathrm{BE} \;&= E(\text{substrate, i.e., anion, free base or cation}) + E(\mathrm{M}_n \text{with M} = \text{Au, Pd}) \\ &\quad - E(\text{substrate adduct to } \mathrm{M}_n). \end{aligned} \tag{1}$$

Figure 6 shows the Au_n–IL anion binding configurations and the variation of the BE with cluster size *n*. Figure 7 illustrates other substrate–Au_n binding configurations and the variation of the BE with cluster size *n* for $[BF_4]^-$ in comparison with other common substrate ligands. The BE of $[C_4C_1Im]^+$ is very weak and not included here [74, 119]. The BE of $[C_4C_1Im]^+$ is only 0.35 eV towards Au_6 or

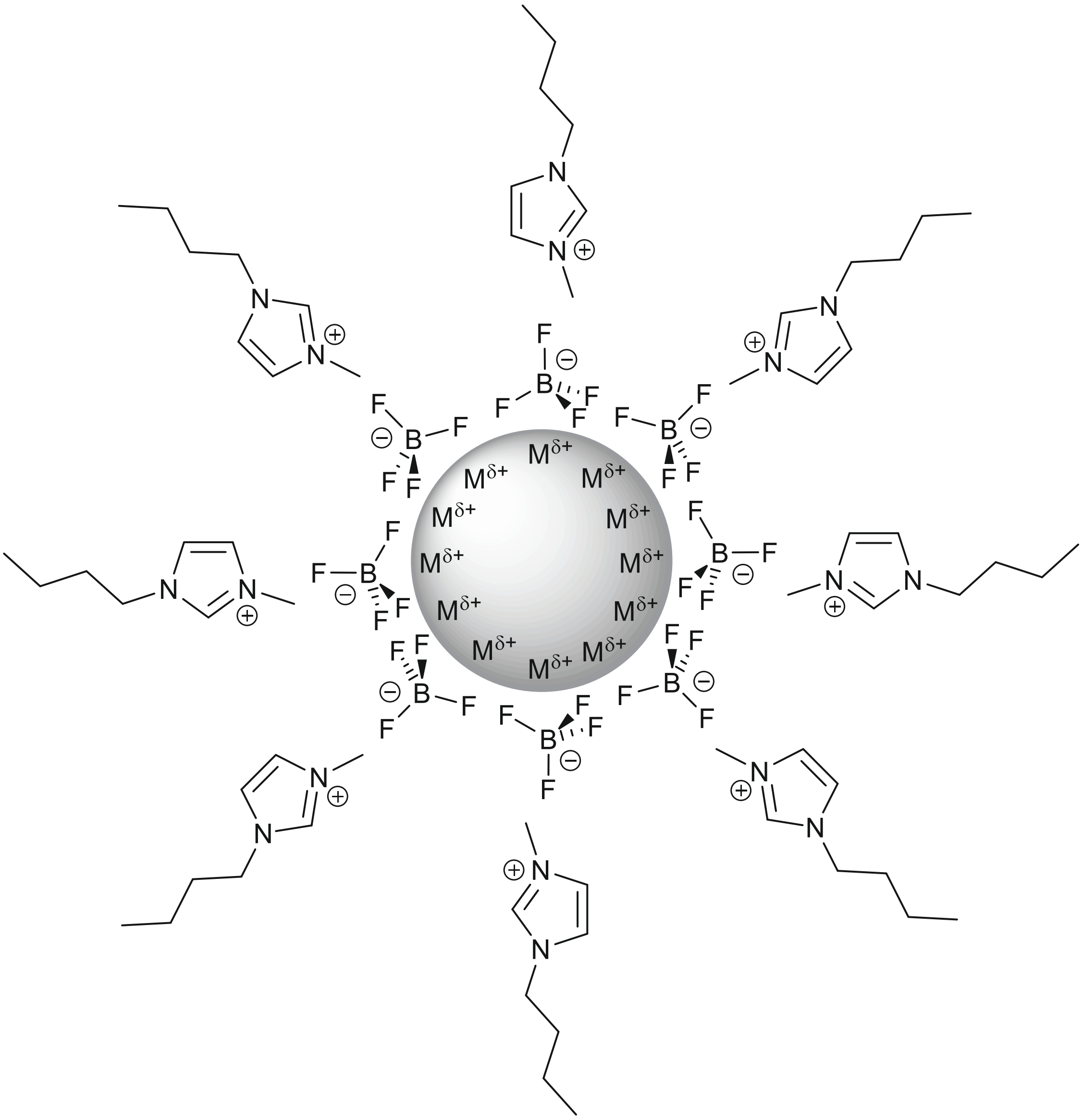

Fig. 5 Schematic depiction of proposed interactions between immediate IL anions, shown here for $[BF_4]^-$ anions and the metal nanoparticle surface with the IL-cations forming the second shell of the ionic double layer around a metal nanoparticle [118]

0.43 eV towards Au_{19} while the BE of $[BF_4]^-$ towards Au_6 and Au_{19} is 1.08 and 1.2 eV, respectively (1 eV = 23.06 kcal/mol). The BE comparison with chloride, citrate, PH_3 and H_2O illustrates the critical influence of the ionic charge and electron delocalization from the ligand to Au_n (Fig. 7). The softer the anion or ligand, that is, the more charge transfer or electron delocalization (according to Pearson's hard-soft concept and the nephelauxetic series) [120] to Au_n is possible, the better the stabilizing effect. H_2O as a hard and neutral ligand offers the least stabilization, hence, reduction of gold salts by $SnCl_2$ in water led immediately to the red purple solution (known as the Purple of Cassius). Remarkably, the relatively soft chloride anion shows the largest BE in agreement with the strong covalent binding of chloride ions to the Au(111) surface found in recent DFT simulations [121].

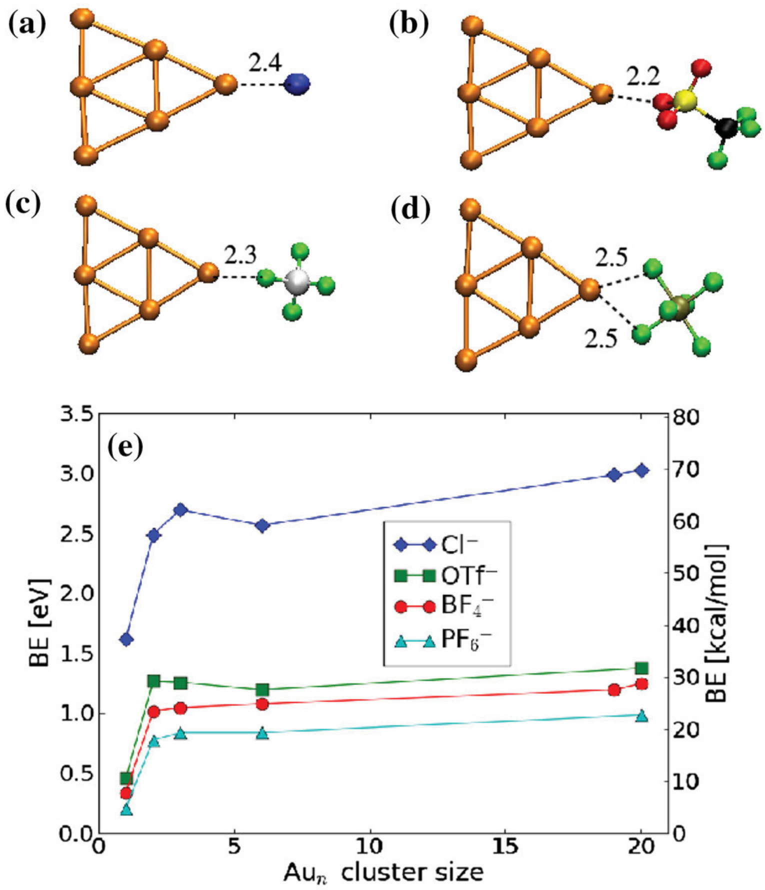

Fig. 6 Relaxed configurations of Au_6 bound to **a** Cl^-, **b** $[OTf]^-$, **c** $[BF_4]^-$ and **d** $[PF_6]^-$. The bond lengths are given in Å. **e** Binding energy. All the anions show a similar behavior in their BE: The BE to a single gold atom $n = 1$ is quite low and more than doubles for Au_2 ($n = 2$), therefrom is stays rather invariant with increasing the cluster size to $n = 20$, i.e., the BE is already saturated for Au_2. The chloride anion shows the largest BE of all anions and can be expected to bind to the clusters if it is present in the dispersion. Reprinted with permission from the author of Ref. [119]. Copyright Wiley–VCH 2009

A later combined DFT/vibrational spectroscopy approach found that palladium nanoparticles interact more strongly with the $[BF_4]^-$ anions than with the 1,3-dimethylimidazolium ($[C_1C_1Im]^+$) and 1-ethyl-3-methylimidazolium ($[C_2C_1Im]^+$) cations of the considered ILs. This suggested an important role of the anions in Pd-NP formation and stabilization in ILs. At the same time, the binding between isolated Pd atoms and the C atoms of the 1,3-dimethylimidazolium cation is stronger than Pd–$[BF_4]^-$ binding [122].

A similar DFT binding energy (BE) calculation with the 1-(2′-hydroxylethyl)-3-methylimidazolium cation $[HOC_2C_1Im]^+$ and a Pd_5 cluster pointed to the interaction of Pd_5 lying above the plane of the imidazolium ring and being in short contacts with C4 and C5 atoms of the imidazolium moiety and the oxygen atom of the hydroxyl group [123]. Yet, even with the added interaction of the functional hydroxyl group the binding energy is ca. 11 kcal/mol smaller than the BE of $[BF_4]^-$ anion to the Pd_5 cluster, suggesting a less important role of the cations with respect to stabilization of Pd-NPs relative to the role of the anions. This is in agreement with the above BE results, obtained earlier, for the Au_n clusters [119].

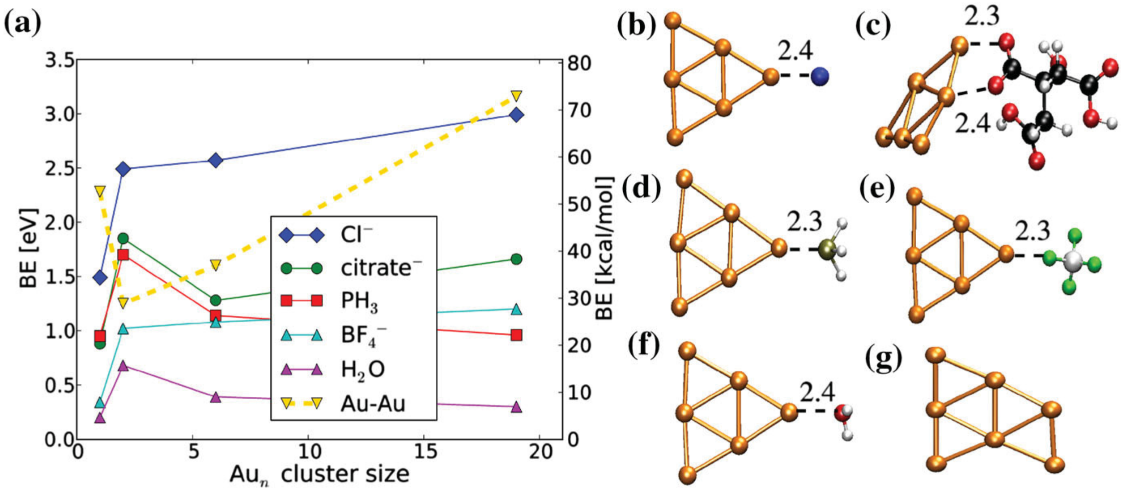

Fig. 7 **a** Binding energies (BE) and Au-atom addition energies depending on the cluster size. **b–f** Relaxed configurations of Au_6 bound to **b** Cl^-, **c** citrate$^-$ ($C_6H_7O_7{}^-$), **d** PH_3, **e** $BF_4{}^-$ and (f) H_2O. **g** Relaxed configuration of Au_7. The bond lengths are in Å [74]. Reproduced from Ref. [74] with permission, copyright 2010 The Royal Society of Chemistry

The order of the calculated BEs was obtained for interaction energies between a Pd_5 cluster and the anions was $[CF_3CO_2]^-$ (~47 kcal/mol) > $[BF_4]^-$ (~41 kcal/mol) > $[OTf]^-$ (~34 kcal/mol) > $[PF_6]^-$ (~31 kcal/mol) ≅ $[NTf_2]^-$ (~31 kcal/mol) [124].

For further examples of cation and anion effects on the formation of metal nanoparticles in ILs, see also the separate section on “cation and anion effects” below.

The IL-cations with alkyl chains can further contribute to the steric stabilization of nanoparticles. If the ionic liquid cation contains a long alkyl side chain, e.g., from imidazolium- or pyrazolium-based cations, the cations on or near the nanoparticle surface can provide steric forces by stretching out their bulky side-chains, thus hindering the nanoparticles from approaching each other (cf. Figure 5) [125]. ILs can also be designed with functional coordinating groups primarily in the alkyl chains of the cations, which thereby act as coordinating capping ligands (see Sect. 6 with Fig. 12 below) [126].

As noted above for stabilizing ionic components the cations and anions of ionic liquids, possibly as charged ion clusters, will surround the nanoparticle surface to build an electric double-layer, thus providing an electrostatic force to keep the nanoparticles apart from each other [65]. The role of electrostatics in stabilizing the nanoparticles in ionic liquids has been well recognized [115, 127–133].

The interaction energies of ILs with different cations and anions to Ru-NPs were compared by titration calorimetry and by molecular simulation. Structural information from the molecular simulation suggests that the charged parts of both the IL cation and the anion are in contact with the surface of the nanoparticle, with only small charge separation at the interface. The results of this study suggest an IL-dependent balance between electrostatic, van der Waals, and H-bond forces for the stabilization of metal nanoparticles [128].

For nanoparticles in ionic liquids, steric stabilization can emerge from bulky groups in the IL cation (or anion) and/or from the addition of macromolecules, both of which hinder nanoparticles from contacting each other and from aggregation [125]. When only small amounts of polymer are added to the nanoparticle–ionic liquid dispersion, the nanoparticle surfaces are partially covered by polymers and polymer coils extend from one particle surface to another particle. Thereby, the polymers chains can function as bridges between nanoparticles. As an excess of polymer is added, the polymers can fully cover the nanoparticle surface to form an adsorbed polymer layer [134]. Then steric repulsion and stabilization arises from the adsorbed polymer layers of neighboring nanoparticles as noted above. Block copolymers have been utilized to stabilize nanoparticle dispersion [105]. PEO–PPO–PEO block copolymer Pluronic P123 ($EO_{20}PO_{70}EO_{20}$) formed a lamellar lyotropic liquid crystal structure in pyrrolidinium nitrate ($[Pyrr][NO_3]$) ionic liquid at the 58–82 wt% polymer concentration range. Gold nanoparticles were prepared by reducing $HAuCl_4$ in this lyotropic liquid crystal [135].

Various and also yet unknown factors influence the stability of nanoparticles in ionic liquids and lead to nanoparticle size [136–139] and/or morphology [140–145] changes during synthesis. Smaller diameter and narrower distributions of synthesized nickel metal and zinc oxide nanoparticles were prepared in ionic liquids with longer side chains [137, 141]. Larger size or varied morphologies of synthesized nanoparticles can be caused by conglomeration of unstable primary nanoparticles, which may result from smaller ionic liquid anions exhibiting stronger cation–anion Coulomb attraction [145], or less coordinating anions of ionic liquids [116, 144] or higher temperature decreasing the viscosity of the ionic liquid and increasing the diffusive velocities of the nanoparticles [146, 147]. An improved understanding of the stability of nanoparticle dispersions in ionic liquids is still needed to assist efforts directed toward the synthesis of nanoparticles with controlled size and morphology in ionic liquids [125].

5.2 Hydrogen Bonding Interactions

Imidazolium cations through their imidazolium-C–H groups can form hydrogen bonds to the fluorine or oxygen atoms of the IL anions [148–150] that induce structural directionality (IL effect). This is different from tetraalkylammonium ILs that, by contrast, display charge-ordered structures. The ILs act as stabilizing media, but importantly also display self-organization on the nanomolecular scale. The imidazolium ILs form extended hydrogen-bond networks at the liquid state and therefore are by definition ‘‘supramolecular’’ fluids. This structural organization of ILs can be used as ‘‘entropic drivers’’ (the so-called ‘‘IL effect’’) for the spontaneous, well-defined and extended ordering of nanoscale structures. The properties of especially the imidazolium-based ILs are based on their formation of aggregates rather than on their isolated cations and anions [151, 152]. The structures of 1,3-dialkylimidazolium salts form an extended network of cations and anions connected together by hydrogen bonds in the condensed phase, which is maintained to a great extent in the gas phase [152].

Thus, hydrogen bond interactions are present in imidazolium-based ionic liquid nanoparticle dispersions in addition to electrostatic, van der Waals and steric interactions [153, 154]. Metal nanoparticles can possess hydroxido and/or oxido ligands on their surface, which can also hydrogen bond with ionic liquids [155]. Such metal-surface bound oxygen species can be derived from crystal water of the metal salt precursor (cf. Table 1), from difficult to remove residual water in the IL or from gaseous dioxygen (as impurity even when working under inert gas). The IL-cation–anion hydrogen bond and NP–IL hydrogen bond compete with each other and contribute to nanoparticle stabilization in ionic liquids, as shown in Fig. 8 [156, 157].

The interaction energies of ILs with an additional alkyl group in the C-2 position of the imidazolium cation ($[C_4C_1C_1Im][NTf_2]$ with 1-butyl-2,3-dimethylimidazolium) and a *N*-butyl-*N*-methylpyrrolidinium cation ($[C_4C_1Pyrr][NTf_2]$) to Ru-NPs were compared to other $[C_nC_1Im]^+$-ILs by titration calorimetry and by molecular simulation. Ionic liquids with cations which are less likely to form hydrogen bonds such as $[C_4C_1C_1Im]^+$ or $[C_4C_1Pyrr]^+$ also interact less favorably with Ru-NPs [113].

Qualitative direct comparison (for the same IL-anion) of an IL with the $[C_4C_1Im]^+$-cation which has hydrogen-bonding possibility and a cation with no significant H-bond formation reveals the former to be better stabilizers for Au- or Cu-NPs whereas in the latter ILs fast particle growth and agglomeration was observed [156]. The stable time of the colloidal dispersion in $[C_4C_1Im][N(CN)_2]$ and trihexyltetradecylphosphonium dicyanamide $[P_{66614}][N(CN)_2]$ was 3 days versus 1 day. In $[C_4C_1Im][BF_4]$ or $[C_4C_1Im][NTf_2]$ Au-NPs were stable for 1 week while in *N*-butyl-*N*-methyl-pyrrolidinium, $[C_4C_1Pyr][NTf_2]$ or in *N*-butyl-pyridinium$[C_4Py][NTf_2]$ fast precipitation occurred due to fast particle growth and agglomeration [156].

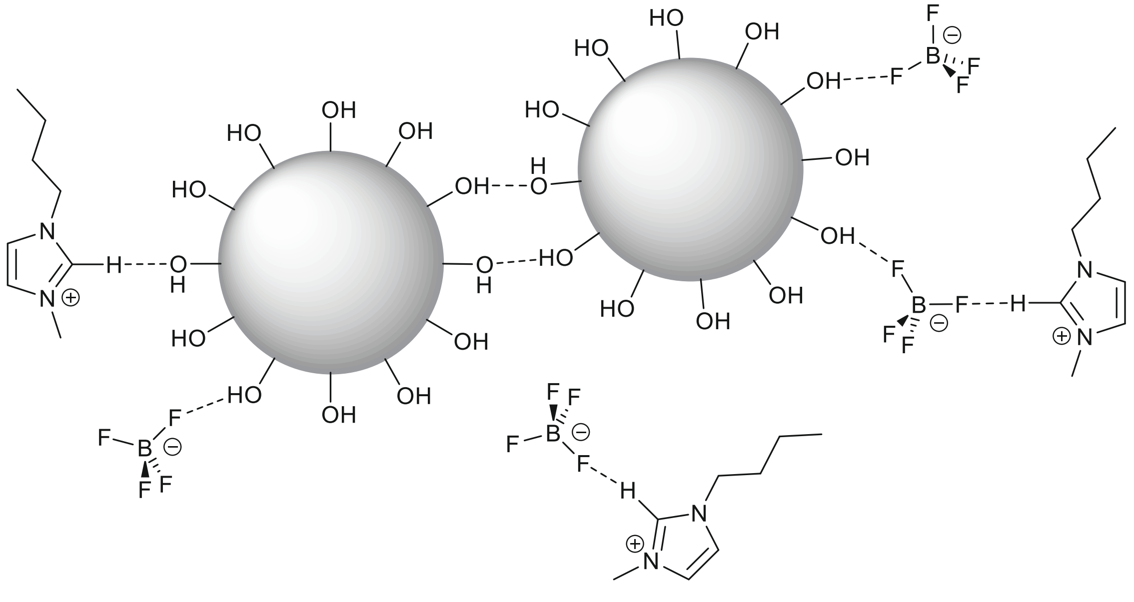

Fig. 8 Hydrogen bonds formed between the surface hydroxyl-groups of metal nanoparticles and ions of ionic liquids and between cations and anions of ionic liquids

5.3 Influence of Polar and Non-Polar Domains in ILs

The segregation of hydrophilic or hydrophobic regions, polar and non-polar domains in imidazolium-based ILs is an important physicochemical property which effects their solvation and interaction with dissolved species (Fig. 9) [158–160]. Expectedly polar substrates, like metal salts are preferentially dissolved in polar domains and non-polar compounds like organometallic precursors in non-polar IL regions [159, 161]. Consequently, the nature of the metal precursor—ionic or neutral for instance—is also a key determinant of the size and shape of the prepared metal NPs as the polarity and the volume of these IL nanoregions may modulate this. The nanoparticle growth process is probably controlled by the local concentration of the precursor and possibly limited to the size and shape of the IL polar or non-polar domains (Fig. 9) [65].

5.4 Cation and Anion Effects

Nanoparticle preparation in ILs is often accompanied by heating to over 100 °C or even 200 °C. Changing the anions or the cations can have a strong influence on the thermal behavior, density, viscosity (see below), or conductivity [160]. For example, the simple sum of the cationic and anionic self-diffusion coefficients ($D_{\text{cation}} + D_{\text{anion}}$) for selected room temperature ILs follows the (anion) order $[C_4C_1Im][NTf_2] > [C_4C_1Im][CF_3CO_2] > [C_4C_1Im][OTf] > [C_4C_1Im][BF_4] > [C_4C_1Im][(F_5C_2SO_2)_2N] > [C_4C_1Im][PF_6]$ at 30 °C. This order of the diffusion coefficients is as expected the reverse of the order of the viscosity (see below). The degree of ionic association can be estimated from the ratio of the molar conductivity obtained from the impedance measurement (Λ_{imp}) and the molar conductivity calculated from the ionic diffusivity (Λ_{NMR}). For the anions at the given $[C_4C_1Im]^+$ cation the degree of association increases according to $[PF_6]^- < [BF_4]^- < [(F_5C_2SO_2)_2N]^- < [NTf_2]^- < [OTf]^- < [CF_3CO_2]^-$. In the order from $[PF_6]^-$ to $[NTf_2]^-$ electronegative fluorine atom and electron-withdrawing perfluorosulfonyl groups contribute to the distribution of the anionic

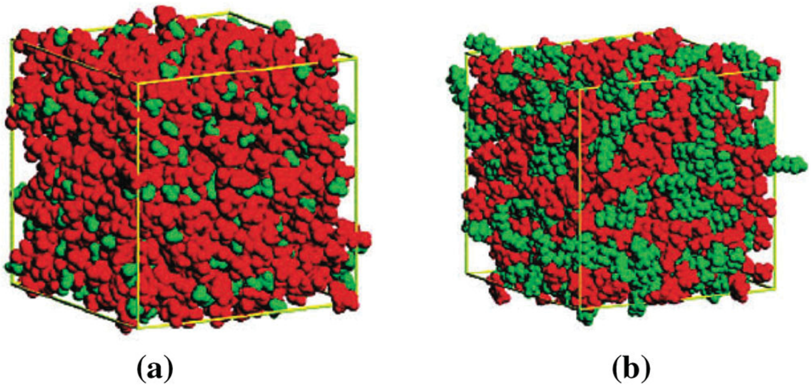

Fig. 9 Simulation study of two imidazolium-based hexafluorophosphate ILs (each *box* contains 700 ions) showing polar (*red*) and non-polar (*green*) domains for **a** 1-ethyl-3-methylimidazolium, $[C_2C_1Im]^+$ and **b** 1-methyl-3-*n*-octylimidazolium $[C_8C_1Im]^+$. Reprinted with permission from Ref. [162]. Copyright 2006 American Chemical Society

charge. Also, the surface coverage of the anion backbone by fluorine atoms may be a significant factor for only weak interactions with the $[C_4C_1Im]^+$ cation. Whereas, the relatively higher anionic charge localization in $[OTf]^-$ ($=[CF_3SO_3]^-$ and $[CF_3CO_2]^-$) leads to their stronger interaction with the $[C_4C_1Im]^+$ cation [160]. The interaction energies of ILs with $[C_4C_1Im]^+$ and the anions $[NTf_2]^-$ or $[PF_6]^-$ were compared by titration calorimetry and by molecular simulation to Ru-NPs. No significant differentiating effect of the two anions was observed. Structural information from the molecular simulation suggests that the charged parts of both the IL cation and the anion are in contact with the surface of the nanoparticle, with only small charge separation at the interface [128]. The relative order of anion stabilities for ILs with the $[C_1C_4Im]^+$ cation was observed as $[NTf_2]^- > [PF_6]^- > [BF_4]^- \gg Cl^-$ [163].

The size of M-NPs was found to increase with the molecular volume of the anion of the IL. Metal nanoparticles synthesized in $[C_4C_1Im]^+$ ILs increased in size with the size of the IL-anion from small $[BF_4]^-$ over $[OTf]^-$ to the large $[NTf_2]^-$ anion [20, 164, 165]. The IL-anion molecular volume was taken as the size of the IL-anion. The effect was shown for Rh- [164], Ag- [20] and W-NPs [165]. Figure 10 depicts the correlation between the nanoparticle size of W- and Rh-NPs and the molecular volume of the anion.

The influence of the anion to metal nanoparticles was also observed by several other research groups [116, 167–170]. 1-*n*-Butyl-methyl-imidazolium salts $[C_4C_1Im]^+$ with weakly coordinating perfluorinated counter anions ($[BF_4]^-$, $[PF_6]^-$ or $[NTf_2]^-$) were qualitatively found to be better stabilizers compared to ILs with anions of higher coordination strength (dicyanamide, $[N(CN)_2]^-$). In the former ILs Au- or Cu-NPs were stable colloidal dispersions, that is, without precipitation or aggregation for 1 week to several weeks. In $[C_4C_1Im][N(CN)_2]$ Au-NPs were stable for only 3 days due to fast particle growth and agglomeration [156].

The IL-anion had an effect on the dissolution and reaction rate when fabricating copper nanoparticles from Cu flakes (of 1–5 µm) in ILs [171]. When $[C_4C_1Im][BF_4]$, $[C_4C_1Im][PF_6]$ and $[C_2C_1Im][BF_4]$ were used, it took a relatively long

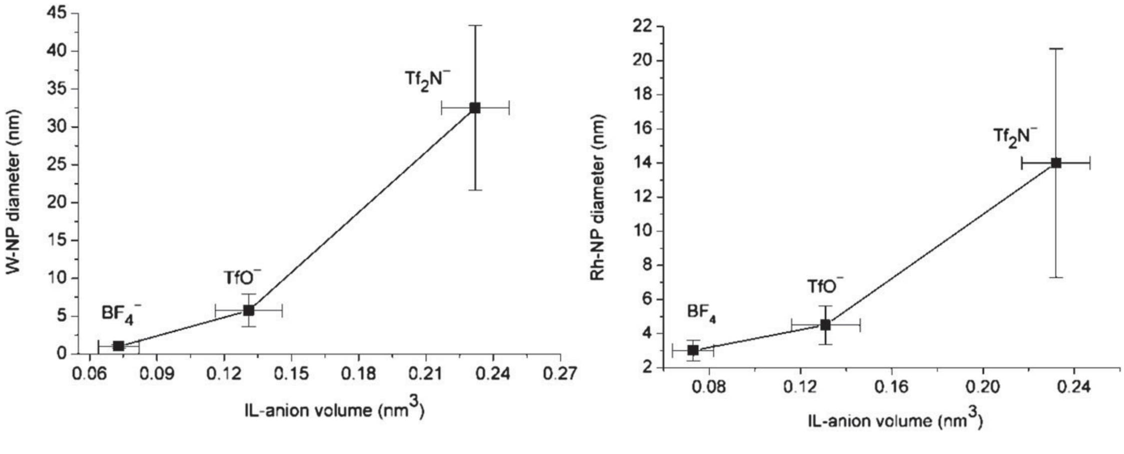

Fig. 10 Correlation between nanoparticle size of W- and Rh-NPs from TEM measurements and the IL anion molecular volume with standard deviation (1σ) as *error bars* [164, 165]. Left part is reproduced from Ref. [165] with permission, copyright 2008 The Royal Society of Chemistry; right part is adapted from Ref. [164] with permission, copyright 2009 Elsevier B.V.

time, of 24 h to obtain the copper nanoparticles while in $[C_4C_1Im][NO_3]$ dissociation of Cu flakes to Cu nanoparticles took place in about 5 min. It was suggested that the favorable interaction between free nitrate anion of $[C_4C_1Im][NO_3]$ and the Cu metal surface caused the flakes to dissociate in the ionic liquid, forming as much smaller nanoparticles than in the other ILs. From TEM the average diameter of the obtained Cu-NPs in $[C_4C_1Im][NO_3]$ was 10 nm [171] while the size range in $[C_4C_1Im][BF_4]$ was 50–100 nm [172] or 20–200 nm [124] and in $[C_4C_1Im][PF_6]$ and $[C_2C_1Im][BF_4]$ it was 80–100 nm [172]. Overall, these results suggested that the pristine micro-sized copper flakes were already clusters of primary nanoparticles, which were dis-agglomerated to nanoparticles by introduction in ILs to a different extent.

Decomposition of $Pd(OAc)_2$ in a series of hydroxyl-functionalized ionic liquids (ILs) with the 1-(2′-hydroxylethyl)-3-methylimidazolium cation $[HOC_2C_1Im]^+$ and the anions $[BF_4]^-$, $[PF_6]^-$, $[OTf]^-$ $[CF_3CO_2]^-$ ($[ATf]^-$) or $[NTf_2]^-$ gave Pd-NPs with slightly different medium diameters from 2.3 ± 0.4 nm in $[HOC_2C_1Im][ATf]$ or 2.4 ± 0.5 nm in $[HOC_2C_1Im][OTf]$ to 4.0 ± 0.6 nm in $[HOC_2C_1Im][BF_4]$ [124]. Noteworthy from comparison with the non-functionalized IL, $[C_4C_1Im][NTf_2]$ (medium diameter 6.2 ± 1.1 nm) significantly smaller nanoparticles were obtained. More importantly, the ease of formation of the Pd-NPs in the $[HOC_2C_1Im]^+$-based ILs followed the order $[NTf_2]^-$, $[PF_6]^- > [BF_4]^- > [OTf]^- > [ATf]^-$ based on the residual unreacted amount of $Pd(OAc)_2$ in the dispersion. This order does not relate to the stability towards aggregation. For this, it could only be noted that in $[HOC_2C_1Im][PF_6]$ a series of larger Pd-NPs over 8 nm (compared to the average 3.1 ± 0.7 nm) were also present and the Pd-NPs were least stable in this $[PF_6]^-$ IL. From the ratio of metallic Pd to PdO observed in the XPS the relative resistance of the Pd-NPs towards oxidation may be determined. The ability of the $[HOC_2C_1Im]^+$-ILs to prevent the Pd NPs from undergoing oxidation follows the trend $[NTf_2]^- > [PF_6]^- > [ATf]^- > [OTf]^- > [BF_4]^-$. For example, only 12.6% of PdO was present in the NPs isolated with the $[NTf_2]^-$-anion whereas nearly half the Pd amount was oxidized to PdO in the case of the $[BF_4]^-$-anion. Studies for $[PF_6]^-$ and $[NTf_2]^-$ showed that these are the least nucleophilic anions [173] and also the most hydrophobic ones in the series while $[BF_4]^-$ is the least hydrophobic/most hydrophilic one of the anions used in this comparison. Therefore, the oxidation-protecting effect may be accounted for by the fact that water and oxygen are repelled most by the $[PF_6]^-$ and $[NTf_2]^-$ anions [124].

Strong anion effects were seen on gold nanoparticle formation in ionic liquids of $[C_2C_1Im]^+$ with ethyl sulfate ($[EtSO_4]^-$), $[OTf]^-$ and methanesulfonate ($[CH_3SO_3]^-$) anions [78]. Face-centered cubic gold nanoparticles were grown by reduction of $HAuCl_4 \cdot 3H_2O$ with glycerol at temperatures between 120 and 180 °C. The $[CH_3SO_3]^-$ anion yielded nanoparticles with diameters between 5 and 7 nm, which increasingly aggregate at higher reaction temperatures but the primary particle size is not affected. Thus, the $[CH_3SO_3]^-$ anion or more accurate the anion-cation ($[C_2C_1Im]^+$) combination under the given reaction conditions is able to efficiently trap very small gold nanoparticles. High temperatures like 180 °C do not lead to a further growth of the particles, but rather to a controlled aggregation. From $[OTf]^-$ also small 5–7 nm particles formed, but only at low temperatures whereas above ca. 160 °C, large, ill-defined and aggregated particles were obtained. Apparently the $[OTf]^-$ anion is only partially able to stabilize small gold particles and above a certain reaction temperature the stabilization exerted by the IL is broken and led to larger aggregates. With the $[EtSO_4]^-$ anion polydisperse samples formed at all temperatures except 160 °C. In the temperature window around 160 °C individual, controlled ca. 15–20 nm particles were grown from $[C_2C_1Im][EtSO_4]$ [78].

It is evident from many reports on cation and anion effects of ILs that the interaction between an IL and a (growing) nanocrystal is far from understood but that a detailed understanding of the IL–nanoparticle interaction, of the thermodynamics and kinetics, and of the initial nucleation process would be needed for a more rational design of nanomaterials in ILs [78].

5.5 Alkyl Chain Effects

The interaction energies of ILs with different alkyl chain lengths ($[C_nC_1Im][NTf_2]$ ($n = 2, 4, 6, 8, 10$)), an additional alkyl group in the C-2 position of the imidazolium cation ($[C_4C_1C_1Im][NTf_2]$ with 1-butyl-2,3-dimethylimidazolium) and a *N*-butyl-*N*-methylpyrrolidinium cation ($[C_4C_1Pyrro][NTf_2]$) to Ru-NPs were compared by titration calorimetry and by molecular simulation. The interaction energy of $[C_nC_1Im][NTf_2]$ ($n = 6, 8, 10$) with Ru-NPs is larger than that of $[C_4C_1Im][NTf_2]$ indicating that longer alkyl side chains enhance the interactions with Ru-NPs. Here $[C_2C_1Im][NTf_2]$ also has stronger interactions with the nanoparticles, but this deviation was explained by the cation not having a significant nonpolar moiety. Structural information from the molecular simulation suggests that the alkyl chains tend to point away from the surface but are still within interaction range [128].

Trends for the influence of the alkyl chain length were invoked by many other research groups [174–177] such that the alkyl chain length has an influence of the particle size of M-NPs [21, 174]. In the well-designed series of mono- and dicationic imidazolium ILs with different alkyl chain length and $[NTf_2]^-$ as anion (Fig. 11) Ni-NPs were synthesized by spontaneous decomposition of [bis(1,5-cyclooctadiene)nickel(0)], $Ni(COD)_2$. Well dispersed Ni-NPs with a small mean size and narrow size distribution could be obtained. The Ni-NP size increased with increasing chain lengths from 2.4 ± 0.8 nm in $[C_{12}C_1Im][NTf_2]$ over 2.9 ± 0.4 nm in $[C_{18}C_1Im][NTf_2]$, 4.0 ± 0.5 nm in $[C_{12}C_{12}Im][NTf_2]$ about equal to 4.4 ± 0.7 nm in $[C_{12}C_1C_{12}Im][NTf_2]$, 5.4 ± 1.6 nm in $[C_{12}Im\text{-}\mu\text{-}C_6\text{-}ImC_{12}][NTf_2]$, (200 nanoparticle were measured in the first four cases, 50 NPs in the last case). When an ethereal oxygen donor atom was introduced in the functional IL $[C_{12}Im\text{-}\mu\text{-}C_2OC_2\text{-}ImC_{12}][NTf_2]$ the particle size decreased to 3.4 ± 0.2 nm (based on 200 NPs). In addition, formation of regularly interspaced NP arrays was also observed in such long chain ILs [174].

For Au-NPs in imidazolium-based ILs the particles diameter increases from 0.75 to 3.5 nm diameter for $[C_2C_1Im]^+$, $[C_4C_1Im]^+$ and $[C_8C_1Im]^+$ cations and $[BF_4]^-$ as counter ion [178, 179]. Further, decomposition of $Ni(COD)_2$ in $[C_nC_1Im][NTf_2]$ ILs gave Ni-NPs with an average diameter from 2.4 to 5.4 nm [174] or 4.9 to

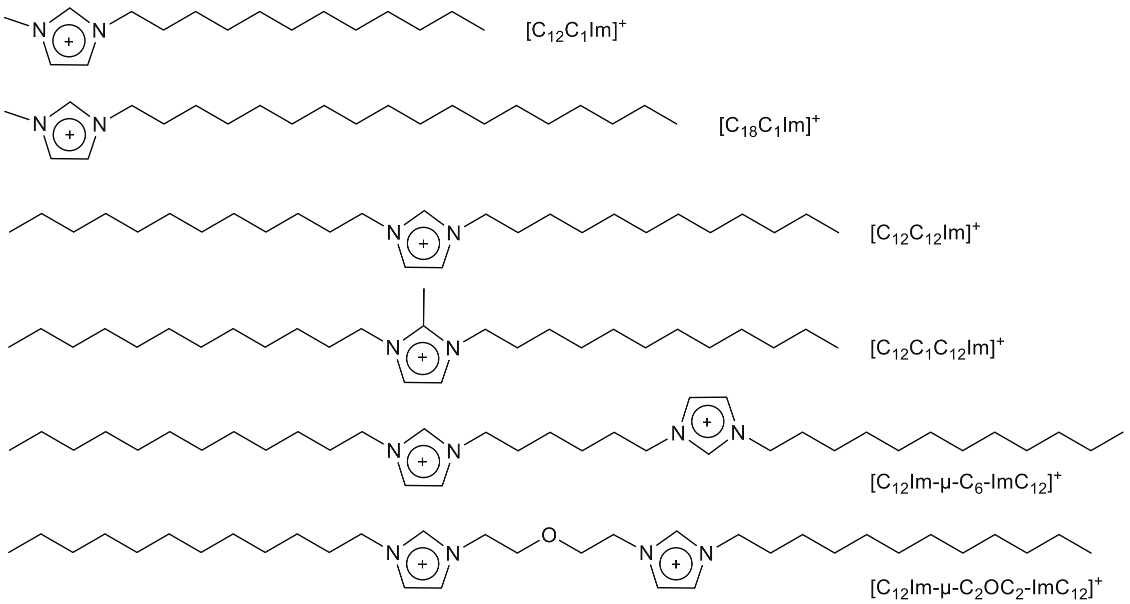

Fig. 11 Series of ionic liquid cations with increasing chain length and $[NTf_2]^-$ as the common anion used in the comparative synthesis of Ni-NPs from $Ni(COD)_2$ to elucidate the chain-length effect on the metal nanoparticle size [174]

5.9 nm [180] with conflicting trends such that the particle diameter increased or decreased with the cation size.

When interpreting such trends with seemingly small differences in nanoparticle size, the standard deviation σ of the size distribution must be considered, however. The, at first sight, slightly larger nanoparticle size may still well be within 1σ or certainly within 3σ of the average diameter of another size.

In another study, nickel nanoparticles were obtained by decomposition of $Ni(COD)_2$, again with different nanoparticle diameter, depending on the chain length of the imidazolium cation with $[NTf_2]^-$ as anion. The results were 5.9 ± 1.4 nm for $[C_4C_1Im]^+$, 5.6 ± 1.3 nm for $[C_8C_1Im]^+$, 4.9 ± 0.9 nm for $[C_{10}C_1Im]^+$, 5.1 ± 0.9 nm for $[C_{14}C_1Im]^+$ and 5.5 ± 1.1 nm for $[C_{16}C_1Im]^+$. While it may appear that an increase of the alkyl chain (from *n*-butyl to *n*-hexadecyl) induces the formation of nanoparticles with a smaller diameter and size-distribution, all distributions are strongly overlapped within their 1σ regions already. The differences in diameter and size distribution are relatively small and could be a TEM artefact (sample preparation and/or particle counting, for instance) as the authors admit themselves [180].

Table 2 illustrates that a change in imidazolium cation or rather in 1-*n*-alkyl chain length does not give a clear trend in the size of the Ni-NPs synthesized by nickel(II)-bis(amidinate) or $Ni(COD)_2$ precursor decomposition through microwave assisted heating. The size distributions overlap considerably already within the 1σ standard deviation. Only in the case of the $Ni(COD)_2$ precursor there is an indication of Ni-NP size increase from n-butyl over *n*-octyl to *n*-dodecyl which is reverse from the aforementioned trend [181].

In terms of stabilization, short alkyl-chain-methyl-imidazolium salts $[C_4C_1Im]^+$ with weakly coordinating perfluorinated counter anions ($[BF_4]^-$, $[PF_6]^-$ or $[NTf_2]^-$)

Table 2 Ni-NP diameter and distribution from different precursors and in different ILs

Ni-precursor[a], IL	TEM Ø (1σ) [nm][bc]
$[Ni(AMD)_2]$	
$[C_4C_1Im][BF_4]$	5 (±2)
$[C_{12}C_1MIm][BF_4]$	7 (±2)
$[C_4C_1Im][PF_6]$	7 (±4)
$[C_8C_1Im][PF_6]$	7 (±1)
$[C_{12}C_1Im][PF_6]$	9 (±3)
$[C_4C_1Im][NTf_2]$	10 (±2)
$[C_8C_1Im][NTf_2]$	10 (±3)
$[C_{12}C_1Im][NTf_2]$	10 (±4)
$Ni(COD)_2$	
$[C_4C_1Im][PF_6]$	8 (±3)
$[C_8C_1Im][PF_6]$	10 (±2)
$[C_{12}C_1Im][PF_6]$	15 (±2)

[a] 1.0 wt. % Ni-NP/IL dispersions obtained by microwave-assisted heating with 100 W for 10 min at 220 °C

[b] The size distribution was calculated from a manual diameter determination over a minimum of 50 isolated particles

[c] Average diameter and standard deviation

were qualitatively found to be better stabilizers compared to ILs with cations bearing long alkyl chains (trihexyltetradecylphosphonium $[P_{66614}]^+$, 1-octyl-3-methylimidazolium $[C_8C_1Im]^+$) and anions of higher coordination strength (dicyanamide, $[N(CN)_2]^-$) (see above). In $[C_4C_1Im]^+$ with $[BF_4]^-$, $[PF_6]^-$ or $[NTf_2]^-$ anions Au- or Cu-NPs were stable colloidal dispersions, that is, without precipitation or aggregation for 1 week to several weeks. In $[C_4C_1Im][N(CN)_2]$ Au-NPs were stable for 3 days. In comparison in $[C_8C_1Im][PF_6]$ or in $[P_{66614}][N(CN)_2]$ fast precipitation or stability for only 1 day, respectively, was observed due to fast particle growth and agglomeration [156].

5.6 Viscosity

Viscosity of the reaction medium can be expected to have a crucial influence on the growth and agglomeration of nanoparticles. Unfortunately, differences in viscosity cannot be treated separately from concomitant changes in alkyl chain length or anion. Thus, viscosity dependence for nanoparticle size and size distribution appears to be seldom addressed [64].

For example, for $[C_4C_1Im]^+$-ILs the viscosity at 30 °C follows the anion order $[PF_6]^- > [(F_5C_2SO_2)_2N]^- > [BF_4]^- > [OTf]^- > [CF_3CO_2]^- > [NTf_2]^-$, which is as expected opposite to the order of the diffusion coefficients (see above).

For the $[C_nC_1Im][BF_4]$ ($n = 2, 4, 6$) [182], $[C_nC_1Im][PF_6]$ ($n = 4$–9) and $[C_nC_1Im][NTf_2]$ ($n = 2$–10) series the viscosity increases with increasing the number n of carbon atoms in the linear alkyl chain in the imidazolium cation. However, the trends are quite different. An almost linear dependence of the viscosity as a function of the alkyl chain length group is observed for the $[NTf_2]^-$ ILs while the dependence for the $[PF_6]^-$ ILs is more like an exponential increase with a local maximum at $n = 7$. Also, the $[C_nC_1Im][PF_6]$ ionic liquids are much more viscous than their $[NTf_2]^-$ analogs [183].

6 Influence of Functional ILs to Metal Nanoparticles

Functionalized imidazolium ILs can be used to modify the surface of metal NPs [184, 185], in particular to provide stable dispersion of NPs in water [113, 186], which is important to many applications [187]. Thiol- [184, 188, 189], ether- [113], carboxylic acid- [115], amino- [190] and hydroxyl-functionalized imidazolium ILs are available (Fig. 12), for example, to prepare aqueous dispersions of noble metal NPs.

From comparison of the decomposition of $Pd(OAc)_2$ in a series of hydroxyl-functionalized ionic liquids (ILs) with the 1-(2′-hydroxylethyl)-3-methylimidazolium cation $[HOC_2C_1Im$ or $HOEMIm]^+$ and the anions $[BF_4]^-$, $[PF_6]^-$, $[OTf]^-$, $[CF_3CO_2]^-$ or $[NTf_2]^-$ and the non-functionalized IL, $[C_4C_1Im][NTf_2]$ it appeared that the hydroxyl group accelerated the formation of the NPs, and also helped to protect the NPs from oxidation once formed. Significantly smaller Pd-NPs were obtained in the $[HOEMIm$ or $HOC_2C_1Im]^+$-ILs with average diameters from 2.3 ± 0.4 nm in the $[CF_3CO_2]^-$ salt to 4.0 ± 0.6 nm in the $[BF_4]^-$ analog while in non-functionalized $[C_4C_1Im][NTf_2]$ the average diameter was 6.2 ± 1.1 nm [124].

An X-ray photoelectron spectroscopic study of purified aminoethyl-methylimidazolium bromide, $[H_2NC_2C_1Im$ or $AEMIm]Br$-stabilized Au-NPs suggested that both the imidazolium ring and the functional amino group were involved in the interaction with the NP surface (cf. Figure 4) [115]. A shift in binding energies in the peaks of the carbon and nitrogen atoms in the imidazolium ring and amino N atom and a change in the width of the N1 s peak were observed. The XPS results were interpreted as either an electrostatic interaction between the imidazolium cation and the negatively charged metal surface, an interaction between the amino group and surface metal atom or the simultaneous coordination of the imidazolium cation and the functional group with the metal NPs. The electrostatic imidazolium-metal interaction would change the positive charge density of the imidazole ring. Amino group coordination to the metal NPs surface would induce a shift in N atom binding energies in the peak of the amino group and a change in the width of the N1 s peak [115].

Comparison between the closely related di-cationic ILs $[C_{12}Im\text{-}\mu\text{-}C_6\text{-}ImC_{12}][NTf_2]$, and $[C_{12}Im\text{-}\mu\text{-}C_2OC_2\text{-}ImC_{12}][NTf_2]$ (cf. Figure 11) revealed a significant decrease in Ni-NP size (obtained from spontaneous decomposition of $Ni(COD)_2$) from 5.4 ± 1.6 nm to 3.4 ± 0.2 nm when an ethereal oxygen donor atom was introduced. This indicates a better templating and stabilization effect due to coordination of the negatively polarized O-atom on the metal surface [174].

The synthesis of Co-NPs and Mn-NPs by microwave-heating induced decomposition of the metal carbonyls $Co_2(CO)_8$ and $Mn_2(CO)_{10}$, respectively, yields smaller and better separated particles in the functionalized IL 1-(3-carboxyethyl)-3-methyl-imidazolium tetrafluoroborate $[CEMIm$ or $HO_2CC_2C_1Im][BF_4]$ (1.6 ± 0.3 and 4.3 ± 1.0 nm, respectively) than in the non-functionalized IL $[C_4C_1Im][BF_4]$. The particles are stable in the absence of capping ligands (surfactants) for more than 6 months although some variation in particle size could be observed by TEM (Fig. 13) [191].

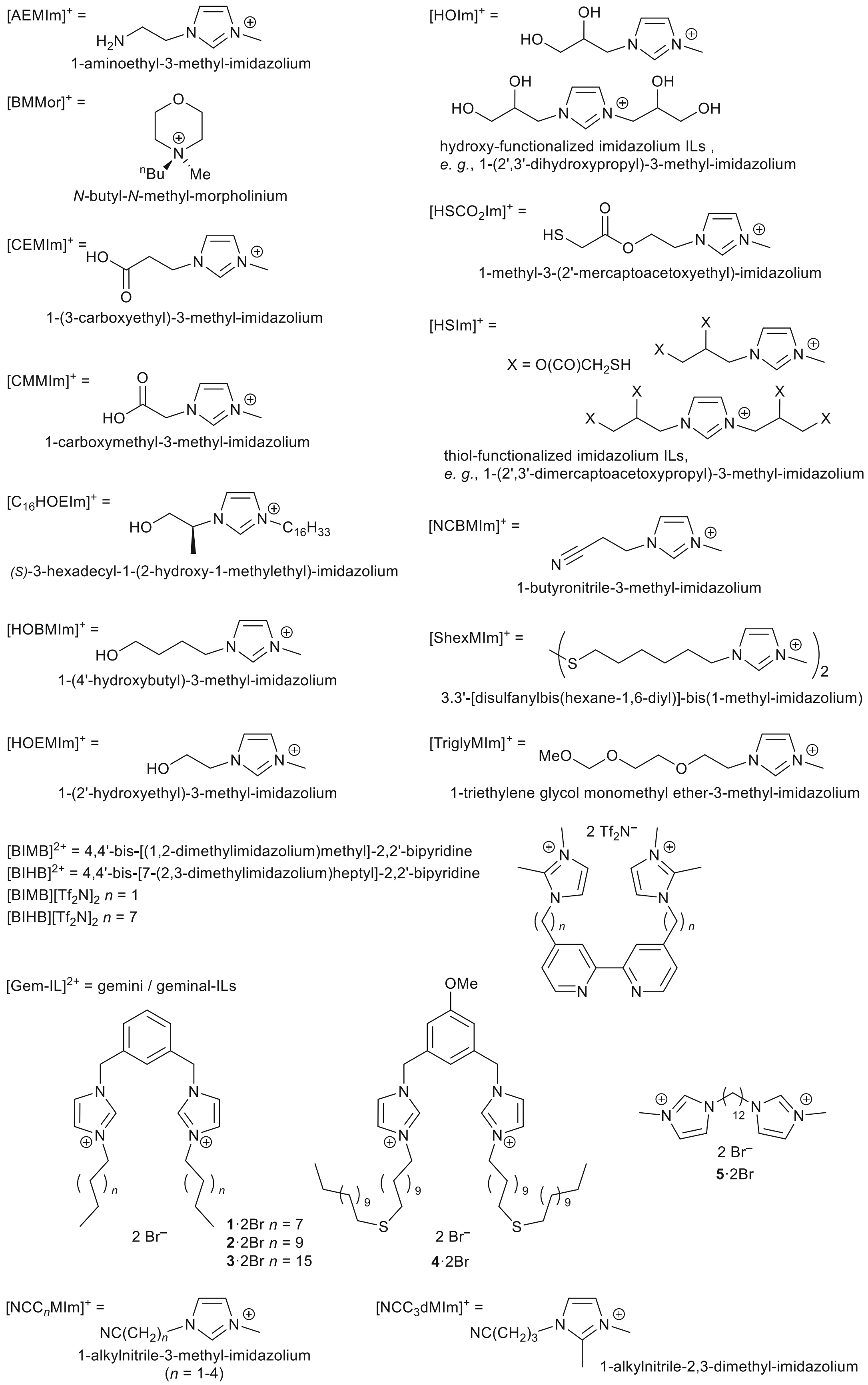

Fig. 12 Examples of functionalized imidazolium ILs. Graphical collection reprinted with permission from the author of Ref. [30]. Copyright Wiley-VCH 2013

A special type of functionalized ILs are gemini imidazolium amphiphiles (cf. Figure 12) [192]. Gemini-type ILs based on imidazolium salts are investigated as simultaneous nanoparticle stabilizers, surfactants and transfer agents into organic media. Au-NPs with imidazolium ligands of the gemini-ILs **1**·2Br to **4**·2Br (cf. Figure 12) that are stable in dispersion and where the IL plays a triple role: phase transfer of the gold precursor salt $H[AuCl_4]$ from an aqueous phase to toluene during the synthesis, stabilization of the gold colloid, and binding agent for an ibuprofenate guest. The bis-imidazolium IL ions around the gold nanoparticles do not exchange with thiolate ligands. When both species are present the gold surface prefers the IL cation and anion to thioether ligands. The long alkyl chains in **3**·2Br (cf. Figure 12) could incorporate ibuprofenate, a model for carboxylate-containing anionic drugs, and release it at a slower rate [192].

7 *N*-Heterocyclic Carbene Formation During Metal Nanoparticle Synthesis in Imidazolium ILs

During the last 20 years *N*-heterocyclic carbenes (NHCs) established themselves as a leading class of ligands in molecular organometallic chemistry [193]. NHCs are neutral electron-rich σ-donor ligands, which often form very strong metal ligand σ-bonds. These properties would also be very attractive for the stabilization and reactivity modulation of metal NPs [194–197]. NHCs have been proven to bind efficiently to the surfaces of Ru- [198–201], Ag- [202], Au- [202–205], Pd- [205, 206] and Pt-NPs [207]. Furthermore, there is evidence that NHCs could be intermediate species, by in situ deprotonation of the imidazolium cation at the acidic C2-H position when NPs are formed and stabilized in imidazolium-based ionic liquids for Au-NPs [208], Pd-NPs [208, 209], Rh-NPs [210], Ir-NPs [210, 211] and Ni-NPs [212].

NHC-stabilization of Au- and Pd-NPs was promoted by deprotonation of the bis(*N*,*N*'-*n*-hexyl)imidazolium cation $[C_6C_6Im]^+$ prior to reduction. This was achieved by treating the imidazolium salt $[C_6C_6Im]^+{}_n[MCl_4]^{n-}$ with sodium

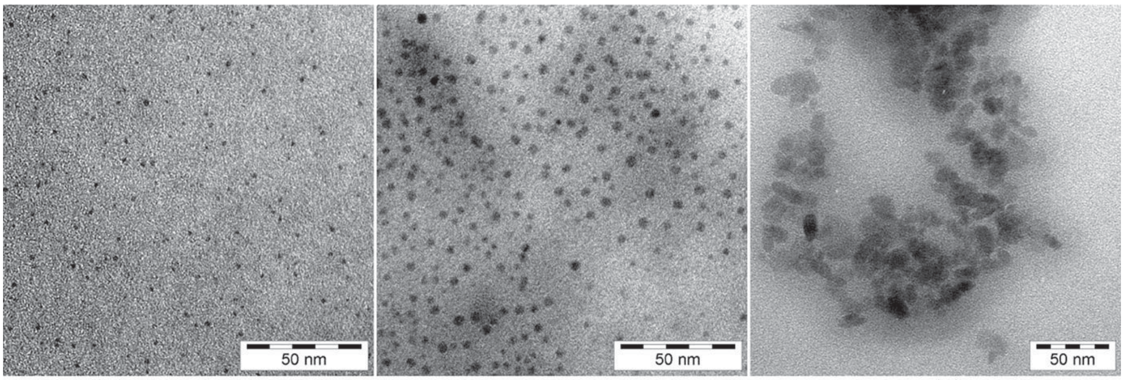

(a) (b) (c)

Fig. 13 TEM-images of Co-NPs in $[CEMIm\ or\ HO_2CC_2C_1Im][BF_4]$ (cf. Figure 12) **a** 6 weeks after synthesis; **b** 6 months after synthesis; **c** Co-NPs from $Co_2(CO)_8$ in [BMIm]$[BF_4]$. Reprinted with permission. Copyright the Royal Society of Chemistry, 2011 [191] hydride in 1: 1 dichloromethane–toluene, before adding sodium borohydride to reduce the tetrachloridoaurate(III) ($n = 1$) and dibromidodichloridopalladate(II) ($n = 2$) metal precursor. The ^{1}H NMR spectrum of the Au-NPs revealed the disappearance of the acidic imidazolium C2 proton resonance, while broadening and splitting was observed for the other peaks, which is typical of NP-coordinated ligands. ^{13}C NMR also failed to locate a peak for C2, which is probably due to anisotropy resulting from the NHC to Au-NP surface coordination. Conversely, the C2 ^{1}H peak was observed for the Pd-NPs produced without prior imidazolium deprotonation. TEM analysis gave slightly larger sizes of 2.7 ± 0.9 nm for the NHC-capped Pd-NPs than for the imidazolium halide surfactant stabilized Pd-NPs with 1.8 ± 0.4 nm [208].

The Pd-NHC complex (C_4C_1Im-NHC)Pd(PPh_3)X (X = Br, Cl) formed from [Pd(Ar)Br(PPh_3)$_2$] and [$PdCl_2(PPh_3)_2$] in [C_4C_1Im][BF_4] when aqueous Na_2CO_3 was added for imidazolium deprotonation [209].

NHC complexes of rhodium and iridium were obtained in neat [C_4C_1Im][NTf_2] from metal complexes with basic anionic ligands, [M(COD)(PPh_3)X], X = OEt, $MeCO_2$, which reacted with the imidazolium cation under deprotonation giving the M-NHC moiety and the free protonated base HOEt, $MeCO_2H$ [210].

The synthesis of Ir nanoparticles by reduction of [(COD)Ir(CH_3CN)$_2$]BF_4 with H_2 or D_2 in the presence of Proton Sponge (PS^{TM}) in acetone with set but variable amounts of [C_4C_1Im][NTf_2] gave evidence for the formation of at least transiently surface-ligand-coordinated NHCs. When using D_2 deuterium incorporation was apparent from ^{2}H NMR spectroscopy at the imidazolium C2-H, C4-H, C5-H, and butyl –(CH_2CH_2)C8–H(CH_3) positions of the [C_4C_1Im]$^+$ cation. Conversely, ^{1}H NMR spectra showed a decreased intensity of the 2-, 4-, 5-, and 8-H hydrogens in the [C_4C_1Im]$^+$ cation. Without the presence of Ir-NPs no D incorporation into the imidazolium cation occured. A sequence of N-heterocyclic carbene formation by oxidative addition of the imidazolium cation, followed by H/D scrambling atop the nanoparticle surface, then reductive elimination of a imidazolium-C-D bond is suggested [211].

During the auto-decomposition of Ni(COD)$_2$ in imidazolium ILs the formation of bis(imidazolylidene)nickel complexes [(NHC)$_2$NiH]$^+$ was detected by mass spectrometry [212].

8 Conclusion

In the last years many different M-NPs (monometallic and bimetallic) in ILs were obtained. Especially ILs with imidazolium cations feature prominently in the formation and stabilization of M-NPs. Such imidazolium ILs simultaneously act as reaction media, hydrogen sources, catalysts, templating agents and stabilizers for the synthesis of metal nanoparticles.

Various and also yet unknown factors influence the stability of nanoparticles in ionic liquids and lead to nanoparticle size and/or morphology changes during synthesis. An improved understanding of the stability of nanoparticle dispersions in ionic liquids is still needed to assist efforts directed toward the synthesis of nanoparticles with controlled size and morphology in ionic liquids.

An influence of the anion to metal nanoparticles was also observed by several other research groups. Qualitatively, the size of M-NPs was found to increase with the molecular volume of the anion of the IL. Also, an influence of the imidazolium alkyl-chain length on the particle size of M-NPs is often invoked, yet the unclear direction. It is both found that the NP size increased with increasing chain lengths whereas in other studies an increase of the alkyl chain gave nanoparticles with a smaller diameter and size-distribution.

It is evident from many reports on cation and anion effects of ILs that the interaction between an IL and a (growing) nanocrystal is far from understood but that a detailed understanding of the IL–nanoparticle interaction would be needed for a more rational design of nanomaterials in ILs.

Furthermore, thiol-, ether-, carboxylic acid-, amino- and hydroxyl-functionalized ILs can be used to coordinate to the surface of metal NPs akin to the action of coordinating capping ligands. Also, for imidazolium-based ionic liquids there is evidence that *N*-heterocyclic carbenes, NHCs could be formed by in situ deprotonation of the imidazolium cation at the acidic C2-H position, at least as intermediate species, during the nanoparticle seeding and growth process.

References

1. Sankar M, Dimitratos N, Miedziak PJ, Wells PP, Kiely CJ, Hutchings GJ (2012) Chem Soc Rev 41:8099–8139
2. Turkevich J, Stevenson PC, Hillier J (1951) Discuss Faraday Soc 11:55–75
3. Brust M, Walker M, Bethell D, Schriffrin DJ, Whyman RJ (1994) J Chem Soc Chem Commun 801–802
4. Bönnemann H, Braun G, Brijoux W, Brinkmann R, Schulze Tilling A, Seevogel K, Siepen K (1996) J Organomet Chem 520:143–162
5. Aiken JD III, Finke RG (1999) J Mol Catal A 145:1–44
6. Schmid G (2001) Nanoscale materials in chemistry In: Klabunde KJ (ed) Wiley-Interscience, New York, p 15
7. Faraday M (1857) Philos Trans R Soc. London 147:145–181
8. Manojkumar K, Sivaramakrishna A, Vijayakrishna K (2016) J Nanopart Res 18:103–125
9. Lu AH, Salabas EL, Schüth F (2007) Angew Chem Int Ed 46:1222–1244
10. Feldheim DL, Foss CA (2001) Metal nanoparticles: synthesis, characterization and applications. Taylor and Francis, London
11. Bruchez M, Moronne M, Gin P, Weiss S, Alivisatos AP (1998) Science 281:2013–2016
12. Saha K, Agasti SS, Kim C, Li X, Rotello VM (2012) Chem Rev 112:2739–2779
13. Li JH, Zhang JZ (2009) Coord Chem Rev 253:3015–3041
14. Barnes WL, Dereux A, Ebbesen TW (2003) Nature 424:824–830
15. Poizot P, Laruelle S, Grugeon S, Dupont L, Tarascon JM (2000) Nature 407:496–499
16. Armelao L, Quici S, Barigelletti F, Accorsi G, Bottaro G, Cavazzini M, Tondello E (2010) Coord Chem Rev 254:487–505
17. Navalon S, Dhakshinamoorthy A, Alvaro M, Garcia H (2016) Coord Chem Rev 312:99–148
18. Walker JM, Zaleski JM (2016) Nanoscale 8:1535–1544
19. Zhao P, Feng X, Huang D, Yang G, Astruc D (2015) Coord Chem Rev 287:114–136
20. Redel E, Thomann R, Janiak C (2008) Inorg Chem 47:14–16

21. Migowski P, Zanchet D, Machado G, Gelesky MA, Teixeira SR, Dupont J (2010) Phys Chem Chem Phys 12:6826–6833
22. Pachon LD, Rothenberg G (2008) Appl Organomet Chem 22:288–299
23. Lee W, Scholz R, Nielsch K, Gösele U (2005) Angew Chem 117:6204–6208
24. Davar F, Loghman-Estarki MR, Salavati-Niasari M, Mazaheri M (2016) J Clust Sci 27:593–603
25. Wang H, Xu JZ, Zhu JJ, Chen HY (2002) J Cryst Growth 244:88–94
26. Chen WX, Lee JY, Liu Z (2002) Chem Commun 2588-2589
27. Sreeju N, Rufus A, Philip D (2016) J Mol Liq 221:1008–1021
28. Qin Y, Ji X, Jing J, Liu H, Wu H, Yang W (2010) Colloids Surf A 372:172–176
29. Goesmann H, Feldmann C (2010) Angew Chem Int Ed 49:1362–1395
30. Janiak C (2013) Z Naturforschung B 68:1059–1089. doi:10.5560/ZNB.2013-3140
31. Hostetler MJ, Wingate JE, Zhong C-J, Harris JE, Vachet RW, Clark MR, Londono JD, Green SJ, Stokes JJ, Wignall GD, Glish GL, Porter MD, Evans ND, Murray RW (1998) Langmuir 14:17–30
32. Templeton AC, Wuelfing WP, Murray RW (2000) Acc Chem Res 33:27–36
33. Weare WW, Reed SM, Warner MG, Hutchison JE (2000) J Am Chem Soc 122:12890–12891
34. Schmid G, Pfeil R, Boese R, Bandermann F, Meyer S, Calis GHM, van der Velden JWA (1981) Chem Ber 114:3634–3642
35. Yang J, Deivaraj TC, Too H-P, Lee JY (2004) Langmuir 20:4241–4245
36. Pan C, Pelzer K, Philippot K, Chaudret B, Dassenoy F, Lecante P, Casanove MJ (2001) J Am Chem Soc 123:7584–7593
37. Lee CL, Wan CC, Wang YY (2001) Adv Funct Mater 11:344–347
38. Tiwari AK, Gangopadhyay S, Chang CH, Pande S, Saha SK (2015) J Colloid Interface Sci 445:76–83
39. Esumi K, Hara J, Aihara N, Usui K, Torigoe K (1998) J Colloid Interface Sci 208:578–581
40. Xu J, Hu J, Peng C, Liu H, Hu Y (2006) J Colloid Interface Sci 298:689–693
41. Bakshi MS, Sharma P, Banipal TS (2007) Mater Lett 61:5004–5009
42. Song C, Wu D, Zhang F, Liu P, Lu Q, Feng X (2012) Chem Commun 48:2119–2121
43. Kumar KS, Vasuki R, Priya R (2016) J Pharm Techn 8:12130–12143
44. Demir MM, Gulgun MA, Menceloglu YZ, Erman B, Abramchuk SS, Makhaeva EE, Khokhlov AR, Matveeva VG, Sulman MG (2004) Macromolecules 37:1787–1792
45. Crespy D, Landfester K (2009) Polymer 50:1616–1620
46. Huang H, Yang X (2004) Carbohydr Res 339:2627–2631
47. Vollmer C, Janiak C (2011) Coord Chem Rev 255:2039–2057
48. Wender H, Migowski P, Feil AF, Teixeira SR, Dupont J (2013) Coord Chem Rev 257:2468–2483
49. Welton T (2004) Coord Chem Rev 248:2459–2477
50. Welton T (1999) Chem Rev 99:2071–2083
51. Hallett JP, Welton TT (2011) Chem Rev 111:3508–3576
52. Morris RE (2009) Chem Commun 2990–2998
53. Voronchikhina LI, Zhuralev OE, Verolainen NV, Krotova NI (2016) Russ J Gen Chem 86:1314–1318
54. Villanueva M, Coronas A, Garcia J, Salgado J (2013) Ind Eng Chem Res 52:15718–15727
55. Kosmulski M, Gustafsson J, Rosenholm JB (2004) Thermochim Acta 412:47–53
56. Ngo HL, LeCompte K, Hargens L, McEwen AB (2000) Thermochim Acta 357–358:97–102
57. Chen G, Kang S, Ma Q, Chen W, Tang Y (2014) Magn Reson Chem 52:673–679
58. Craig SL (2009) Angew Chem Int Ed 48:2645–2647
59. Daniel MC, Astruc D (2004) Chem Rev 104:246–293
60. Parvulescu VI, Hardacre C (2007) Chem Rev 107:2615–2665
61. Steinrück HP, Wasserscheid P (2015) Catal Lett 145:380–397
62. Freudenmann D, Wolf S, Wolff M (2011) Feldmann C. Angew Chem 123:11244–11255
63. Dupont J, de Souza RF, Suarez PAZ (2002) Chem Rev 102:3667–3691
64. Tokuda H, Hayamizu K, Ishii K (2005) Susan MdABH, Watanabe M. J Phys Chem B 109:6103–6110
65. Dupont J, Scholten JD (2010) Chem Soc Rev 39:1780–1804
66. Marcos Esteban R, Janiak C (2017) In Nanocatalysis in Ionic Liquids In: Prechtl M (ed) chapter 8. Wiley-VCH, Weinheim, p 147–169
67. Janiak C (2014) in Catalysis in ionic liquids: from catalyst synthesis to application In: Hardacre C, Parvulescu V, chapter 11. RSC Publishing, Cambridge, p 537–577
68. Janiak C (2015) Topics Organomet Chem 51:17–53. doi:10.1007/3418_2013_70

69. Antonietti M, Kuang D, Smarsly B, Zhou Y (2004) Angew Chem Int Ed 43:4988–4992
70. Fonseca GS, Umpierre AP, Fichtner PFP, Teixeira SR, Dupont J (2003) Chem Eur J 9:3263–3269
71. Huang J, Jiang T, Han B, Gao H, Chang Y, Zhao G, Wu W (2003) Chem Commun 1654-1655
72. Krämer J, Redel E, Thomann R, Janiak C (2008) Organometallics 27:1976–1978
73. Silveira ET, Umpierre AP, Rossi LM, Machado G, Morais J, Soares GV, Baumvol IJR, Teixeira SR, Fichtner PFP, Dupont J (2004) Chem Eur J 10:3734–3740
74. Redel E, Walter M, Thomann R, Hussein L, Krüger M, Janiak C (2010) Chem Commun 46:1159–1161
75. Stellaci F, Bauer CA, Meyer-Friedrichsen T, Wenseleers W, Alain V, Kuebler SM, Pond SJK, Zhang Y, Marder SR, Perry JW (2002) Adv Mater 14:194–198
76. Mohan B, Woo H, Jang S, Lee S, Park S, Park KH (2013) Solid State Sci 22:16–20
77. Zhang B, Yuan Y, Philippot K, Yan N (2015) Catal Sci Technol 5:1683–1692
78. Khare V, Li Z, Mantion A, Ayi AA, Sonkaria S, Voelkl A, Thünemann AF, Taubert A (2010) J Mater Chem 20:1332–1339
79. Jiang HY, Zheng HH (2015) Appl Cat A 499:118–123
80. Dewan M, De A (2015) Mozumdar. Inorg Chem Commun 53:92–96
81. Esteban RM, Meyer H, Kim J, Gemel C, Fischer RA, Janiak C (2016) Eur J Inorg Chem 2106-2113
82. Schütte K, Meyer H, Gemel C, Barthel J, Fischer RA, Janiak C (2014) Nanoscale 6:3116–3126
83. Esteban RM, Schütte K, Brandt P, Marquardt D, Meyer H, Beckert F, Mülhaupt R, Kölling H, Janiak C (2015) Nano-Struct Nano-Objects 2:11–18
84. Ayi AA, Anyama CA, Khare V (2015) J Mat, vol. 2015, Article ID 372716, http://dx.doi.org/10.1155/2015/372716
85. Andanson JM, Marx S, Baiker A (2012) Catal Sci Technol 2:1403–1409
86. Schütte K, Doddi A, Kroll C, Meyer H, Wiktor C, Gemel C, van Tendeloo G, Fischer RA, Janiak C (2014) Nanoscale 6:5532–5544
87. Wegner S, Saito M, Barthel J, Janiak C (2016) J Organomet Chem 821:192–196
88. Wang Y, Yang H (2005) J Am Chem Soc 127:5316–5317
89. Arquillière PP, Helgadottir IS, Santini CC, Haumesser P-H, Aouine M, Massin L, Rousset J-L (2013) Top Catal 56:1192–1198
90. Dash P, Dehm NA, Scott RWJ (2008) J Mol Catal A 286:114–119
91. Stankus DP, Lohse SE, Hutchison JE, Nason JA (2010) Environ Sci Technol 45:3238–3244
92. Astruc D (2008) Nanoparticles and catalysis. Wiley Online Library, Weinheim
93. Jiang J, Oberdörster G, Biswas P (2009) J Nanopart Res 11:77–89
94. Kim T, Lee K, Gong M-s, Joo S-W (2005) Langmuir 21:9524–9528
95. Derjaguin B, Landau L (1940) Acta Phys Chem USSR 14:1–30
96. Verwey EJW, Overbeek JThG (1948) Theory of the stability of lyophobic colloids. Elsevier, Amsterdam
97. Li Q, Jonas U, Zhao XS, Kappl M (2008) Asia-Pac J Chem Eng 3:255–268. doi:10.1002/apj.144
98. Ninham BW (1999) Adv Col Interf Sci 83:1–17
99. Raveendran P, Fu J, Wallen SL (2003) J Am Chem Soc 125:13940–13941
100. Verwey EJW, Overbeek JTG (1999) Theory of the stability of lyophobic colloids. Dover Publications Mineola, New York
101. Finke RG (2002) Metal nanoparticle: synthesis, characterization and applications. Marcel Dekker, New York
102. Ott LS, Finke RG (2006) Inorg Chem 45:8283–8393
103. Boström M, Williams DRW, Ninham BW (2001) Phys Rev Lett 87:168103–168107
104. Liang Y, Hilal N, Langston P, Starov V (2007) Adv Col Interf Sci 134–135:151–166
105. Sarkar B, Venugopal V, Tsianou M, Alexandridis P (2013) Col Surf 422:155–164
106. Napper DH (1977) J Col Interf Sci 58:390–407
107. Lin Y, Smith TW, Alexandridis P (2002) J Col Interf Sci 255:1–9
108. Luckham PF (1991) Adv Col Interf Sci 34:191–215
109. Morrison ID, Ross S (2002) Colloidal dispersions: suspensions, emulsions, and foams. Wiley-Interscience, New York
110. Zhao M, Li N, Zheng L, Li G, Yu L (2008) J Dispers Sci Technol 29:1103–1105
111. Obliosca JM, Arellano IHJ, Huang MH, Arco SD (2010) Mater Lett 64:1109–1112
112. Rubim JC, Trindade FA, Gelesky MA, Aroca RF, Dupont J (2008) J Phys Chem C 112:19670–19675

113. Schrekker HS, Gelesky MA, Stracke MP, Schrekker CML, Machado G, Teixeira SR, Rubim JC, Dupont J (2007) J Col Interf Sci 316:189–195
114. Chun YS, Shin JY, Song CE, Lee SG (2008) Chem Commun 942–944
115. Zhang H, Cui H (2009) Langmuir 25:2604–2612
116. Scheeren CW, Machado G, Teixeira SR, Morais J, Domingos JB, Dupont J (2006) J Phys Chem B 110:13011–13020
117. Fonseca GS, Machado G, Teixeira SR, Fecher GH, Morais J, Alves MCM, Dupont J (2006) J Col Interf Sci 301:193–204
118. Kang SW, Char K, Kang YS (2008) Chem Mater 20:1308–1311
119. Redel E, Walter M, Thomann R, Vollmer C, Hussein L, Scherer H, Krüger M, Janiak C (2009) Chem Eur J 15:10047–10059
120. Pearson RG (1997) Chemical hardness. Application from molecules to solids. Wiley-VCH, Weinheim
121. Baker TA, Friend CM, Kaxiras E (2008) J Am Chem Soc 130:3720–3721
122. Katsyuba SA, Zvereva EE, Yan N, Yuan X, Kou Y, Dyson PJ (2012) ChemPhysChem 13:1781–1790
123. Kim J, Kang SW, Mun SH, Kang YS (2009) Ind Eng Chem Res 48:7437–7441
124. Yuan X, Yan N, Katsyuba SA, Zvereva EE, Kou Y, Dyson PJ (2012) Phys Chem Chem Phys 14:6026–6033
125. He Z, Alexandridis P (2015) Phys Chem Chem Phys 17:18238–18261
126. Kang X, Sun X, Han B (2016) Adv Mater 28:1011–1030
127. Vanecht E, Binnemans K, Patskovsky S, Meunier M, Seo JW, Stappers L, Fransaer J (2012) Phys Chem Chem Phys 14:5662–5671
128. Podgorsek A, Pensado A, Santini C, Gomes M, Padua A (2013) J Phys Chem C 117:3537–3547
129. Frolov AI, Kirchner K, Kirchner T, Fedorov MV (2012) Faraday Discuss 154:235–247
130. Cheng P, Liu C, Yang Y, Huang S (2015) Chem Phys 452:1–8
131. Pensado AS, Padua AAH (2011) Angew Chem 123:8842–8846
132. Knapp R, Wyrzgol SA, Reichelt M, Hammer T, Morgner H, Müller TE, Lercher JA (2010) J Phys Chem C 114:13722–13729
133. Bernardi F, Scholten JD, Fecher GH, Dupont J, Morais J (2009) Chem Phys Lett 479:113–116
134. Rosen MJ, Kunjappu JT (2012) Surfactants and Interfacial Phenomena. Wiley, Weinheim
135. Li Q, Li A (2012) Asian J Chem 24:847–850
136. Wender H, de Oliveira LF, Migowski P, Feil AF, Lissner E, Prechtl MHG, Teixeira SR, Dupont J (2010) J Phys Chem C 114:11764–11768
137. Torimoto T, Okazaki KI, Kiyama T, Hirahara K, Tanaka N, Kuwabata S (2006) Appl Phys Lett 89:243117
138. Hatakeyama Y, Okamoto M, Torimoto T, Kuwabata S, Nishikawa K (2009) J Phys Chem C 113:3917–3922
139. Kessler MT, Hentschel MK, Heinrichs C, Roitsch S, Prechtl MHG (2014) RSC Adv 4:14149–14156
140. Scariot M, Silva DO, Scholten JD, Machado G, Teixeira SR, Novak MA, Ebeling G, Dupont J (2008) Angew Chem Int Ed 47:9075–9078
141. Wang L, Chang L, Zhao B, Yuan Z, Shao G, Zheng W (2008) Inorg Chem 47:1443–1452
142. Li X, Liu Y, Guo W, Chen J, He W, Peng F (2014) Electrochim Acta 135:550–557
143. Lorbeer C, Cybinska J, Mudring AV (2014) J Mater Chem C 2:1862–1868
144. Patil AB, Bhanage BM (2014) Phys Chem Chem Phys 16:3027–3035
145. Liu CH, Mao BH, Gao J, Zhang S, Gao X, Liu Z, Lee ST, Sun XH, Wang SD (2012) Carbon 50:3008–3014
146. Hatakeyama Y, Takahashi S, Nishikawa K (2010) J Phys Chem C 114:11098–11102
147. Kameyama T, Ohno Y, Kurimoto T, Okazaki KI, Uematsu T, Kuwabata S, Torimoto T (2010) Phys Chem Chem Phys 12:1804–1811
148. Tsuzuki S, Tokuda H, Hayamizu K, Watanabe M (2005) J Phys Chem B 109:16474–16481
149. Hardacre C, Holbrey JD, McMath SEJ, Bowron DT, Soper AK (2003) J Chem Phys 118:273–278
150. Dupont J, Suarez PAZ (2006) Phys Chem Chem Phys 8:2441–2452
151. Gozzo FC, Santos LS, Augusti R, Consorti CS, Dupont J, Eberlin MN (2004) Chem Eur J 10:6187–6193
152. Neto BAD, Santos LS, Nachtigall FM, Eberlin MN, Dupont J (2006) Angew Chem 118:7409–7412
153. Dupont J (2011) Acc Chem Res 44:1223–1231
154. Dong K, Zhang SJ (2012) Chem Eur J 18:2748–2761

155. Chang HC, Hung TC, Chang SC, Jiang JC, Lin SH (2011) J Phys Chem C 115:11962–11967
156. Richter K, Birkner A, Mudring AV (2011) Phys Chem Chem Phys 13:7105–7110
157. Wittmar A, Ulbricht M (2012) Ind Eng Chem Res 51:8425–8433
158. Dupont J (2004) J Braz Chem Soc 15:341–350
159. Schröder U, Wadhawan JD, Compton RG, Marken F, Suarez PAZ, Consorti CS, de Souza RF, Dupont J (2000) New J Chem 24:1009–1015
160. Tokuda H, Hayamizu K, Ishii K, Hasan Susan MdAB, Watanabe M (2004) J Phys Chem B 108:16593–16600
161. Anderson JL, Armstrong DW (2003) Anal Chem 75:4851–4858
162. Lopes JNA, Padua AAH (2006) J Phys Chem B 110:3330–3335
163. Reddy RG (2006) J Phase Equilib Diffus 27:210–211
164. Redel E, Krämer J, Thomann R, Janiak C (2009) J Organomet Chem 694:1069–1075
165. Redel E, Thomann R, Janiak C (2008) Chem Commun 15:1789–1791
166. Neouze MA (2010) J Mater Chem 20:9593–9607
167. Peng H, Lin L, Ding G (2015) Energy 89:410–420
168. Navolotskaya DV, Toh HS, Batchelor-McAuley C, Compton RG (2015) ChemistryOpen 4:595–599
169. Wang XM, Zhou DD, Zou QQ, Xia YY (2012) J Mater Chem 22:15418–15426
170. Keul HA, Ryu HJ, Möller M, Bockstaller MR (2011) Phys Chem Chem Phys 13:13572–13578
171. Hong GH, Kang SW (2013) Ind Eng Chem Res 52:794–797
172. Han KI, Kang SW, Kim J, Kang YS (2011) J Membr Sci 374:43–48
173. Lancaster NL, Welton T (2004) J Org Chem 69:5986–5992
174. Yang M, Campbell PS, Santini CC, Mudring AV (2014) Nanoscale 6:3367–3375
175. Gutel T, Santini CC, Philippot K, Padua A, Pelzer K, Chaudret B, Chauvin Y, Basset JM (2009) J Mater Chem 19:3624–3631
176. Banerjee A, Theron R, Scott RWJ (2012) ChemSusChem 5:109–116
177. Jacquemin J, Husson P, Majer V, Costa Gomes MF (2007) J Solut Chem 36:967–979
178. Hatakeyama Y, Okamoto M, Torimoto T, Kuwabata S, Nishikawa K (2009) J Phys Chem C 113:3917–3922
179. Hatakeyama Y, Onishi K, Nishikawa K (2011) RSC Adv 1:1815–1821
180. Migowski P, Machado G, Texeira SR, Alves MCM, Morais J, Traverse A, Dupont J (2007) Phys Chem Chem Phys 9:4814–4821
181. Wegner S, Rutz C, Schütte K, Barthel J, Bushmelev A, Schmidt A, Dilchert K, Fischer RA, Janiak C (2017) Chem Eur J 23:6330–6340 (http://dx.doi.org/10.1002/chem.201605251)
182. Wittmar A, Gajda M, Gautam D, Dörfler U, Winterer M, Ulbricht M (2013) J Nanopart Res 15:1–12
183. Dzyuba S, Bartsch RA (2002) ChemPhysChem 2:161–166
184. Itoh H, Naka K, Chujo Y (2004) J Am Chem Soc 126:3026–3027
185. Chen H, Dong S (2007) Langmuir 23:12503–12507
186. Wei GT, Yang Z, Lee CY, Yang HY, Wang CRC (2004) J Am Chem Soc 126:5036–5037
187. Lewis LN (1993) Chem Rev 93:2693–2730
188. Kim KS, Demberelnyamba D, Lee H (2004) Langmuir 20:556–560
189. Gao S, Zhang H, Wang X, Mai W, Peng C, Ge L (2005) Nanotechnology 16:1234–1237
190. Marcilla R, Mecerreyes D, Odriozola I, Pomposo JA, Rodriguez J (2007) NANO Br Rep Rev 2:169–173
191. Marquardt D, Xie Z, Taubert A, Thomann R, Janiak C (2011) Dalton Trans 40:8290–8293
192. Casal-Dujat L, Rodrigues M, Yagüe A, Calpena AC, Amabilino DB, Gonzalez-Linares J, Borras M, Perez-Garcia L (2012) Langmuir 28:2368–2381
193. Diez-Gonzalez S, Marion N, Nolan SP (2009) Chem Rev 109:3612–3676
194. Richter C, Schaepe K, Glorius F, Ravoo BJ (2014) Chem Commun 50:3204–3207
195. Magna L, Chauvin Y, Niccolai GP, Basset JM (2003) Organometallics 22:4418–4425
196. Lecocq V, Olivier-Bourbigou H (2007) Oil Gas Sci Technol 62:761–773
197. Holloczki O, Gerhard D, Massone K, Szarvas L, Nemeth B, Veszpremi T, Nyulaszi L (2010) New J Chem 34:3004–3009
198. Martinez-Prieto LM, Ferry A, Lara P, Richter C, Philippot K, Glorius F, Chaudret B (2015) Chem Eur J 21:17495–17502
199. Martinez-Prieto LM, Urbaneja CC, Palma P, Campora J, Philippot K, Chaudret B (2015) Chem Commun 51:4647–4650
200. Lara P, Rivada-Wheelaghan O, Conejero S, Poteau R, Philippot K, Chaudret B (2011) Angew Chem Int Ed 50:12286–12290

201. Gonzalez-Galvez D, Lara P, Rivada-Wheelaghan O, Conejero S, Chaudret B, Philippot K, van Leeuwen PWNM (2013) Catal Sci Technol 3:99–105
202. Ling X, Schaeffer N, Roland S, Pileni M (2013) Langmuir 29:12647–12656
203. Roland S, Ling X, Pileni MP (2016) Langmuir 32:7683–7696
204. Vignolle J, Tilley TD (2009) Chem Commun 7230–7232
205. Hurst EC, Wilson K, Fairlamb IJS, Chechik V (2009) New J Chem 33:1837–1840
206. Rühling A, Schaepe K, Rakers L, Vonhören B, Tegeder P, Ravoo BJ, Glorius F (2016) Angew Chem Int Ed 55:5856–5860
207. Baquero EA, Tricard S, Flores JC, de Jesus E, Chaudret B (2014) Angew Chem Int Ed 53:1–6
208. Serpell CJ, Cookson J, Thompson AL, Brown CM, Beer PD (2013) Dalton Trans 42:1385–1393
209. Mathews CJ, Smith PJ, Welton T, White AJP, Williams DJ (2001) Organometallics 20:3848
210. Hintermair U, Gutel T, Slawin AMZ, Cole-Hamilton DJ, Santini CC, Chauvin Y (2008) J Organomet Chem 693:2407–2414
211. Ott LS, Cline ML, Deetlefs M, Seddon KR, Finke RG (2005) J Am Chem Soc 127:5758–5759
212. Prechtl MHG, Campbell PS, Scholten JD, Fraser GB, Machado G, Santini CC, Dupont J, Chauvin Y (2010) Nanoscale 2:2601–2606

2. Motivation

Die vorliegende Arbeit setzt sich Schwerpunktmäßig mit der Synthese von mono – und intermetallischen Nanopartikeln in ionischen Flüssigkeiten auseinander. Des Weiteren wird in dieser Arbeit näher auf die Stabilisierung von Nanopartikeln und insbesondere auf die Wechselwirkungen zwischen Nanopartikeln und ILs eingegangen (Abschnitt 1.1).

Zur Synthese von monometallischen Nanopartikeln sind bereits in der Diplomarbeit Ni Nanopartikel aus bis{*N*,*N'*-Diisopropylacetamidinat}nickel(II) ($[\mathrm{Ni}\{\mathrm{MeC}(\mathrm{N}i\mathrm{Pr})_2\}_2]$) in verschiedenen ILs synthetisiert worden [3] und der Zusammenhang zwischen der Variation der Kationen, Anionen sowie der Alkylkettenlänge und der Morphologie der Nanopartikel untersucht worden. Die Forschung an diesen Ni Nanopartikeln sollte in der Promotion fortgeführt werden. Dafür sollte in der vorliegenden Arbeit untersucht werden, inwieweit die Wahl des Ni Precursors ($[\mathrm{Ni}\{\mathrm{MeC}(\mathrm{N}i\mathrm{Pr})_2\}_2]$ oder $[\mathrm{Ni(COD)_2}]$) Einfluss auf die Größe der Nanopartikel nimmt und wie sich die Partikelgrößen der Ni-NPs aus den unterschiedlichen Precursoren in der gleichen IL unterscheiden. Ebenfalls untersucht werden sollten die magnetischen Eigenschaften sehr kleiner < 5 nm großer Ni-NPs und größerer, > 10 nm großer Ni-NPs (Abschnitt 3.1).

Die Synthesen intermetallischer Nanopartikel sollten aus den Single-Source Vorläuferverbindungen eines neutralen Triple-Decker Ruthenocens und eines anionischen Ruthenocens, beide mit einem Stannolliganden, geschehen und dabei untersucht werden, inwieweit sich durch die mikrowellengestützte Synthese bimetallische Ru/Sn-NPs in der IL $[\mathrm{BMIm}][\mathrm{BF_4}]$ darstellen lassen (Abschnitt 3.2). Beide Precursoren wurden im Rahmen einer Kooperation mit der Saitama Universität in Japan, von Herrn Prof. Dr. Masaichi Saito erhalten. Des Weiteren sollten diese Ru/Sn-NPs auf eine mögliche katalytische Anwendung, vor allem in Bezug auf Semihydrierung, hin untersucht werden (Abschnitt 4.2.2). Durch die Kooperation mit Herrn Prof. Dr. Saito war es ferner möglich, von ihm einen (cod)Rh-Stannol-RuCp* heterotrimetallischen Triple-Decker Komplex zu erhalten, aus dem sowohl durch mikrowellengestützte Zersetzung des Precursors als auch durch Hydrierung bei milden Bedingungen Ru/Rh/Sn-NPs synthetisiert werden sollten (Abschnitt 4.3).

3. Kumulativer Teil

Die Abschnitte 3.1 und 3.2 beinhalten die Ergebnisse der Dissertation, die in Form von Veröffentlichungen bei internationalen Journalen publiziert wurden und kumulativ dargestellt werden. Jede Veröffentlichung steht mit eigenem Quellenverzeichnis für sich. Ein kurzer Überblick über die Veröffentlichung und der Anteil des Autors an der Arbeit zu dieser Publikation sind dem jeweiligen Kapitel vorangestellt.

3.1 Soft, Wet-Chemical Synthesis of Metastable Superparamagnetic Hexagonal Close-Packed Nickel Nanoparticles in Different Ionic Liquids

Susann Wegner, Christina Rutz, Kai Schütte, Juri Barthel, Alexey Bushmelev, Annette Schmidt, Katharina Dilchert, Roland A. Fischer, Christoph Janiak

Chem. Eur. J. **2017**, *23*, 6330-6340.
DOI: 10.1002/chem.201605251, Quelle [2]

Die mikrowelleninduzierte Zersetzung von bis{*N,N'*-Diisopropylacetamidinat}nickel(II) ($[Ni\{MeC(N\textit{i}Pr)_2\}_2]$) oder bis(1,5-Cyclooctadien)nickel(0) ($[Ni(COD)_2]$) in Imidazolium-, Pyridinium- oder Thiophenium-basierten ionischen Flüssigkeiten (ILs) mit verschiedenen Anionen (Tetrafluoroborat, $[BF_4]^-$, Hexafluorophosphat,, $[PF_6]^-$ und Bis(trifluromethylsulfonyl)-imid, $[NTf_2]^-$) liefert kleine, einheitliche Nickel-Nanopartikel (Ni NPs), welche für mehr als acht Wochen in Abwesenheit von Capping Liganden (Tensiden) stabil sind. Die milde, nasschemische Synthese liefert die metastabile Ni-hexagonale dicht gepackte Phase (hcp) und nicht die stabile flächenzentrierte kubische Phase (fcc). Die Größe der Nickel Nanopartikelsteigt mit dem molekularen Volumen der Anionen von ca. 5 nm für $[BF_4]^-$ bis 10 nm für $[NTf_2]^-$ (mit 1-Alkyl-3-methyl-imidazolium-Kationen). N-Butyl-pyrdinium, $[BPy]^+$, Kation-ILs liefern reproduzierbar sehr kleine Ni Nanopartikel mit einem mittleren Durchmesser von 2 (±1) nm. Die Ni NPs wurden mittels hochauflösender Transmissions-Elektronen-Mikroskopie (HR-TEM) und Röntgenpulverdiffraktometrie. Eine Röntgenphotoelektronenspektroskopie (XPS) Analyse zeigt eine Erhöhung der Bindungsenergie (EB) der Elektronen aus dem Ni $2p_{3/2}$-Orbital der sehr kleinen kleinen 2 (±1) nm großen Ni Nanopartikel um ca. 0,3 eV bis EB = 853,2 eV im Vergleich zu Bulk Ni0, was auf die kleine Cluster Größe zurückzuführen ist. Die Nickel Nanopartikel zeigen von 150 K bis Raumtemperatur superparamagnetisches Verhalten. Die Sättigungsmagnetisierung einer Ni (2±1 nm) Probe aus $[BPy][NTf_2]$ ergibt 2,08 A m^2 kg^{-1} und einer Ni (10±4 nm) Probe aus $[LMIm][NTf_2)$ 0,99 A m^2 kg^{-1} ([LMIm] = 1-Lauryl-3-methylimidazolium). Die Ni NPs waren aktive Katalysatoren für die 1-Hexen- oder Benzolhydrierung in IL-Dispersionen. Über 90% Umsatz wurden für 1-Hexen unter 5 bar H_2 in 1 h bei 100 °C und einer Umsatzhäufigkeit (TOF) bis zu 1330 $mol_{Hexan}(mol_{Ni})^{-1}h^{-1}$ erreicht und für Benzol in 60 h bei 100 °C eine TOF bis zu 23 $mol_{Cyclohexan}(mol_{Ni})^{-1}h^{-1}$.

Anteil an der Veröffentlichung:

- Die Synthese des Precursors $[Ni\{MeC(N\textit{i}Pr)_2\}_2]$, die mikrowelleninduzierte Zersetzung desselben zu Ni Nanopartikeln sowie die Synthesen der ILs erfolgten bereits im Rahmen der Diplomarbeit [3]. Ebenso wurde der Zusammenhang zwischen Anionen- bzw. Kationengröße und der Alkylkettenlänge in Bezug auf die Größe der Nickel Nanopartikel in der Diplomarbeit vorgestellt. Die Hydrierungen von 1-Hexen und Benzol sind ebenfalls bereits in der Diplomarbeit durchgeführt worden.
- Schreiben der Publikation und Konzipierung sowie die dazu erforderliche Literaturrecherche. Bearbeitung des Manuskripts und Durchführung weiterer erforderlicher Synthesearbeiten und Auswertung dieser nach Revision.
- TEM- und PXRD-Aufnahmen sowie Auswertungen zu den Ni NPs aus $[Ni\{MeC(N\textit{i}Pr)_2\}_2]$.
- Die Unterstützung bei den HR-TEM-Aufnahmen sowie Berechnungen der Gitterparameter erfolgte über Herrn Dr. Juri Barthel.
- Die Synthese des Precursors $[Ni(COD)_2]$ sowie die Zersetzung zu Ni NPs daraus und die Ergebnisse zu diesem Precursor und den daraus entstandenen Ni NPs sind von Herrn Dr. Kai Schütte beigetragen worden.
- Ein Teil des Precursors $[Ni(COD)_2]$ wurde im Rahmen des DFG Forschungsschwerpunktprogramms SPP 1708 von Frau Katharina Dilchert und Herrn Prof. Dr. Roland A. Fischer zur Verfügung gestellt.
- Die Charakterisierung der ILs über Ionenchromatographie und die Bestimmung des Wassergehaltes der ILs mittels Karl-Fischer-Titration wurden von Frau Dr. Christina Rutz durchgeführt.
- Die magnetischen Messungen und Auswertungen dazu wurden von Herrn Dr. Alexey Bushmelev und Frau Prof. Dr. Annette Schmidt durchgeführt.
- Die Korrekturen des Manuskripts erfolgten über Herrn Prof. Dr. Christoph Janiak, ebenso erfolgte die Koordination zwischen den Co-Autoren über ihn.

ChemPubSoc Europe

DOI: 10.1002/chem.201605251

CHEMISTRY
A European Journal
Full Paper

Magnetic Nanoparticles

Soft, Wet-Chemical Synthesis of Metastable Superparamagnetic Hexagonal Close-Packed Nickel Nanoparticles in Different Ionic Liquids

Susann Wegner,[a] Christina Rutz,[a] Kai Schütte,[a] Juri Barthel,[b] Alexey Bushmelev,[c] Annette Schmidt,[c] Katharina Dilchert,[d] Roland A. Fischer,[d] and Christoph Janiak*[a]

Dedicated to Professor Walter Frank on the occasion of his 60th birthday

Abstract: The microwave-induced decomposition of bis{*N*,*N'*-diisopropylacetamidinate}nickel(II) [Ni{MeC(N*i*Pr)$_2$}$_2$] or bis(1,5-cyclooctadiene)nickel(0) [Ni(COD)$_2$] in imidazolium-, pyridinium-, or thiophenium-based ionic liquids (ILs) with different anions (tetrafluoroborate, $[BF_4]^-$, hexafluorophosphate, $[PF_6]^-$, and bis(trifluoromethylsulfonyl)imide, $[NTf_2]^-$) yields small, uniform nickel nanoparticles (Ni NPs), which are stable in the absence of capping ligands (surfactants) for more than eight weeks. The soft, wet-chemical synthesis yields the metastable Ni hexagonal close-packed (hcp) and not the stable Ni face-centered cubic (fcc) phase. The size of the nickel nanoparticles increases with the molecular volume of the used anions from about 5 nm for $[BF_4]^-$ to ≈10 nm for $[NTf_2]^-$ (with 1-alkyl-3-methyl-imidazolium cations). The *n*-butyl-pyridinium, $[BPy]^+$, cation ILs reproducibly yield very small nickel nanoparticles of 2(±1) nm average diameter. The Ni NPs were characterized by high-resolution transmission electron microscopy (HR-TEM) and powder X-ray diffraction. An X-ray photoelectron spectroscopic (XPS) analysis shows an increase of the binding energy (E_B) of the electron from the Ni $2p_{3/2}$ orbital of the very small 2(±1) nm diameter Ni particles by about 0.3 eV to $E_B = 853.2$ eV compared with bulk Ni^0, which is traced to the small cluster size. The Ni nanoparticles show superparamagnetic behavior from 150 K up to room temperature. The saturation magnetization of a Ni (2±1 nm) sample from [BPy][NTf$_2$] is 2.08 $A\,m^2\,kg^{-1}$ and of a Ni (10±4 nm) sample from [LMIm][NTf$_2$] it is 0.99 $A\,m^2\,kg^{-1}$, ([LMIm] = 1-lauryl-3-methylimidazolium). The Ni NPs were active catalysts in IL dispersions for 1-hexene or benzene hydrogenation. Over 90% conversion was reached under 5 bar H_2 in 1 h at 100 °C for 1-hexene and a turnover frequency (TOF) up to 1330 $mol_{hexane}(mol_{Ni})^{-1}\,h^{-1}$ or in 60 h at 100 °C for benzene hydrogenation and TOF = 23 $mol_{cyclohexane}(mol_{Ni})^{-1}\,h^{-1}$.

Introduction

Nickel nanoparticles are widely used as catalysts, for example, in reductive hydrogenation[1] or Suzuki coupling reactions.[2,3] Also, applications as sensor electrodes[4] or anode materials in fuel cells[5] or as a graphene–nickel nanoparticle hybrids for the enrichment of proteins and peptides have been reported.[6] Functionalized nickel nanoparticles show a cytotoxic effect against leukemia cancer cells.[7]

Soft, wet-chemical synthesis in organic solvents from metal–organic complexes is an important route to nanometals and allows the preparation of metals and alloys in the nanometer scale regime.[8–11] Metal amidinates (Scheme 1) have been investigated and widely used as precursors for metal nanoparticles[12,13] and thin metal films in low-pressure chemical vapor deposition (CVD) or atomic layer deposition (ALD).[14,15]

Zero-valent organometallic compounds such as [Ru(COD)(COT)] and [Ni(COD)$_2$] (COD = 1,5-cyclooctadiene, COT = 1,3,5-cyclooctatriene) are already employed as metal nanoparticles precursors in imidazolium-based ionic liquids (ILs).[16–20] Hydrogen has been used to hydrogenate the ligands COD and COT to cyclooctane, which was subsequently lost from the Ru^0 or Ni^0 metal atom and removed under reduced pressure from the reaction mixture.

For nickel nanoparticle synthesis, we selected and compared different ionic liquids as reaction media for the following reasons. In recent years ionic liquids have been developed as an alternative to traditional solvents.[21,22] They appear particularly

---

[a] S. Wegner, Dr. C. Rutz, Dr. K. Schütte, Prof. Dr. C. Janiak
Institut für Anorganische Chemie und Strukturchemie, Heine-Universität Düsseldorf, 40204 Düsseldorf (Germany)
E-mail: janiak@uni-duesseldorf.de

[b] Dr. J. Barthel
Gemeinschaftslabor für Elektronenmikroskopie RWTH-Aachen
Ernst Ruska-Centrum für Mikroskopie und Spektroskopie mit Elektronen, 52425 Jülich (Germany)

[c] Dr. A. Bushmelev, Prof. Dr. A. Schmidt
Physical Chemistry Department, University of Cologne
Luxemburger Str. 116, 50939 Cologne (Germany)

[d] K. Dilchert, Prof. Dr. R. A. Fischer
Lehrstuhl für Anorganische und Metallorganische Chemie
TU München, Lichtenbergstr. 4, 85748 Garching (Germany)

Supporting information and the ORCID identification number for the author of this article can be found under: http://dx.doi.org/10.1002/chem.201605251.

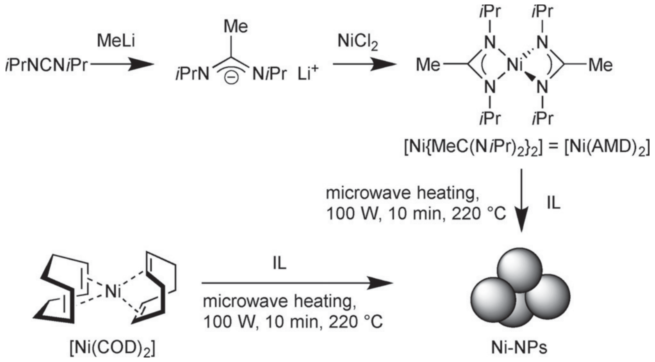

Scheme 1. Synthesis of nickel nanoparticles, Ni NPs, from nickel amidinate $[Ni\{MeC(NiPr)_2\}_2]$, in short $[Ni(AMD)_2]$, or $[Ni(COD)_2]$ by microwave-assisted thermal decomposition in ILs.

suited for the preparation of metal nanoparticles (M NPs).[23–25] The ionothermal synthesis in ionic liquids appears highly promising, because of IL properties such as negligible vapor pressure, high thermal stability, high ionic conductivity, a broad liquid-state temperature range, and the ability to dissolve a variety of materials.[23,26–35] Ionic liquids, especially with imidazolium cations (Scheme 2), are reported for the preparation and stabilization of metal nanoparticles,[23] which were prepared from metal salts with[36,37] or without reducing H_2 gas,[12,38] from organometallic π-complexes,[16–20,39,40] and from metal carbonyls[41,42,43] through thermal or photochemical[44] decomposition or electroreduction/electrodeposition.[23,45] The electrostatic and steric properties of ionic liquids allow for the stabilization of M NPs without the need of additional stabilizers, surfactants, or capping ligands.[23–26,37–46]

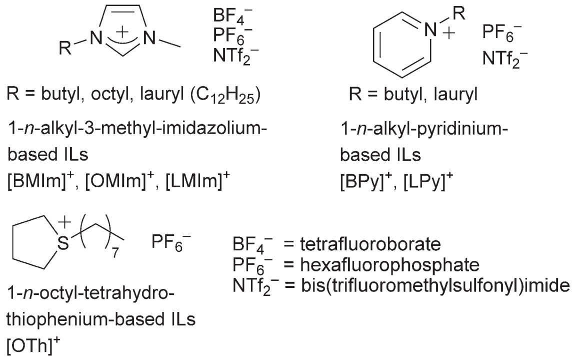

Scheme 2. Ionic liquids used here for nickel nanoparticle synthesis and stabilization (lauryl = dodecyl).

Herein, we compare nickel(II) amidinate $[Ni\{MeC(NiPr)_2\}_2]$, in short $[Ni(AMD)_2]$, and $[Ni(COD)_2]$ (Scheme 1) as precursors in different ionic liquids to yield nickel nanoparticles as stable colloids. The different ILs contained the cations 1-*n*-butyl-, 1-*n*-octyl-, and 1-*n*-lauryl-3-methyl-imidazolium, 1-*n*-butyl- and 1-*n*-lauryl-pyridinium, and 1-*n*-octyl-tetrahydrothiophenium in combination with tetrafluoroborate $[BF_4]^-$, hexafluorophosphate $[PF_6]^-$, and bis(trifluoromethylsulfonyl)imide $[NTf_2]^-$ anions (Scheme 2). No additional capping agents were used during particle synthesis.

Results and Discussion

Ni NPs in imidazolium-based ILs

Bis{*N*,*N*′-diisopropylacetamidinate}nickel(II), $[Ni(AMD)_2]$ or bis(1,5-cyclooctadiene)nickel(0), $[Ni(COD)_2]$ were dissolved or suspended under a nitrogen atmosphere in dried and deoxygenated ionic liquid. Complete decomposition by microwave (MW) heating of both precursors in IL was achieved after only 10 min when using a low power of 100 W to give an approximate temperature of 220 °C in the reaction mixture (Scheme 1).

Comparative NMR analyses of selected neat ILs before and after 10 min microwave heating to approximately 220 °C indicated no IL decomposition (see Figures S5.1–S5.9 in the Supporting Information). Black Ni NP/IL dispersions were reproducibly obtained by repeated decompositions of $[Ni(AMD)_2]$ or $[Ni(COD)_2]$. ^1H NMR analysis after the decomposition of the nickel amidinate in $[BMIm][NTf_2]$ shows signals in addition to the IL (Figure S1.1b in the Supporting Information), which we assign to the formation of 1-butyl-3-methylimidazoliumylidene from 2-H deprotonation of the 1-butyl-3-methylimidazolium cation by amidinate to give *N*,*N*′-diisopropylacetamidine according to Equation (S1) in the Supporting Information. GC/MS analysis of a hexane extract of the IL dispersion after decomposition gave as the only non-IL peak $m/z = 97$, which is assigned to $[MeC(NiPr)_2{-}HiPr]^+$.

For $[Ni(COD)_2]$, there were only very minor signals in the NMR analyses after decomposition (Figure S1.2 in the Supporting Information). More clear was the observation of 1,5-COD and 1,3-COD at $m/z = 108$ by GC/MS in a hexane extract of the IL dispersion after decomposition, together with cyclooctene at m/z 110. The differentiation of 1,5-COD and 1,3-COD was achieved by their difference in GC retention times upon comparison with genuine COD samples. The formation of 1,5- and 1,3-COD was already reported by Prechtl et al. from the spontaneous decomposition of $[Ni(COD)_2]$ in [EMIm] and [BMIm] $[NTf_2]$.[47]

Analyses of the Ni NP/IL dispersions by high-resolution transmission electron microscopy (HR-TEM; Figure 1, Figure 2, Figure 3, and Figures S2 and S3 in the Supporting Information) indicate the formation of Ni nanoparticles with typical diameters between 5 and 10 nm for imidazolium ILs with $[BF_4]^-$, $[PF_6]^-$, and $[NTf_2]^-$ anions (Table 1). Because of their superparamagnetic behavior, the samples show agglomerated, but still isolated particles. In direct comparison, both precursors yield Ni NPs of very similar size. In the imidazolium ILs, the at first sight slightly larger nanoparticle size from $[Ni(COD)_2]$ than from $[Ni(AMD)_2]$ is still well within the experimental error (see also Figure 6). Thus, the nature of the Ni precursor does not affect the nanoparticle size.

Work by others has shown that decomposition of $[Ni(COD)_2]$ in 1-alkyl-3-methyl-imidazolium ILs with different alkyl chain lengths and the bis(trifluoromethylsulfonyl)imide anion gave

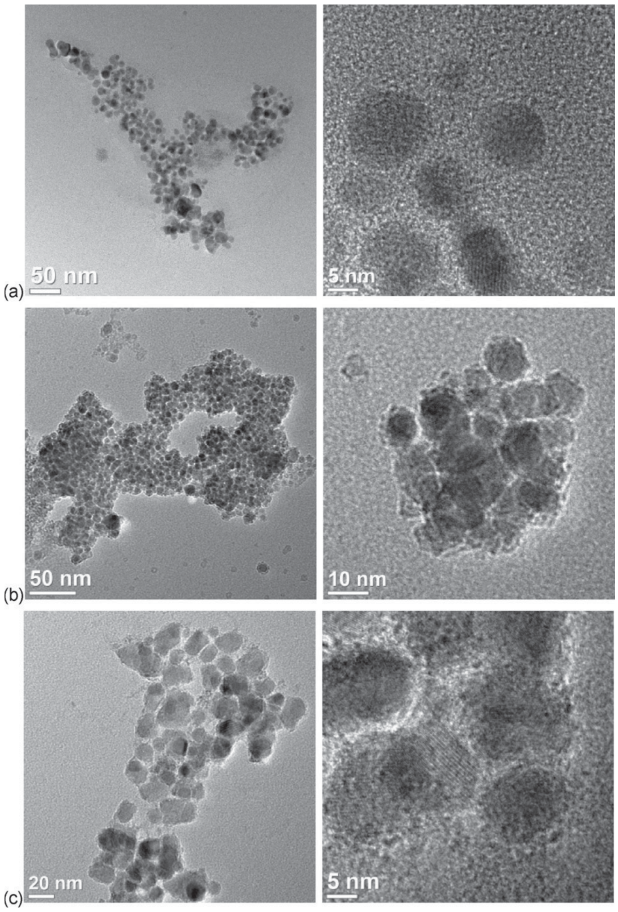

Figure 1. TEM images of 1.0 wt% Ni NP/IL dispersions from [Ni(AMD)$_2$] for [BMIm]$^+$ cations with: a) [BF$_4$]$^-$, b) [PF$_6$]$^-$, and c) [NTf$_2$]$^-$ anions. For images of Ni NP/IL dispersions from [Ni(COD)$_2$], see Figures S3.1–S3.7 in the Supporting Information.

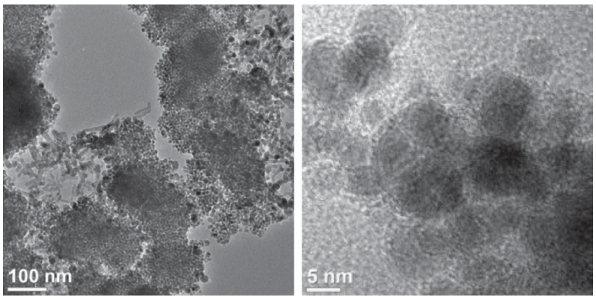

Figure 2. TEM images of Ni NP/IL dispersions from [Ni(AMD)$_2$] in [OMIm][PF$_6$]. For images of Ni NP/IL dispersions from [Ni(COD)$_2$], see Figure S3.8 in the Supporting Information.

Ni NPs with an average diameter of 2.4–5.4 nm[49] or 4.9–5.9 nm.[16]

Prechtl et al. observed spontaneous decomposition of [Ni(COD)$_2$] in the ILs [EMIm][NTf$_2$] and [BMIm][NTf$_2$] with the formation of 1,5- and 1,3-COD. It was concluded that decomposition of [Ni(COD)$_2$] in imidazolium ILs with short alkyl chains involved attack on the acidic C2–H and formation of the respective N-heterocyclic carbene (NHC) on the Ni NP surface

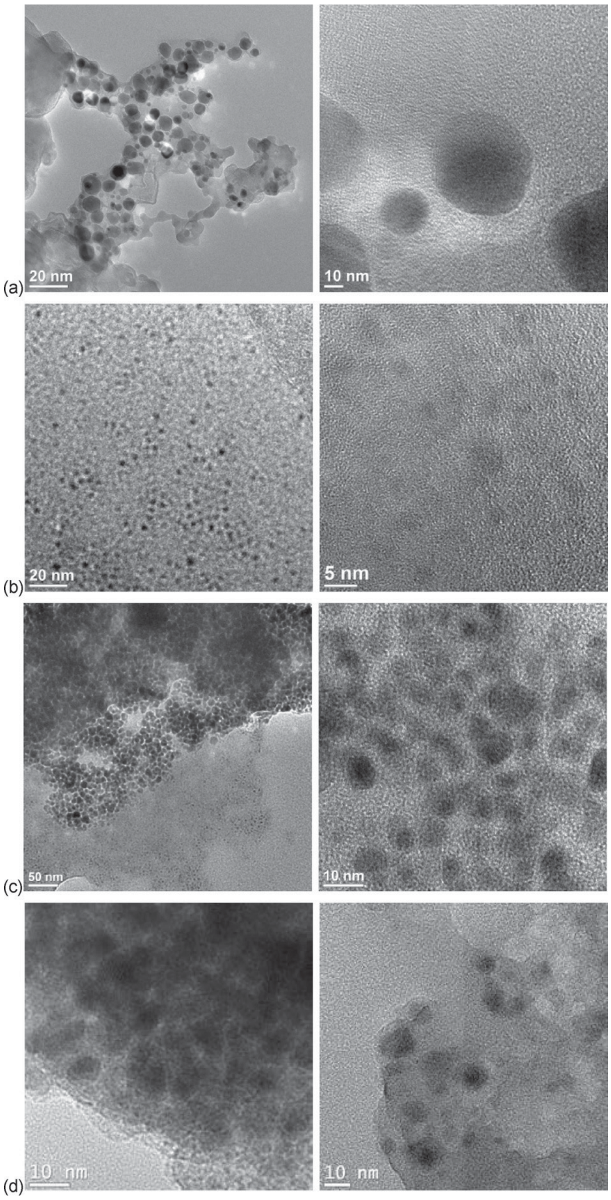

Figure 3. TEM images of 1.0 wt% Ni NP/IL dispersions from [Ni(AMD)$_2$] for [LMIm]$^+$ cations with: a) [BF$_4$]$^-$, b) [PF$_6$]$^-$, and c) [NTf$_2$]$^-$ anions. For images of Ni NP/IL dispersions from [Ni(COD)$_2$], see Figure S3.11 in the Supporting Information. d) TEM images of 1.0 wt% Ni NP/IL dispersions from [Ni(AMD)$_2$] (left) and [Ni(COD)$_2$] (right) with addition of 5.0 wt% KF to [BMIm][NTf$_2$].

was proposed.[47] Such surface-coordinated NHC formation was also reported for Ir^0 NPs formed from [(1,5-COD)Ir(CH$_3$CN)$_2$]BF$_4$ under H$_2$ in the presence of a proton sponge (PS) in acetone in the IL [BMIm][NTf$_2$].[50]

A combined TEM and energy dispersive X-ray spectroscopic analysis (EDX, Figure 4) shows only the expected nickel emission lines. The peaks in the powder X-ray diffractogram (PXRD, Figure 5) are positively matched to metastable hexagonal close-packed (hcp) nickel metal with space group *P*6$_3$/*mmc*. The stable bulk nickel metal phase is face-centered cubic (fcc) or body-centered cubic (bcc).[2,51,52] Also, Ni NPs (2 nm diameter) stabilized with ethylene glycol[53] and Ni NPs (10–36 nm diameter) stabilized with the cationic surfactants cetyltrimethy-

Table 1. Ni NP crystal phase, diameter, and distribution from different precursors and in different ILs.[a]

Ni precursor,[a] IL	Phase[b]	TEM Ø (σ) [nm][c]	Image
Imidazolium cations			
A, [BMIm][BF$_4$]	Ni	5(±2)	Figure 1 a
B, [BMIm][BF$_4$]	Ni	5(±2)	Figure S3.1
A, [BMIm][PF$_6$]	Ni	7(±4)	Figure 1 b, S2.1
B, [BMIm][PF$_6$]	n.d.	8(±3)	Figure S3.4
A, [BMIm][NTf$_2$]	Ni	10(±2)	Figure 1 c, S2.3
B, [BMIm][NTf$_2$]	Ni	11(±2)	Figure S3.6
A, [OMIm][PF$_6$]	Ni[d] (NiF$_2$)[d]	7(±1)	Figure 2, S2.7
B, [OMIm][PF$_6$]	n.d.	10(±2)	Figure S3.8
A, [OMIm][NTf$_2$]	Ni	10(±3)	Figure S2.11
A, [LMIm][BF$_4$]	Ni[d] (NiO)[d]	7(±2)	Figure 3 a, S2.14
A, [LMIm][PF$_6$]	Ni[d] (NiF$_2$)[d]	9(±3)	Figure 3 b, S2.18
B, [LMIm][PF$_6$]	Ni	15(±2)	Figure S3.11
A, [LMIm][NTf$_2$]	Ni[d]	10(±4)	Figure 3 c, S2.21
Pyridinium cations			
A, [BPy][PF$_6$]	Ni[e]	2(±1)	Figure 7, S2.25
A, [BPy][NTf$_2$]	Ni[e]	2(±1)	Figure 7
B, [BPy][NTf$_2$]	Ni[e]	2(±1)	Figure S3.12
A, [LPy][PF$_6$]	Ni (NiO,[d] NiF$_2$)	3(±1)	Figure S2.27
Tetrahydrothiophenium cation			
A, [OTh][PF$_6$]	n.d.	9(±1)	Figure S2.31

[a] A = [Ni(AMD)$_2$]; B = [Ni(COD)$_2$]. 1.0 wt% Ni NP/IL dispersions obtained by MW irradiation with 100 W for 10 min at 220 °C. [b] From PXRD unless noted otherwise (see d) based on positive matching to the Crystallography Open Database, COD;[48] Ni stands for Ni with hcp packing; Ni(hcp) reference COD 9008509; NiO reference COD 1010095; NiF$_2$ reference COD 9007538; n.d. = not determined. [c] Average diameter (Ø) and standard deviation (σ). Histograms are included in Figures S2 and S3 in the Supporting Information. See experimental section for TEM measurement conditions. [d] Supported by SAED measurement of selected nanocrystals. [e] Because of the small size of the Ni NPs, no PXRD could be obtained and phase analysis is based on HR-TEM.

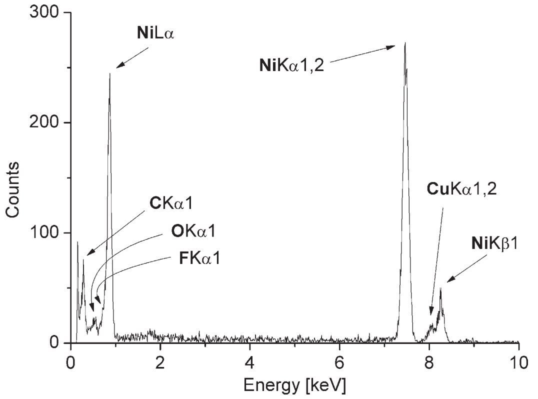

Figure 4. Example EDX spectrum of 1.0 wt% Ni NPs in [BMIm][BF$_4$] from [Ni(AMD)$_2$]. See Figure S2.4 in the Supporting Information for the EDX spectrum in [BMIm][NTf$_2$].

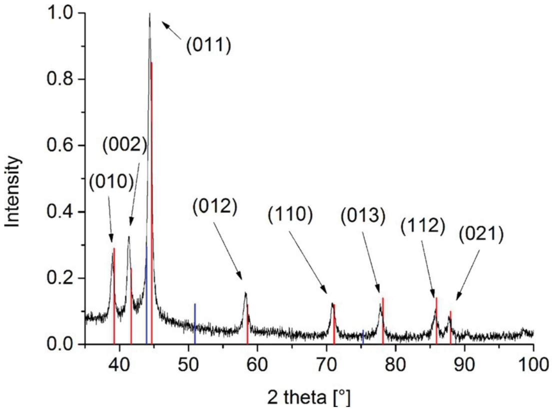

Figure 5. Example PXRD of 1.0 wt% Ni NPs in [BMIm][BF$_4$] from [Ni(AMD)$_2$]; Ni(hcp) reference peaks in red (COD 9008509) and possible Ni fcc reference peaks in blue (COD 9009862). See Figures in the Supporting Information for additional PXRD patterns. Small shifts in PXRD patterns are not uncommon for nanoparticles. A number of effects can be considered for such shifts including range of stoichiometric composition, partly inhomogeneous element distribution, defects such as stacking and twin faults, and nanosized crystalline domains being much smaller than the bulk reference material causing lattice contraction or expansion and strain.[63,64]

lammonium bromide (CTAB)/TC$_{12}$AB had the fcc structure.[54] Nickel nanoparticles with an hcp phase[55] were obtained with 62(±9) nm diameter stabilized by trioctylphosphine oxide (TOPO) from the decomposition of nickel acetate[56] or stabilized with citrate from a sol-gel method.[57] Ni NPs with the hcp structure and a diameter between 13 and 25 nm are also formed in polyethylene glycol, oleic acid, and oleyl amine.[58] There are also other possibilities to obtain nickel compounds in an hcp phase.[59,60,61]

Concerning the oxidation of nickel, we note that traces of oxygen in the EDX spectrum (signal at 0.52 eV) are ubiquitous and always present, also on noble metal samples and pure carbon grids (from surface oxidation). For Ni NPs in ILs with [BF$_4$]$^-$ or [PF$_6$]$^-$ anions, small amounts of NiO and NiF$_2$ are obtained in three cases (see Table 1) as identified by phase analysis in the powder X-ray and electron diffractograms (Figures S2.9, S2.16, and S2.29 in the Supporting Information). It is known in the literature that [BF$_4$]$^-$ or [PF$_6$]$^-$ anions in ILs hydrolyze or decompose to fluoride, F$^-$, which then leads to the formation of metal fluoride, here NiF$_2$.[62] Alternatively, reactive metal nanoparticles may also abstract fluoride from [BF$_4$]$^-$ or [PF$_6$]$^-$ anions.

It is evident from Table 1 that variation of the IL cation and anion influences the particle size and crystal phase.[34,65] The average diameter of the Ni NPs from both precursors increases slightly with the IL anion volume[66] in the series [BMIm][BF$_4$], [BMIm][PF$_6$], and [BMIm][NTf$_2$] (Figure 6). It might be assumed that fluoride ions formed from [BF$_4$]$^-$ and [PF$_6$]$^-$ could have been responsible for preventing the NP growth. To check or disprove this assumption, we added 5 wt% KF as a fluoride source (soluble in IL) to the Ni precursor/[BMIm][NTf$_2$] disper-

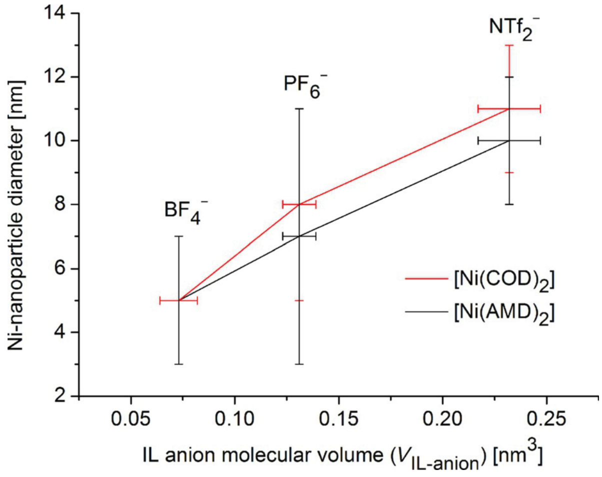

Figure 6. Correlation between Ni NP size and the molecular volume of the IL anion[66] for [BMIm]$^+$ cations from $[Ni(AMD)_2]$ (black) and $[Ni(COD)_2]$ (red line). Errors bars indicate the standard deviation (Table 1).

sion before starting the MW heating. TEM analysis (Figure 3 d) of the obtained Ni NPs in the presence of KF showed Ni NPs from $[Ni(AMD)_2]$ with average diameters of 10 ± 2 nm, and from $[Ni(COD)_2]$ with average diameters of 11 ± 2 nm. This size and size dispersion is identical to the Ni NPs formed from $[Ni(AMD)_2]$ (10 ± 2 nm) and $[Ni(COD)_2]$ (11 ± 2 nm) in [BMIm][NTf_2] without the addition of KF (Table 1). Thus, it can be assumed that the formation of F^- from $[BF_4]^-$ and $[PF_6]^-$ does not prevent the NP growth. A change in imidazolium cation or rather in 1-*n*-alkyl chain length does not give a similar trend. Only in the case of the $[PF_6]^-$ anion and $[Ni(COD)_2]$ as precursor there is a steady increase from 1-butyl over 1-octyl to 1-lauryl.

The influence of the IL cation/anion size on nanoparticle diameters has already been reported for silver,[37] cobalt,[67] rhodium,[42] and tungsten,[41] where the NP diameter increased with the IL anion volume (for $[BF_4]^-$, $[PF_6]^-$, triflate, and $[NTf_2]^-$) with [BMIm]$^+$, [methyl-trioctyl-ammonium]$^+$, and [1-butyl-3-methyl-pyrrolidinium]$^+$ as cations. Also, ruthenium nanoparticles from [Ru(COD)(COT)]/H_2 in various 1-alkyl-3-methyl-imidazolium ionic liquids showed a relationship between the Ru NP diameter and the size of the IL non-polar domains.[17] This suggested that the size of the nanoparticles is governed by the degree of self-organization of the imidazolium ionic liquid in which they are generated, such that more structured ionic liquids, lead to smaller metal particle sizes.[18] The dependence of nanoparticle size in imidazolium-based ILs was also investigated for Au NPs[68,69] where the particles vary from 0.75 to 3.5 nm in diameter for 1-ethyl-3-methyl-imidazolium, 1-butyl-3-methyl-imidazolium, and 1-methyl-3-octyl-imidazolium cations and $[BF_4]^-$ as the counter ion.[68] Further, decomposition of $[Ni(COD)_2]$ in 1-alkyl-3-methyl-imidazolium $[NTf_2]^-$ ILs with different 1-alkyl chain lengths gave Ni NPs with an average diameter from 2.4 to 5.4 nm[49] or 4.9 to 5.9 nm[16] such that the particle diameter increased with the cation size. A correlation between the size of palladium nanoparticles and different organic solvents was reported as well.[70]

Ni NPs in pyridinium-based ILs

Ni NPs from the decomposition of $[Ni(AMD)_2]$ and $[Ni(COD)_2]$ in pyridinium-based ILs had an average diameter of 2–3(± 1) nm, which rendered them significantly smaller than the Ni NPs synthesized in imidazolium-based ILs (compare Figure 7 and Figure 1). It can be assumed that the pyridinium cation leads to high structuring through π–π self-organizing interactions,[71] as well as by π–anion interactions, which are very stable.[72] Apparently, these self-organizing interactions are retained to some extent even at 220 °C as we should have otherwise obtained larger nanoparticles as for the imidazolium ILs.

The crystal structure of these small Ni NPs had to be elucidated by HR-TEM as no PXRD could be obtained. The distances between the Ni atom columns in the high-resolution TEM image of Figure 7 c correspond to those of the Ni(hcp) structure (COD 9008509).

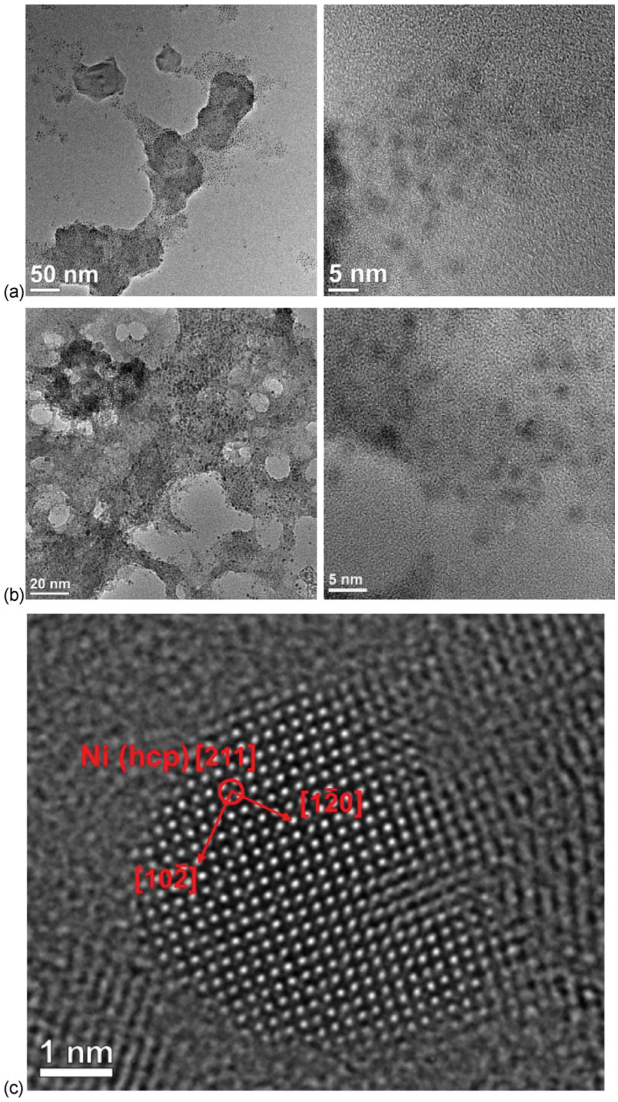

Figure 7. TEM images of 1.0 wt % Ni NP/IL dispersion from $[Ni(AMD)_2]$ for [BPy]$^+$ cations with: a) $[PF_6]^-$, and b, c) $[NTf_2]^-$ anions, where the HR-TEM image in (c) shows a well-oriented Ni(hcp) particle. For a further HR-TEM image of a single Ni NP from [BPy][NTf_2], see Figure S3.12 in the Supporting Information.

Ni NPs in thiophenium IL

Ni NPs obtained from [Ni(AMD)$_2$] in the IL 1-octyl-thiophenium hexafluorophosphate have an average particle diameter of 9(± 1) nm, which is in the range of imidazolium-based ILs. However, the particles are strongly agglomerated (Figure 8). Still, the crystallinity based on the diffraction pattern of the interference levels can be seen from the HR-TEM images. An additional PXRD, which would show the crystallinity of the particles, could not be obtained even after long measurement time possibly because of the amorphous particles.

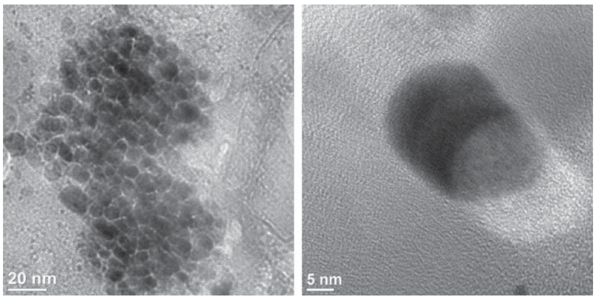

Figure 8. HR-TEM of 1.0 wt % Ni NPs in IL from [Ni(AMD)$_2$] in [OTh][PF$_6$].

X-ray photoelectron spectroscopy (XPS) study of Ni NPs in [BPy][NTf$_2$]

To determine the oxidation state of the nickel nanoparticle sample Ni/[BPy][NTf$_2$], an X-ray photoelectron spectroscopic (XPS) analysis was carried out. In a number of measurements, the binding energy of the electron from the Ni 2p$_{3/2}$ orbital of the 2(± 1) nm diameter Ni particles was shifted by about 0.3 eV to the higher binding energy of $E_B = 853.2$ eV compared with bulk Ni^0 (Figure 9). This is not typical for Ni NPs or any other nickel compounds. An instrumental error could be excluded by direct calibration with an ultrapure nickel standard (99.99 % Ni foil, polished and cleaned by sputtering) with reference to argon Ar 2p$_{3/2}$ (Ar gas was used for sputtering, added in traces as an internal standard and could be found physisorbed on the probe surface). We could also exclude an influence from chemi- or physisorbed species as this shift in binding energy was not seen for larger Ni(hcp) nanoparticles from the same or related ILs.

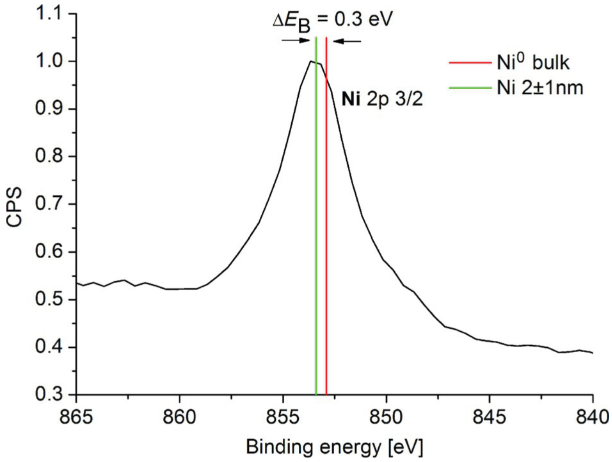

Figure 9. Shift (ΔE_B) of the Ni 2p$_{3/2}$ binding energy in small Ni particles from [BPy][NTf$_2$] in the X-ray photoelectron spectrum.

In the literature, this shift in binding energy of the photoelectrons to higher values is described for very small clusters.[73,74] For very small silicon clusters (Si$_4$ to Si$_{720}$) Ganteför et al. could show a cluster-size dependent shift in binding energy of the photoelectron from the outer layers.[73,74] It could also be shown that the electronic structure of a free cluster varies with every atom and that also the position of an atom in the cluster has an influence on the binding energy shift of the corresponding photoelectron spectrum.

Magnetic properties of Ni(hcp) NPs

Magnetic measurements of two isolated nickel nanoparticle samples from [BPy][NTf$_2$] and from [LMIm][NTf$_2$] were carried out to examine their magnetic properties.[75] The Ni NPs were isolated in powder form from the IL dispersion by precipitation with acetonitrile, centrifugation, washing with acetonitrile, and drying under vacuum.

Both samples show slightly hysteretic curves at room temperature. On the timescale of the experiment (approximately 1 h), no oxidation is observed (the saturation magnetization is unchanged for positive and negative branches, see Figure 10). The characteristic values calculated on the base of the magnetization curves are shown in Table 2. The saturation magnetization M_s of a Ni (2 ± 1 nm) sample from [BPy][NTf$_2$] is 2.08 A m^2 kg^{-1}, and of a Ni (10 ± 4 nm) sample from [LMIm][NTf$_2$] it is 0.99 A m^2 kg^{-1}. These values are comparable with the values for hcp Ni found in the literature, which vary from 0.82 A m^2 kg^{-1} for ≈60 nm nanoparticles[76] to 7.4 A m^2 kg^{-1} for micrometer-sized clusters.[77] Remanence magnetization (M_r/M_s) and coercivity (H_c) values were calculated as an average between the positive and the negative values. Both samples show a narrow hysteresis ($H_c < 15$ kAm^{-1}) with a moderate relative remanence $M_r/M_s \approx 0.1$. This value is thus clearly below the

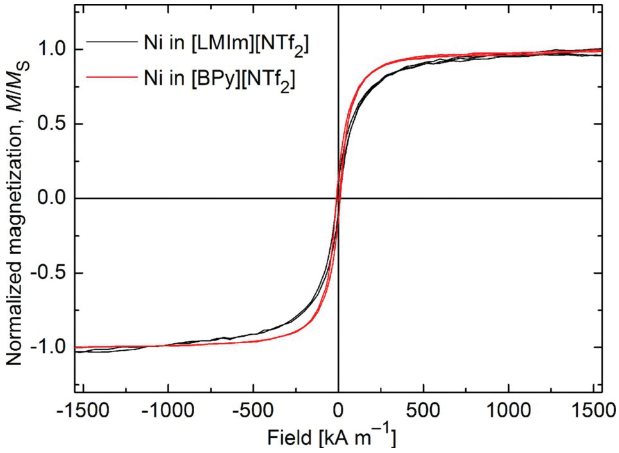

Figure 10. Magnetization curves of an isolated Ni (2 ± 1 nm) sample from [BPy][NTf$_2$] (red line) and an isolated Ni (10 ± 4 nm) sample from [LMIm][NTf$_2$] (black line) at room temperature.

Table 2. Data obtained from the magnetization curves at room temperature.

Sample	χ_{ini}[a] [10^5 m^3 kg^{-1}]	χ_{ini}[a] $10^5/M_s$ [m A^{-1}]	M_s[b] [A m^2 kg^{-1}]	M_r/M_s[c]	H_c[d] [A m^{-1}]
Ni (2 ± 1 nm) from [BPy][NTf$_2$][e]	0.23	0.11	2.08	0.14	11500
Ni (10 ± 4 nm) from [LMIm][NTf$_2$][f]	0.08	0.08	0.99	0.09	8400

[a] χ_{ini} = initial susceptibility. [b] M_s = saturation magnetization. [c] M_r/M_s = remanence magnetization. [d] H_c = coercivity. [e] Sample amount 0.97 mg. [f] Sample amount 0.4 mg.

expected relative remanence for an ensemble of magnetically blocked Stoner–Wohlfarth-like particles $(M_r/M_s)_{SW} = 0.5$, but clearly deviating from pure superparamagnetic behavior ($(M_r/M_s)_{sp} = 0$). For purely non-interacting Ni nanoparticles of the present size regime, a superparamagnetic behavior would be expected above the blocking temperature.[58] However, in temperature-dependent measurements in the temperature range between 150 and 300 K, performed on samples synthesized under the same conditions, no indication for a magnetic transition in the temperature range is identified. The blocking temperature is thus expected to be below 150 K. Based on these observations,[58] the slight hysteresis is ascribed to a significant contribution of particle interaction to the quasi-static magnetic behavior, caused by the strong magnetic moment inherent to single-domain nickel nanostructures.

Catalytic hydrogenation of alkenes with Ni nanoparticles

The hydrogenation of a C=C double bond to a C–C single bond is an important reaction in industrial and synthetic organic chemistry.

Freshly synthesized Ni/IL nanoparticle dispersions (1.0 wt% in metal) were tested for the hydrogenation of 1-hexene and benzene in a Büchi high-pressure, stainless-steel autoclave within IL phase under organic-solvent-free conditions. In a typical catalytic procedure, the high-pressure autoclave was charged with the Ni/IL colloid dispersion (0.1 g) and the substrate (2.0 g). The reaction mixture was heated to 100 °C. After reaching the reaction temperature, the autoclave was pressurized with 5 bar of H_2. After a selected time, the reaction was stopped, cooled down, and a 0.5 g sample was analyzed for its content by GC and NMR.

Expectedly, the Ni/IL dispersion proved to be an active catalyst for hydrogenation reactions.[40] The catalytic activity did not significantly depend on the nanoparticle size. At first sight, the activity of smaller Ni nanoparticles (Ni/[BPy][NTf$_2$], 2 ± 1) was very similar (insignificantly higher) to the larger Ni nanoparticles (Ni/[BMIm][NTf$_2$], 11(±2)).

The activity as a turnover frequency (TOF) for metal nanoparticle catalysts is often calculated on the number of moles of the metal used. Clearly, only the surface atoms of the metal nanoparticle can be catalytically active. Thus, an activity that is based only the surface atoms can be one order of magnitude larger than the TOF referenced to the total amount of metal. Further, as only a fraction of the surface atoms will be catalytically active, such as corners, edges, or defect sites, even the TOF based on surface atoms will still underestimate of the true activity of the active sites.[78]

From TEM, we obtained an average Ni NP diameter of 2 nm for Ni/[BPy][NTf$_2$] (from both [Ni(AMD)$_2$] and [Ni(COD)$_2$]) and 11 nm for Ni/[BMIm][NTf$_2$] (from [Ni(COD)$_2$]). From these average diameters D the total number of metal atoms (N_T) in the nanocrystal can be calculated according to Equations (1), (2), and (3):[78–81]

$$N_T = \frac{N_A \rho V}{A_r} \text{ and } V = \frac{4}{3}\pi\left(\frac{D}{2}\right)^3 \tag{1}$$

with N_A = Avogadro's number (6.022×10^{23} mol^{-1}), ρ = metal density, A_r = relative atom mass [g mol^{-1}].[78]

$$N_T = 4\pi\left(\frac{D}{2b}\right)^3 / 3V_g \tag{2}$$

with $b = 1.105$ for close-packed (cp), face-centered cubic, or hexagonal-cp (fcc or hcp) crystallographic structures, V_g = volume of a single metal atom according to $V_g = (4/3)\pi r^3$, r = atomic (metal) radius. The constant b accounts for the free space between the atom spheres in the metal packing.

$$N_T = \left(\frac{D}{2rb}\right)^3 \tag{3}$$

With the values for nickel ($\rho = 8.90$ g cm^{-3}, $A_r = 58.69$ g mol^{-1}, $b = 1.105$ for Ni with hcp packing, $V_g = 0.00810$ nm^3, $r = 0.1246$ nm), Equations (1), (2), and (3) give $N_T = 383$ atoms for Ni NPs of 2 nm mean diameter and $N_T = 63\,745$, rounded to 64 000, for the 11 nm Ni NPs.

Under assumption that Ni clusters have a icosahedral shell structure,[82] it is possible to calculate the number of surface atoms (N_S) from the number of shells m, which can be derived from the total number of atoms (N_T).[83]

The total average atom number N_T of 383 is between the total atom number of $N_m = 309$ for an icosahedron with $m = 5$ shells and $N_m = 561$ for an icosahedron with $m = 6$ shells ($N_m = (1/3)(2m-1)(5m^2-5m+3)$).[83] The number of surface atoms for a five-shell icosahedron is $N_S = 162$ and for a six-shell icosahedron $N_S = 252$ ($N_S = 10m^2-20m+12$).[83] In our rough approximation, we take here $N_S = 200$ for the number of surface atoms for $N_T = 383$. This gives a fraction of exposed or surface atoms $N_S/N_T \approx 200/383 = 0.52$ or 52% on average.

The total average atom number N_T of 64000 is between the total atom number of $N_m = 62062$ for an icosahedron with $m = 27$ shells and $N_m = 69354$ for an icosahedron with $m = 28$ shells. The number of surface atoms for a 27-shell icosahedron is $N_S = 6762$ and for a 28-shell icosahedron $N_S = 7292$. In our approximation, we take here $N_S = 6900$ for the number of surface atoms for $N_T = 64000$. This gives a fraction of exposed or surface atoms $N_S/N_T \approx 6900/64000 \approx 0.11$ or 11 % on average.

Thus, when the number or rather fraction of surface atoms is taken into account, the activity (TOF) of the larger 11 nm particles from [BMIm][NTf$_2$] is about four times higher than the activity of the smaller 2 nm Ni particles from [BPy][NTf$_2$]. This finding is similar to results by Campbell et al. for Ru NPs with different nanoparticle sizes in [BMIm][NTf$_2$] in the catalytic hydrogenation of 1,3-cyclohexadiene and cyclohexene.[84]

After catalysis, the Ni nanoparticles had increased in size to 21 ± 6 nm but were still separate nanoparticles (Figure 11). EDX showed nickel and a low content of oxygen.

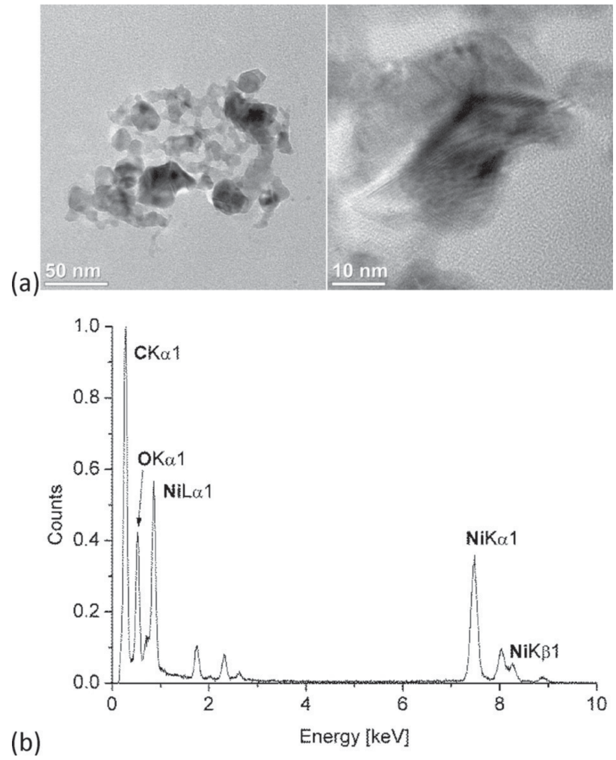

Figure 11. a) TEM, and b) EDX (averaged over 10 particles) of Ni/[BMIm][NTf$_2$] dispersion after catalytic hydrogenation of 1-hexene at 100 °C and 60 min.

Conclusions

We describe here a simple, reproducible, and broadly applicable microwave-induced decomposition of nickel amidinate, [Ni(AMD)$_2$], or [Ni(COD)$_2$] for the synthesis of small and uniform Ni NPs in different ionic liquids. The results nicely show the advantages of metal–organic precursor concepts together with non-conventional ionic liquid solvents and microwave-assisted pyrolysis[85] for a controlled synthesis of rather small metal nanoparticles without additional surfactants and reducing agents (e.g., hydrogen) for soft, wet-chemical nanoparticle formation.

The Ni NPs are mostly formed in the rarely occurring metastable hexagonal close-packed (hcp) structure. Magnetic measurements of two Ni nanoparticle samples showed very similar magnetic properties.

The obtained Ni nanoparticles were active in [BMIm][NTf$_2$] or [BPy][NTf$_2$] IL dispersions for catalytic alkene or benzene hydrogenation with over 90 % conversion.

Experimental Section

All synthesis experiments were carried out with Schlenk techniques under nitrogen or argon as the nickel amidinate is hygroscopic and air sensitive. The solvents (acetone, acetonitrile, *n*-hexane, toluene, tetrahydrofuran) were dried by using a MBraun solvent purification system. 1,3-Diisopropylcarbodiimide (> 99 %), nickel(II) chloride (> 99 %), methyllithium, 1-chlorobutane (> 99 %), 1-chlorooctane (> 99 %), 1-iodolaurate (> 99 %), 1-methylimidazole (> 99 %), pyridine (> 99 %), and tetrahydrothiophene (> 98 %) were obtained from Sigma–Aldrich and used without further purification.

Synthesis of precursors and ILs

[Ni{MeC(N*i*Pr)$_2$}$_2$] ([Ni(AMD)$_2$]) was synthesized by deprotonation and methylation of 1,3-diisopropylcarbodiimide with methyllithium. The resulting lithium amidinates were then reacted with nickel(II) chloride according to literature procedures.[86,87]

Ni(COD)$_2$ was synthesized by suspending bis-(acetylacetonato)nickel in THF and adding 1,5-cyclooctadiene and diisobutylaluminiumhydride (DIBAL-H) according to literature procedures.[88]

The ionic liquids were synthesized by reacting 1-methylimidazole, tetrahydrothiophene, or pyridine with 1-halo-alkanes to yield first the alkylated iminum halide salts, which were further reacted with HBF$_4$, NH$_4$PF$_6$, or LiNTF$_2$ to give the respective ionic liquid. The ILs were dried under high vacuum (10^{-7} mbar) at 80 °C for several days. Quantitative anion exchange and, thus, IL anion purity was assessed to be mostly near or over 99 % from analysis by ion chromatography (Dionex ICS-1100, with IonPac® AS22, 4 × 250 mm column);, for example, [BMIm][BF$_4$] 99.05 %, [BMIm][PF$_6$] 98.87 %, [BMIm][NTf$_2$] 99.29 %, [OMIm][PF$_6$] 99.10 %, [OMIm][NTf$_2$] 99.21 %, [BPy][PF$_6$] 99.28 %, [BPy][NTf$_2$] 99.75 %, [LPy][PF$_6$] 98.85 %.

The water content was measured by coulometric Karl Fischer titration (ECH/Analytik Jena AQUA 40.00): [BMIm][BF$_4$] < 10 ppm, [BMIm][PF$_6$] < 30 ppm, [BMIm][NTf$_2$] < 300 ppm, [OMIm][PF$_6$] < 10 ppm, [OMIm][NTf$_2$] < 10 ppm, [BPy][PF$_6$] < 300 ppm, [BPy][NTf$_2$] < 300 ppm, [LPy][PF$_6$] < 20 ppm.

NMR analyses of selected ILs before (and after) 10 min MW heating at a power of 100 W to an approximate temperature of 220 °C (see Figures 5.1–5.9 in the Supporting Information; for the NMR assignment see ref. [89]):

[BMIm][NTf$_2$]: ^{1}H NMR (300.13 MHz, CD$_3$CN): $\delta = 8.39$ (s, 1 H), 7.37 (s, 1 H), 7.34 (s, 1 H), 4.21 (t, $^3J = 7.3$ Hz, 2 H), 3.81 (s, 3 H), 1.80 (quintet, $^3J = 7.5$, 2 H), 1.32 (sextet, $^3J = 7.36$, 2 H), 0.94 ppm (t, $^3J = 7.4$ Hz, 3 H); ^{13}C NMR (75 MHz, CD$_3$CN): $\delta = 13.6$, 19.9, 32.5, 36.8, 50.3, 123.2, 124.6, 136.8 ppm.

[OMIm][NTf$_2$]: ^{1}H NMR (300.13 MHz, CD$_3$CN): $\delta = 8.38$ (s, 1 H), 7.36 (d, $^3J = 3.6$ Hz, 1 H), 7.32 (d, $^3J = 3.6$ Hz, 1 H), 4.10 (t, $^3J = 7.10$ Hz, 3 H), 3.81 (s, 3 H) 1.81 (m, 2 H), 1.30 (m, 10 H), 0.89 ppm (t, $^3J = 6.45$ Hz, 3 H); ^{13}C NMR (75 MHz, CD$_3$CN): $\delta = 14.3$, 23.3, 26.6, 29.7, 32.4, 36.8, 123.2, 124.6, 136.7, 120.9 ppm (q, $^1J = 318$ Hz, CF$_3$S).

[LMIm][PF$_6$]: ^{1}H NMR (300.13 MHz, CD$_3$CN): $\delta = 8.36$ (s, 1 H), 7.35 (d, $^3J = 3.4$ Hz, 1 H), 7.32 (d, $^3J = 3.4$ Hz, 1 H), 4.09 (t, $^3J = 7.1$ Hz, 2 H), 3.80 (s, 3 H), 1.80 (m, 2 H), 1.27 (m, 18 H), 0.86 ppm (t, $^3J = 7.4$ Hz, 3 H); ^{13}C NMR (75 MHz, CD$_3$CN): $\delta = 13.1$, 22.1, 25.3, 28.8, 29.0, 31.31, 49.2, 121.94, 123.3, 135.7 ppm.

Metal nanoparticle (M NP) synthesis

In a typical reaction, the nickel amidinate powders (58 mg, 0.17 mmol, [Ni{MeC(N*i*Pr)$_2$}$_2$]) or Ni(COD)$_2$ (49 mg, 0.83 mmol) were dissolved or suspended (≈12 h) under a nitrogen atmosphere at room temperature in dried and deoxygenated ionic liquid (1.0 g) to give a 1.0 wt% total metal/IL dispersion. For the decomposition, the mixture was placed in a microwave (CEM, Discover) under an inert nitrogen atmosphere and the conversion was finished within 10 min at a microwave power of 50 W and a temperature reading of 220 °C. Each decomposition reaction was carried out at least twice.

Characterization

Thermogravimetric analysis (TGA) was carried out with a Netzsch TG 209 F3 Tarsus, equipped with Al crucible and using a heating rate of 5 K min^{-1} under inert atmosphere (N_2).

XPS (ESCA) measurements were performed with a Fisons/VG Scientific ESCALAB 200X xp-spectrometer, operating at room temperature, a pressure of 1.0×10^{-8} bar, and a sample angle of 30°. Photoelectron spectra were recorded by using polychromatic $Al_{K\alpha}$ excitation (14 kV, 20 mA) and an emission angle of 0°. Calibration of the XPS was carried out by recording spectra, using $Al_{K\alpha}$ X-rays, from clean samples of copper, silver, and gold, at 20 eV and 10 eV pass energies and comparison with reference values.

PXRD data were measured at ambient temperature with a Bruker D2 Phaser using a flat, low-background sample holder with a dome for exclusion of air and moisture and $Cu_{K\alpha}$ radiation ($\lambda =$ 1.54182 Å, 35 kV). Samples had been precipitated with acetone from the NP/IL dispersion and washed with acetonitrile. PXRDs were measured for 2–12 h.

GC/MS data were recorded with a Thermo Finnigan Trace DSQ; ionization method: EI, 70 eV, 200 °C.

NMR spectra were recorded with a Bruker Avance DRX 200 (^{1}H, 300.13 MHz) and Avance DRX 500 (^{13}C, 125.57 MHZ) at 298 K in C_6D_6, CD_3CN, or $CDCl_3$ and the chemical shifts are referenced to the residual proton solvent peaks against TMS.

Transmission electron microscopy (TEM) micrographs were taken at room temperature with a Tecnai FEI G20 TEM operating at an accelerating voltage of 200 kV. Samples were deposited on 200 μm carbon-coated gold grids. The size distribution was calculated from a manual diameter determination over a minimum of 50 isolated particles.

TEM with energy-dispersive X-ray spectrometry (TEM-EDX) was recorded with a FEI Tecnai f20, 136 kV, exposure time for individual EDX spectra, 3 min. EDX analysis always shows traces of oxygen. Preparation on the grids was done in a glovebox. However, there is an unavoidable 30 s air contact upon placing the grid in the TEM chamber before evacuation. A low intensity oxygen signal at 0.52 eV is ubiquitous and always present also on noble metal samples and pure carbon grids (from surface oxidation).

Powder TED measurements: Selected-area electron diffraction (SAED) patterns and high-resolution TEM images were recorded with an FEI Titan 80–300 TEM,[90] operated at 300 kV accelerating voltage. The area selection was achieved with a round aperture placed in the first intermediate image plane with a corresponding diameter of 0.64 μm in the object plane. For each acquisition, a sample region with a significant amount of material was placed inside the aperture. The objected was illuminated with widespread parallel beam obtaining focused diffraction patterns. The diffraction images were calibrated with Debye–Scherrer patterns recorded from a gold reference sample (S106, Plano GmbH, Wetzlar, Germany). Several diffraction patterns were recorded for each of the investigated Ni samples and were averaged after compensating for unavoidable small diffraction shifts occurring between successive acquisitions. To compare the recorded diffraction signal to reference structure data, the signals from the Debye–Scherrer pattern were accumulated along the azimuthal direction.

The five samples investigated by SAED were found to contain Ni(hcp), NiO, and NiF_2 species in different amounts (cf. Figures S2.10, S2.17, S2.20, S2.24, and S2.30 in the Supporting Information). According to the calibration with the gold sample, the measured Ni(hcp) lattice constant is decreased by approximately 1% compared with the bulk material,[91] whereas the lattice constants of NiO and NiF_2 are increased by about 2–3% when compared with the respective bulk parameters.[92,93]

The magnetization curves were monitored at room temperature with an ADE Magnetics Vibrating Sample Magnetometer EV7 up to a maximum field strength of 1600 kA m^{-1}. A typical experiment consisted of a virgin curve, followed by a full hysteresis loop. The Ni NPs were isolated in powder form from the 1.0 wt% IL dispersion by precipitation with 2 mL acetonitrile, centrifugation, washing twice with 2 mL acetonitrile each with intermittent centrifugation, and finally drying under vacuum. The isolated Ni (2±1 nm) sample from [BPy][NTf$_2$] was measured in a sealed Teflon vessel, placed on a glass sample holder between two poles of an electromagnet, and vibrated at a frequency of 75 Hz. The isolated Ni (10±4 nm) sample from [LMIm][NTf$_2$] was measured under similar conditions in a sealed Teflon vessel in a nitrogen flow. The raw data was corrected by subtraction of the signal of the paramagnetic material. The saturation magnetization (M_s), magnetic moment (m), remanence magnetization (M_r), coercive field (H_c), and initial susceptibility (χ_{ini}) were calculated. The remanence magnetization (M_r) and coercive field (H_c) were calculated as an average between the positive and the negative values.

Temperature-dependent magnetization (M) measurements were performed in the temperature range from 150 K to 300 K at a constant field strength of 800 kA m^{-1}. The lower temperature value was limited by the liquid nitrogen cooling setup. A typical zero-field cooled (ZFC) measurement consisted of cooling the sample to a minimum temperature in zero field, followed by applying the magnetic field, and slow heating at a rate of 1 K min^{-1}. In a field-cooled (FC) measurement, the magnetic field was applied during slow cooling of the sample (1 K min^{-1}). Samples were measured in the same vessels as for the room temperature measurements.

Catalysis

A Büchi stainless-steel autoclave with a glass inlet was charged with freshly synthesized Ni/IL dispersion (0.1 g, 1.0 wt% in total metal, 17 μmol Ni). Degassed, dry substrate (2 g) was added. For benzene, the Ni/substrate ratio was 1:1505 and for 1-hexene the Ni/substrate ratio was 1:1400. The reaction mixture was heated to 60–100 °C (see Table 3). After reaching the reaction temperature, the autoclave was pressurized with H_2 to 5 bar (Büchi pressflow gas controller, bpc), which was kept constant by the Büchi bpc. After the chosen time (1–60 h), the reaction was stopped, cooled down and a 0.5 g sample was analyzed for its content by GC/MS and NMR analysis. Conversion and selectivity were determined by using a Shimadzu GC2014 for Ni/IL samples from [Ni(COD)$_2$] [column Ultra2, crosslinked 5% PhMe silicone, 25 m×0.2 mm×11 μm] or a PerkinElmer headspace GC 8500 [column HS-6B, FID detector]. ^{1}H NMR spectra were recorded by dissolving 0.1 mL of the sample in 0.65 mL deuterated chloroform.

Table 3. Catalytic data for the hydrogenation of 1-hexene or benzene to hexane or cyclohexane, respectively, with Ni/IL dispersions.[a]

Ni precursor[a]	Catalyst (av. particle size [nm])	Substrate	t [h]	T [°C]	Conv. [%]	TOF[b]	$\text{TOF}_{\text{surface}}$[c]
B	Ni/[BMIm][NTf_2] (11)	benzene	2	100	15	113	1027
B	Ni/[BMIm][NTf_2] (11)	benzene	10	100	31	47	427
B	Ni/[BMIm][NTf_2] (11)	benzene	60	100	91	23	209
B	Ni/[BMIm][NTf_2] (11)	1-hexene	1	100	93	1302	11836
B	Ni/[BMIm][NTf_2] (11)	1-hexene	1	60	89	1246	11327
–	blank, [BMIm][NTf_2]	1-hexene	2	100	1.5	10	
–	blank, [BMIm][NTf_2]	benzene	10	100	0.5	1	
–	blank, [BPy][NTf_2]	benzene	10	100	0	–	
–	blank, [BPy][NTf_2]	1-hexene	2	100	1	2	
A	Ni/[BPy][NTf_2] (2)	benzene	2	100	18	136	262
B	Ni/[BPy][NTf_2] (2)	benzene	10	100	34	51	98
A	Ni/[BPy][NTf_2] (2)	1-hexene	1	100	95	1330	2560
A	Ni/[BPy][NTf_2] (2)	1-hexene	1	60	90	1260	2420

[a] A = [Ni(AMD)$_2$]; B = [Ni(COD)$_2$]. In a typical catalytic test reaction, Ni/IL dispersion (0.1 g, 1.0 wt% = 0.001 g in total metal, 17 μmol Ni) and degassed dry substrate (2.0 g, benzene: 25.6 mmol, 1-hexene: 23.8 mmol) were stirred under 5 bar H_2 at 60–100 °C for 1–60 h. [b] TOF = [$\text{mol}_{\text{product}}\,(\text{mol}_{\text{Ni}})^{-1}\,\text{h}^{-1}$]. [c] $\text{TOF}_{\text{surface}}$ = [$\text{mol}_{\text{product}}\,(\text{mol}_{\text{Ni}})^{-1}\,\text{h}^{-1}$]/($N_S/N_T$) with the fraction of surface atoms $N_S/N_T = 0.11$ for Ni/[BMIm][NTf_2] and 0.52 for Ni/[BPy][NTf_2] (see estimation in text).

Acknowledgments

The authors are thankful to the Deutsche Forschungsgemeinschaft (DFG) for financial support in the priority project SPP 1708 through grant Ja466/31-1 and Fi502/32-1, and in the core-facilities program through grant MA 1280/40-1.

Keywords: hexagonal close-packing · ionic liquids · nickel amidinate · nickel nanoparticles · soft wet-chemical synthesis

[1] L. Yang, J. Kong, D. Zhou, J. M. Ang, S. L. Phua, W. A. Yee, H. Liu, Y. Huang, X. Lu, *Chem. Eur. J.* **2014**, *20*, 7776–7783; S. Vivek, P. Arunkumar, K. S. Babu, *RSC Adv.* **2016**, *6*, 45947–45956; W. Zuo, G. Yu, Z. Dong, *RSC Adv.* **2016**, *6*, 11749–11753; R. Shu, Q. Zhang, Y. Xu, J. Long, L. Ma, T. Wang, P. Chen, Q. Wu, *RSC Adv.* **2016**, *6*, 5214–5222; B. Karimi, F. Mansouri, H. Vali, *ChemPlusChem* **2015**, *80*, 1750–1759; F. K. Shmidt, Y. Y. Titova, L. B. Belykh, *Kinet. Catal.* **2015**, *56*, 574–583.

[2] J. Park, E. Kang, S. U. Son, H. M. Park, M. K. Lee, J. Kim, K. W. Kim, H. J. Noh, J. H. Park, C. J. Bae, *Adv. Mater.* **2005**, *17*, 429–434.

[3] A. Dhakshinamoorthy, K. Pitchumani, *Tetrahedron Lett.* **2008**, *49*, 1818–1823.

[4] N. Akhtar, S. A. El-Safty, M. E. Abdelsalam, H. Kawarada, *Nano-Structures Nano-Objects* **2015**, *2*, 35–44.

[5] H. Wang, G. Wang, Y. Ling, F. Qian, Y. Song, X. Lu, S. Chen, Y. Tong, Y. Li, *Nanoscale* **2013**, *5*, 10283–10290.

[6] W. Qu, H. Bao, L. Zhang, G. Chen, *Chem. Eur. J.* **2012**, *18*, 15746–15752.

[7] D. Guo, C. Wu, X. Li, H. Jiang, X. Wang, B. Chen, *J. Nanosci. Nanotechnol.* **2008**, *8*, 2301–2307.

[8] Review: M. R. Kim, Z. Xu, G. Chen, D. Ma, *Chem. Eur. J.* **2014**, *20*, 11256–11275.

[9] X. Zan, H. Bai, C. Wang, F. Zhao, H. Duan, *Chem. Eur. J.* **2016**, *22*, 5204–5210.

[10] a) P. Lara, O. R. Wheelaghan, S. Conejero, R. Poteau, K. Philippot, B. Chaudret, *Angew. Chem. Int. Ed.* **2011**, *50*, 12080–12084; *Angew. Chem.* **2011**, *123*, 12286–12290; b) T. C. Golindano, S. I. Martínez, O. Z. Delgado, G. P. Rivas, *Nanotechnology* **2005**, *16*, 634–637; c) N. Cordente, C. Amiens, B. Chaudret, M. Respaud, F. Senocq, *J. Appl. Phys.* **2003**, *94*, 6358–6365; d) Y. Li, J. Liu, Y. Wang, Z. L. Wang, *Chem. Mater.* **2001**, *13*, 1008–1014.

[11] a) B. Cormary, F. Dumestre, N. Liakakos, K. Soulantica, B. Chaudret, *Dalton Trans.* **2013**, *42*, 12546–12553; b) M. V. Kovalenko, C. Coperet, *Dalton Trans.* **2013**, *42*, 12520; c) Ö. Metin, X. Sun, S. Sun, *Nanoscale* **2013**, *5*, 910–912; d) C. Kumara, A. Dass, *Nanoscale* **2012**, *4*, 4084–4086; e) Z.-C. Zhang, J.-F. Hui, Z.-G. Guo, Q.-Y. Yu, B. Xu, X. Zhang, Z.-C. Liu, C.-M. Xu, J.-S. Gao, X. Wang, *Nanoscale* **2012**, *4*, 2633–2639; f) C. Kumara, A. Dass, *Nanoscale* **2011**, *3*, 3064–3067; g) R. Marcos Esteban, K. Schütte, D. Marquardt, J. Barthel, F. Beckert, R. Mülhaupt, C. Janiak, *Nano-Structures Nano-Objects* **2015**, *2*, 28–34.

[12] K. Schütte, H. Meyer, C. Gemel, J. Barthel, R. A. Fischer, C. Janiak, *Nanoscale* **2014**, *6*, 3116–3126.

[13] A. Glaria, J. Cure, K. Piettre, Y. Coppel, C.-O. Turrin, B. Chaudret, P. Fau, *Chem. Eur. J.* **2015**, *21*, 1169–1178.

[14] N. Bahlawane, K. Kohse-Hoinghaus, P. A. Premkumar, D. Lenoble, *Chem. Sci.* **2012**, *3*, 929–941.

[15] V. Krisyuk, L. Aloui, N. Prud'homme, S. Sysoev, F. Senocq, D. Samelor, C. Vahlas, *Electrochem. Solid-State Lett.* **2011**, *14*, D26–D29.

[16] P. Migowski, G. Machado, S. R. Teixeira, M. C. M. Alves, J. Morais, A. Traverse, J. Dupont, *Phys. Chem. Chem. Phys.* **2007**, *9*, 4814–4821.

[17] T. Gutel, C. C. Santini, K. Philippot, A. Padua, K. Pelzer, B. Chaudret, Y. Chauvin, J.-M. Basset, *J. Mater. Chem.* **2009**, *19*, 3624–3631.

[18] T. Gutel, J. Garcia-Anton, K. Pelzer, K. Philippot, C. C. Santini, Y. Chauvin, B. Chaudret, J.-M. Basset, *J. Mater. Chem.* **2007**, *17*, 3290–3292.

[19] G. Salas, A. Podgorsek, P. S. Campbell, C. C. Santini, A. A. H. Pádua, M. F. Costa Gomes, K. Philippot, B. Chaudret, M. Turmine, *Phys. Chem. Chem. Phys.* **2011**, *13*, 13527–13536.

[20] E. T. Silveira, A. P. Umpierre, L. M. Rossi, G. Machado, J. Morais, G. V. Soares, I. J. R. Baumvol, S. R. Teixeira, R. F. P. Fichtner, J. Dupont, *Chem. Eur. J.* **2004**, *10*, 3734–3740.

[21] T. Welton, *Chem. Rev.* **1999**, *99*, 2071–2084.

[22] C. Feldmann, *Z. Naturforsch. B* **2013**, *68*, 1057.

[23] a) C. Janiak, *Z. Naturforsch. B* **2013**, *68*, 1059–1089; b) D. Marquardt, C. Janiak, *Nachr. Chem.* **2013**, *61*, 754–757.

[24] C. Janiak, *Topics Organomet. Chem.* **2015**, *51*, 17–53.

[25] C. Janiak, Metal Nanoparticle Synthesis in Ionic Liquids, in *Catalysis in Ionic Liquids: From Catalyst Synthesis to Application* (Eds.: C. Hardacre, V. Parvulescu), RSC, Cambridge, **2014**, Ch. 11, pp. 537–577.

[26] Y. Lin, S. Dehnen, *Inorg. Chem.* **2011**, *50*, 7913–7915.

[27] P. Lodge, *Science* **2008**, *321*, 50–51.

[28] P. S. Campbell, M. H. G. Prechtl, C. C. Santini, P.-H. Haumesser, *Curr. Org. Chem.* **2013**, *17*, 414–429.

[29] D. Freudenmann, S. Wolf, M. Wolff, C. Feldmann, *Angew. Chem. Int. Ed.* **2011**, *50*, 11050–11060; *Angew. Chem.* **2011**, *123*, 11244–11255.

[30] a) E. Ahmed, J. Breternitz, M. F. Groh, M. Ruck, *CrystEngComm* **2012**, *14*, 4874–4885; b) E. Ahmed, M. Ruck, *Dalton Trans.* **2011**, *40*, 9347–9357; c) M. F. Groh, U. Müller, E. Ahmed, A. Rothenberger, M. Ruck, *Z. Naturforsch. B* **2013**, *68*, 1108–1122.

[31] R. E. Morris, *Chem. Commun.* **2009**, 2990–2998.

[32] E. R. Parnham, R. E. Morris, *Acc. Chem. Res.* **2007**, *40*, 1005–1013.

[33] E. R. Cooper, C. D. Andrews, P. S. Wheatley, P. B. Webb, P. Wormald, R. E. Morris, *Nature* **2004**, *430*, 1012–1016.

[34] J. Dupont, J. D. Scholten, *Chem. Soc. Rev.* **2010**, *39*, 1780–1804.

[35] K. Klauke, B. Hahn, K. Schütte, J. Barthel, C. Janiak, *Nano-Structures Nano-Objects* **2015**, *1*, 24 – 31.

[36] a) G. S. Fonseca, G. Machado, S. R. Teixeira, G. H. Fecher, J. Morais, M. C. M. Alves, J. Dupont, *J. Colloid Interface Sci.* **2006**, *301*, 193 – 204; b) G. S. Fonseca, J. B. Domingos, F. Nome, J. Dupont, *J. Mol. Catal. A* **2006**, *248*, 10 – 16; c) G. S. Fonseca, A. P. Umpierre, P. F. P. Fichtner, S. R. Teixeira, J. Dupont, *Chem. Eur. J.* **2003**, *9*, 3263 – 3269; d) J. Dupont, G. S. Fonseca, A. P. Umpierre, P. F. P. Fichter, S. R. Teixeira, *J. Am. Chem. Soc.* **2002**, *124*, 4228 – 4229.

[37] E. Redel, R. Thomann, C. Janiak, *Inorg. Chem.* **2008**, *47*, 14 – 16.

[38] a) E. Redel, M. Walter, R. Thomann, L. Hussein, M. Krüger, C. Janiak, *Chem. Commun.* **2010**, *46*, 1159 – 1161; b) E. Redel, M. Walter, R. Thomann, C. Vollmer, L. Hussein, H. Scherer, M. Krüger, C. Janiak, *Chem. Eur. J.* **2009**, *15*, 10047 – 10059.

[39] D. Marquardt, J. Barthel, M. Braun, C. Ganter, C. Janiak, *CrystEngComm* **2012**, *14*, 7607 – 7615.

[40] K. Schütte, A. Doddi, C. Kroll, H. Meyer, C. Wiktor, C. Gemel, G. van Tendeloo, R. A. Fischer, C. Janiak, *Nanoscale* **2014**, *6*, 5532 – 5544.

[41] E. Redel, R. Thomann, C. Janiak, *Chem. Commun.* **2008**, 1789 – 1791.

[42] E. Redel, J. Krämer, R. Thomann, C. Janiak, *J. Organomet. Chem.* **2009**, *694*, 1069 – 1075.

[43] a) C. Vollmer, C. Janiak, *Coord. Chem. Rev.* **2011**, *255*, 2039 – 2057; b) R. Marcos Esteban, K. Schütte, P. Brandt, D. Marquardt, H. Meyer, F. Beckert, R. Mülhaupt, H. Kölling, C. Janiak, *Nano-Structures Nano-Objects* **2015**, *2*, 11 – 18; c) C. Vollmer, M. Schröder, Y. Thomann, R. Thomann, C. Janiak, *Appl. Catal. A* **2012**, *425 – 426*, 178 – 183; d) D. Marquardt, C. Vollmer, R. Thomann, P. Steurer, R. Mülhaupt, E. Redel, C. Janiak, *Carbon* **2011**, *49*, 1326 – 1332; e) D. Marquardt, Z. Xie, A. Taubert, R. Thomann, C. Janiak, *Dalton Trans.* **2011**, *40*, 8290 – 8293; f) C. Vollmer, E. Redel, K. Abu-Shandi, R. Thomann, H. Manyar, C. Hardacre, C. Janiak, *Chem. Eur. J.* **2010**, *16*, 3849 – 3858; g) J. Krämer, E. Redel, R. Thomann, C. Janiak, *Organometallics* **2008**, *27*, 1976 – 1978.

[44] a) J. M. Zhu, Y. H. Shen, A. J. Xie, L. G. Qiu, Q. Zhang, X. Y. Zhang, *J. Phys. Chem. C* **2007**, *111*, 7629 – 7633; b) M. A. Firestone, M. L. Dietz, S. Seifert, S. Trasobares, D. J. Miller, N. J. Zaluzec, *Small* **2005**, *1*, 754 – 760.

[45] F. Endres, D. MacFarlane, A. Abbott, *Electrodeposition from Ionic Liquids*, Wiley-VCH, Weinheim, **2008**.

[46] a) G. Schmid, *Nanoparticles*, Wiley-VCH, Weinheim, **2004**, pp. 185 – 238; b) M. Antonietti, D. Kuang, B. Smarly, Y. Zhou, *Angew. Chem. Int. Ed.* **2004**, *43*, 4988 – 4992; *Angew. Chem.* **2004**, *116*, 5096 – 5100; c) D. Astruc, F. Lu, J. R. Aranzaes, *Angew. Chem. Int. Ed.* **2005**, *44*, 7852 – 7872; *Angew. Chem.* **2005**, *117*, 8062 – 8083; d) H. Kaper, F. Endres, I. Djerdj, M. Antonietti, B. M. Smarsly, J. Maier, Y.-S. Hu, *Small* **2007**, *3*, 1753 – 1763.

[47] M. H. G. Prechtl, P. S. Campbell, J. D. Scholten, G. B. Fraser, G. Machado, C. C. Santini, J. Dupont, Y. Chauvin, *Nanoscale* **2010**, *2*, 2601 – 2606.

[48] J. I. Langford, A. J. C. Wilson, *J. Appl. Crystallogr.* **1978**, *11*, 102 – 113.

[49] M. Yang, P. S. Campbell, C. C. Santini, A.-V. Mudring, *Nanoscale* **2014**, *6*, 3367 – 3375.

[50] L. S. Ott, M. L. Cline, M. Deetlefs, K. R. Seddon, R. G. Finke, *J. Am. Chem. Soc.* **2005**, *127*, 5758 – 5759.

[51] F. Davar, Z. Fereshteh, M. Salavati-Niasari, *J. Alloys Compd.* **2009**, *476*, 797 – 801.

[52] S. B. Dalavi, R. N. Panda, *J. Magn. Magn. Mater.* **2015**, *374*, 411 – 416.

[53] S.-H. Wu, D.-H. Chen, *J. Colloid Interface Sci.* **2003**, *259*, 282 – 286.

[54] D.-H. Chen, C.-H. Hsieh, *J. Mater. Chem.* **2002**, *12*, 2412 – 2415.

[55] C. N. Chinnasamy, B. Jeyadevan, K. Shinoda, K. Tohji, *J. Appl. Phys.* **2005**, *97*, 10J309.

[56] X. Luo, Y. Chen, G.-H. Yue, D.-L. Peng, X. Luo, *J. Alloys Compd.* **2009**, *476*, 864 – 868.

[57] J. Gong, L. L. Wang, Y. Liu, J. H. Jang, Z. G. Zong, *J. Alloys Compd.* **2008**, *457*, 6 – 9.

[58] V. Tzitzios, G. Basina, M. Gjoka, V. Alexandrakis, V. Georgakilas, D. Niarchos, N. Boukos, D. Petridis, *Nanotechnology* **2006**, *17*, 3750 – 3755.

[59] A. S. Bolokang, M. J. Phasha, *Mater. Lett.* **2011**, *65*, 59 – 60.

[60] L. A. García-Cerda, K. M. Bernal-Ramos, S. M. Montemayor, M. A. Quevedo-Lopez, R. Betancourt-Galindo, D. Bueno-Baques, *J. Nanomater.* **2011**, 1 – 5.

[61] A. Kotoulas, M. Gjoka, K. Simeonidis, I. Tsiaoussis, M. Angelakeris, O. Kalogirou, C. Dendrinou-Samara, *J. Nanopart. Res.* **2011**, *13*, 1897 – 1908.

[62] M. G. Freire, C. M. S. S. Neves, I. M. Marrucho, J. A. P. Coutinho, A. M. Fernades, *J. Phys. Chem. A* **2010**, *114*, 3744 – 3749.

[63] J. D. Makinson, J. S. Lee, S. H. Magner, R. J. De Angelis, W. N. Weins, A. S. Hieronymus, *Advances in X-ray Analysis* **2000**, *42*, 407 – 411; F. Zhang, S.-W. Chan, J. E. Spanier, E. Apak, Q. Jin, R. D. Robinson, I. P. Herman, *Appl. Phys. Lett.* **2002**, *80*, 127 – 129. K. Madhusudan Reddy, S. V. Manorama, A. R. Reddy, *Mater. Chem. Phys.* **2002**, *78*, 239 – 245.

[64] M. Kurian, C. Kunjachan, *Nano-Structures Nano-Objects* **2015**, *1*, 15 – 23; M. Manhas, V. Kumar, V. Sharma, O. M. Ntwaeaborwa, H. C. Swart, *Nano-Structures Nano-Objects* **2015**, *3*, 9 – 16.

[65] H. Jin, B. O'Hare, J. Dong, S. Arzhantsev, G. A. Baker, J. F. Wishard, A. J. Benesi, M. Maroncelli, *J. Phys. Chem. B* **2008**, *112*, 81 – 92.

[66] a) I. Krossing, J. M. Slattery, *Z. Phys. Chem.* **2006**, *220*, 1343 – 1359; b) J. M. Slattery, C. Daguenet, P. Dyson, I. Krossing, H. Weingärtner, A. Oleinikova, C. Wakai, *J. Phys. Chem. B* **2006**, *110*, 12682 – 12688.

[67] S. Behrens, S. Essig, *J. Mater. Chem.* **2012**, *22*, 3811 – 3816.

[68] Y. Hatakeyama, M. Okamoto, T. Torimoto, S. Kuwabata, K. Nishikawa, *J. Phys. Chem. C* **2009**, *113*, 3917 – 3922.

[69] Y. Hatakeyama, K. Onishi, K. Nishikawa, *RSC Adv.* **2011**, *1*, 1815 – 1821.

[70] E. Ramirez, S. Jansat, K. Philippot, P. Lecante, M. Gomez, A. M. Masdeu-Bultó, B. Chaudret, *J. Organomet. Chem.* **2004**, *689*, 4601 – 4610.

[71] T. Dorn, C. Janiak, K. Abu-Shandi, *CrystEngComm* **2005**, *7*, 633 – 641.

[72] A. M. Fernandes, M. A. A. Rocha, M. G. Freire, I. M. Marrucho, J. A. P. Coutinho, L. M. N. B. F. Santos, *J. Phys. Chem. B* **2011**, *115*, 4033 – 4041.

[73] M. Grass, D. Fischer, M. Mathes, G. Ganteför, P. Nielaba, *Appl. Phys. Lett.* **2002**, *81*, 3810.

[74] F. v. Gynz-Rekowski, W. Quester, R. Dietsche, D. C. Lim, N. Bertram, T. Fischer, G. Ganteför, M. Schach, P. Nielaba, Y. D. Kim, *Eur. Phys. J. D* **2007**, *45*, 409 – 413.

[75] T.-J. Park, G. C. Papaefthymiou, A. J. Viescas, A. R. Moodenbaugh, S. S. Wong, *Nano Lett.* **2007**, *7*, 766 – 772.

[76] M. Han, Q. Liu, J. He, Y. Song, Z. Xu, J. M. Zhu, *Adv. Mater.* **2007**, *19*, 1096 – 1100.

[77] Y. Mi, D. Yuan, Y. Liu, J. Zhang, Y. Xiao, *Mater. Chem. Phys.* **2005**, *89*, 359 – 361.

[78] A. P. Umpierre, E. de Jesús, J. Dupont, *ChemCatChem* **2011**, *3*, 1413 – 1418.

[79] O. M. Wilson, M. R. Knecht, J. C. Garcia-Martinez, R. M. Crooks, *J. Am. Chem. Soc.* **2006**, *128*, 4510 – 4511.

[80] A. Borodzinski, M. Bonarowska, *Langmuir* **1997**, *13*, 5613 – 5620.

[81] H. Hosseini-Monfared, H. Meyer, C. Janiak, *J. Mol. Catal. A* **2013**, *372*, 72 – 78.

[82] M. Pellarin, B. Baguenard, J. L. Vialle, J. Lermé, M. Broyer, J. Miller, A. Perez, *Chem. Phys. Lett.* **1994**, *217*, 349 – 356.

[83] R. E. Benfield, *J. Chem. Soc. Faraday Trans.* **1992**, *88*, 1107 – 1110.

[84] P. S. Campbell, C. C. Santini, F. Bayard, Y. Chauvin, V. Collière, A. Podgorsek, F. Costa Gomes, J. Sá, *J. Catal.* **2010**, *275*, 99 – 107.

[85] I. Bilecka, M. Niederberger, *Nanoscale* **2010**, *2*, 1358 – 1374.

[86] B. S. Lim, A. Rahtu, J.-S. Park, R. G. Gordon, *Inorg. Chem.* **2003**, *42*, 7951 – 7958.

[87] S. Schmidt, S. Schulz, D. Blaeser, R. Boese, M. Bolte, *Organometallics* **2010**, *29*, 6097 – 6103.

[88] S. Otsuka, M. Rossi, *J. Chem. Soc. A* **1968**, 2630 – 2633.

[89] N. V. Ignat'ev, P. Barthen, A. Kucheryna, H. Willner, P. Sartori, *Molecules* **2012**, *17*, 5319 – 5338.

[90] A. Thust, J. Barthel, K. Tillmann, *JLSRF* **2016**, *2*, 41.

[91] H. Weik, P. Hemenger, *Bull. Am. Phys. Soc.* **1965**, *10*, 1140.

[92] S. Sasaki, K. Fujino, Y. Takeuchi, *Proceed. Jap. Acad.* **1979**, *55*, 43 – 48.

[93] W. H. Baur, A. A. Khan, *Acta Crystallogr. Sect. B* **1971**, *27*, 2133 – 2139.

Manuscript received: November 10, 2016
Accepted Article published: February 14, 2017
Final Article published: April 7, 2017

CHEMISTRY
A European Journal

Supporting Information

Soft, Wet-Chemical Synthesis of Metastable Superparamagnetic Hexagonal Close-Packed Nickel Nanoparticles in Different Ionic Liquids

Susann Wegner,[a] Christina Rutz,[a] Kai Schütte,[a] Juri Barthel,[b] Alexey Bushmelev,[c] Annette Schmidt,[c] Katharina Dilchert,[d] Roland A. Fischer,[d] and Christoph Janiak*[a]

chem_201605251_sm_miscellaneous_information.pdf

Thermal stability of nickel amidinate $[\mathrm{Ni}\{\mathrm{MeC}(\mathrm{N}^{i}\mathrm{Pr})_2\}_2]$

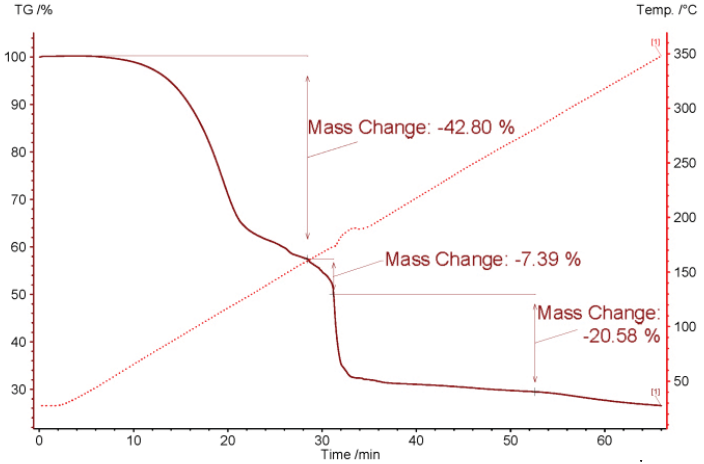

Fig. S1 Thermogravimetric analysis (TGA) of Ni amidinate $[\mathrm{Ni}\{\mathrm{MeC}(\mathrm{N}^{i}\mathrm{Pr})_2\}_2]$ between 25-350 °C, heating rate 5 K/min under N_2 atmosphere.

The observed step after 32 min suggesting decomposition at about 180 °C and a residual mass of about 27% is in full agreement with a literature report on the TG behavior of $[\mathrm{Ni}\{\mathrm{MeC}(\mathrm{N}^{i}\mathrm{Pr})_2\}_2]$.[1]

---

[1] B. S. Lim, A. Rahtu, J.-S. Park, R. G. Gordon, *Inorg. Chem.* **2003**, *42*, 7951-7958.

NMR study of decomposition of [Ni{MeC(N^{i}Pr)$_2$}$_2$] and [Ni(COD)$_2$] in [BMIm][NTf$_2$]:

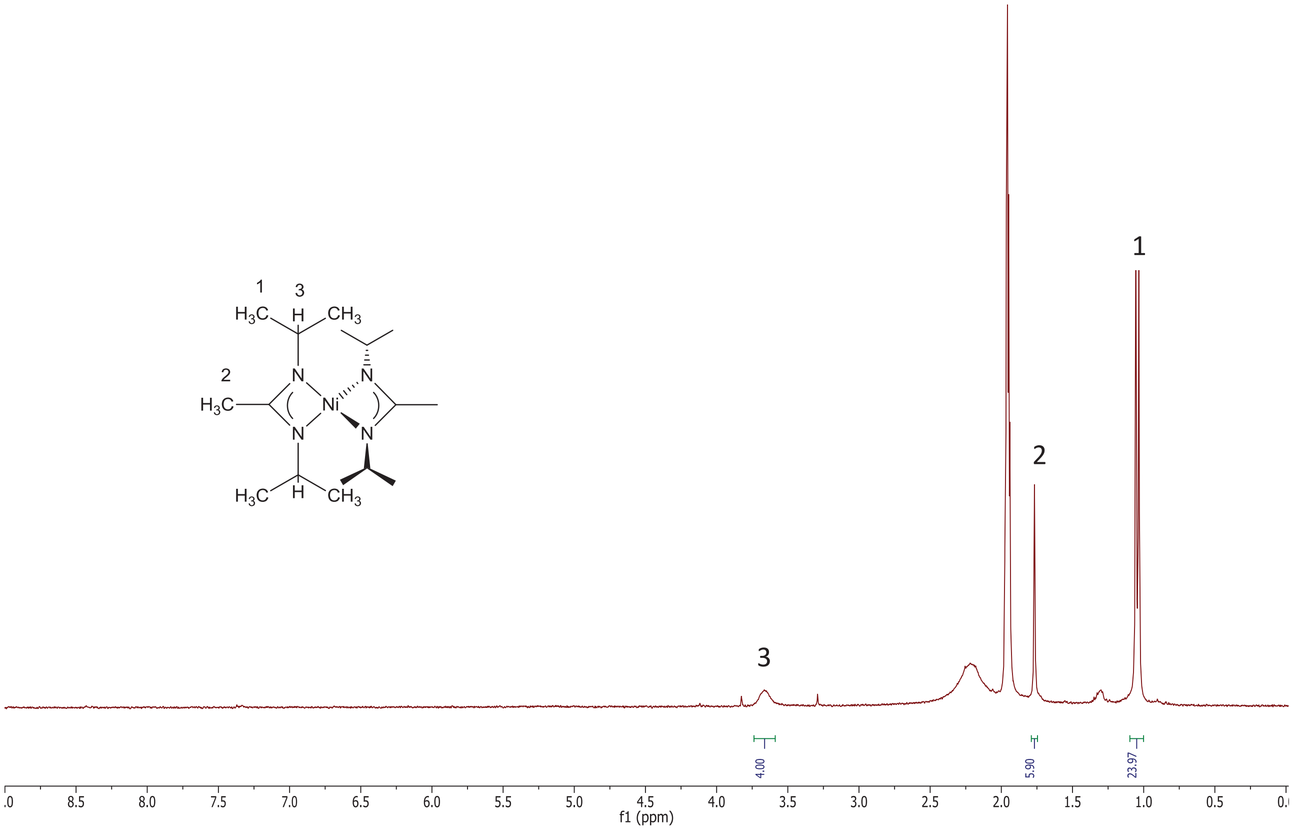

Fig. S1.1a ^{1}H-NMR analysis (CD_3CN, 300.13 MHz, 298 K) of [Ni{MeC(N^{i}Pr)$_2$}$_2$] solution.

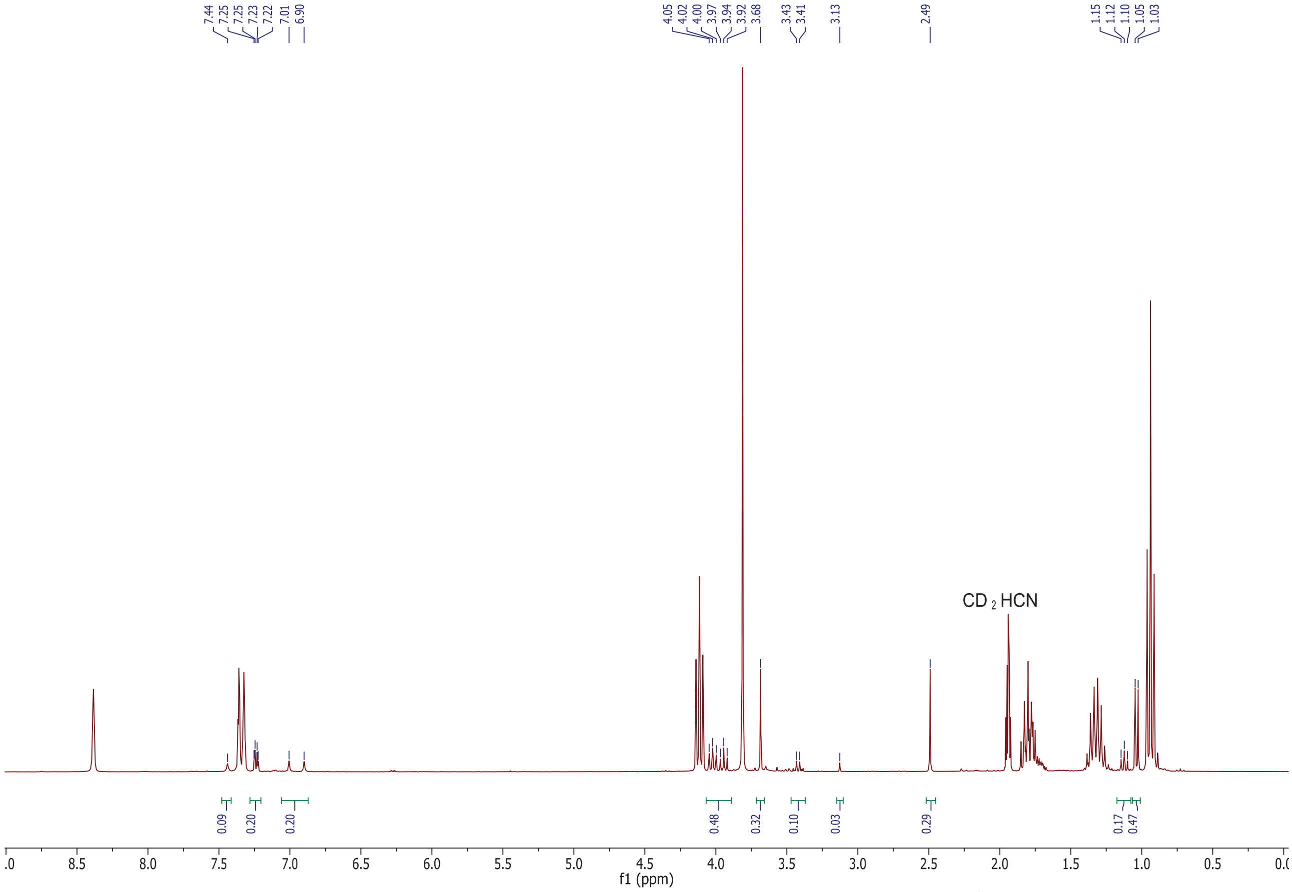

Fig. S1.1b ^{1}H-NMR analysis (CD_3CN, 300.13 MHz, 298 K) of [Ni{MeC(N^{i}Pr)$_2$}$_2$]/[BMIm][NTf$_2$] after 10 min MW heating at a power of 100 W to an approximate temperature of 220 °C in the IL. For comparison the spectrum of the IL after microwave treatment is given below in Fig. S1.1c.

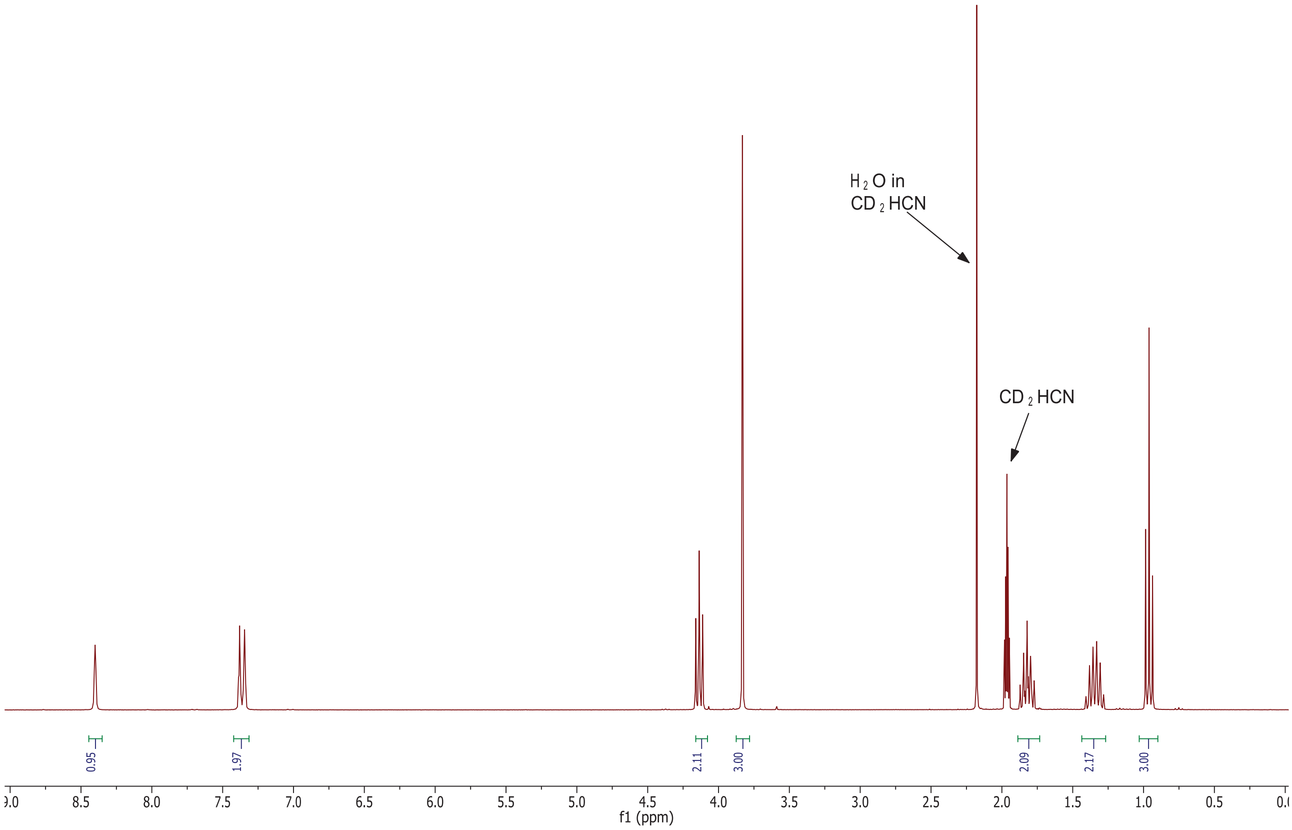

Fig. S1.1c ^{1}H-NMR analysis (CD_3CN, 300.13 MHz, 298 K) of [BMIm][NTf_2] after 10 min MW heating at a power of 100 W to an approximate temperature of 220 °C.

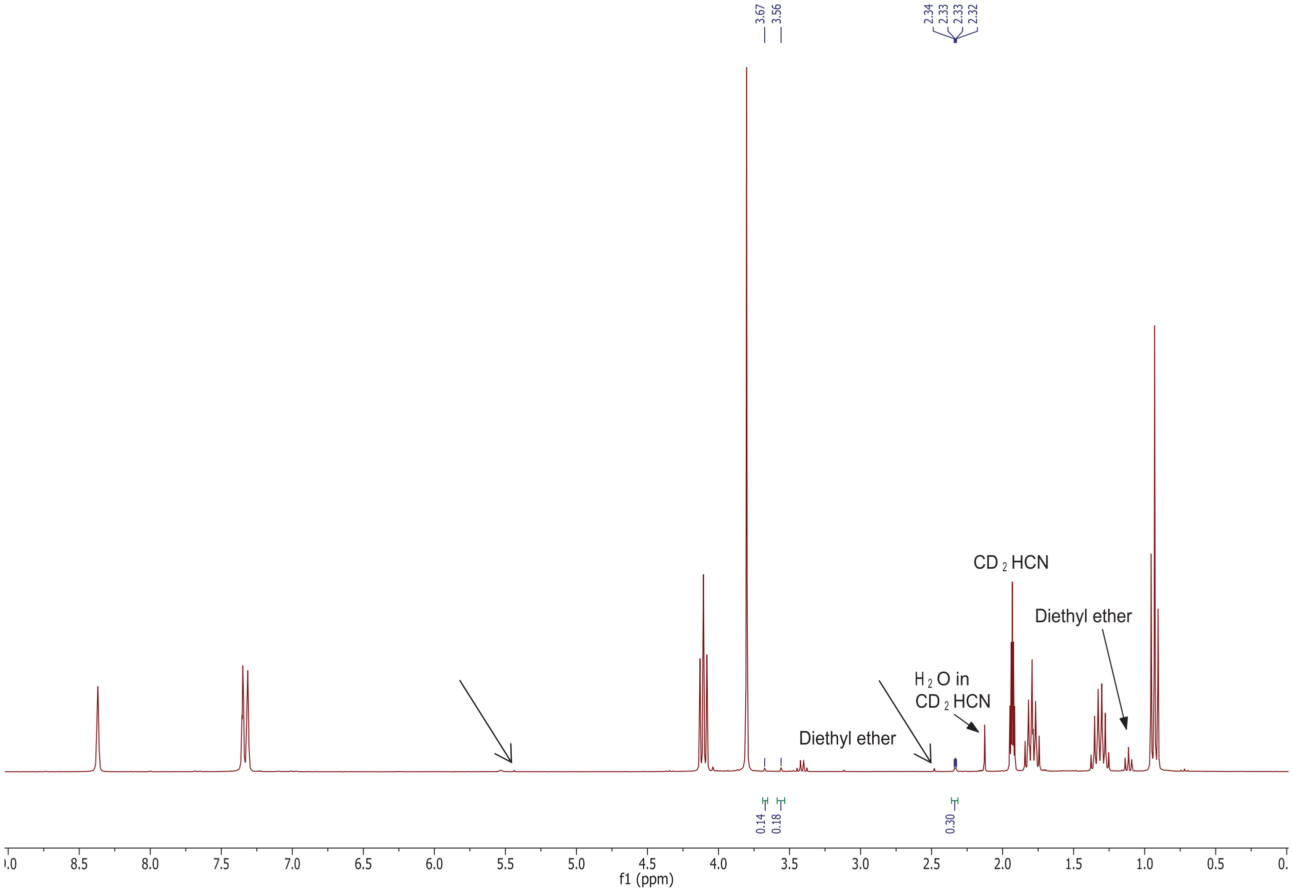

Fig. S1.2a ^{1}H-NMR analysis (CD_3CN, 300.13 MHz, 298 K) of bis(1,5-cyclooctadiene)nickel(0) [Ni(COD)$_2$]/[BMIm][NTf_2] after 10 min MW heating at a power of 100 W to an approximate temperature of 220 °C in the IL. Diethyl ether is a residue from the synthesis of [Ni(COD)$_2$].

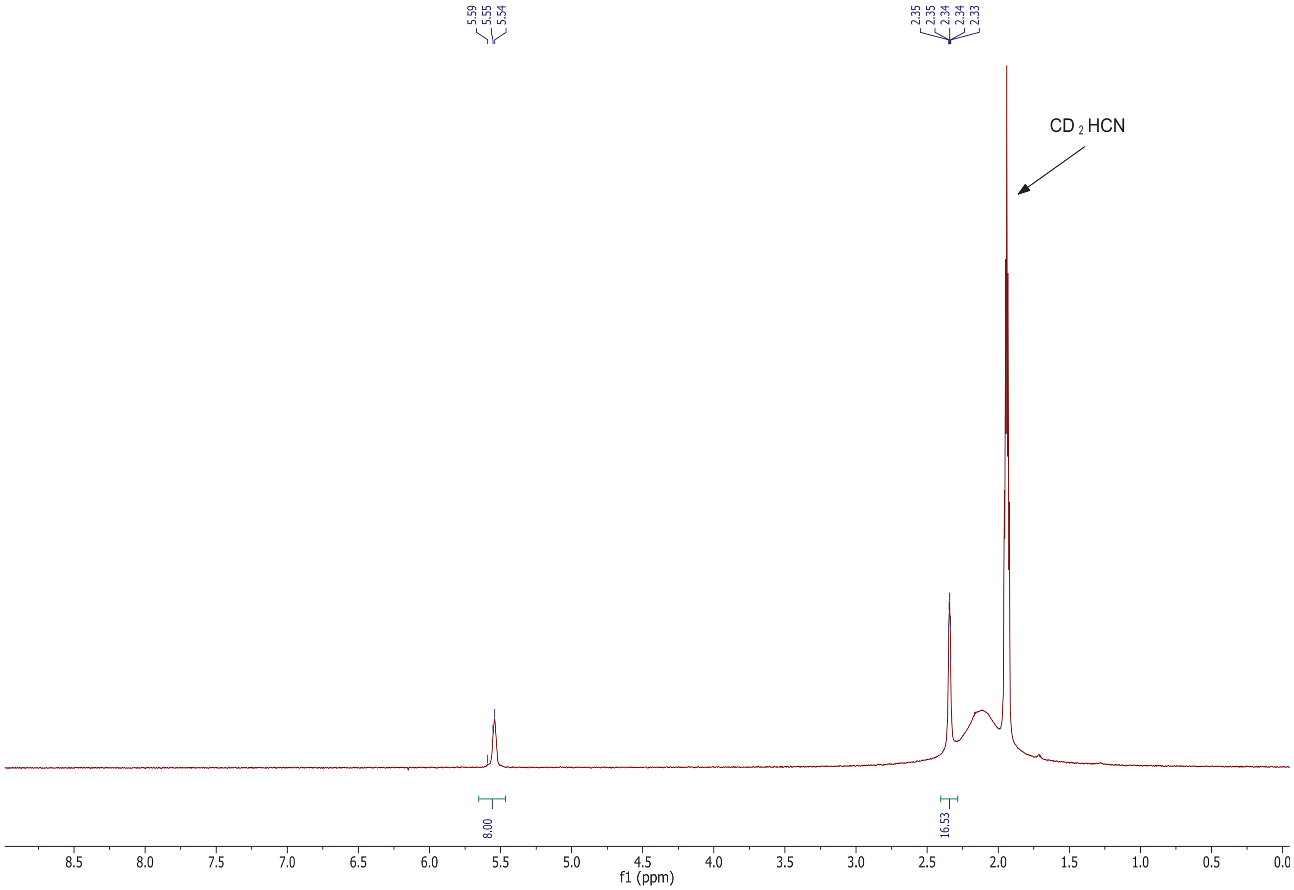

Fig. S1.2b ^{1}H-NMR analysis (CD_3CN, 300.13 MHz, 298 K) of bis(1,5-cyclooctadiene)nickel(0) [Ni(COD)$_2$] solution.

NMR analysis of decomposition of [Ni{MeC(N^{i}Pr)$_2$}$_2$] in [BMIm][NTf$_2$]:
(see. Figs. S1.1a-c)
The small additional signals in Fig. S1.1b at
δ (ppm) = ~0.8 (just to the right of the IL-triplet at 0.9), ~1.7(just to the right of the IL-quintet at 1.8), 3.68 (s), 3.92 (t) or 4.02 (t), 6.90 (s), 7.01 (s) are assigned to the formation of 1-methyl-3-butylimidazoliumylidene by deprotonation of the 2-H proton from the 1-methyl-3-butylimidazolium cation and concomitant protonation of the amidinate to (N,N'-diisopropylacetamidine according to eq. (S1).

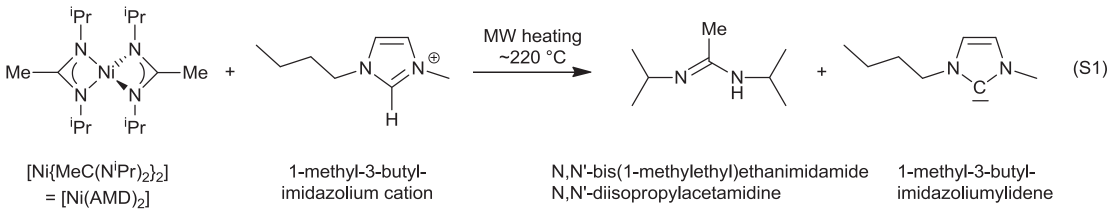

In the literature[2] the ^{1}H NMR of 1-methyl-3-butylimidazoliumylidene is given as
^{1}H-NMR (C_6D_6, 300 MHz): δ = 0.72 ppm (*t*, 3H, -C*H*$_3$), 1.14ppm (*sx*, 2H, C*H*$_2$-CH$_3$) ,
1.58 ppm (*q*, 2H, N-CH2-C*H*$_2$), 3.44 ppm (*s*, 3H, N-C*H*$_3$), 3.82 ppm (*t*, 2H, N-C*H*$_2$), 6.64 ppm (pd, 2 H, NC*H*C*H*N) (pd = pseudo-doublet).

---

[2] see ESI of T. Linder, J. Sundermeyer, *Chem. Commun.* **2009**, 2914–2916

or shown as[3]

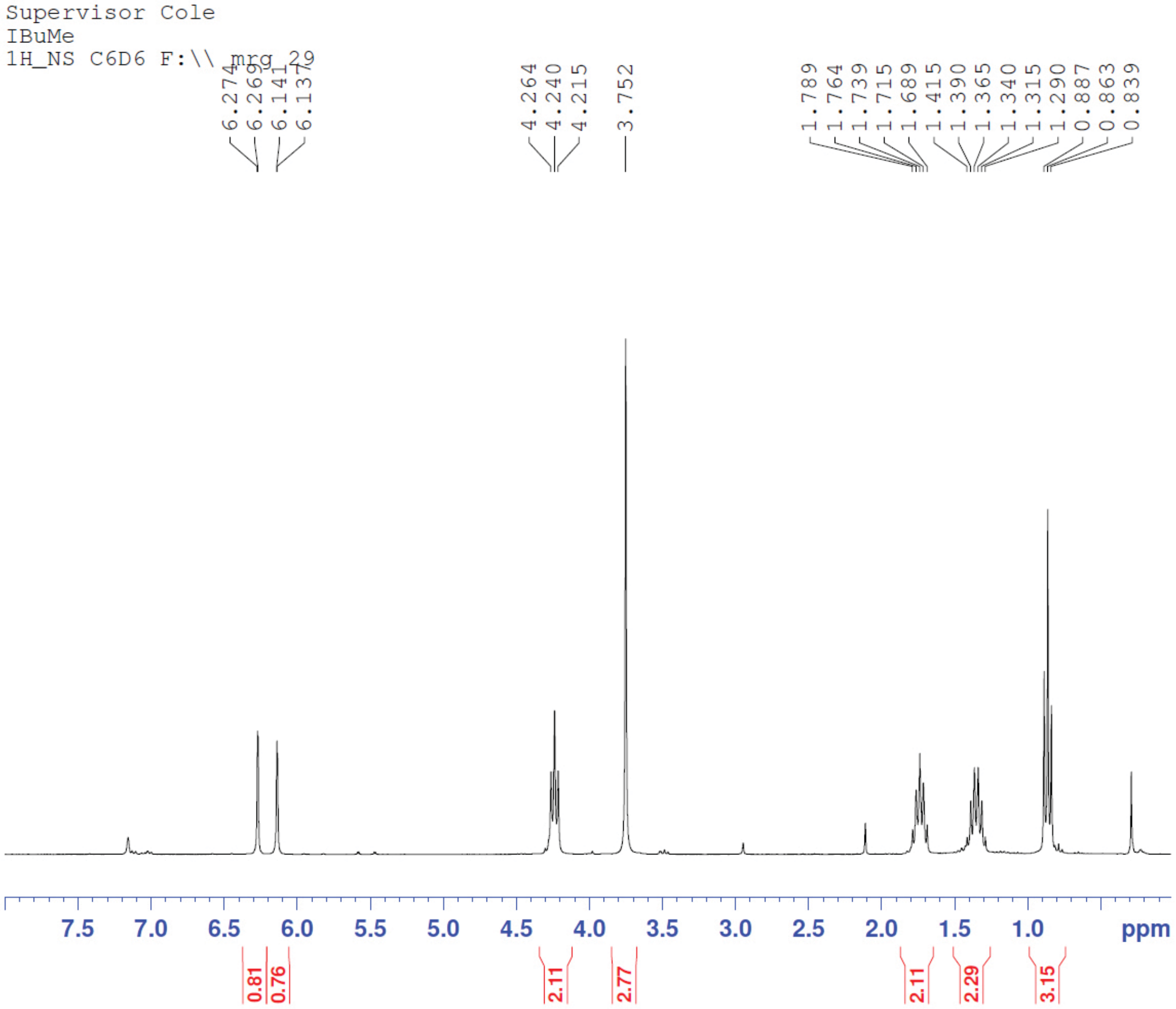

(The signal for CH_2-CH_3 – which is at 1.14 or at 1.36 ppm in the literature NMRs – apparently overlaps in Fig. S1.1b with the quintet at 1.3 ppm).

Concomitantly the NMR signals in Fig. S1.1b at
δ (ppm) = 1.04 (d, 6H, -CH(CH_3)$_2$), 2.49 (s, 3H, N_2C-CH_3) and 3.42 (m, 1H, -CH(CH_3)$_2$) are assigned to the protonated amidinate, N,N'-bis(1-methylethyl)ethanimidamide (N,N'-diisopropylacetamidine) in agreement with an NMR spectral prediction, shown below:[4]

---

[3] see Supp. Info. of M. L. Cole, M. R. Gyton, J. B. Harper, *Aust. J. Chem.* **2011**, *64*, 1133-1140.

[4] Predicted NMR data calculated using Advanced Chemistry Development, Inc. (ACD/Labs) Software V11.01 (© 1994-2016 ACD/Labs)

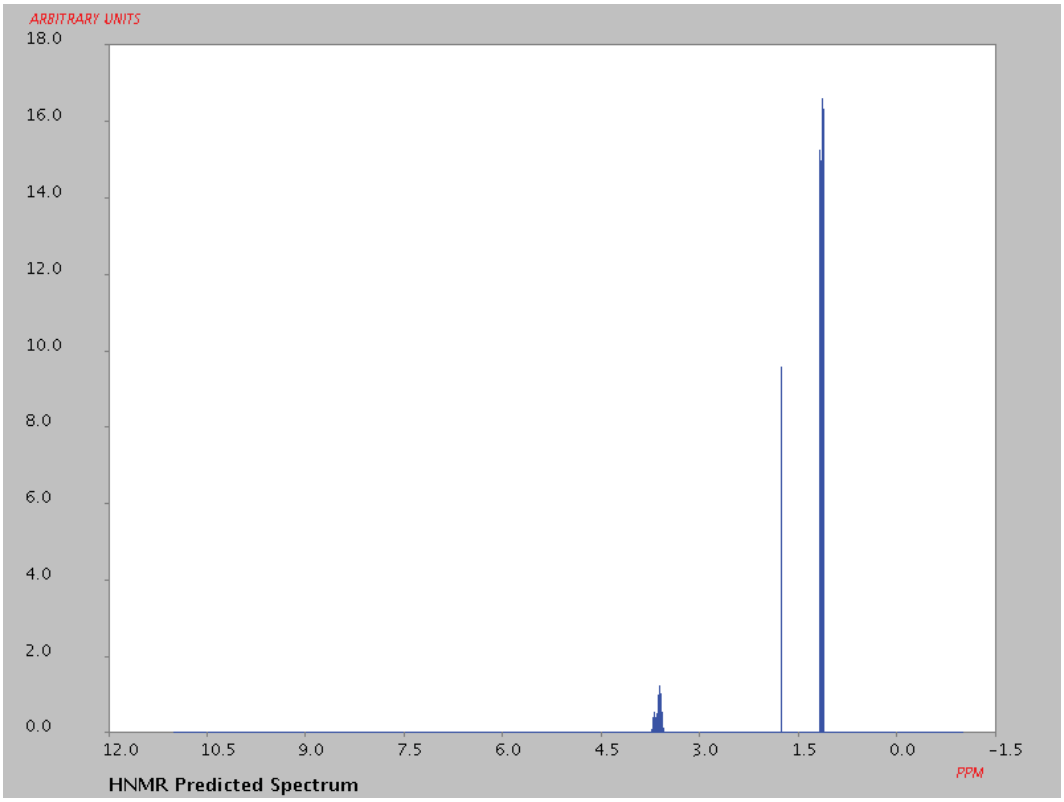

It is also known that metal amidinate compounds can also decompose by β-hydrogen elimination according to eq. (S2),[5] although the resulting acetimidamide is apparently not stable since the compound is unknown in the Scifinder data bank.

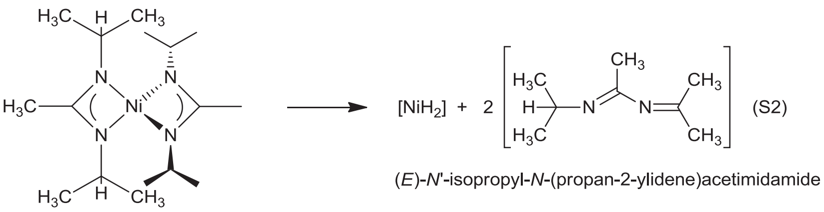

Further, metal amidinate decomposition is said to proceed by destruction of the amidinate itself. Mass spectrometry detected the fragment ^{i}Pr-N=C ($m/z = 69$) from [Cu{MeC(N^{i}Pr)$_2$}]$_2$.[6] Aluminum amidinates (Al{MeC(NiPr)$_2$}$_3$], Al{EtC(NiPr)$_2$}$_3$],Al{MeC(NiPr)$_2$}(Et)$_2$]) were also found to produce N,N'-diisopropylcarbodiimide, ^{i}Pr$_2$CH-N=C=N-CH^{i}Pr$_2$ on heating.[7]

NMR analysis of decomposition of [Ni(COD)$_2$]/[BMIm][NTf$_2$]:

(see Fig. S1.2a and b)

The NMR spectrum of the dispersion (taken up in CD_3CN) of [Ni(COD)$_2$]/[BMIm][NTf$_2$] after 10 min MW heating at a power of 100 W to an approximate temperature of 220 °C shows essentially only signals of the IL, some diethyl ether (brought in with [Ni(COD)$_2$]).

Small signals of [Ni(COD)$_2$] can still be seen at 2.33 ppm and 5.55 ppm (cf. to the [Ni(COD)$_2$] spectrum in Fig. S1.2b.

---

[5] Z. Li, S. T. Barry, R. G. Gordon, *Inorg. Chem.* **2005**, *44*, 1728-1735. S. T. Barry, *Coord. Chem. Rev.* **2013**, *257*, 3192-3201.

[6] J. P. Coyle, W. H. Monillas, G. P. A. Yap, S. T. Barry, *Inorg. Chem.* **2008**, *47*, 683-689.

[7] A. L. Brazeau, G. A. DiLabio, K. A. Kreisel, W. H. Monillas, G. P. A. Yap, S. T. Barry, *Dalton Trans.* **2007**, 3297–3304.

There are two very small peaks at 2.5 and 5.5 ppm in Fig. S1.2 which we assign to 1,5-COD in line with a literature spectrum:

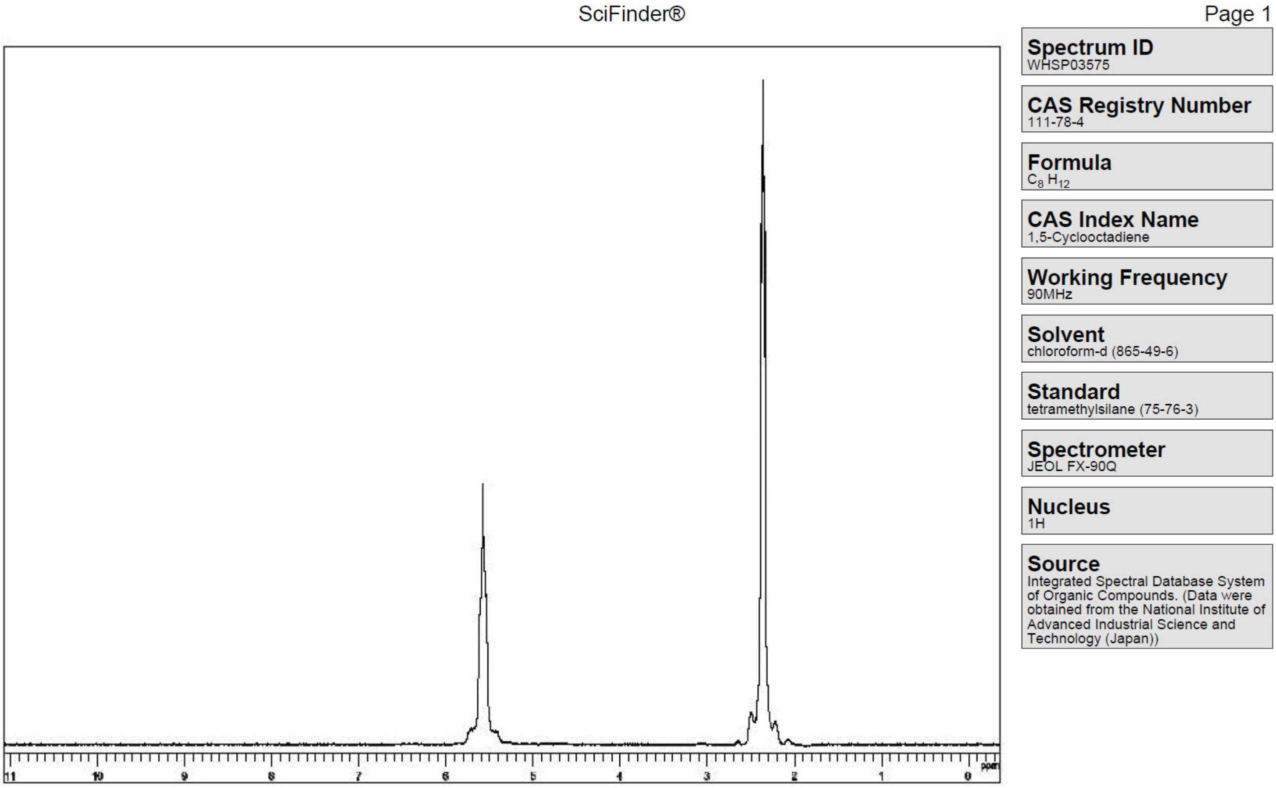

SciFinder®

Page 1

Spectrum ID
WHSP03575

CAS Registry Number
111-78-4

Formula
C_8H_{12}

CAS Index Name
1,5-Cyclooctadiene

Working Frequency
90MHz

Solvent
chloroform-d (865-49-6)

Standard
tetramethylsilane (75-76-3)

Spectrometer
JEOL FX-90Q

Nucleus
1H

Source
Integrated Spectral Database System of Organic Compounds. (Data were obtained from the National Institute of Advanced Industrial Science and Technology (Japan))

Ni-NPs from Ni amidinate [Ni{MeC(N^{i}Pr)$_2$}$_2$] as precursor

Ni-NPs from [Ni{MeC(N^{i}Pr)$_2$}$_2$] in [BMIm][PF$_6$]

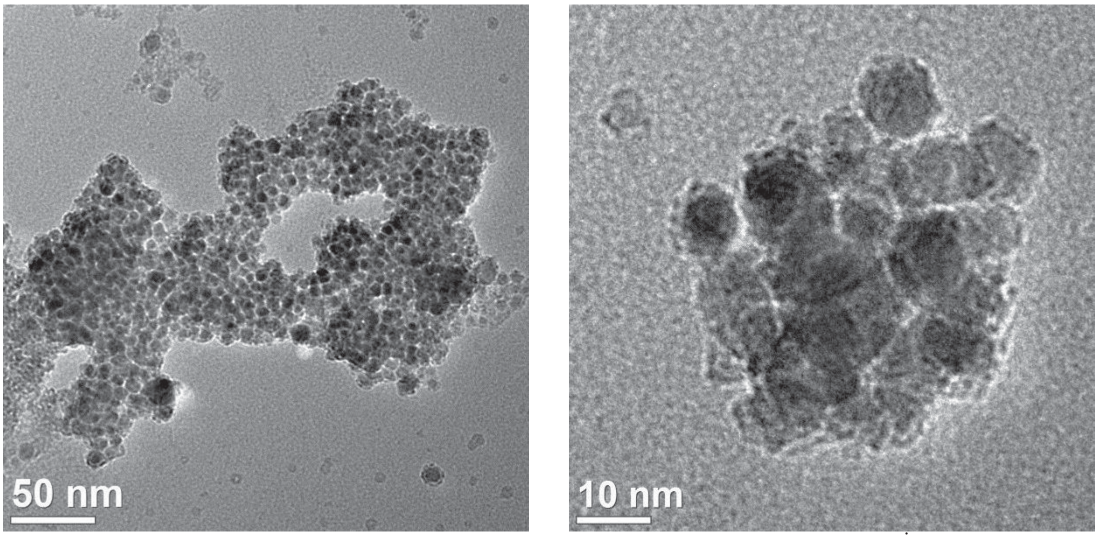

Fig. S2.1 TEM of Ni-NPs in [BMIm][PF$_6$] (1 wt.%) from [Ni{MeC(N^{i}Pr)$_2$}$_2$].

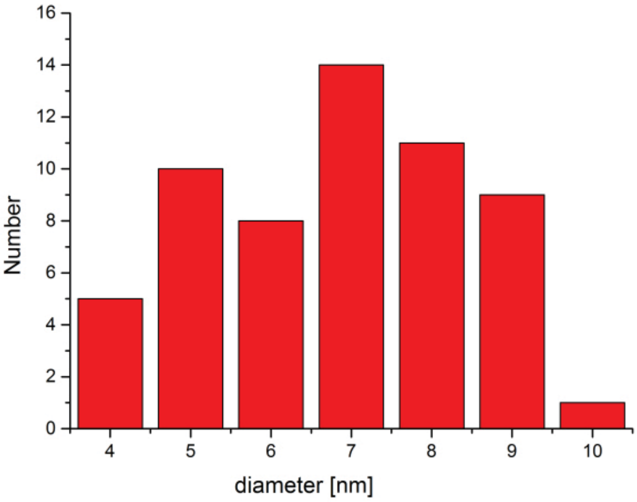

Fig. S2.2 Histogram from 63 Ni-NPs from [Ni{MeC(N^{i}Pr)$_2$}$_2$] in [BMIm][PF$_6$].

Ni-NPs from $[Ni\{MeC(N^iPr)_2\}_2]$ in $[BMIm][NTf_2]$

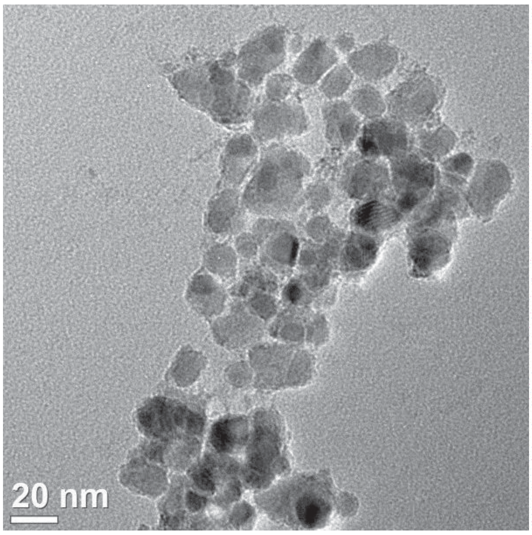

Fig. S2.3 TEM of Ni-NPs in $[BMIm][NTf_2]$ (1 wt.%) from $[Ni\{MeC(N^iPr)_2\}_2]$

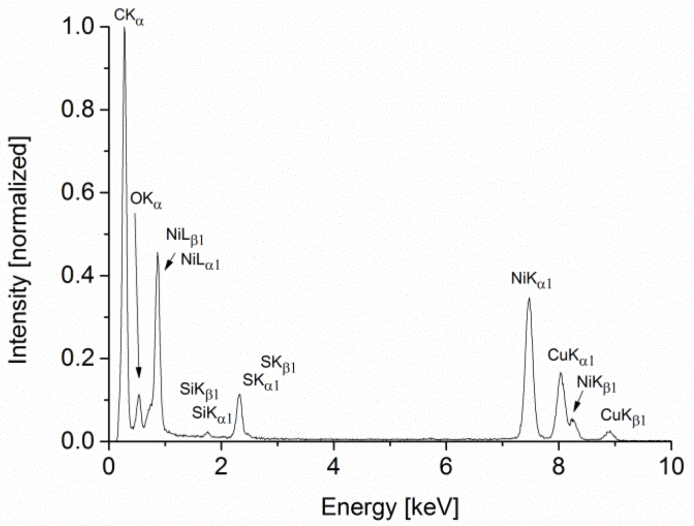

Fig. S2.4 EDX spectrum of 1.0 wt% Ni-NPs in $[BMIm][NTf_2]$ from $[Ni\{MeC(N^iPr)_2\}_2]$.

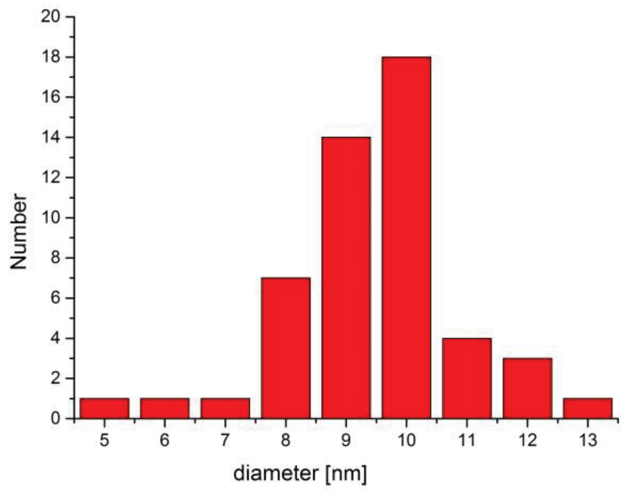

Fig. S2.5 Histogram from 50 Ni-NPs from $[Ni\{MeC(N^iPr)_2\}_2]$ in $[BMIm][NTf_2]$.

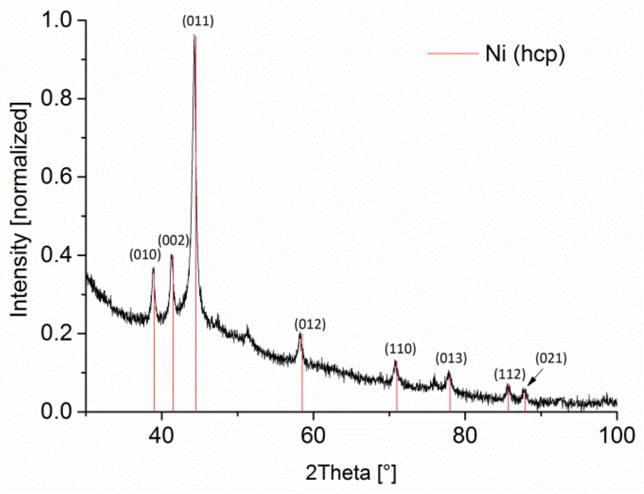

Fig. S2.6 PXRD of $Ni/[BMIm][NTf_2]$ (Ni-hcp reference peaks in red, COD 94715) before catalysis.

Ni-NPs from [Ni{MeC(N^{i}Pr)$_2$}$_2$] in [OMIm][PF$_6$]

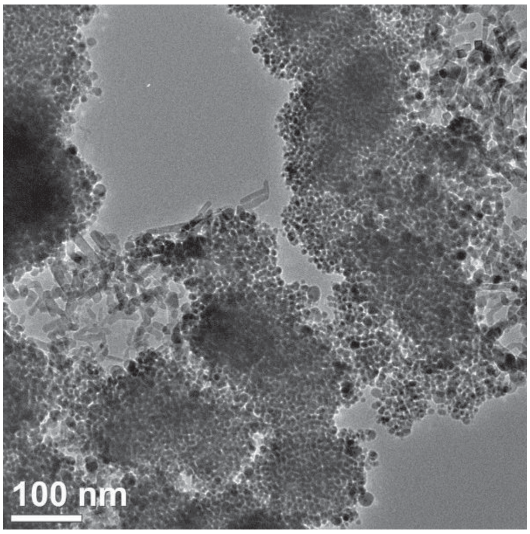

Fig. S2.7 TEM of Ni-NPs in [OMIm][PF$_6$] (1 wt.%) from [Ni{MeC(N^{i}Pr)$_2$}$_2$].

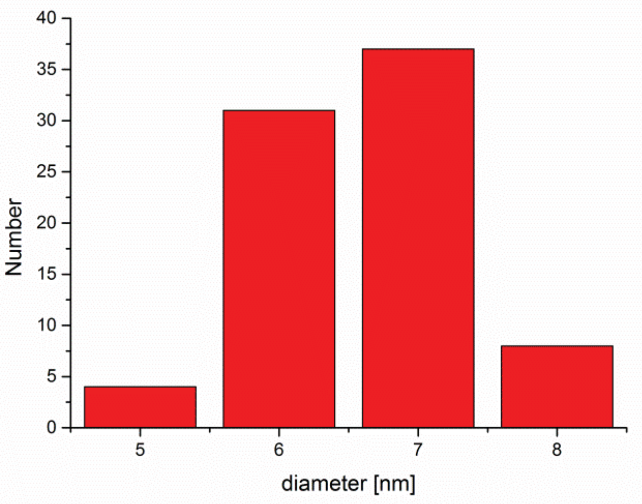

Fig. S2.8 Histogram from 80 Ni-NPs from [Ni{MeC(N^{i}Pr)$_2$}$_2$] in [OMIm][PF$_6$].

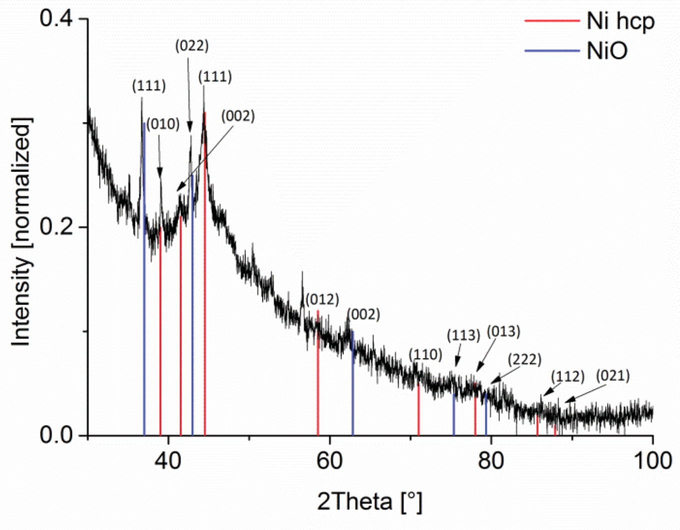

Fig. S2.9 PXRD of Ni/[OMIm][PF$_6$]
(Ni-hcp reference peaks in red, COD 94715)
(NiO reference peaks in blue, COD 1010095).

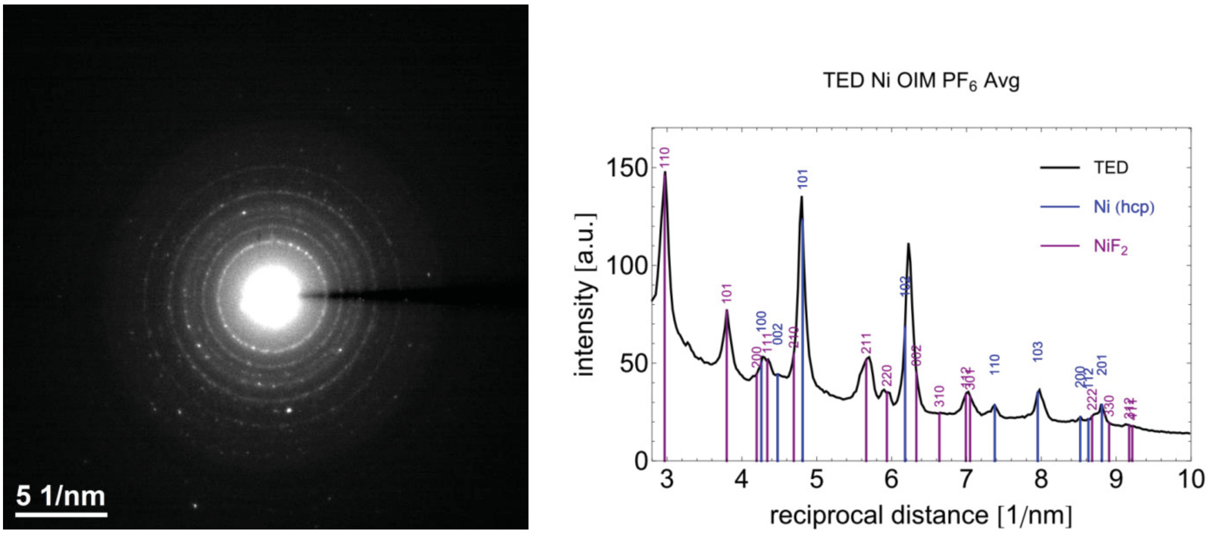

Fig. S2.10 Selected-area powder transmission electron diffraction (TED) showing a Debye-Scherrer pattern of Ni (hcp) and NiF_2 crystals (left) and azimuthal average of the Debye-Scherrer pattern in comparison to the reflexions of Ni (hcp) and NiF_2.

Ni-NPs from $[\mathrm{Ni}\{\mathrm{MeC}(\mathrm{N}^{i}\mathrm{Pr})_2\}_2]$ in $[\mathrm{OMIm}][\mathrm{NTf}_2]$

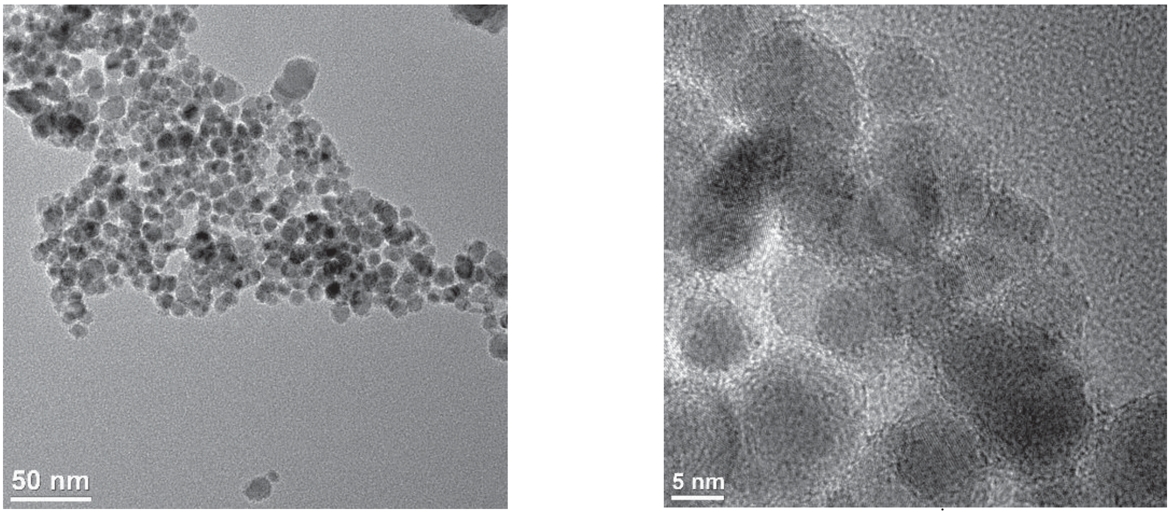

Fig. S2.11 TEM of Ni-NPs in $[\mathrm{OMIm}][\mathrm{NTf}_2]$ (1 wt.%) from $[\mathrm{Ni}\{\mathrm{MeC}(\mathrm{N}^{i}\mathrm{Pr})_2\}_2]$.

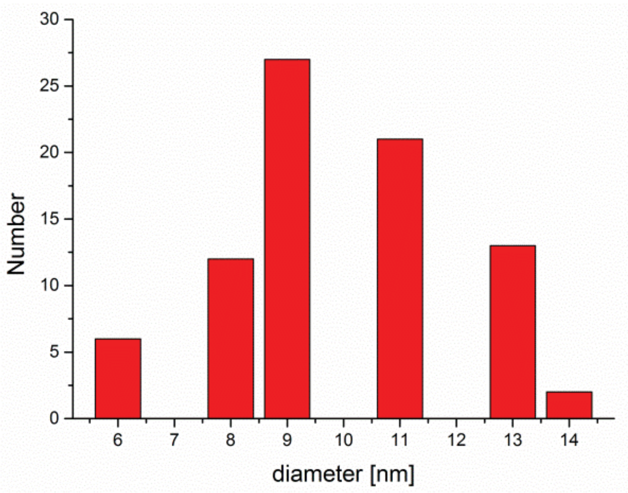

Fig. S2.12 Histogram from 85 Ni-NPs from $[\mathrm{Ni}\{\mathrm{MeC}(\mathrm{N}^{i}\mathrm{Pr})_2\}_2]$ in $[\mathrm{OMIm}][\mathrm{NTf}_2]$.

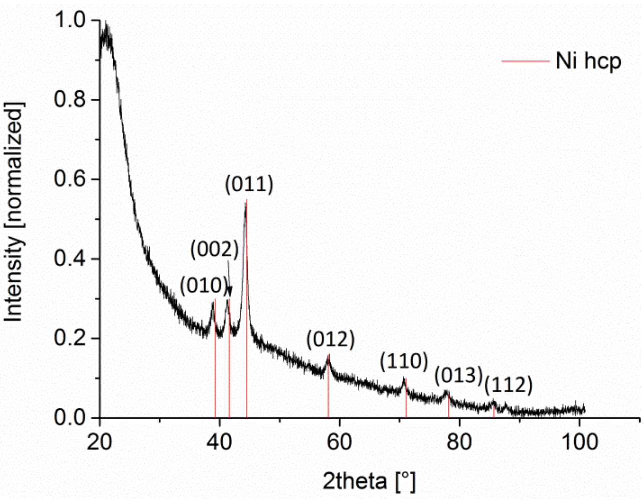

Fig. S2.13 PXRD of $\mathrm{Ni}/[\mathrm{OMIm}][\mathrm{NTf}_2]$ (Ni-hcp reference peaks in red, COD 9008509).

Ni-NPs from [Ni{MeC(N^iPr)$_2$}$_2$] in [LMIm][BF_4]

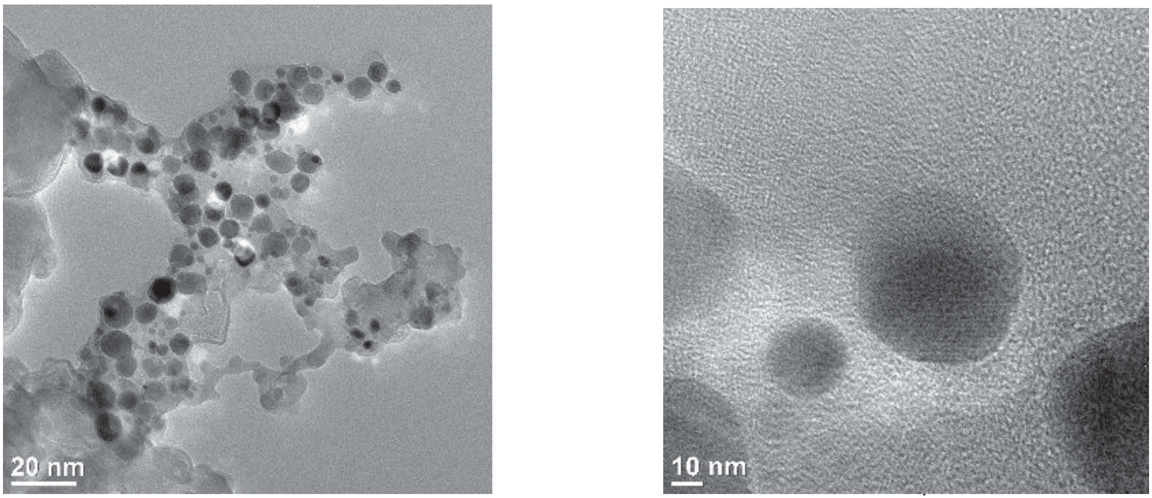

Fig. S2.14 TEM of Ni-NPs in [LMIm][BF_4] (1 wt.%) from [Ni{MeC(N^iPr)$_2$}$_2$].

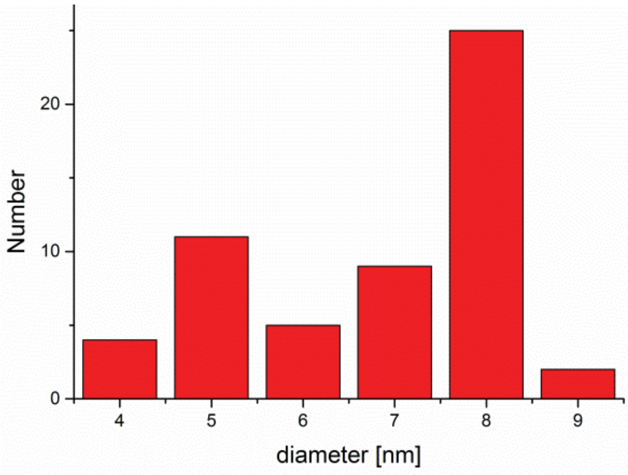

Fig. S2.15 Histogram of 60 particles of Ni/[LMIm][BF_4] (1 wt.%).

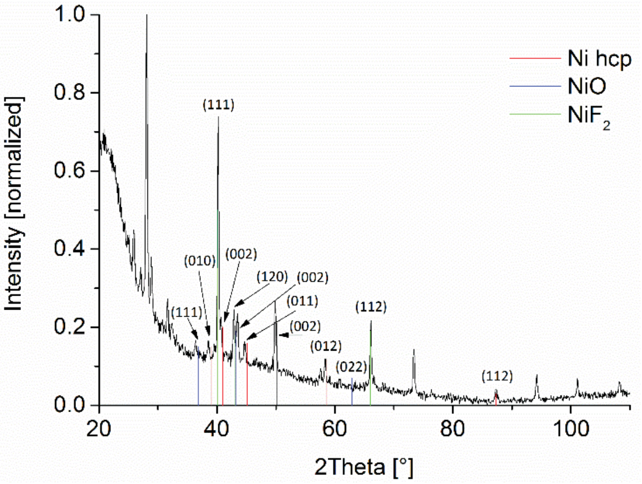

Fig. S2.16 PXRD of Ni/[LMIm][BF_4] (Ni-hcp reference peaks in red, COD 9013007), (NiO reference peaks in blue, COD 1010095), (NiF_2 reference peaks in green, COD 9007538).

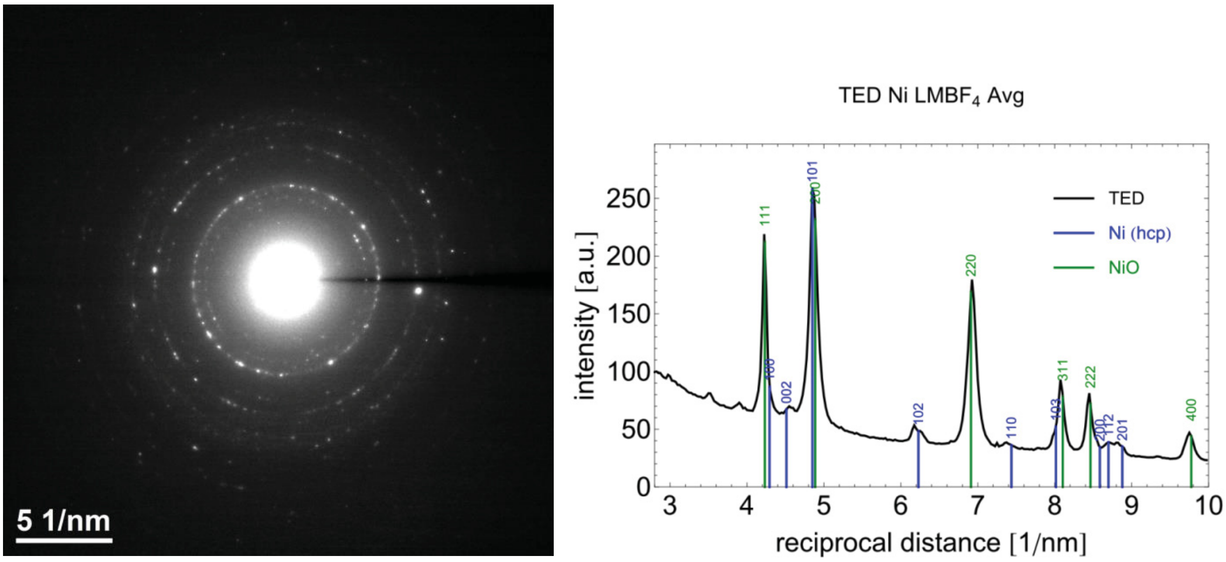

Fig. 2.17 Selected-area powder TED showing a Debye-Scherrer pattern of Ni (hcp) and NiO crystals (left) and azimuthal average of the pattern in comparison to the reflexions of Ni (hcp) and NiO (right).

Ni-NPs from $[\mathrm{Ni}\{\mathrm{MeC}(\mathrm{N}^i\mathrm{Pr})_2\}_2]$ in $[\mathrm{LMIm}][\mathrm{PF}_6]$

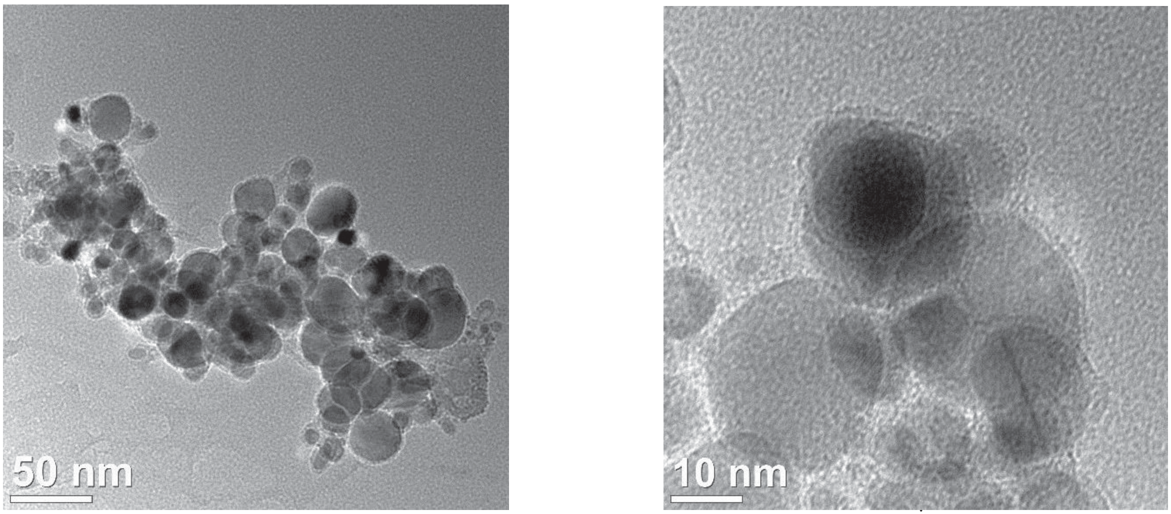

Fig. S2.18 TEM of Ni-NPs in $[\mathrm{LMIm}][\mathrm{PF}_6]$ (1 wt.%) from $[\mathrm{Ni}\{\mathrm{MeC}(\mathrm{N}^i\mathrm{Pr})_2\}_2]$.

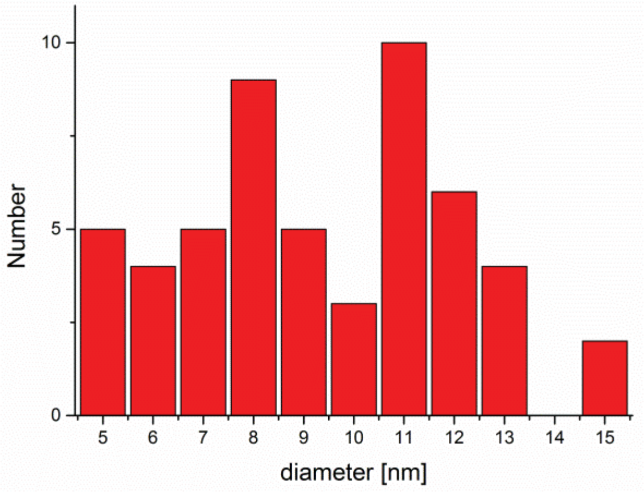

Fig. S2.19 Histogram of 53 particles of Ni/$[\mathrm{LMIm}][\mathrm{PF}_6]$ (1 wt.%).

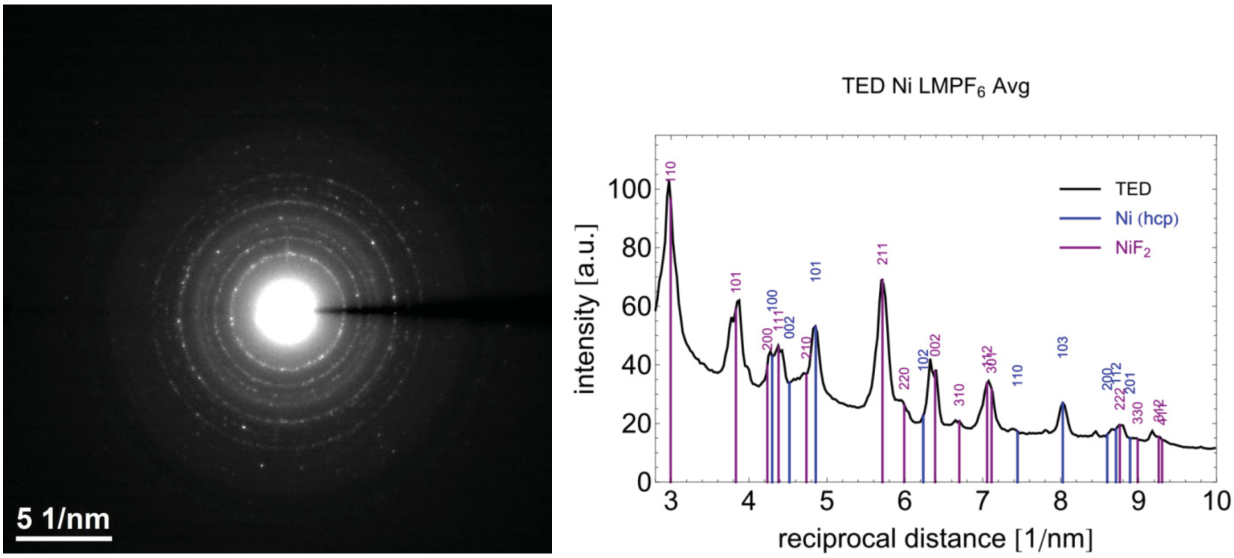

Fig. S2.20 Selected-area powder transmission electron diffraction showing a Debye-Scherrer pattern of Ni (hcp) and NiF$_2$ crystals (left) and azimuthal average of the SAED in comparison to the reflexions of Ni (hcp) and NiF$_2$ (right).

Ni-NPs from $[\mathrm{Ni}\{\mathrm{MeC}(\mathrm{N}^i\mathrm{Pr})_2\}_2]$ in $[\mathrm{LMIm}][\mathrm{NTf}_2]$

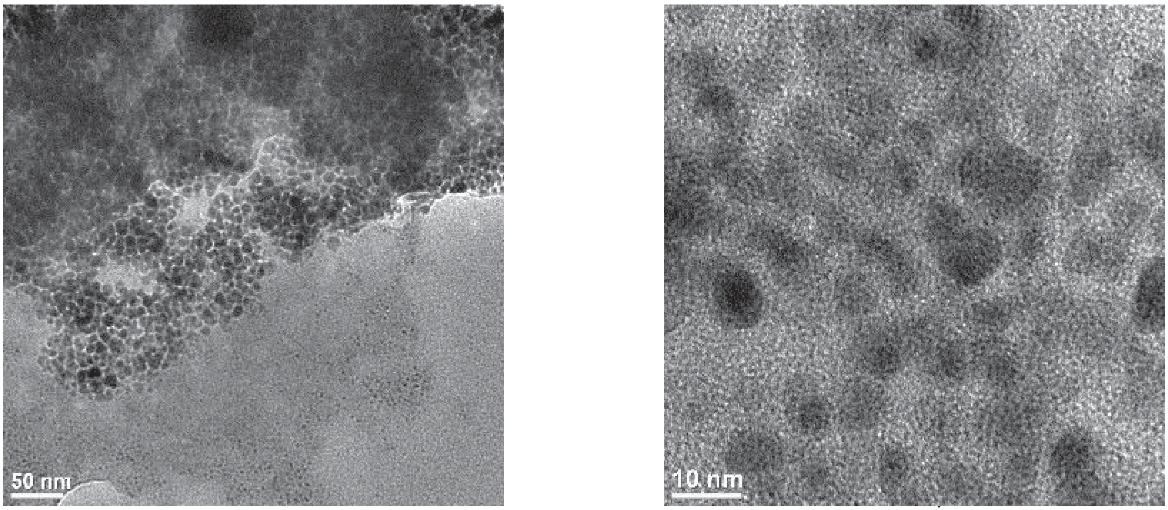

Fig. S2.21 TEM of Ni-NPs in $[\mathrm{LMIm}][\mathrm{NTf}_2]$ (1 wt.%) from $[\mathrm{Ni}\{\mathrm{MeC}(\mathrm{N}^i\mathrm{Pr})_2\}_2]$.

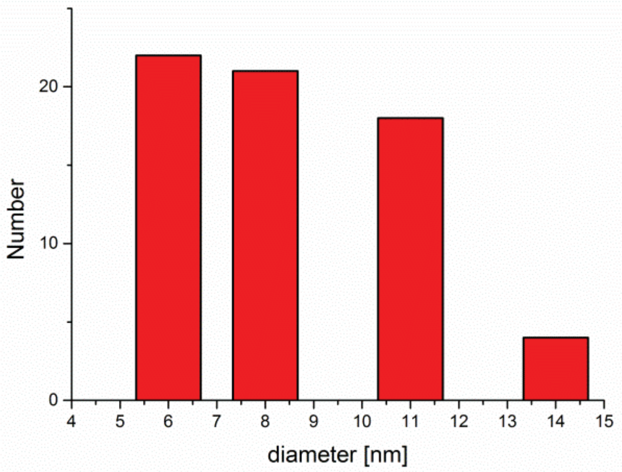

Fig. S2.22 Histogram of 67 particles of $\mathrm{Ni}/[\mathrm{LMIm}][\mathrm{NTf}_2]$ (1 wt.%).

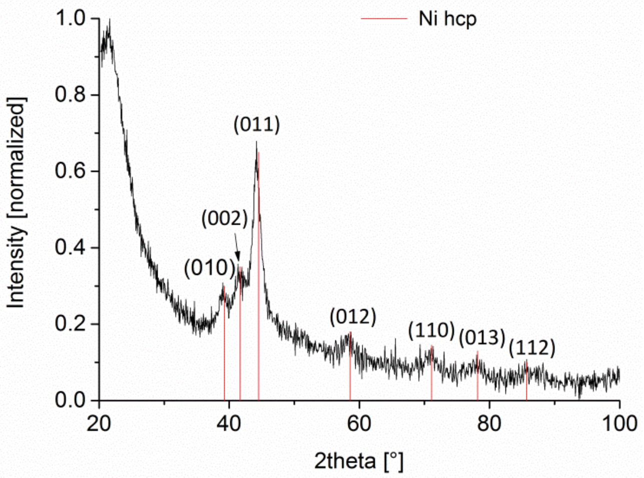

Fig. S2.23 PXRD of $\mathrm{Ni}/[\mathrm{LMIm}][\mathrm{NTf}_2]$ (1 wt.%) (Ni-hcp reference peaks in red, COD 9008509)

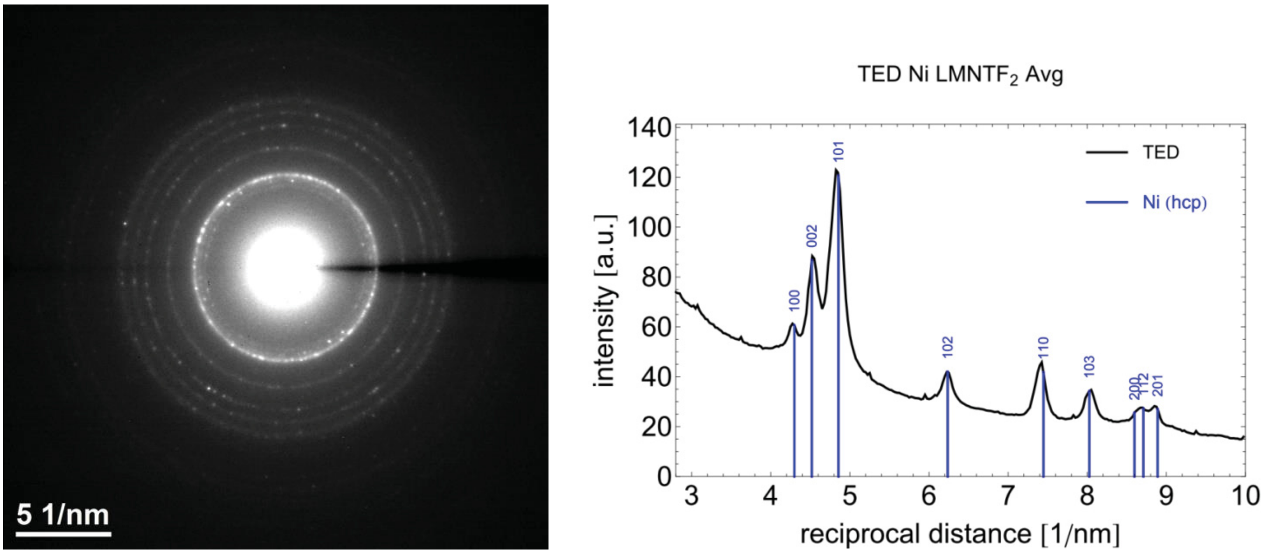

Fig. S2.24 Selected-area powder transmission electron diffraction showing a Debye-Scherrer pattern of Ni (hcp) crystals (left) and azimuthal average of the SAED pattern in comparison to the reflexions of Ni (hcp) (right).

Ni-NPs from $[\mathrm{Ni}\{\mathrm{MeC}(\mathrm{N}^{i}\mathrm{Pr})_2\}_2]$ in $[\mathrm{BuPy}][\mathrm{PF}_6]$

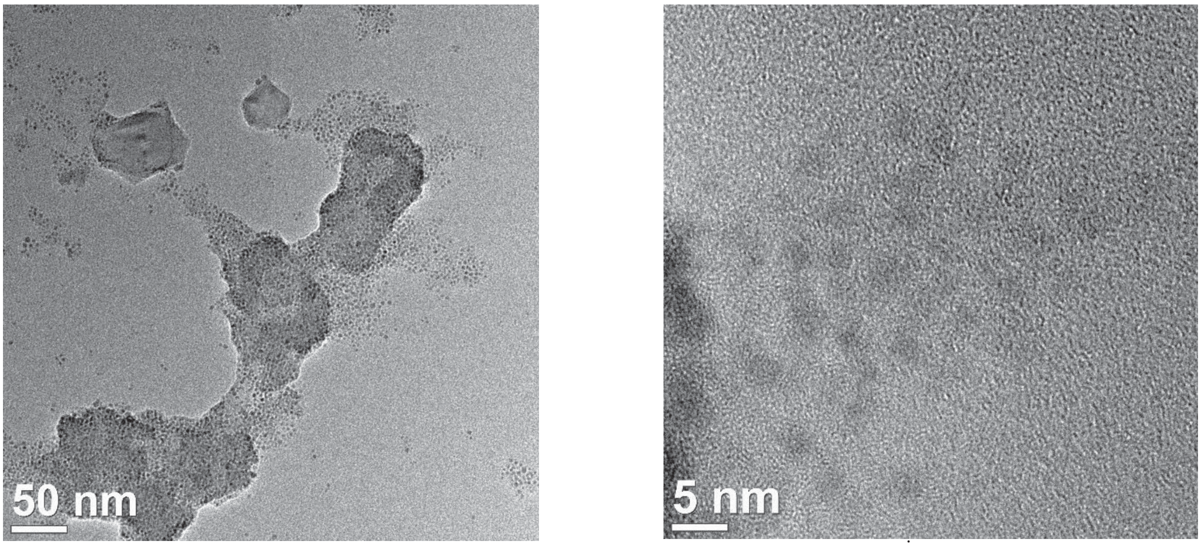

Fig. S2.25 TEM of Ni-NPs in $[\mathrm{BuPy}][\mathrm{PF}_6]$ (1 wt.%) from $[\mathrm{Ni}\{\mathrm{MeC}(\mathrm{N}^{i}\mathrm{Pr})_2\}_2]$.

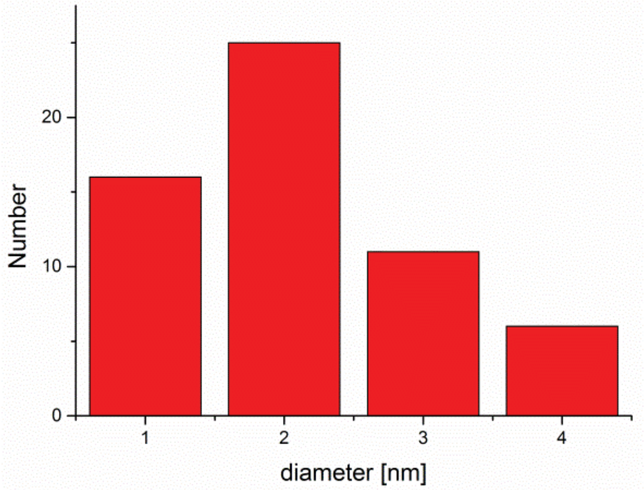

Fig. S2.26 Histogram of 87 Ni-NPs from $[\mathrm{Ni}\{\mathrm{MeC}(\mathrm{N}^{i}\mathrm{Pr})_2\}_2]$ in $[\mathrm{BuPy}][\mathrm{PF}_6]$.

Ni-NPs from $[Ni\{MeC(N^{i}Pr)_2\}_2]$ in $[LPy][PF_6]$

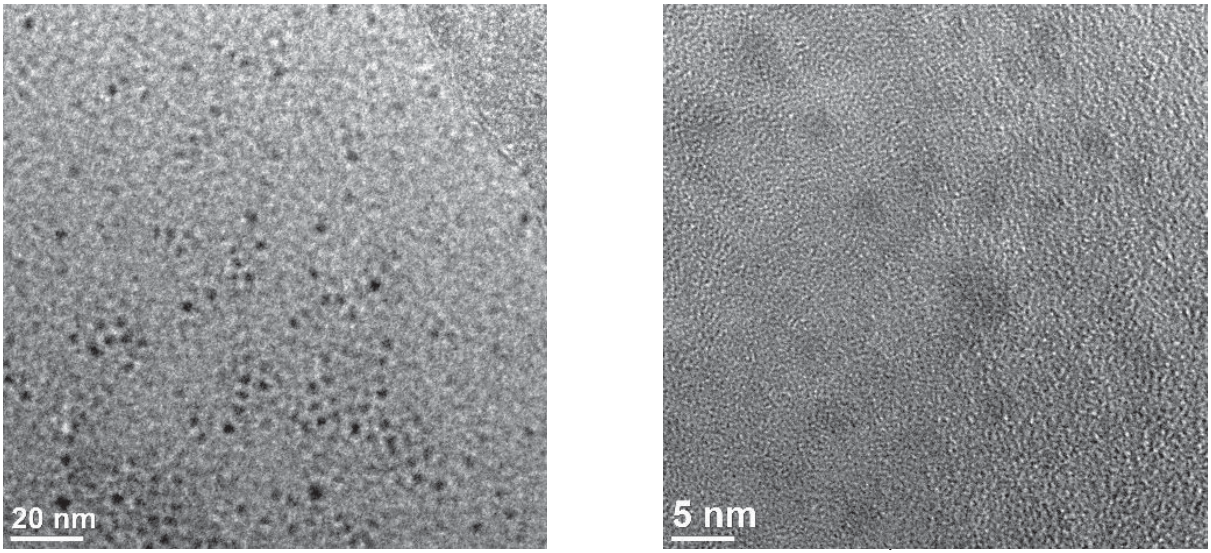

Fig. S2.27 TEM of Ni-NPs in $[LPy][PF_6]$ (1 wt.%) from $[Ni\{MeC(N^{i}Pr)_2\}_2]$.

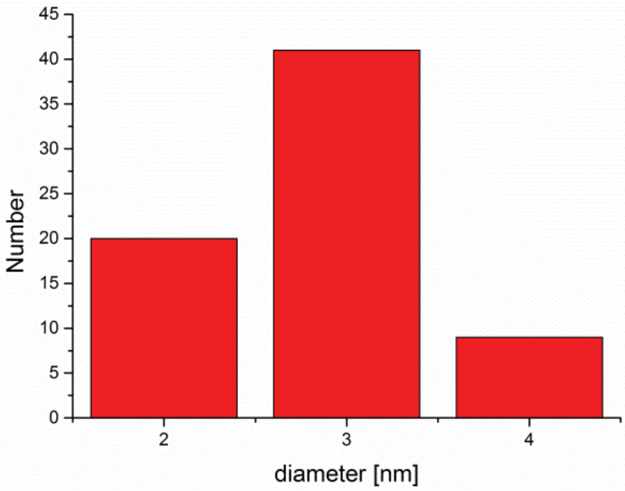

Fig. S2.28 Histogram of 70 Ni-NPs from $[Ni\{MeC(N^{i}Pr)_2\}_2]$ in $[LPy][PF_6]$.

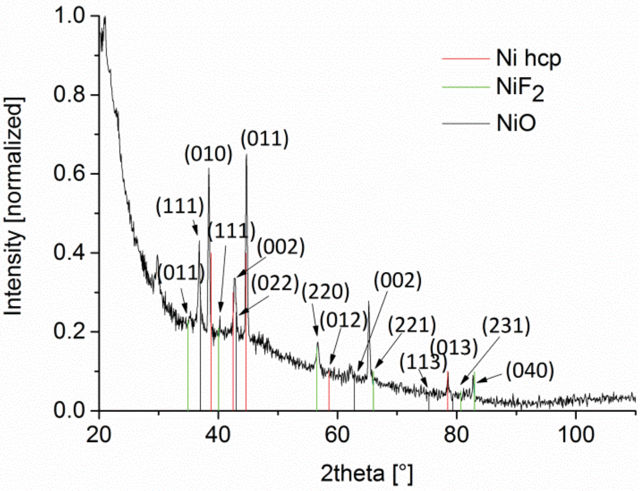

Fig. S2.29 PXRD of 1.0 wt% Ni/$[LPy][PF_6]$. (Ni-hcp, reference peaks in red, COD 9008509), (NiO reference peaks in black, COD 1010095), (NiF_2 reference peaks in green, COD 9007538)

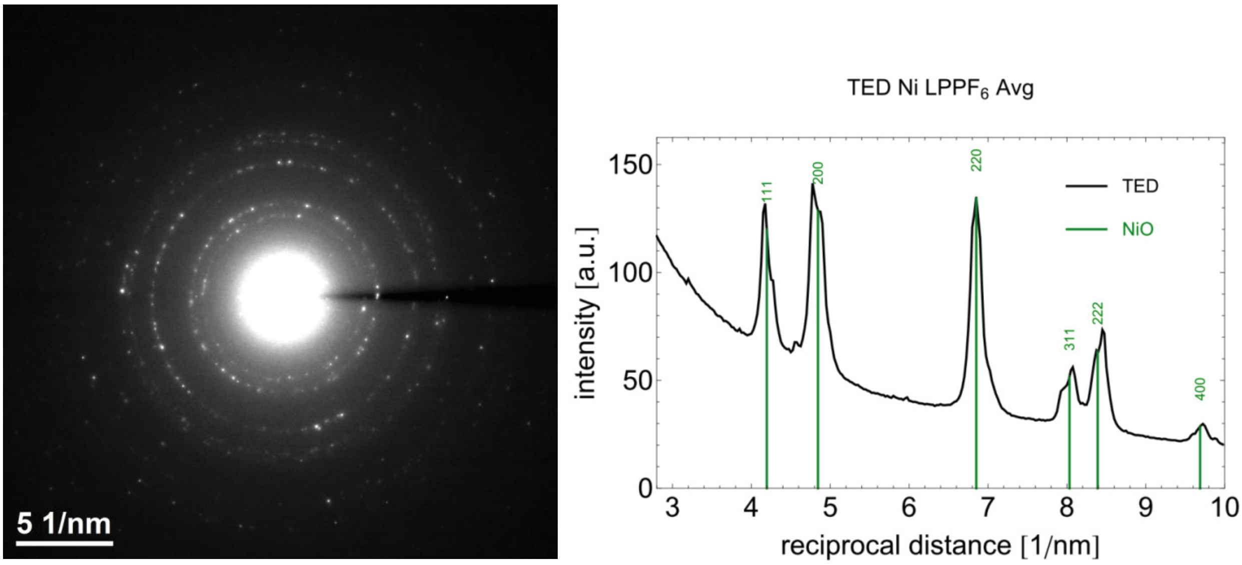

Fig. S2.30 Selected-area powder transmission electron diffraction showing a Debye-Scherrer pattern of NiO crystals (left) and azimuthal average of the SAED pattern in comparison to the reflexions of NiO (right).

Ni-NPs from [Ni{MeC(N^iPr)$_2$}$_2$] in [OTh][PF_6]

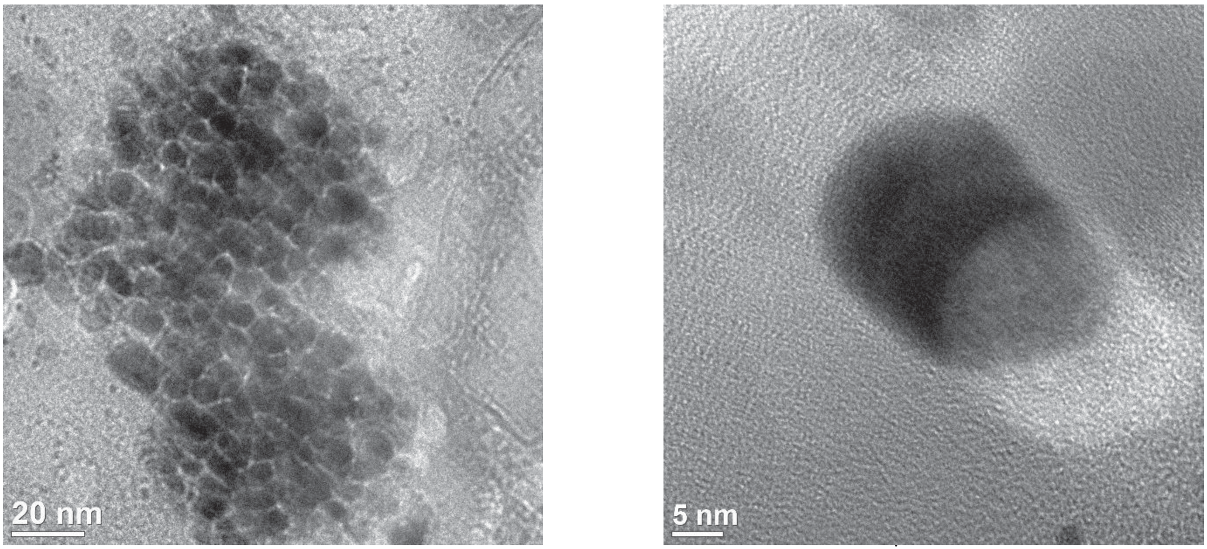

Fig. S2.31 TEM of Ni-NPs in [OTh][PF_6] (1 wt.%) from [Ni{MeC(N^iPr)$_2$}$_2$].

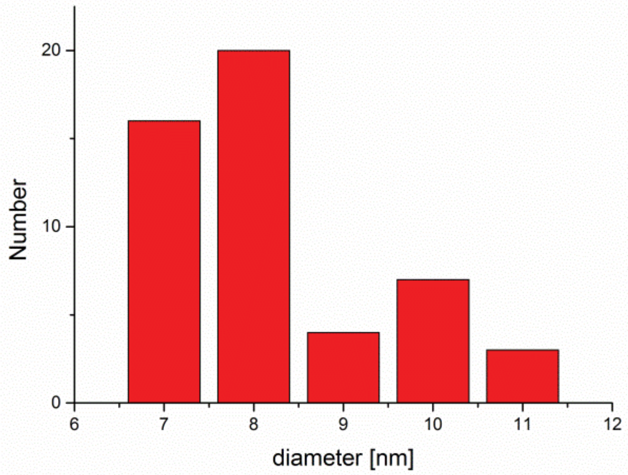

Fig. S2.32 Histogram of 50 Ni-NPs from [Ni{MeC(N^iPr)$_2$}$_2$] in [OTh][PF_6].

Ni-NPs from $[Ni(COD)_2]$ as precursor

Ni-NPs from $[Ni(COD)_2]$ in $[BMIm][BF_4]$

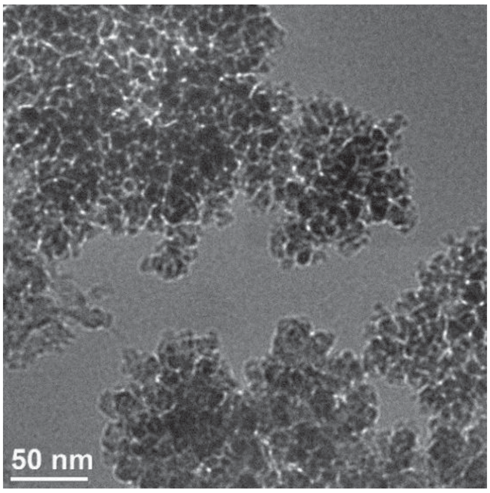

Fig. S3.1 TEM of Ni/$[BMIm][BF_4]$. (1 wt.%)

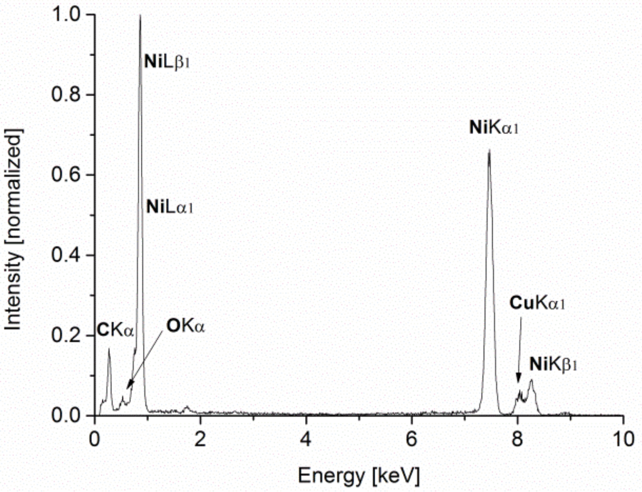

Fig. S3.2 EDX of Ni-NPs from $[Ni(COD)_2]$ in $[BMIm][BF_4]$.

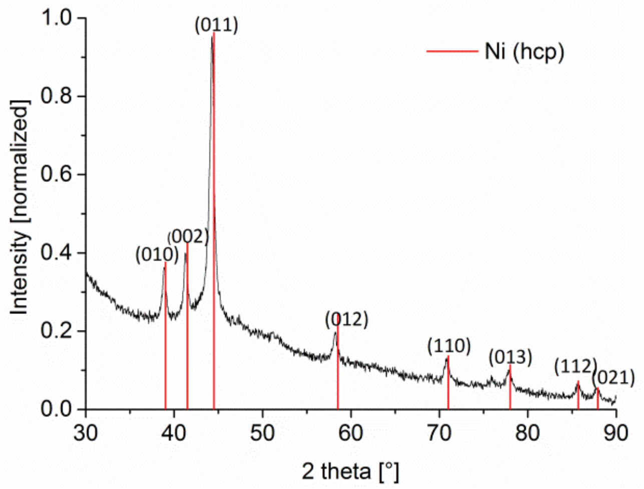

Fig. S3.3 PXRD of 1.0 wt% Ni/$[BMIm][BF_4]$. (Ni-hcp reference peaks in red, COD 9013007).

Ni-NPs from $[Ni(COD)_2]$ im $[BMIm][PF_6]$

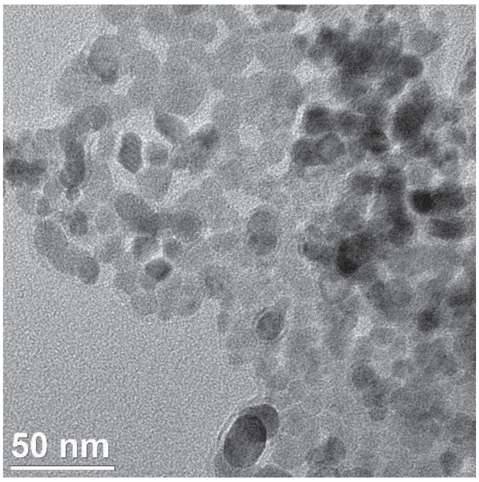

Fig. S3.4 TEM of Ni/$[BMIm][PF_6]$ (1 wt.%).

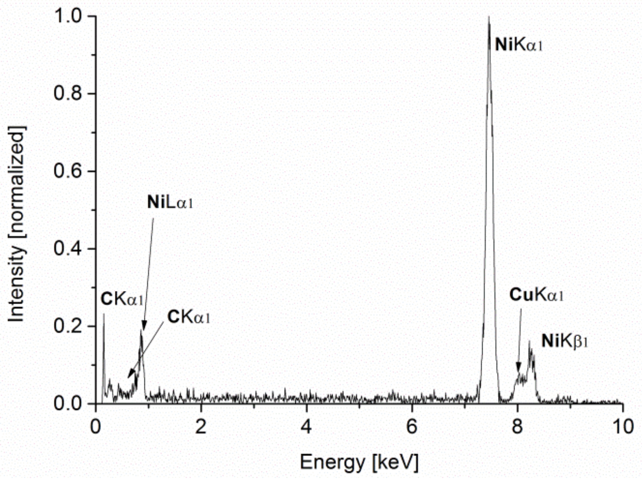

Fig. S3.5 EDX of Ni-NPs from $[Ni(COD)_2]$ in $[BMIm][PF_6]$.

Ni-NPs from [Ni(COD)$_2$] in [BMIm][NTf$_2$]

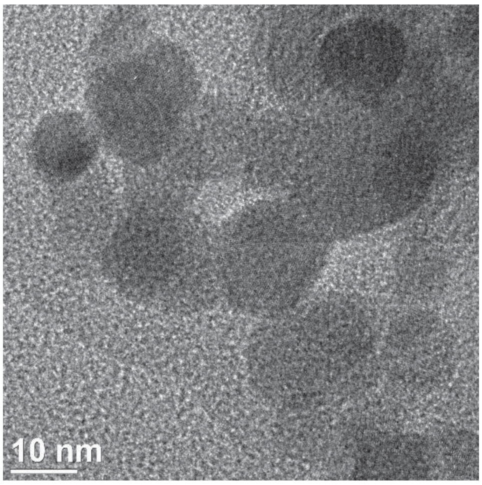

Fig. S3.6 TEM of Ni/[BMIm][NTf$_2$] (1 wt.%).

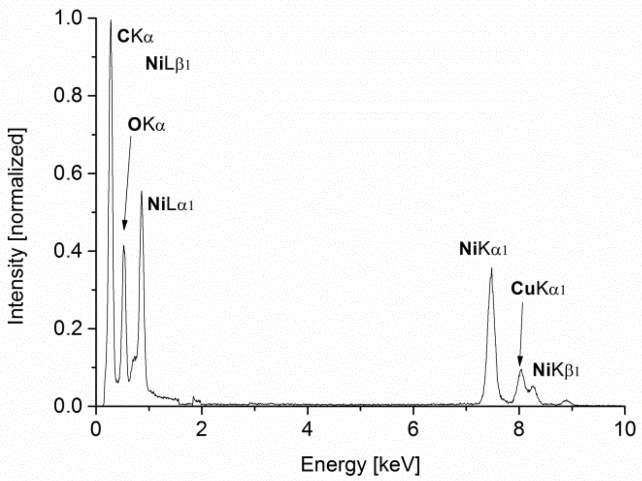

Fig. S3.7 EDX of Ni-NPs from [Ni(COD)$_2$] in [BMIm][NTf$_2$].

Ni-NPs from [Ni(COD)$_2$] in [OMIm][PF$_6$]

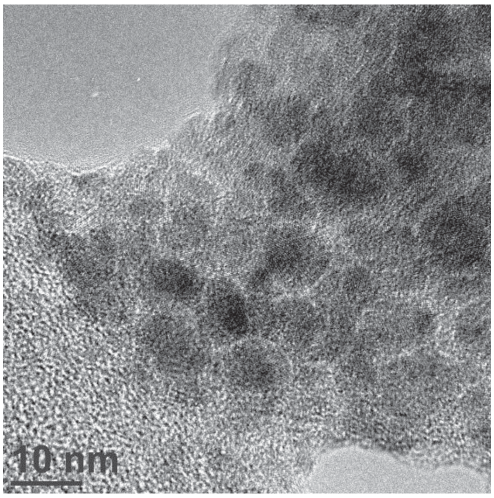

Fig. S3.8 TEM of Ni/[OMIm][PF$_6$] (1 wt.%).

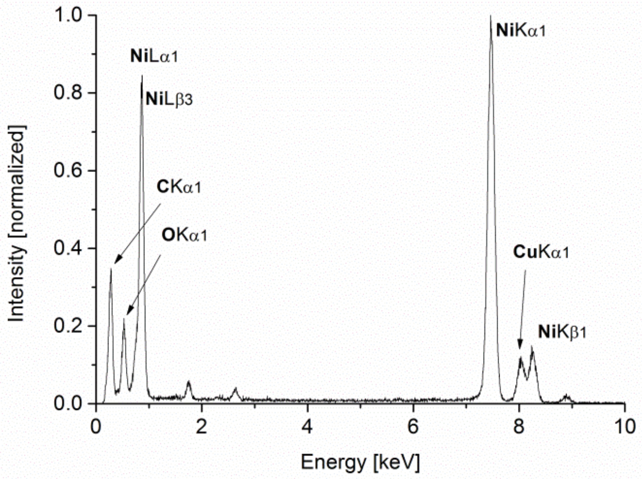

Fig. S3.9 EDX of Ni-NPs from [Ni(COD)$_2$] in [OMIm][PF$_6$].

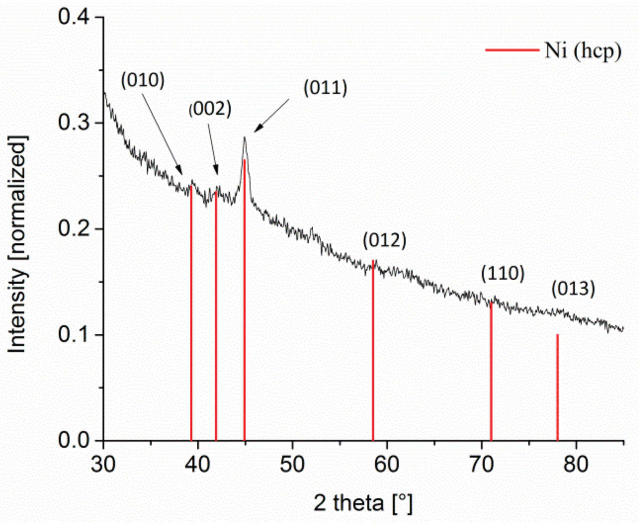

Figure S3.10 PXRD of 1.0 wt% Ni-NPs in [OMIm][PF$_6$]. (Ni-hcp reference peaks in red, COD 9013007).

Ni-NPs from [Ni(COD)$_2$] in [LMIm][PF$_6$]

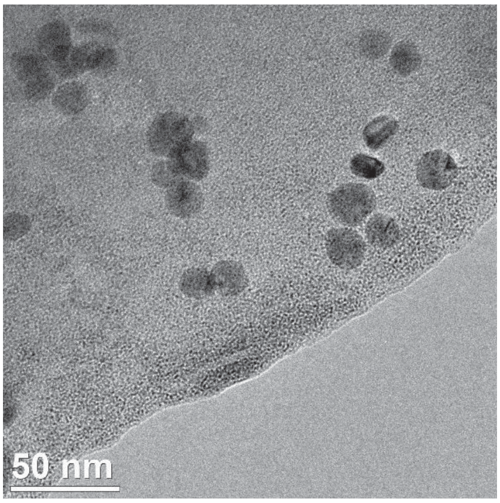

Fig. S3.11 TEM of Ni/[LMIm][PF$_6$] (1 wt.%).

Ni-NPs from [Ni(COD)$_2$] in [BuPy][NTf$_2$]

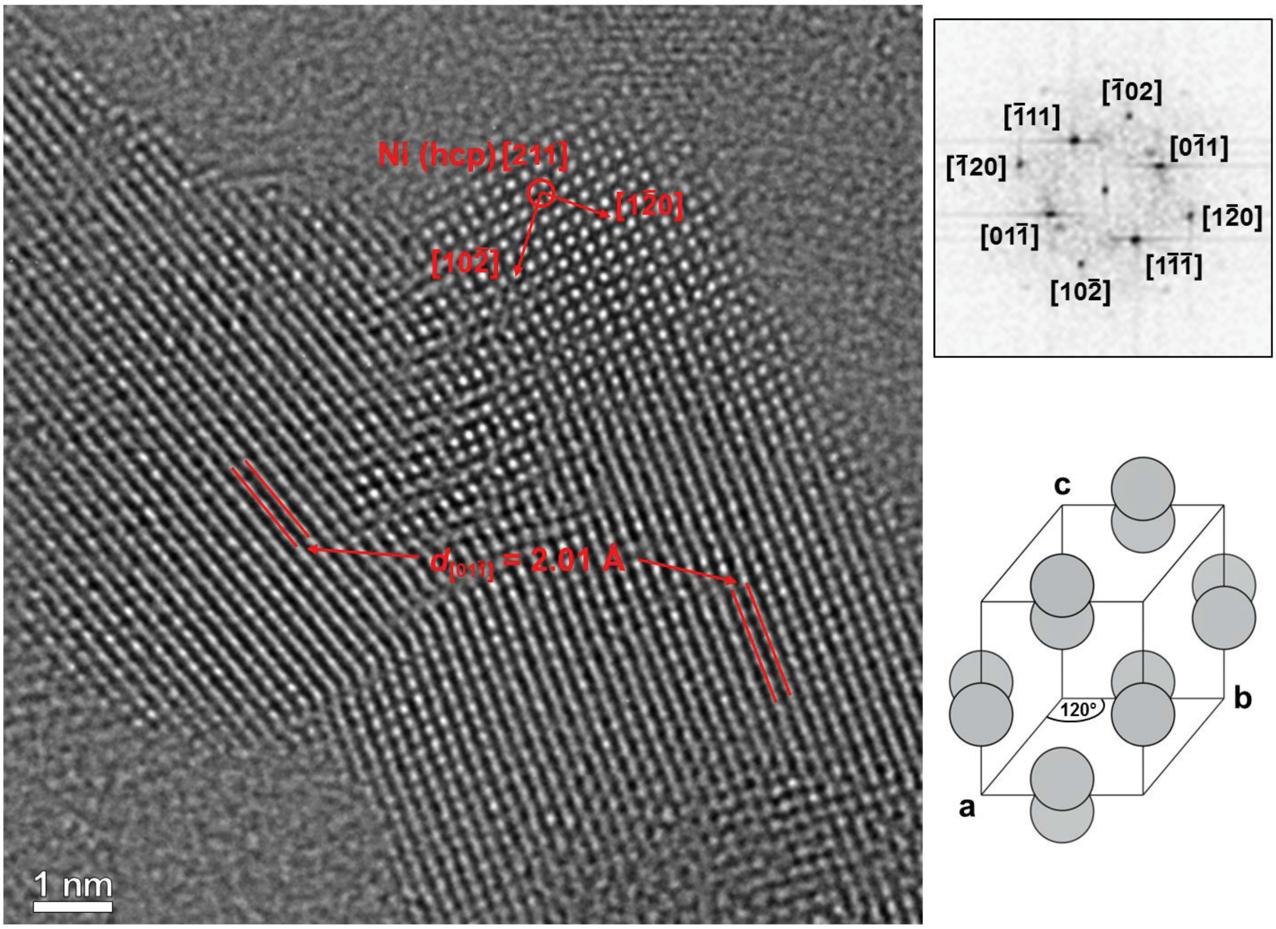

Fig. S3.12 (Left) HR-TEM image of Ni/[BuPy][NTf$_2$] with 1.0 wt% Ni-NPs in IL from Ni(COD)$_2$ showing several attached nanoparticles with lattice fringes. (Top right) Diffractogram of the well oriented particle from the left image showing Bragg reflexions of the [211] orientation of Ni (hcp). (Bottom right) Structure model of Ni (hcp) (COD 9008509) projected along [211] with the unit cell axes and the angle γ = 120° indicated.

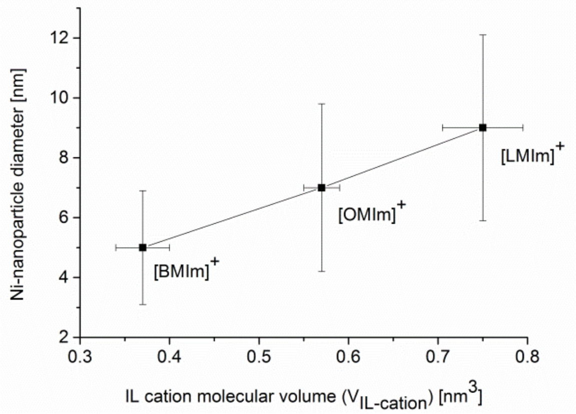

Fig. S4.1 Size of Ni nanoparticles from Ni-amidinate in different imidazolium based ILs depending on the cation size $[BMIm]^+$, $[OMIm]^+$, $[LMIm]^+$ with the same anion $[PF_6]^-$.

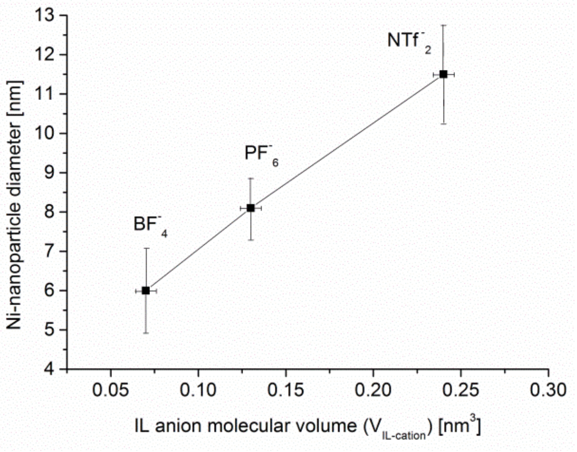

Fig. S4.2 Size of Ni nanoparticles from $Ni(COD)_2$ in different imidazolium based ILs depending on the anion size $[BF_4]^-$, $[PF_6]^-$, $[NTf_2]^-$.

Table S1 Phase and average diameter of Ni-NPs from $[Ni\{MeC(N^iPr)_2\}_2]$ (1 wt.%) in different ILs

IL	phase of Ni-NPs from PXRD	Ø – Ni-NPs [nm] from HR-TEM	Ø – Ni-NPs [nm from PXRD*
$[LMIm][BF_4]$	Ni, hcp, NiO	7 ± 2	30
$[LMIm][NTf_2]$	Ni, hcp	10 ± 4	14
$[OMIm][NTf_2]$	Ni, hcp	10 ± 3	---
$[LPy][PF_6]$	NiO	3 ± 1	28

* PXRD, from Scherrer equation (Scherrer factor = 1)

NMR analysis of selected ILs before and after microwave heating:

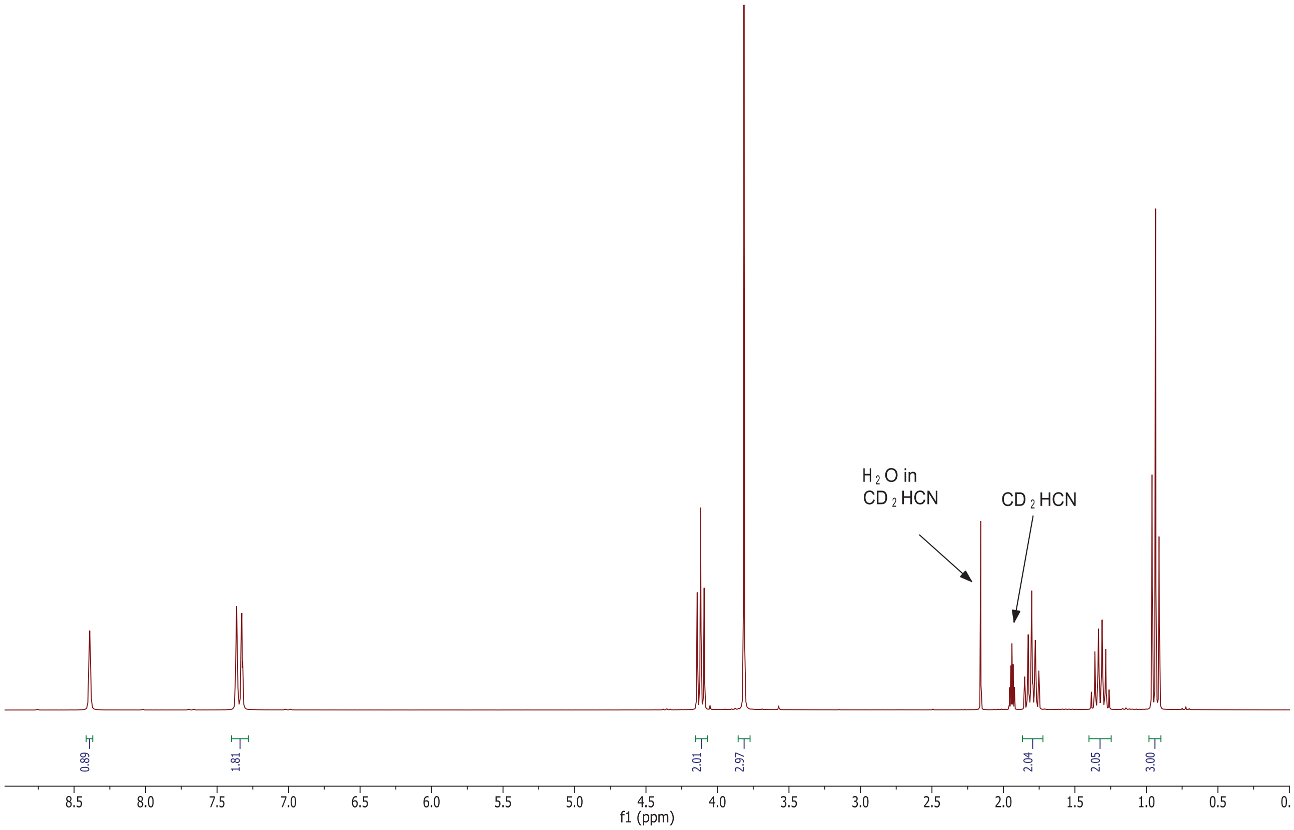

Fig. S5.1 ^{1}H-NMR analysis (CD$_3$CN, 300.13 MHz, 298 K) of [BMIm][NTf$_2$] before 10 min MW heating at a power of 100 W to an approximate temperature of 220 °C.

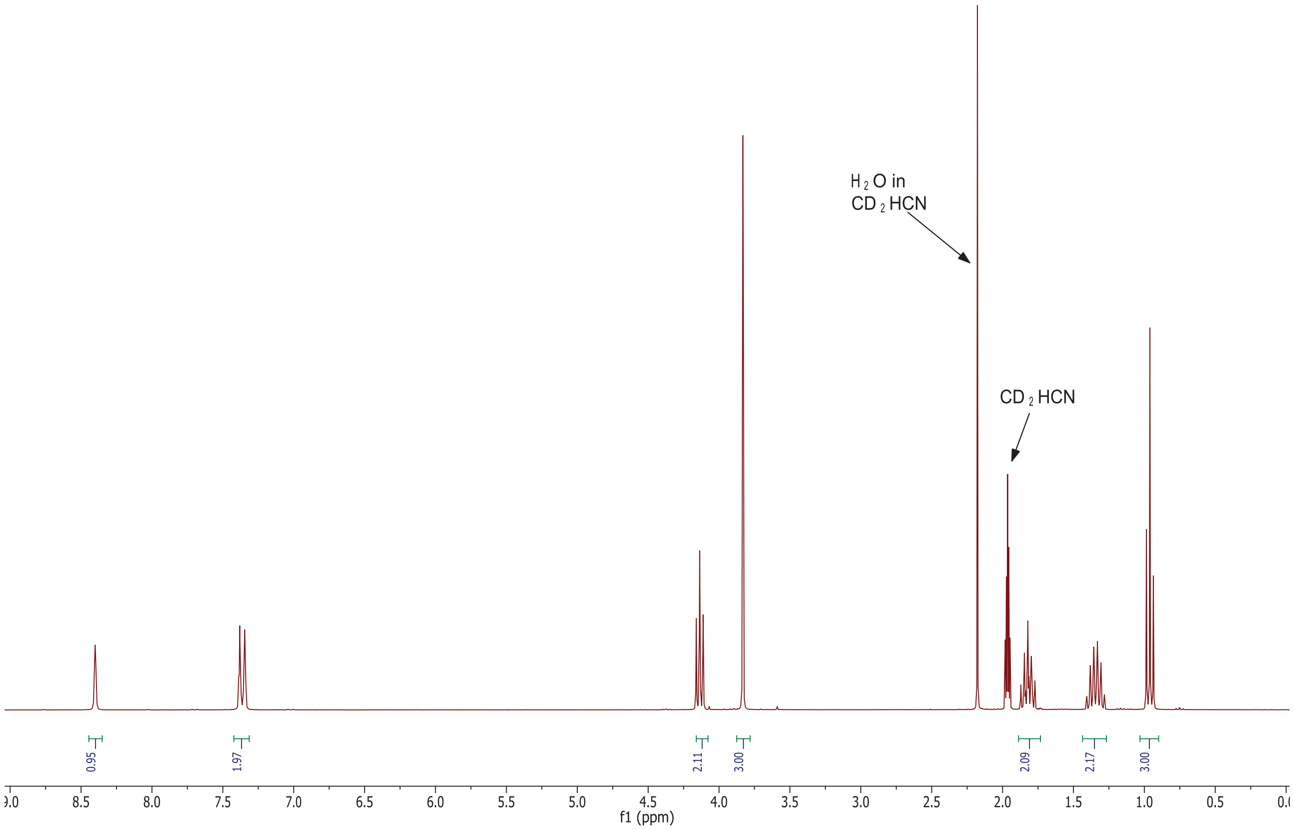

Fig. S5.2 ^{1}H-NMR analysis (CD$_3$CN, 300.13 MHz, 298 K) of [BMIm][NTf$_2$] after 10 min MW heating at a power of 100 W to an approximate temperature of 220 °C.

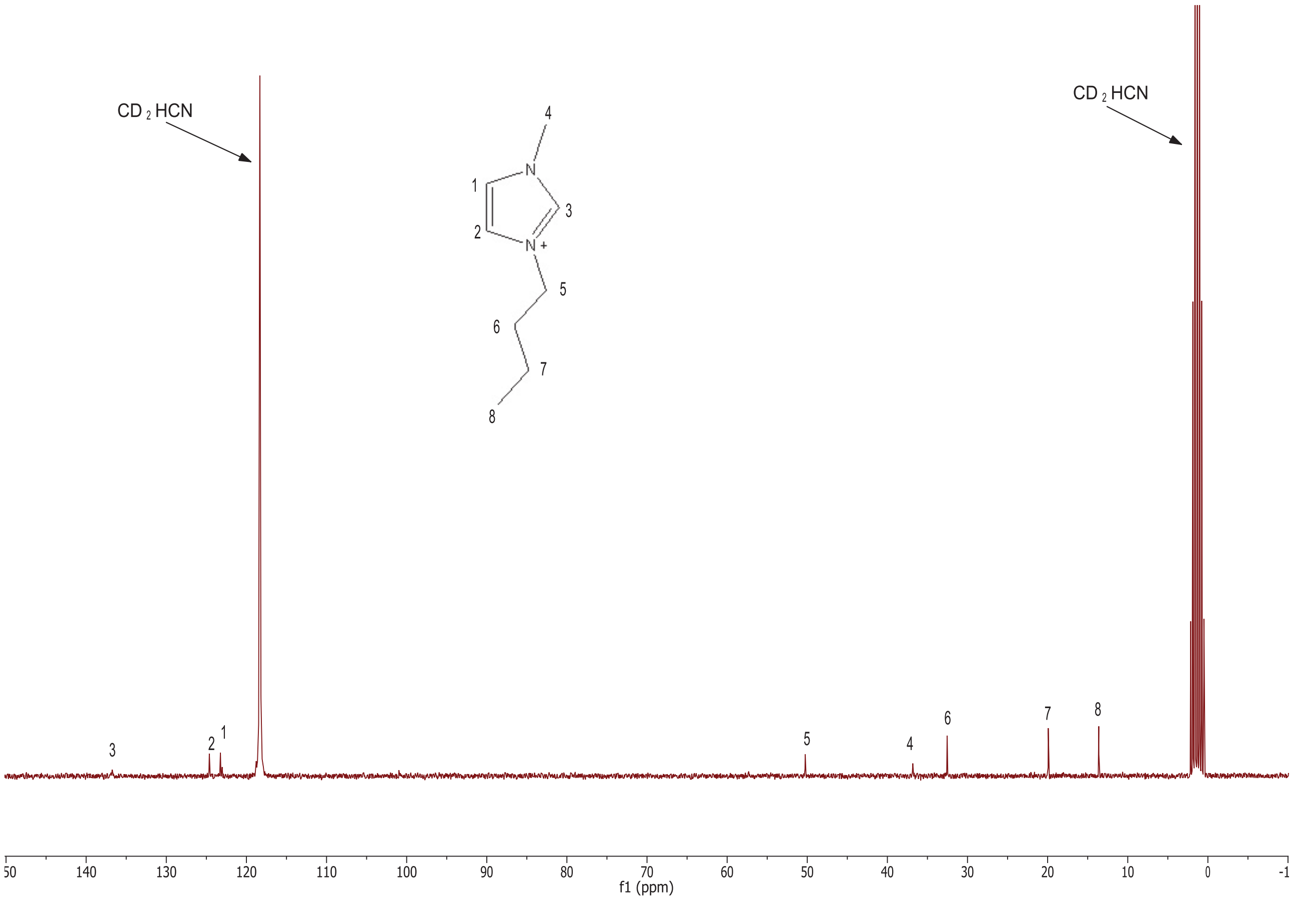

Fig. S5.3 ^{13}C-NMR analysis (CD_3CN, 75 MHz, 298 K) of [BMIm][NTf_2] after 10 min MW heating at a power of 100 W to an approximate temperature of 220 °C.

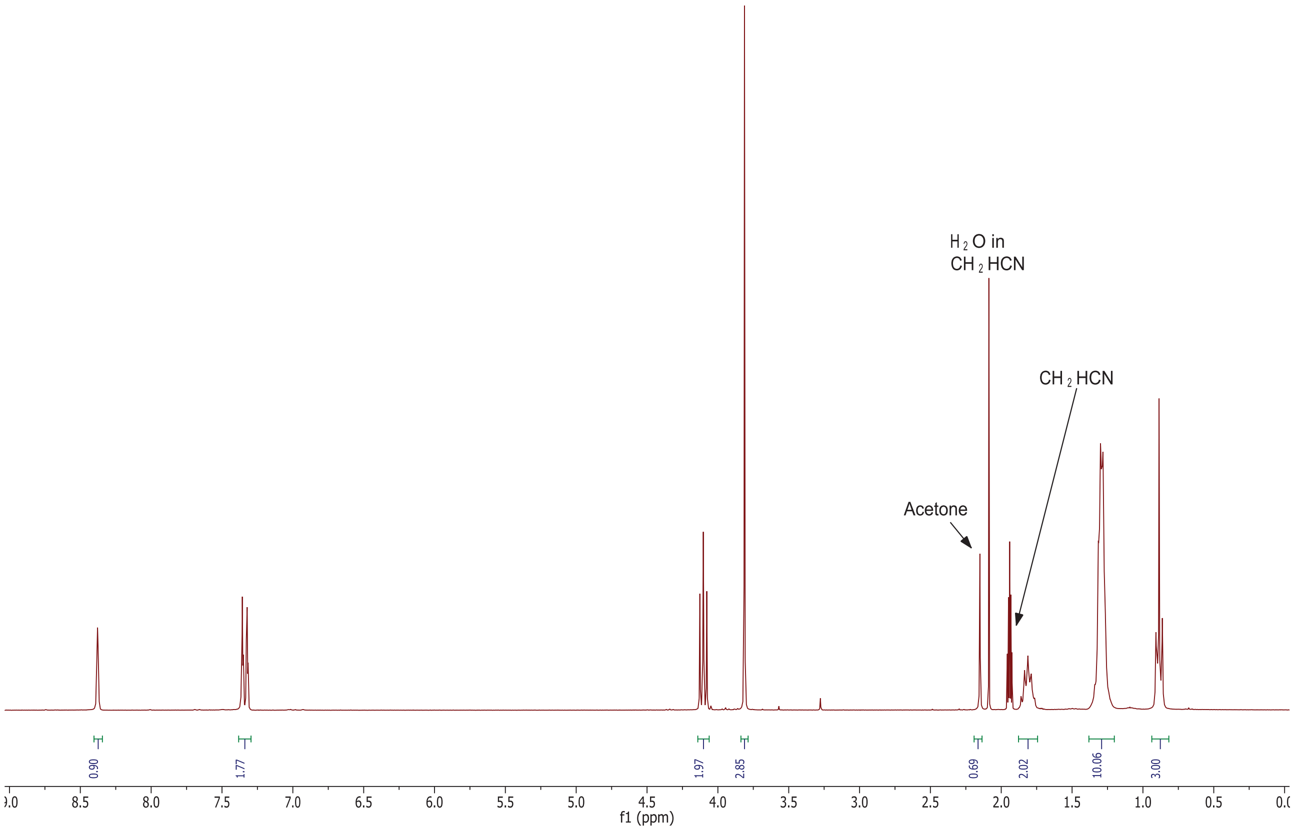

Fig. S5.4 ^{1}H-NMR analysis (CD_3CN, 300.13 MHz, 298 K) of [OMIm][NTf_2] before 10 min MW heating at a power of 100 W to an approximate temperature of 220 °C. The acetone signal is due to residual cleaning solvent from incomplete drying of the NMR tubes.

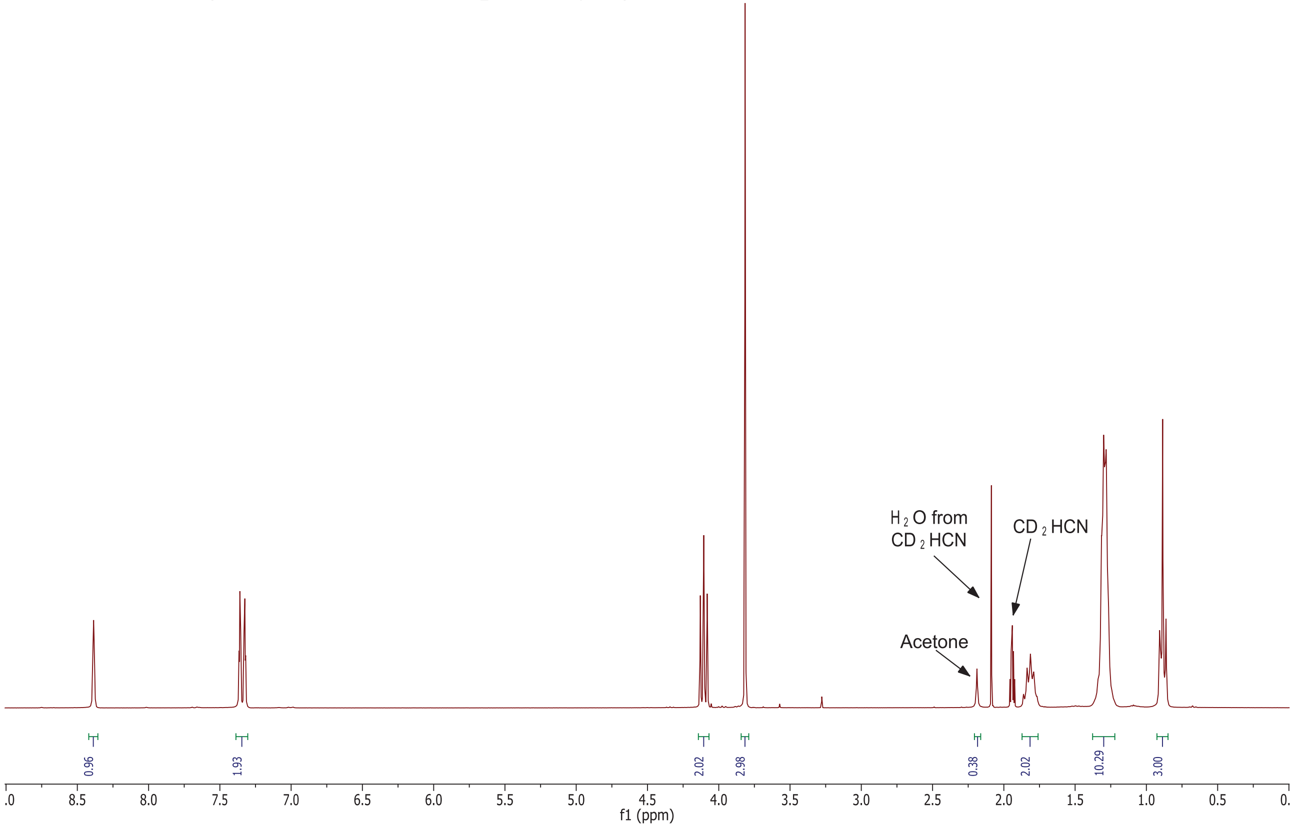

Fig. S5.5 ^{1}H-NMR analysis (CD_3CN, 300.13 MHz, 298 K) of [OMIm][NTf_2] after 10 min MW heating at a power of 100 W to an approximate temperature of 220 °C. The acetone signal is due to residual cleaning solvent from incomplete drying of the NMR tubes.

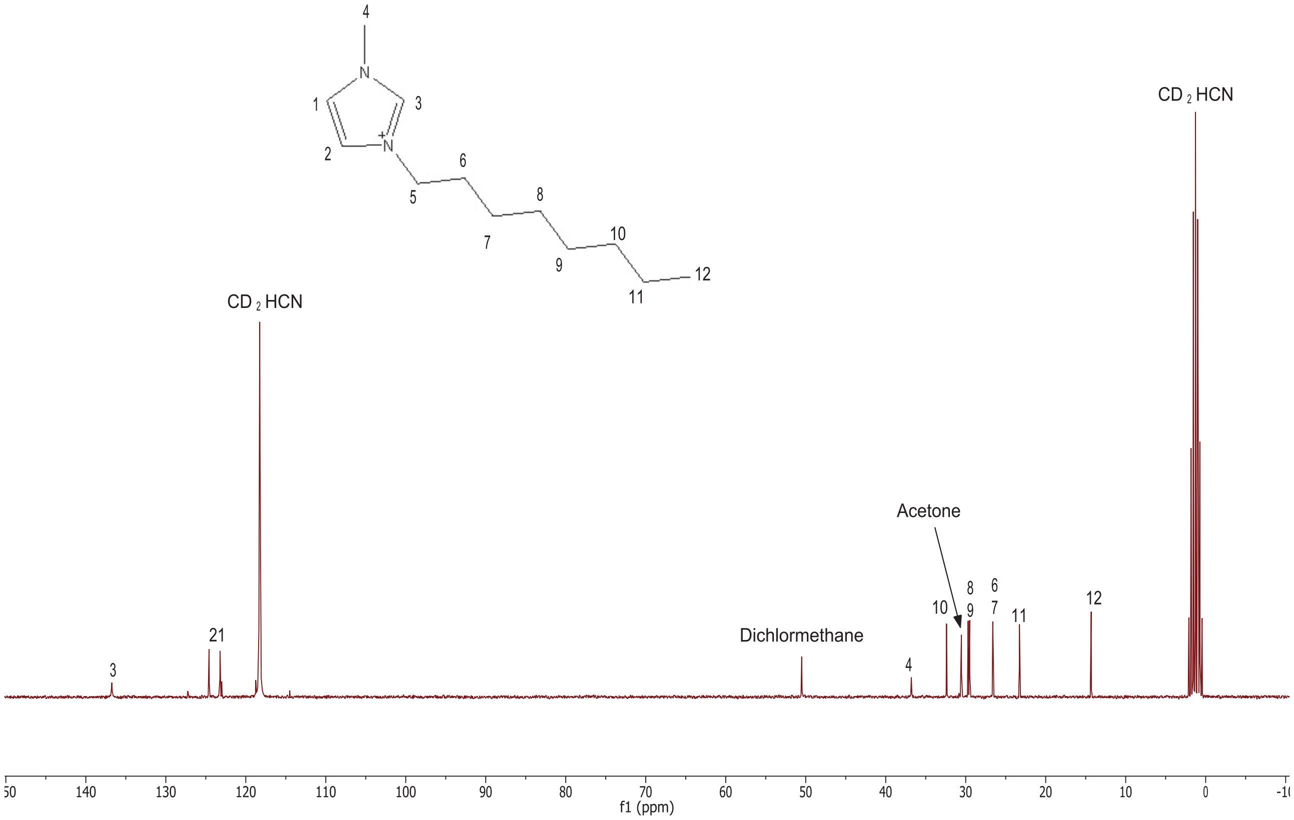

Fig. S5.6 ^{13}C-NMR analysis (CD$_3$CN, 75 MHz, 298 K) of [OMIm][NTf$_2$] after 10 min MW heating at a power of 100 W to an approx. temperature of 220 °C. The acetone signal is due to residual cleaning solvent from incomplete drying of the NMR tubes. Dichloromethane is a residue from extraction of the aqueous phase after anion exchange to recover most of the IL from this aqueous phase.

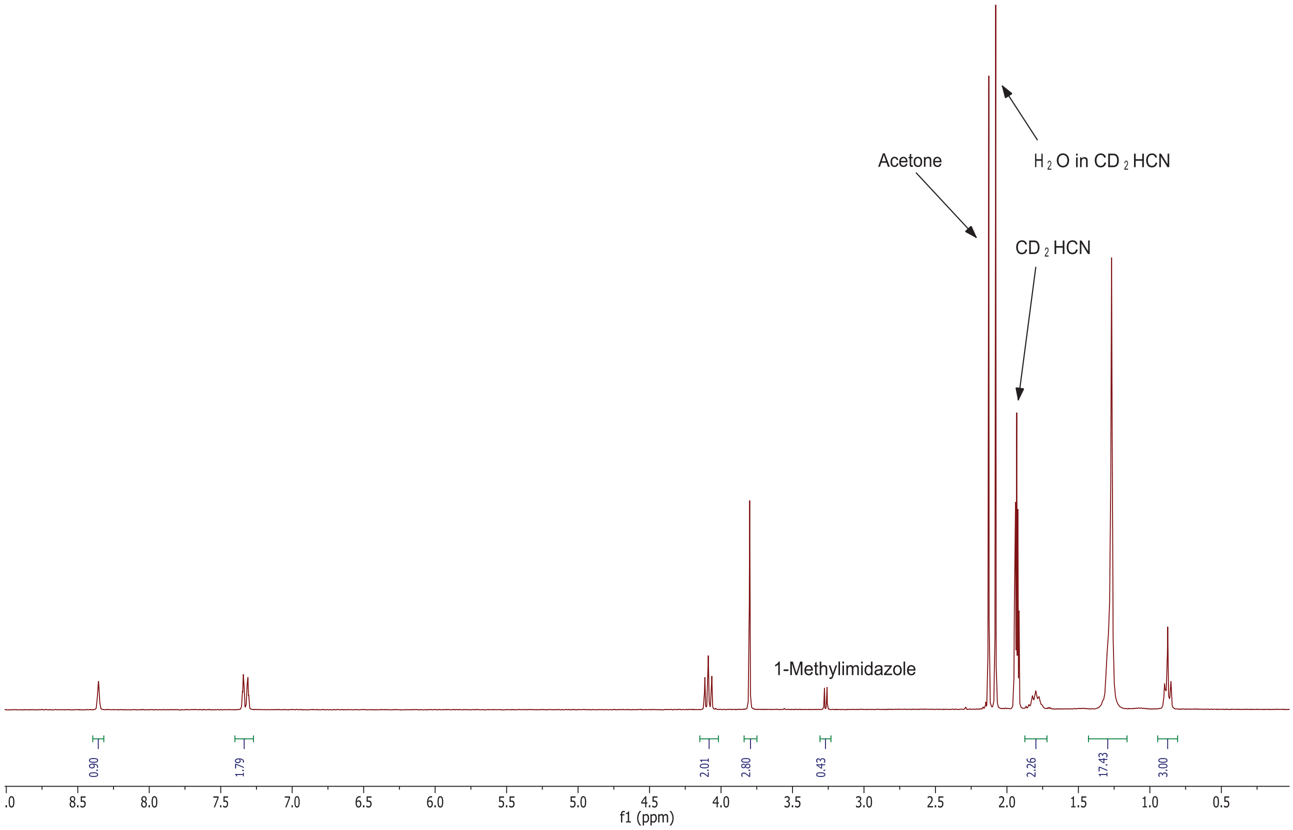

Fig. S5.7 ^{1}H-NMR analysis (CD_3CN, 300.13 MHz, 298 K) of [LMIm][PF_6] before 10 min MW heating at a power of 100 W to an approximate temperature of 220 °C. The acetone signal is due to residual cleaning solvent from incomplete drying of the NMR tubes. 1-Methylimidazole is residual starting material.

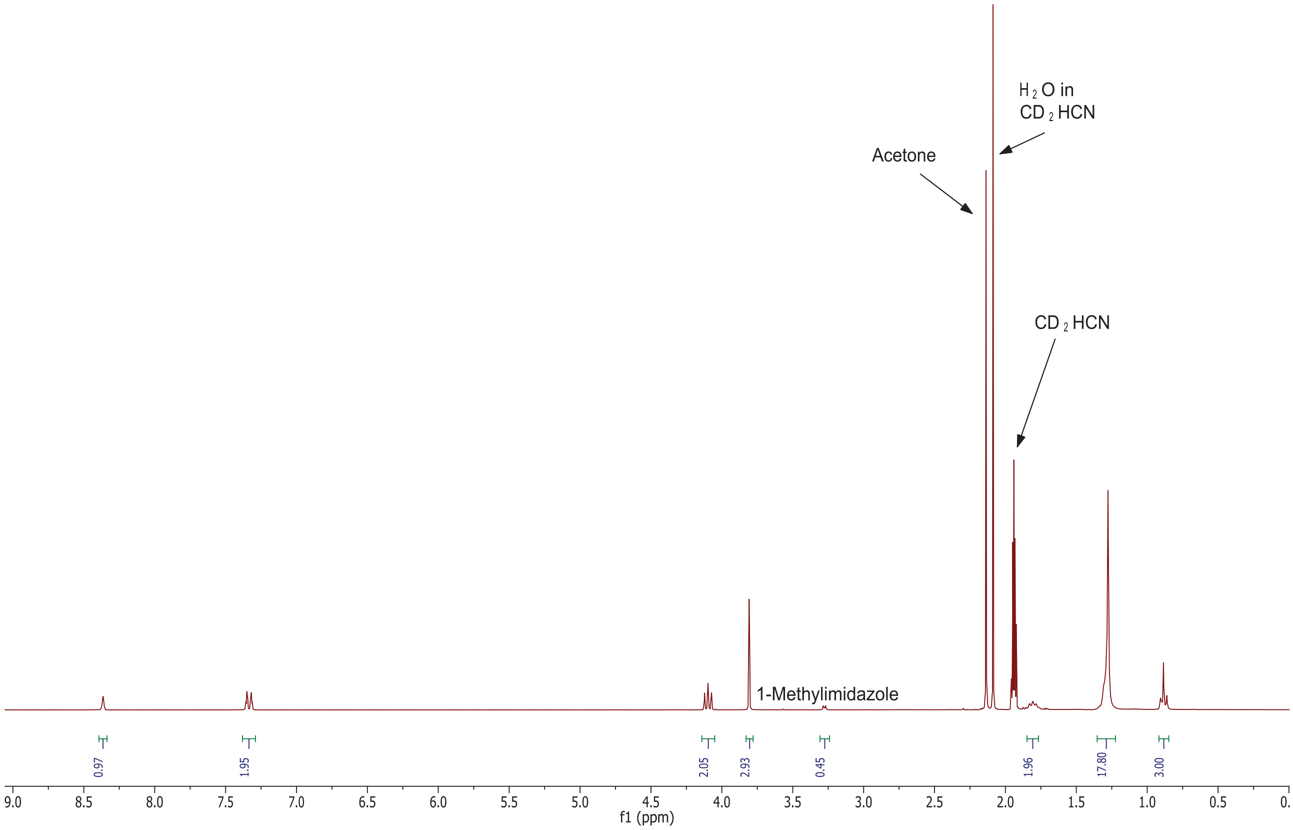

Fig. S5.8 ^{1}H-NMR analysis (CD_3CN, 300.13 MHz, 298 K) of [LMIm][PF_6] after 10 min MW heating at a power of 100 W to an approximate temperature of 220 °C. The acetone signal is due to residual cleaning solvent from incomplete drying of the NMR tubes.

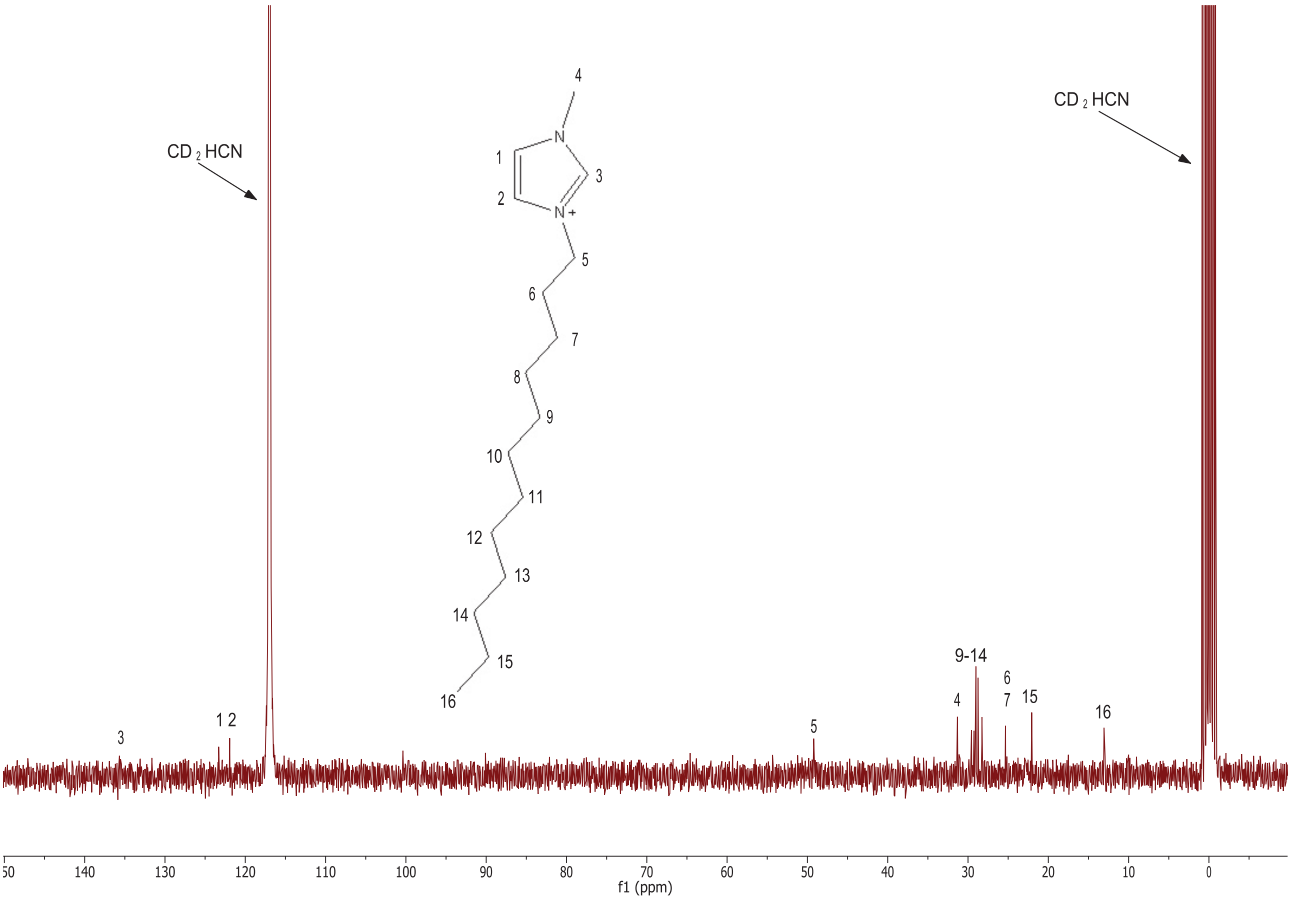

Fig. S5.9 ^{13}C-NMR analysis (CD_3CN, 75 MHz, 298 K) of [LMIm][PF_6] after 10 min MW heating at a power of 100 W to an approximate temperature of 220 °C.

3.2 Soft wet-chemical synthesis of Ru-Sn nanoparticles from single-source ruthenocene-stannole precursors in an ionic liquid

Susann Wegner, Masaichi Saito, Juri Barthel, Christoph Janiak

J. Organomet. Chem. **2016**, *821*, 192-196

DOI: 10.1016/j.jorganchem.2016.05.010, Quelle [4]

Die mikrowelleninduzierte Zersetzung der Single-Source Vorläuferverbindungen eines neutralen Triple-Decker Ruthenocens (1) und eines anionischen Ruthenocens (2), beide einen Stannolliganden enthaltend in der ionischen Flüssigkeit 1-Butyl-3-Methylimidazolium-tetraflouroborat ([BMIm][BF_4]), ergibt bimetallische Ruthenium-Zinn Nanopartikel. Partikel der ungefähren Zusammensetzung Ru_2Sn (aus 1) und Ru_3Sn_7 (aus 2) wurden in dieser milden, nasschemischen Synthese erhalten. Transmissionselektronenmikroskopie (TEM) zeigte die Bildung 2 – 6 nm großer Partikel von Ru_2Sn mit einer mittleren Elementarzusammensetzung, bestimmt mittels energiedispersiver Röntgenspektroskopie (EDX). Kristalline Ru_3Sn_7 Nanopartikel zusammen mit α-Sn Nanopartikeln mit einer Größe von 10 – 50 nm (aus TEM) wurden mittels Röntgenpulverdiffraktogramm und der Elementzusammensetzung aus EDX als Ru_3Sn_7 und α-Sn-Phase aufgeklärt.

Anteil an der Veröffentlichung:

- Synthese der bimetallischen Nanopartikel in der IL [BMIm][BF_4] und vollständige Charakterisierung dieser über PXRD, TEM, SAED und EDX.
- Konzipierung und Schreiben des Manuskripts sowie die Bearbeitung des Manuskripts nach Revision
- Die Precursoren wurden von Herrn Prof. Dr. Masaichi Saito synthetisiert, charakterisiert und bereitgestellt.
- Unterstützung bei TEM- und SAED-Aufnahmen erfolgte über Herrn Dr. Juri Barthel.
- Die Korrekturen des Manuskripts wurden von Herrn Prof. Dr. Christoph Janiak vorgenommen, ebenso erfolgte auch die Koordination zwischen den Co-Autoren über ihn.

Journal of Organometallic Chemistry 821 (2016) 192–196

Contents lists available at ScienceDirect

Journal of Organometallic Chemistry

journal homepage: www.elsevier.com/locate/jorganchem

Communication

Soft wet-chemical synthesis of Ru-Sn nanoparticles from single-source ruthenocene-stannole precursors in an ionic liquid

Susann Wegner [a], Masaichi Saito [b], Juri Barthel [c], Christoph Janiak [a], *

[a] Institut für Anorganische Chemie und Strukturchemie, Heinrich-Heine-Universität Düsseldorf, Universitätsstr. 1, D-40225 Düsseldorf, Germany
[b] Department of Chemistry, Graduate School of Science and Engineering, Saitama University, Shimo-okubo, Sakura-ku, Saitama 338-8570, Japan
[c] Gemeinschaftslabor für Elektronenmikroskopie RWTH-Aachen, Ernst Ruska-Centrum für Mikroskopie und Spektroskopie mit Elektronen, D-52425 Jülich, Germany

ARTICLE INFO

Article history:
Received 15 February 2016
Received in revised form
12 April 2016
Accepted 9 May 2016
Available online 27 May 2016

Dedicated to Prof. Heinrich Lang on the occasion of his 60th birthday.

Keywords:
Nanoparticles
Ruthenium-tin alloy
Soft wet-chemical synthesis
Ionic liquid
Single-source precursor

ABSTRACT

Microwave-induced decomposition of the single-source precursors of a neutral triple-decker ruthenocene (**1**) and an anionic ruthenocene (**2**) both bearing a stannole ligand in the ionic liquid 1-butyl-3-methylimidazolium tetrafluoroborate ([BMIm][BF_4]) gives bimetallic ruthenium-tin nanoparticles. Particles of approximate composition Ru_2Sn (from **1**) and Ru_3Sn_7 (from **2**) were obtained in this soft, wet-chemical synthesis. Transmission electron microscopy (TEM) showed the formation of 2–6 nm particles of Ru_2Sn with its average elemental composition determined from energy dispersive X-ray spectroscopy (EDX). Crystalline Ru_3Sn_7 nanoparticles together with α-Sn nanoparticles of 10–50 nm (from TEM) were elucidated by positive matching of the powder-X-ray diffractogram to the Ru_3Sn_7 and α-Sn phase and the element composition from EDX.

1. Introduction

Intermetallic Ru/Sn alloys are used as bimetallic catalysts, e.g., for the selective hydrogenation of levulinic acid to γ-valerolactone [1,2], lactic acid to 1,2-propanediol [3], or methyl oleate to oleyl alcohol [4]. Such Ru/Sn alloys are, so far synthesized in a dual-source approach by combining the metal chlorides $RuCl_3$, $SnCl_4$, $SnCl_2$ or the nitrates $Ru(NO)(NO_3)_3$, $Ru(NO_3)_3$ and $Sn(OAc)_2$ followed by hydrogen reduction at elevated temperatures up to 723 K [1,3,4].

Particularly bimetallic *nano*alloys are interesting for use in colloidal and heterogeneous catalysis [5–7]. Bottom-up synthesis of nanoalloys by soft, wet-chemical methods [8,9] in organic solvents from organometallic complexes is a mild and controlled access to metals and alloys in the nanometer scale regime [10–12]. Polynuclear ruthenium carbonyl-triphenylstannane cluster complexes can be converted to heterometallic nanoparticles which are active nanoscale catalysts for the hydrogenation of unsaturated organic molecules, such as 1,5,9-cyclododecatriene. The mixing of tin with platinum-group metal catalysts can reduce the amount of precious metal and at the same time give substantial improvements in product selectivities without major losses in activity [10].

Ionic liquids (ILs) have become alternatives to traditional aqueous or organic solvents [11,12] for the preparation of materials through ionothermal synthesis [13–15]. ILs are now established for the inherent stabilization of metal nanoparticles [16] which were prepared from metal salts [17–20] organometallic metal complexes [21,22] and metal carbonyls [23]. Microwave irradiation (MWI) induces thermal decomposition of organometallic compounds in ILs as a fast and energy-saving access to metal nanoparticles. ILs have a high absorption efficiency for microwaves because of their ionic character, high polarity, and high dielectric constant [24] Different to conductive heating, microwave radiation directly heats the reaction mixture and not primarily the vessel. It is the ILs in the reaction mixture, which absorbs the microwave energy. This leads to localized superheating, very fast and efficient heating rates. Temperatures of 200 °C and above are reached within seconds [25–28]. Metal particles formed by thermal decomposition of molecular precursors can also absorb the MW radiation which

---

* Corresponding author.
E-mail addresses: masaichi@chem.saitama-u.ac.jp (M. Saito), Ju.Barthel@fz-juelich.de (J. Barthel), janiak@uni-duesseldorf.de (C. Janiak).

http://dx.doi.org/10.1016/j.jorganchem.2016.05.010
0022-328X/

leads to effective growth and annealing.

Here we communicate the use of the single-source triple-decker ruthenocene (**1**) and the anionic ruthenocene (**2**) both bearing a stannole ligand [29] as metal-organic precursors for the synthesis of bimetallic ruthenium-tin nanoparticles in the ionic liquid 1-butyl-3-methylimidazolium tetrafluoroborate ([BMIm][BF_4]) (Scheme 1).

2. Experimental part

2.1. Materials and methods

All experimental manipulations were performed under an inert nitrogen or argon atmosphere by using standard Schlenk line and glove-box techniques. The Ru-Sn precursors were synthesized as described in Ref. [29].

The ionic liquid [BMIm][BF_4] was synthesized by treating 1-methylimidazole with 1-chlorobutane to yield first [BMIm][Cl] which was further reacted with HBF_4 to give [BMIm][BF_4]. The IL was dried under high vacuum (10^{-7} mbar) at 80 °C for several days. Quantitative anion exchange and, thus, IL purity of >99% was assessed by ion chromatography (Dionex ICS-1100, with IonPac® AS14, 4 × 250 mm column). Water content was measured by coulometric Karl Fischer titration (ECH/Analytik Jena AQUA 40.00) to below 10 ppm.

Powder X-ray diffractograms (PXRD) were measured on a Bruker D2 Phaser using a flat, low background sample holder and Cu-Kα radiation ($\lambda = 1.54182$ E, 35 kV). Samples had been precipitated with acetonitrile from the NP/IL dispersion and washed with acetonitrile. All samples were prepared for the measurement under inert atmosphere on the sample holder, which was closed in the glovebox.

Transmission electron microscopy (TEM) micrographs were taken on a FEI Tecnai G20 operating at an accelerating voltage of 200 kV. Samples were prepared using 200 μm carbon-coated gold grids. The size distribution was determined from a minimum of 60 nanoparticles. Energy dispersive X-ray (EDX) spectra were obtained on a FEI Tecnai f20, at 136 kV; the exposure time for individual EDX spectra was 3 min.

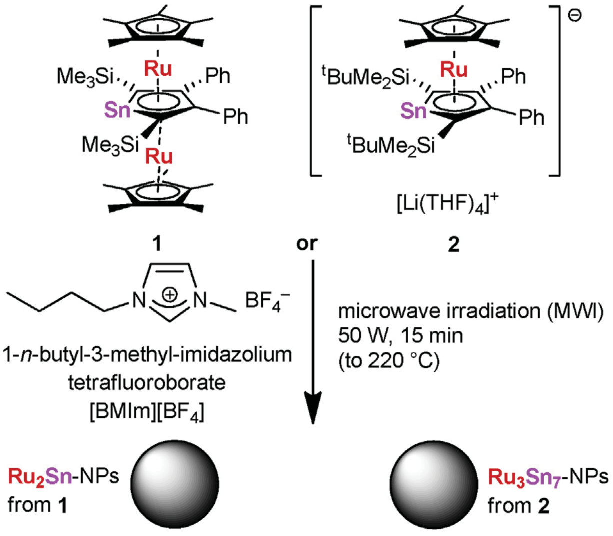

Scheme 1. Microwave-assisted thermal decomposition of single-source ruthenocene-stannole precursors **1** and **2** to bimetallic Ru/Sn-NPs in the IL [BMIm][BF_4].

2.2. Synthesis

Each precursor was dissolved/suspended (24 h) under argon atmosphere in the glovebox at room temperature in dried [BMIm][BF_4] to yield a 0.3 and 0.2 wt% in total metal (Ru + Sn) NP dispersion for **1** and **2**, respectively.

A portion of 1.8 mg (0.0018 mmol) of precursor **1** was combined with 0.15 mL (0.18 g) of [BMIm][BF_4].

A portion of 5.76 mg (0.0052 mmol) of precursor **2** was added to 0.47 mL (0.57 g) of [BMIm][BF_4].

Each mixture was placed in a microwave (CEM, Discover) under an inert nitrogen atmosphere and the precursors were thermally decomposed by microwave irradiation for 15 min at a power of 50 W reaching a temperature reading of 220 °C (see Scheme 1).

3. Results and discussion

From the amounts of precursors (1.8 or 5.76 mg) available only a fraction (33% for **1** and 20% for **2**) corresponds to the Ru + Sn metal content and, hence, only a small mass amount (maximal 0.6 or 1.15 mg, respectively) was formed as metal nanoparticles. Consequently, the analyses, which could be performed with such a small amount, were limited. In this respect, the communication is only a ‘proof-of-principle’ that the ruthenocene-stannole compounds **1** and **2** are suitable precursors to defined bimetallic Ru/Sn-NPs.

The TEM images (Fig. 1a,b) of the nanoparticles from precursor **1** show particles with a diameter from 2 to 6 nm (Ø 4.3 ± 1.5 nm) (see histogram in Fig. 1c). Close-up views during TEM measurements showed interference patterns (lattice planes) in the nanoparticles, which is an indication to crystallinity and is also supported by the reflections in the selected area electron diffraction (SAED) image (Fig. 1d). The energy-dispersive X-ray (EDX) spectrum (Fig. 1e) yielded a molar atom ratio of Ru and Sn as 64%: 36% which matches the composition Ru_2Sn. This is the ratio which was provided by the precursor. The EDX analysis was integrated over a larger sample region. Further studies could check for variations of the individual nanoparticle composition. The EDX spectrum also included a signal of silicon (Si) which was present in the precursor.

The TEM images (Fig. 2a-c) of the nanoparticles from precursor **2** displayed facetted particles with a broader diameter distribution from 10 to 50 nm (Ø 29 ± 12 nm) (see histogram in Fig. 2d). The high-resolution TEM micrographs in Fig. 2b and c display lattice planes giving evidence of crystallinity, which is also supported by the reflections in the SAED pattern of Fig. 2e. The energy-dispersive X-ray (EDX) spectrum (Fig. 2f) yielded a molar atom ratio of Ru to Sn as 17%: 83% or ~1:5, notably different from the 1:1 precursor ratio. Again, the EDX analysis was integrated over a larger sample region. Further studies could check for variations of the individual nanoparticle composition.

The amount of nanoparticle sample from precursor **2** also allowed collecting a powder X-ray diffractogram (PXRD). The PXRD shows reflections which coincide with the reflections of cubic Ru_3Sn_7 (Fig. 3). The PXRD shows also reflections for α-Sn and perhaps traces of hexagonal Ru. All prominent signals are matched by referencing to the Ru_3Sn_7 and α-Sn phase with the reference peaks slightly shifted towards smaller lattice constants. Small shifts in PXRD patterns are not uncommon for nanoparticles. A number of effects can be considered for such shifts including range of stoichiometric composition, partly inhomogeneous element distribution, defects such as stacking and twin faults and nanosized crystalline domains being much smaller than the bulk reference material causing lattice contraction or expansion and strain [30,31]. Known Ru-Sn alloys include the phases Ru_2Sn_3, $RuSn_2$ and Ru_3Sn_7.

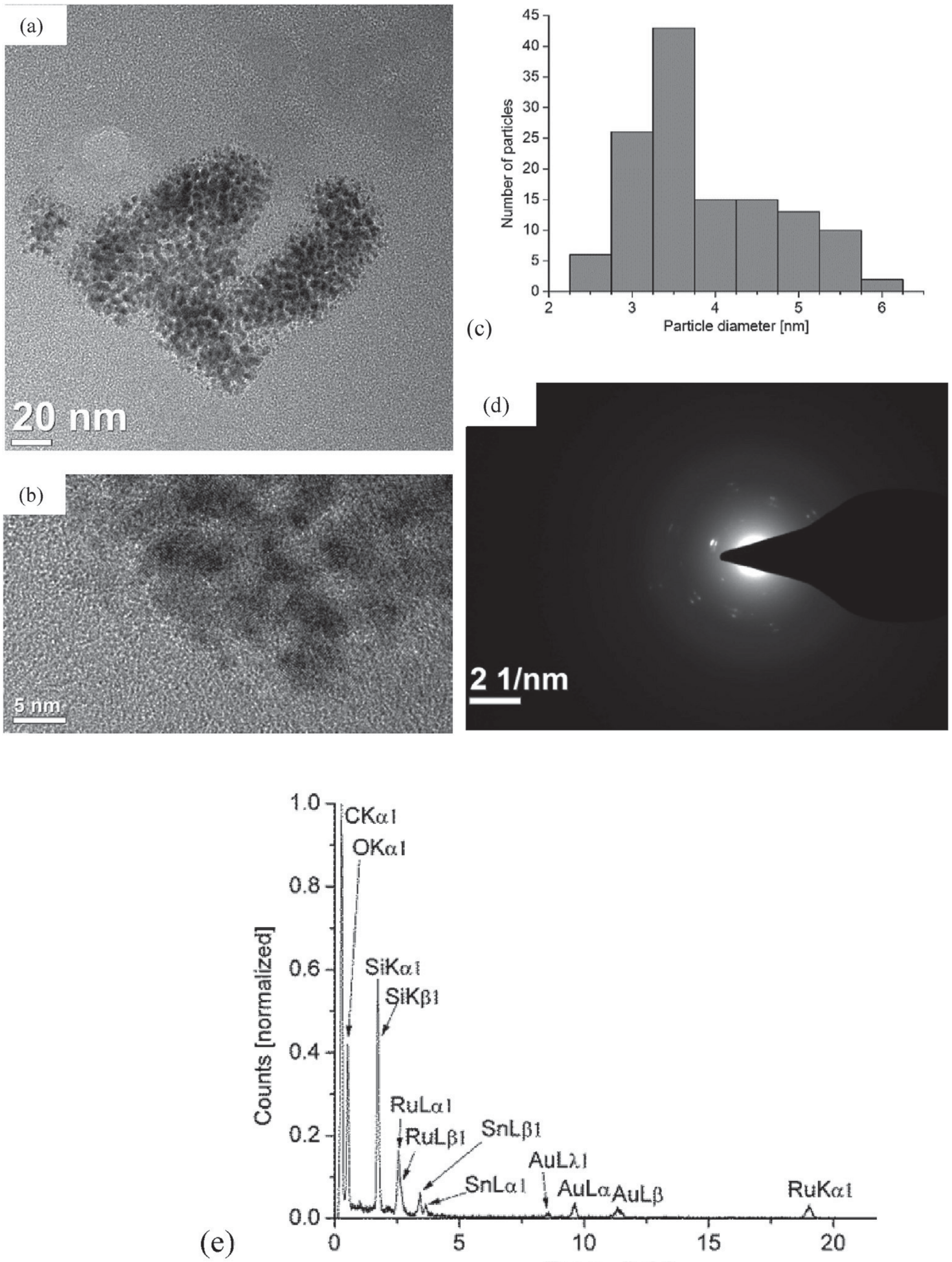

Fig. 1. Analysis of nanoparticles obtained from precursor **1** in the IL [BMIm][BF_4]. (a,b) TEM images; (c) particle diameter histogram based on measuring 130 particles, each bar covers the range of ±0.25 nm around its mid-point; (d) SAED pattern taken from a few particles; (e) EDX spectrum (C and Au signals are due to support film and sample holder, respectively).

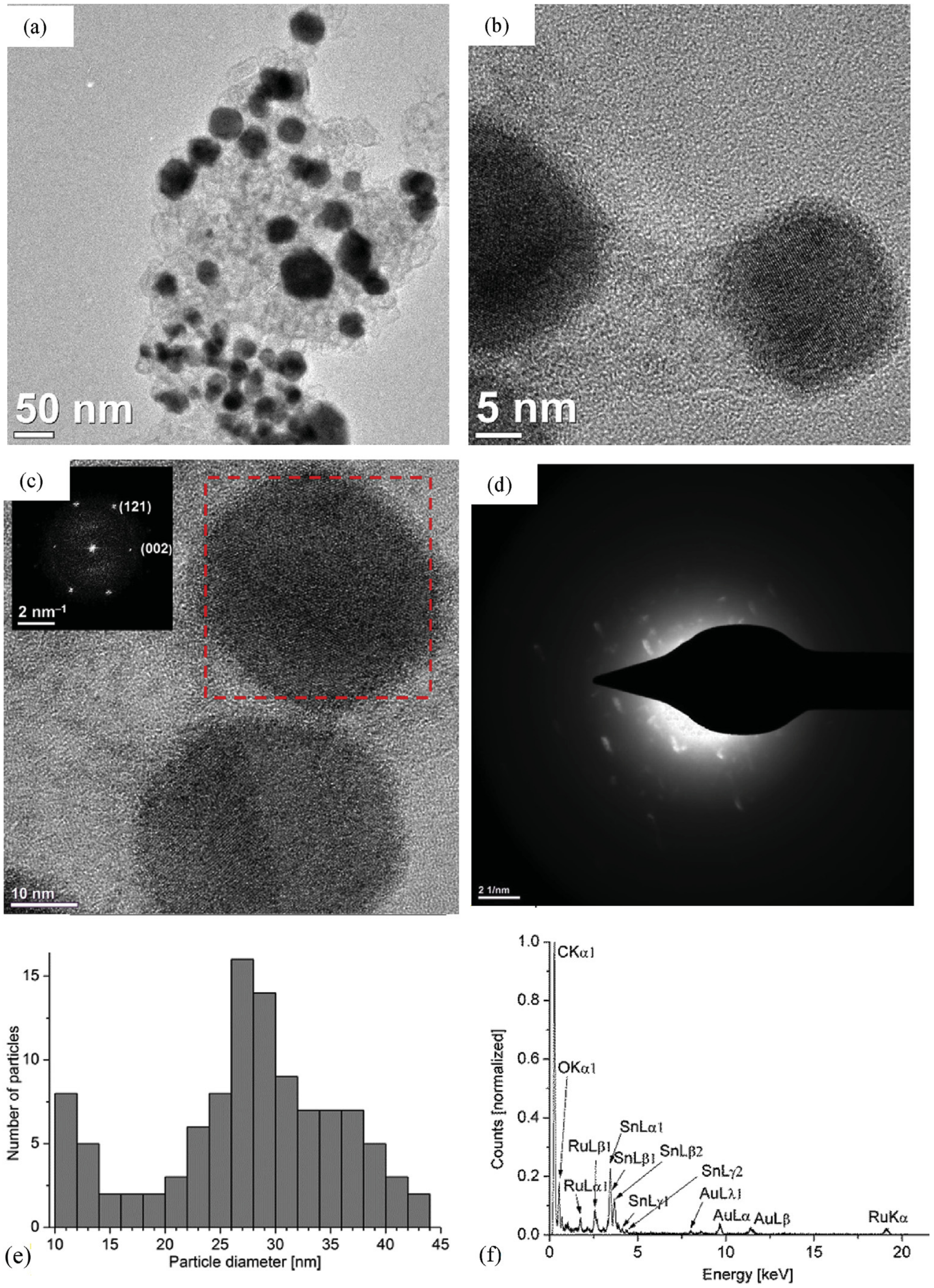

Fig. 2. Analysis of nanoparticles obtained from precursor **2** in the IL [BMIm][BF_4]. (a–c) TEM images; (c) includes a Fourier power spectrum for the red-squared image region corresponding to Ru_3Sn_7 in [$2\bar{1}0$] zone-axis orientation; (d) SAED pattern recorded from a few particles; (e) particle diameter histogram based on measuring 100 particles, each bar covers the range of ±1 nm around its mid-point; (f) EDX spectrum (C and Au signals are due to support film and sample holder material, respectively). (For interpretation of the references to colour in this figure legend, the reader is referred to the web version of this article.)

The latter is found to be the most stable compound in the Ru-Sn system and to be in equilibrium with Sn [32]. We note that small nanoparticles will have a considerable amount of the atoms forming the particles at their surfaces and therefore in large parts the atom packing will also differ from the bulk description of the phase.

4. Conclusions

We have described here in a ‘proof-of-principle’ study a simple way of decomposing organometallic Ru/Sn precursors to obtain Ru/Sn nanoparticles in a soft, wet-chemical synthesis. The organometallic precursors were dispersed in an ionic liquid and subjected to microwave induced heating. No extra stabilizers were added. The

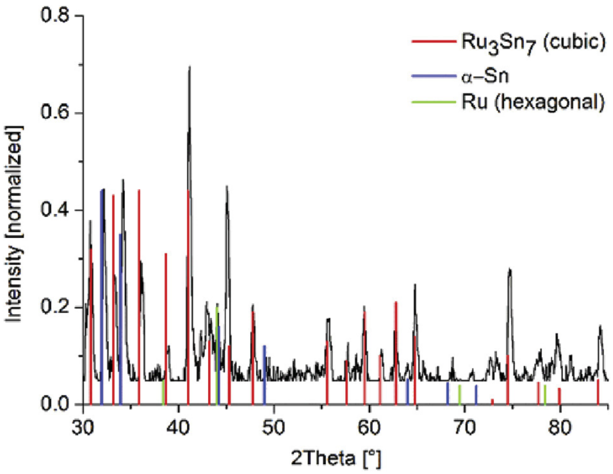

Fig. 3. PXRD of the nanoparticles from precursor **2**. Ru_3Sn_7 reference peaks in red (from crystallographic open database, COD 2200583), α-Sn reference peaks in blue (COD 9008570), potential hexagonal Ru reference peaks in green (COD 9008513). (For interpretation of the references to colour in this figure legend, the reader is referred to the web version of this article.)

nanophase Ru_3Sn_7, obtained from the RuSn precursor **2** could be identified by PXRD.

Acknowledgments

The work of CJ was supported by the Deutsche Forschungsgemeinschaft by grant Ja466/31-1 within the priority project SPP 1708. The work is partially supported by a Grant-in-Aid for Scientific Research on Innovative Areas "π-System Figuration: Control of Electron and Structural Dynamism for Innovative Functions" (No. 26102006 for MS) from the Ministry of Education, Culture, Sports, Science and Technology, Japan. M. Saito acknowledges the Gambrinus fellowship from the Technical University of Dortmund.

References

[1] S.G. Wettstein, J.Q. Bond, D.M. Alonso, H.N. Pham, A.K. Datye, J.A. Dumesic, Appl. Cat. B Environ. 117–118 (2012) 321–329.
[2] J. Han, S.M. Sen, D.M. Alonso, J.A. Dumesic, C.T. Maravelias, Green Chem. 16 (2014) 653–661.
[3] S. Akiyama, T. Kakio, S. Indou, R. Oikawa, K. Ugou, R. Hiraki, M. Sano, T. Suzuki, T. Miyake, J. Jpn. Pet. Inst. 57 (2014) 216–224.
[4] M.A. Sánchez, V.A. Mazzieri, M.A. Vicerich, C.R. Vera, C.L. Pieck, Ind. Eng. Chem. Res. 54 (2015) 6845–6854.
[5] (a) F. Tao, S. Zhang, L. Nguyen, X. Zhang, Chem. Soc. Rev. 41 (2012) 7980–7993;
(b) Y. Pei, G. Zhou, N. Luan, B. Zong, M. Qiao, F. Tao, Chem. Soc. Rev. 41 (2012) 8140–8162.
[6] (a) M. Sankar, N. Dimitratos, P.J. Miedziak, P.P. Wells, C.J. Kiely, G.J. Hutchings, Chem. Soc. Rev. 41 (2012) 8099–8139;
(b) D.M. Alonso, S.G. Wettstein, J.A. Dumesic, Chem. Soc. Rev. 41 (2012) 8075–8098.
[7] (a) K. Schütte, A. Doddi, C. Kroll, H. Meyer, C. Wiktor, C. Gemel, G. van Tendeloo, R.A. Fischer, C. Janiak, Nanoscale 6 (2014) 5532–5544;
(b) K. Schütte, H. Meyer, C. Gemel, J. Barthel, R.A. Fischer, C. Janiak, Nanoscale 6 (2014) 3116–3126.
[8] (a) P. Lara, O.R. Wheelaghan, S. Conejero, R. Poteau, K. Philippot, B. Chaudret, Angew. Chem. Int. Ed. 50 (2011) 12080–12084;
(b) N. Cordente, C. Amiens, B. Chaudret, M. Respaud, F. Senocq, J. Appl. Phys. 94 (2003) 6358–6365.
[9] B. Cormary, F. Dumestre, N. Liakakos, K. Soulantica, B. Chaudret, Dalton Trans. 42 (2013) 12546–12553.
[10] (a) R.D. Adams, E. Trufan, Philos. Trans. R. Soc. Lond. Ser. A 368 (2010) 1473–1493;
(b) R.D. Adams, D.A. Blom, B. Captain, R. Raja, J.M. Thomas, E. Trufan, Langmuir 24 (2008) 9223–9226;
(c) L.O. Paz-Borbón, A. Hellman, J.M. Thomas, H. Grönbeck, Phys. Chem. Chem. Phys. 15 (2013) 9694–9700.
[11] J.P. Hallett, T. Welton, Chem. Rev. 111 (2011) 3508–3576.
[12] C. Janiak, Z. Naturforsch. B 68 (2013) 1059–1089.
[13] (a) E. Ahmed, J. Breternitz, M.F. Groh, M. Ruck, CrystEngComm 14 (2012) 4874–4885;
(b) E. Ahmed, M. Ruck, Dalton Trans. 40 (2011) 9347–9357;
(c) M.F. Groh, U. Müller, E. Ahmed, A. Rothenberger, M. Ruck, Z. Naturforsch. B 68 (2013) 1108–1122;
(d) K. Klauke, B. Hahn, K. Schütte, J. Barthel, C. Janiak, Nano-Structures Nano-Objects 1 (2015) 24–31.
[14] R.E. Morris, Chem. Commun. (2009) 2990–2998.
[15] J. Dupont, J.D. Scholten, Chem. Soc. Rev. 39 (2010) 1780–1804.
[16] (a) V.I. Pârvulescu, C. Hardacre, Chem. Rev. 107 (2007) 2615–2665;
(b) J.D. Scholten, B.C. Leal, J. Dupont, ACS Catal. 2 (2012) 184–200.
[17] (a) E. Redel, M. Walter, R. Thomann, L. Hussein, M. Krüger, C. Janiak, Chem. Commun. 46 (2010) 1159–1161;
(b) E. Redel, M. Walter, R. Thomann, C. Vollmer, L. Hussein, H. Scherer, M. Krüger, C. Janiak, Chem. Eur. J. 15 (2009) 10047–10059.
[18] (a) G.S. Fonseca, G. Machado, S.R. Teixeira, G.H. Fecher, J. Morais, M.C.M. Alves, J. Dupont, J. Colloid Interface Sci. 301 (2006) 193–204;
(b) G.S. Fonseca, J.B. Domingos, F. Nome, J. Dupont, J. Mol. Catal. A Chem. 248 (2006) 10–16.
[19] E.T. Silveira, A.P. Umpierre, L.M. Rossi, G. Machado, J. Morais, G.V. Soares, I.J.R. Baumvol, S.R. Teixeira, P.F.P. Fichtner, J. Dupont, Chem. Eur. J. 10 (2004) 3734–3740.
[20] P. Migowski, G. Machado, S.R. Teixeira, M.C.M. Alves, J. Morais, A. Traverse, J. Dupont, Phys. Chem. Chem. Phys. 9 (2007) 4814–4821.
[21] (a) D. Marquardt, J. Barthel, M. Braun, C. Ganter, C. Janiak, CrystEngComm 14 (2012) 7607–7615;
(b) G. Salas, A. Podgorsek, P.S. Campbell, C.C. Santini, A.A.H. Pádua, M.F. Costa Gomes, K. Philippot, B. Chaudret, M. Turmine, Phys. Chem. Chem. Phys. 13 (2011) 13527–13536;
(c) T. Gutel, J. Garcia-Antón, K. Pelzer, K. Philippot, C.C. Santini, Y. Chauvin, B. Chaudret, J.-M. Basset, J. Mater. Chem. 17 (2007) 3290–3292.
[22] P.S. Campbell, M.H.G. Prechtl, C.C. Santini, P.-H. Haumesser, Curr. Org. Chem. 17 (2013) 414–429.
[23] (a) R. Marcos Esteban, K. Schütte, P. Brandt, D. Marquardt, H. Meyer, F. Beckert, R. Mülhaupt, H. Kölling, C. Janiak, Nano-Structures Nano-Objects 2 (2015) 11–18;
(b) C. Vollmer, C. Janiak, Coord. Chem. Rev. 255 (2011) 2039–2057;
(c) C. Vollmer, M. Schröder, Y. Thomann, R. Thomann, C. Janiak, Appl. Catal. A 425–426 (2012) 178–183;
(d) D. Marquardt, C. Vollmer, R. Thomann, P. Steurer, R. Mülhaupt, E. Redel, C. Janiak, Carbon 49 (2011) 1326–1332;
(e) D. Marquardt, Z. Xie, A. Taubert, R. Thomann, C. Janiak, Dalton Trans. 40 (2011) 8290–8293;
(f) C. Vollmer, E. Redel, K. Abu-Shandi, R. Thomann, H. Manyar, C. Hardacre, C. Janiak, Chem. Eur. J. 16 (2010) 3849–3858;
(g) E. Redel, J. Krämer, R. Thomann, C. Janiak, J. Organomet. Chem. 694 (2009) 1069–1075;
(h) J. Krämer, E. Redel, R. Thomann, C. Janiak, Organometallics 27 (2008) 1976–1978;
(i) E. Redel, R. Thomann, C. Janiak, Chem. Commun. (2008) 1789–1791.
[24] M. Larhed, C. Moberg, A. Hallberg, Acc. Chem. Res. 35 (2002) 717–727.
[25] M.F. Groh, M. Heise, M. Kaiser, M. Ruck, Nachr. Chem. 61 (2013) 26–29.
[26] A.L. Buchachenko, E.L. Frankevich, Chemical Generation and Reception of Radio- and Microwaves, Wiley-VCH, Weinheim, Germany, 1993, pp. 41–56.
[27] V.K. Ahluwulia, Alternative Energy Processes in Chemical Synthesis, Alpha Science International LTD, Oxford, United Kingdom, 2008.
[28] I. Bilecka, M. Niederberger, Nanoscale 2 (2010) 1358–1374.
[29] T. Kuwabara, J.-D. Guo, S. Nagase, T. Sasamori, N. Tokitoh, M. Saito, J. Am. Chem. Soc. 136 (2014) 13059–13064.
[30] (a) J.D. Makinson, J.S. Lee, S.H. Magner, R.J. De Angelis, W.N. Weins, A.S. Hieronymus, Adv. X-ray Anal. 42 (2000) 407–411;
(b) F. Zhang, S.-W. Chan, J.E. Spanier, E. Apak, Q. Jin, R.D. Robinson, I.P. Herman, Appl. Phys. Lett. 80 (2002) 127–129;
(c) K.M. Reddy, S.V. Manorama, A.R. Reddy, Mater. Chem. Phys. 78 (2002) 239–245.
[31] (a) M. Kurian, C. Kunjachan, Nano-Structures Nano-Objects 1 (2015) 15–23;
(b) M. Manhas, V. Kumar, V. Sharma, O.M. Ntwaeaborwa, H.C. Swart, Nano-Structures Nano-Objects 3 (2015) 9–16.
[32] O. Schwomma, H. Nowotny, A. Wittmann, Monatsh. Chem. 95 (1964) 1538–1543.

4.0 Unveröffentlichte Arbeit

4.1 Einleitung

Mono – und bimetallische Nanopartikel und deren Anwendung für die Katalyse

Monometallische Nanopartikel

Innerhalb der letzten 10 Jahre hat sich die Forschung sehr stark auf Metall-Nanopartikel (M-NPs) und deren Anwendung in der Katalyse fokussiert. Vor allem die Kombination von M-NPs und ILs eröffnet ein weites Feld sowohl für die homogene als auch für die heterogene Katalyse [5]. Edle Übergangsmetallnanopartikel wie Pt, Pd und Au eignen sich für selektive Hydrierungsreaktionen von aromatischen Chlornitroverbindungen [6], C-C-Kreuzkupplungsreaktionen [7] und der katalytischen Reduktion von 4-Nitrophenol [8].

Andere Übergangsmetallnanopartikel wie Fe, Co, Ni, Ru, Rh, Os und Ir sind gute Katalysatoren für die Semihydrierung von Alkinen zu Alkenen [9], Fischer-Tropsch Reaktionen [10], Olefin- [11] und Arenhydrierung [12,13] sowie für die Hydrierung von Nitrobenzol [14] und Styrol [15]. Vor allem IL-stabilisierte Ru-NPs finden eine breite Anwendung für Hydrierungsreaktionen. Die Olefin- und Arenhydrierung liefert mit diesem Katalysator sehr gute Ergebnisse [5]. Eine für die Industrie sehr wichtige Katalysereaktion, ist die selektive Hydrierung von Benzol zu Cyclohexen [16]. So erhielten Schwab *et al.* auf Al_2O_3 geträgerte und in Wasser mit wenigen Anteilen IL ([BMIm][OTf], [BMIm][BF_4]) synthetisierte Ru-NPs mit einer Größe von 1.4 – 4.1 nm und konnten zeigen, dass die Zugabe von kleinen Anteilen IL zum Reaktionsgemisch einen Einfluss auf die Selektivität der Hydrierung hat. Einen wesentlichen Vorteil bildet die selektive Hydrierung von Benzol zu Cyclohexen dahingehend, dass die vollständige Hydrierung zu Cyclohexan für die Bildung von Cyclohexanol und weiter zu ε-caprolactam nicht nötig ist [16].

Die Semihydrierung von Benzol zu Cyclohexen mit Ru-NPs in IL ohne Trägermaterial wurde von Silveira *et al.* beschrieben [17]. Die kontrollierte Zersetzung von [Ru(cod)(cot)] in verschiedenen ILs, hier [BMIm][BF_4], [BMIm][PF_6] und [BMIm][CF_3SO_3], lieferte kleine isolierte Nanopartikel (Abb. 4.1.1) mit einem Nanopartikeldurchmesser von 2.6 ± 0.4 nm.

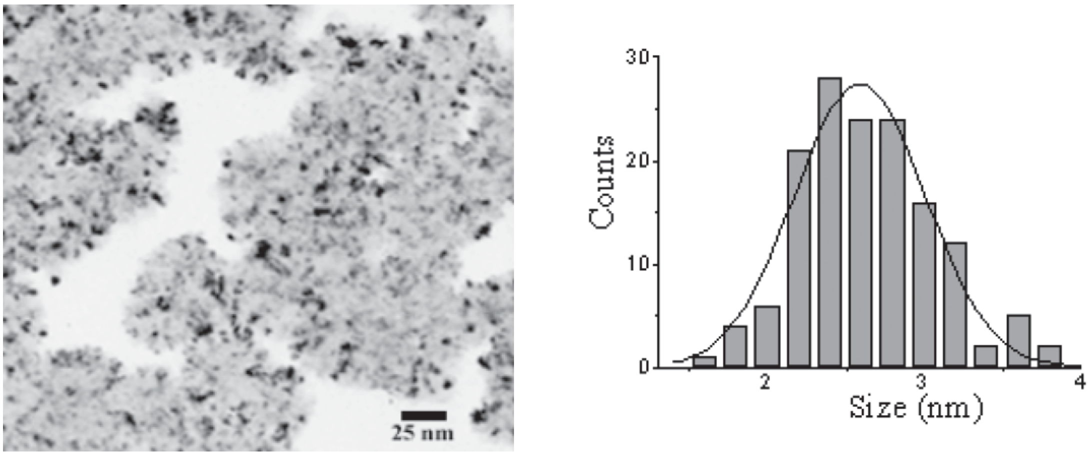

Abb. 4.1.1: TEM-Aufnahme der Ru-NPs in der IL [BMIm][PF_6] mit der dazugehörigen Größenverteilung [17]. Adaptiert mit Erlaubnis von Quelle [17], Copyright 2004 Wiley

Eine Lösung dieser Ru-NPs wurde für die Hydrierung von Benzol zu Cyclohexene unter milden Bedingungen (75 °C, 4 atm) eingesetzt und resultierte in Umsätzen bis zu 73%. Silveira *et al.* konnte zeigen, dass die höchste Cyclohexen-Selektivität mit Ru-NPs in der IL [BMIm][PF_6] erreicht wurden, im Vergleich zu den in [BMIm][BF_4] und [BMIm][CF_3SO_3] synthetisierten Ru-NPs. Des Weiteren wiesen die ungeträgerten Ru-NPs eine höhere katalytische Aktivität auf, als die geträgerten Ru-NPs.

Hohe Selektivitäten und Umsätze werden ebenfalls bei der Hydrierung von Cyclohexen zu Cyclohexan mit geträgerten Ir-NPs und ungeträgerten Ru-NPs erreicht [18,19]. Vollmer *et al.* erhielten mittels mikrowellengestützter Synthese kleine, nicht agglomerierte, kristalline Ru-NPs in der IL [BMIm][BF_4] mit einem Nanopartikeldurchmesser von 1.6 ± 0.3 nm (Abb. 4.1.2) und erreichten mit diesem Katalysator für die Hydrierung von Cyclohexen zu Cyclohexan hohe Umsätze bis zu 95% (Abb. 4.1.3).

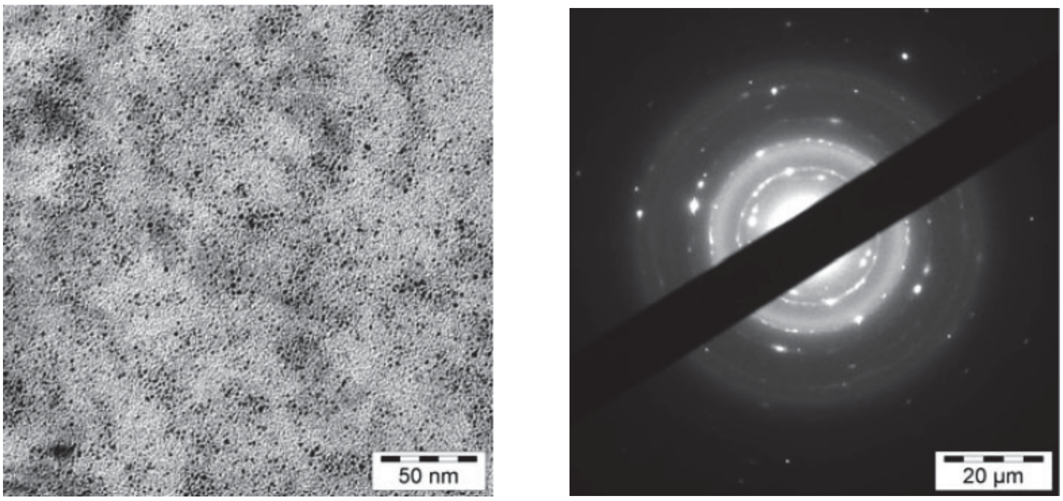

Abb. 4.1.2: TEM-Aufnahme der Ru-NPs in der IL [BMIm][BF_4] mit dazugehörigem Beugungsbild (SAED), welches die Kristallinität der Partikel zeigt [18]. Adaptiert mit Erlaubnis von Quelle [18], Copyright 2010 Wiley

Der Katalysator zeigte eine Aktivität bis zu sieben Runs und die Umsätze wurden mittels H_2-Aufnahmekurven verfolgt.

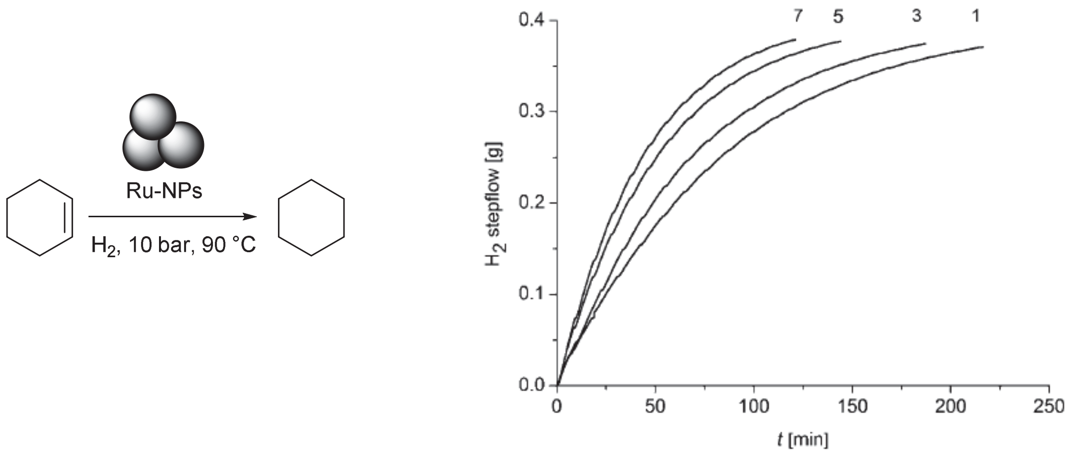

Abb. 4.1.3: Hydrierung von Cyclohexen zu Cyclohexan, katalysiert durch Ru-NPs unter milden Bedingungen (links, bearbeitete Wiederdarstellung nach Lit. [18]). H_2-Aufnahmekurve des ersten bis siebten Hydrierungszyklus in Abhängigkeit der Zeit (rechts) [18]. Adaptiert mit Erlaubnis von Quelle [18], Copyright 2010 Wiley.

Marcos-Esteban *et al.* war es möglich bei der vollständigen Hydrierung von Benzol zu Cyclohexan ebenfalls hohe Umsätze bis zu 91% zu erreichen [19]. Als Katalysator für diese Reaktion wurden sehr kleine Ir-NPs mit einem mittleren Partikeldurchmesser von 1.0 ± 0.4 nm eingesetzt, welche auf thermisch reduziertem Graphitoxid (TRGO) geträgert und mittels Mikrowellenstrahlung synthetisiert wurden. Als Reaktionsmedium diente hier die IL [BMIm][BF_4]. Die Ir-NPs zeigten eine ähnliche katalytische Aktivität bis zu 10 Runs für die Hydrierung von Benzol zu Cyclohexan unter milden Bedingungen (Abb. 4.1.4) [19].

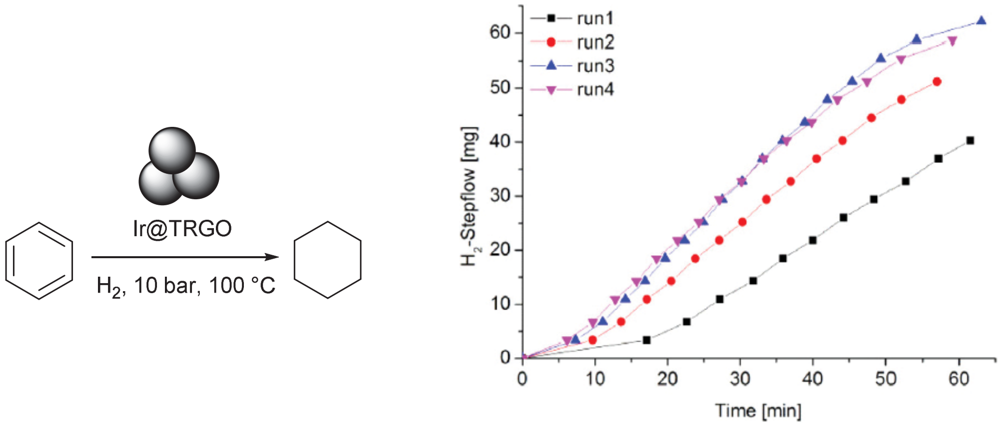

Abb. 4.1.4: Hydrierung von Benzol zu Cyclohexan katalysiert durch Ir-NPs@TRGO in der IL [BMIm][BF_4] (links, bearbeitete Wiederdarstellung nach Lit. [19]). H_2-Aufnahmekurve des ersten bis vierten Hydrierungszyklus in Abhängigkeit der Zeit (rechts) [19]. Nachdruck aus Quelle [19] Copyright 2015 mit Erlaubnis von Elsevier.

Bimetallische Nanopartikel

Bimetallische Nanoverbindungen bilden interessante Katalysatoren im Bereich der heterogenen Katalyse [20]. Die meisten dieser „Nanokatalysatoren“ beinhalten edle Übergangsmetalle, wie Pt, Pd oder Au. So spielen PtRu-NPs als Katalysator eine wichtige Rolle bei der elektrochemischen Oxidation von Methanol in Brennstoffzellen [20]. Verschiedene PdGa Verbindungen wurden von Armbrüster *et al.* für die Semihydrierung von Alkinen zu Alkenen beschrieben [21]. Sie fanden heraus, dass intermetallische Verbindungen, wie Pd_3Ga_7, PdGa sowie auch Pd_2Ga sehr gute Katalysatoren für die Semihydrierung von Acetylen zu Ethylen mit hohen Selektivitäten darstellen (Abb. 4.1.5).

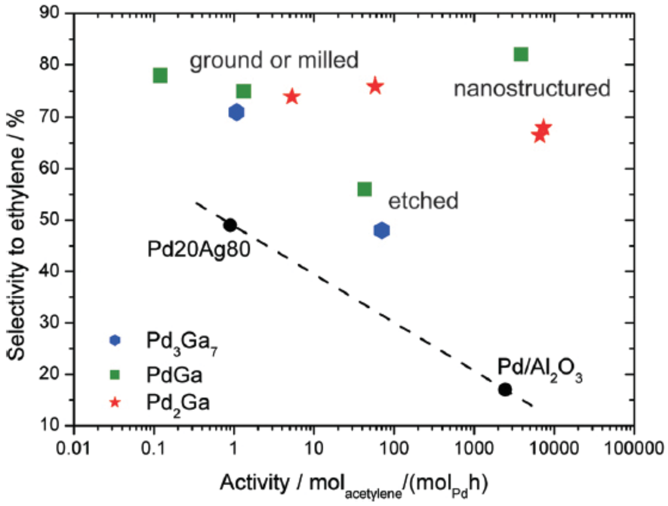

Abb. 4.1.5: Ethylenselektivität in % in Abhängigkeit zur TOF der Acetylenhydrierung im Vergleich zu Modellsystemen und technischen Katalysatoren [21]. Adaptiert mit Erlaubnis von Quelle [21], Copyright 2010 American Chemical Society.

Im Allgemeinen sind Pd Katalysatoren sehr gut für die Actelyenhydrierung geeignet. Ein Problem, welches bei dieser Semihydrierung entstehen kann, ist die „Durchhydrierung“ von Ethylen zu Ethan. Um diesem Problem vorzubeugen ist es möglich, den eingesetzten Pd Katalysator mit Ag zu unterstützen, so, wie es in der Arbeit von Zea *et al.* durchgeführt und beschrieben worden ist [22].

Ein weiterer Nachteil, der alle edlen Übergangsmetallkatalysatoren betrifft, ist, dass diese sehr teuer sind und es sowohl für die industrielle als auch wissenschaftliche Forschung von großer Bedeutung ist, diese durch kostengünstigere Metalle zu ersetzen. Armbrüster *et al.* gelang es für die heterogene Hydrierung eine kostengünstigere Alternative zu den teuren Pd Katalysatoren zu finden [23]. Sie setzen 20 mg ungeträgertes $Al_{13}Fe_4$ für katalytische Tests in Ethylen ein und erhielten mit diesem Katalysator hohe Umsätze und eine hohe Ethylenselektivität von 81 – 84% (Abb. 4.1.6). Die Semihydrierung zu Acetylen wurde 20 h bei einer Temperatur von 200 °C durchgeführt.

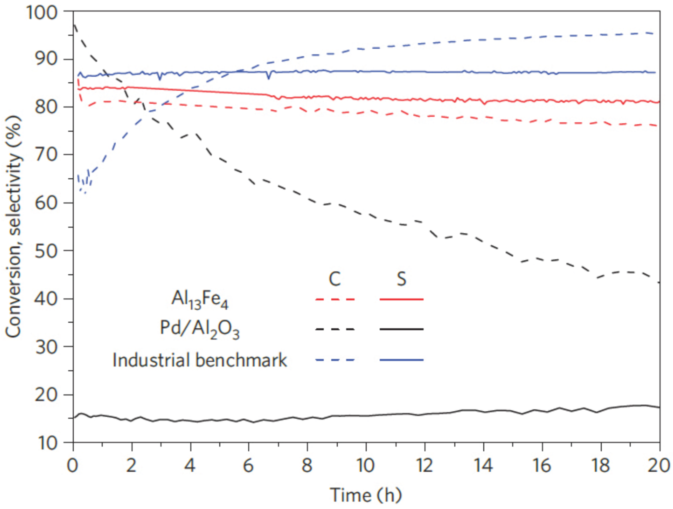

Abb. 4.1.6: Umsatz und Selektivität für Ethylen mit $Al_{13}Fe_4$ als Katalysator im Vergleich zu geträgertem Pd und einem industriellen Katalysator [23]. Adaptiert mit Erlaubnis von Macmillan Publishers Ltd: Nature Materials [23], Copyright 2012.

Eine andere Möglichkeit, edle Übergangsmetalle für die Anwendung in der Katalyse zu ersetzen, wurde von Schütte *et al.* gefunden [24]. Hierbei wurde die Synthese intermetallischer NiGa Nanomaterialien und deren Anwendung für die selektive Semihydrierung von Alkinen zu Alkenen beschrieben. Sowohl für die Semihydrierung von 1-Octin zu 1-Octen, als auch für Diphenylacetylen zu Diphenylethylen ließen sich hohe Selektivitäten von 94 bzw. 87% erzielen. Für den Katalysator wurden unterschiedliche Molverhältnisse von 1:1 und 3:1 des Dual-Source Precursors [Ni(COD)$_2$] und GaCp* gewählt und Nanopartikel mit einer mittleren Partikelgröße von 14 ± 5 nm für NiGa-NPs bzw. 17 ± 4 nm für Ni_3Ga-NPs erhalten. Der Precursor wurde mittels Mikrowellenstrahlung in der IL [BMIm][BF$_4$] zersetzt (Abb. 4.1.7 und Abb. 4.1.8).

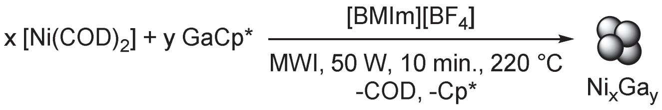

Abb. 4.1.7: Synthese von NiGa und Ni_3Ga Nanopartikeln mittels Mikrowellenstrahlung in der IL [BMIm][BF$_4$] (bearbeitete Wiederdarstellung nach Lit. [24]).

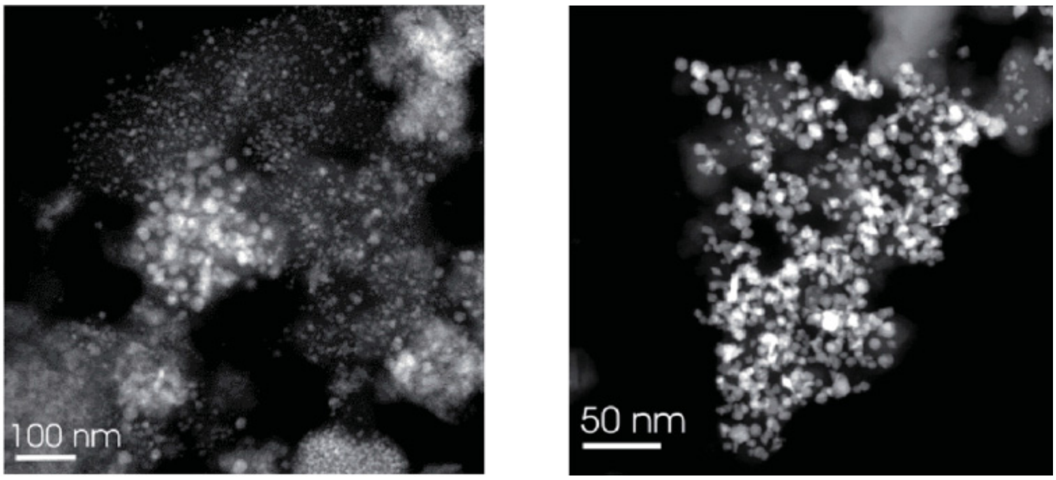

Abb. 4.1.8: HAADF-STEM Aufnahmen der NiGa-NPs (links) und Ni_3Ga-NPs (rechts) [24]-Published by the Royal Society of Chemistry.

Sowohl die NiGa-NPs als auch die Ni_3Ga-NPs eigneten sich als Katalysatoren für die Semihydrierung von 1-Octin zu 1-Octen bzw. Diphenylacetylen zu Diphenylethylen, welche nach nachfolgendem Schema durchgeführt wurde (Abb. 4.1.9).

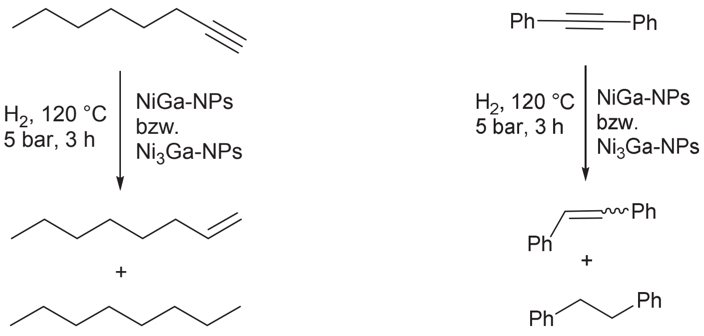

Abb. 4.1.9: Schema der Semihydrierung von 1-Octin zu 1-Octen und Diphenylacetylen zu Diphenylethylen unter milden Bedingungen (bearbeitete Wiederdarstellung nach Lit. [24]).

Des Weiteren beschrieben Schütte *et al.* die Darstellung von CuZn Nanopartikeln für eine mögliche Anwendung in der industriell wichtigen Methanol Synthese [25].

Methanol ist eines der weltweit wichtigsten Chemikalien und wird über die Syntheseroute mit Syngas, CO_2 und einem $Cu/ZnO/Al_2O_3$ Festkörperkatalysator hergestellt. Schütte *et al.* war es möglich, *β*-CuZn Nanopartikel und *γ*-Cu_3Zn Nanopartikel aus den entsprechenden Amidinaten $\{[Me(C(N^iPr)_2]Cu\}_2$ and $[Me(C(N^iPr)_2]_2Zn$ herzustellen und in der IL [BMIm][BF_4] zu stabilisieren. Das für die Synthese eingesetzte Molverhältnis betrug für die *β*-CuZn Nanopartikel 1:1 und für die *γ*-Cu_3Zn Nanopartikel 3:1 (Abb. 4.1.10).

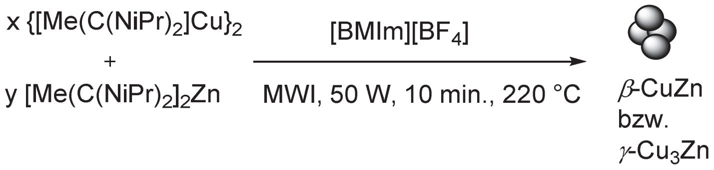

Abb. 4.1.10: Synthese von β-CuZn und γ-Cu_3Zn Nanopartikeln mittels Mikrowellenstrahlung in der IL [BMIm][BF_4] (bearbeitete Wiederdarstellung nach Lit. [25]).

Die β-CuZn und γ-Cu_3Zn Nanopartikel wiesen eine breit verteilte mittlere Partikelgröße von 14 – 51 nm auf und waren kaum agglomeriert (Abb. 4.1.11).

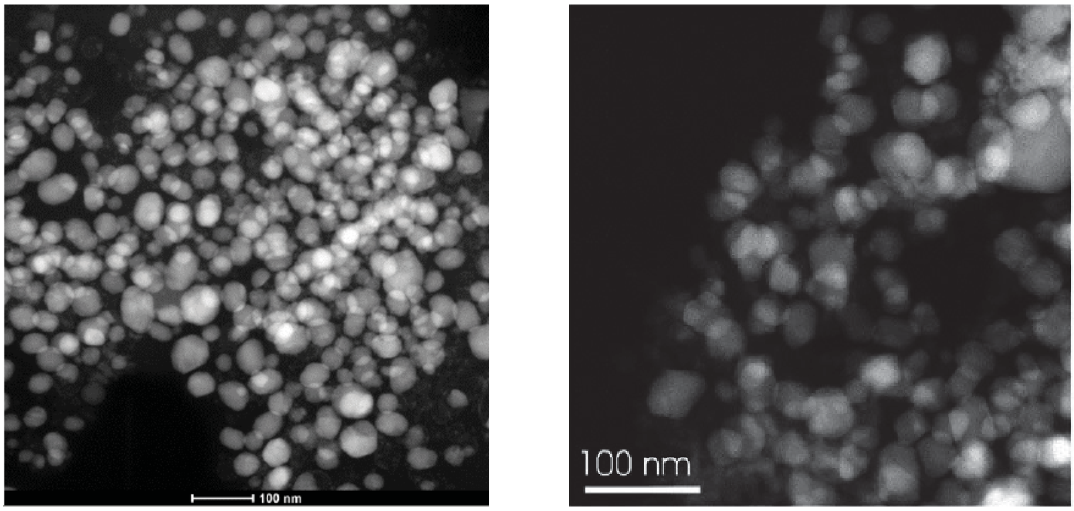

Abb. 4.1.11: HAADF-STEM Aufnahmen der β-CuZn-NPs (links) und γ-Cu_3Zn-NPs (rechts) [25]- Published by the Royal Society of Chemistry.

In den nachfolgenden Studien zur Methanol-Synthese fanden Schütte *et al.* heraus, dass die β-CuZn-NPs, stabilisiert in der IL [BMIm][BF_4], einen guten Katalysator für diese Synthese darstellten (Abb. 4.1.12). Während der Synthese war eine Induktionsphase zwischen der ersten und zweiten Stunde zu beobachten, die notwendig für den Start der Reaktion war. Schütte *et al.* vermuteten, dass sich während der Induktionszeit Cu und ZnO bildeten und wiesen dies auch nach der Katalyse nach [25]. Während der Induktionszeit, wo noch kein Methanol gebildet wurde, bildete sich in der Legierung Cu/ZnO hauptsächlich ZnO. Der Grund für die Zn-Oxidation lag, laut Schütte *et al.* daran, dass sich ein Gleichgewicht zwischen den flüchtigen Komponenten H_2/CO/CO_2 bildete und das sich dabei bildende H_2O mit den Zn-NPs zu ZnO weiter reagierte. Dieser Zusammenhang ist bereits für höhere Temperaturen bekannt [26].

Anhand des Kurvenverlaufs in Abb. 4.1.12 ist zu erkennen, dass die Induktionsphase bei niedrigeren Temperaturen von 140 °C länger andauert (ca. 100 min.) als bei höheren Temperaturen von 180 °C. Nach ca. 150 °C beobachteten Schütte *et al.* eine erhöhte Katalysatoraktivität, die sich in einem erhöhten Umsatz zeigte. Bei sehr hohen Temperaturen von 220 °C liegt die hohe Katalysatoraktivität vermutlich direkt am Anfang vor, sodass bereits unter 100 min. hohe Umsätze erreicht werden können (Abb. 4.1.12). Schütte *et al.* berechneten die Produktivität der Methanol-Synthese über die Steigung der Kurve bei 220 °C und erhielten eine Produktivität von 10.7 mol (MeOH) (kg (Cu) h)$^{-1}$.

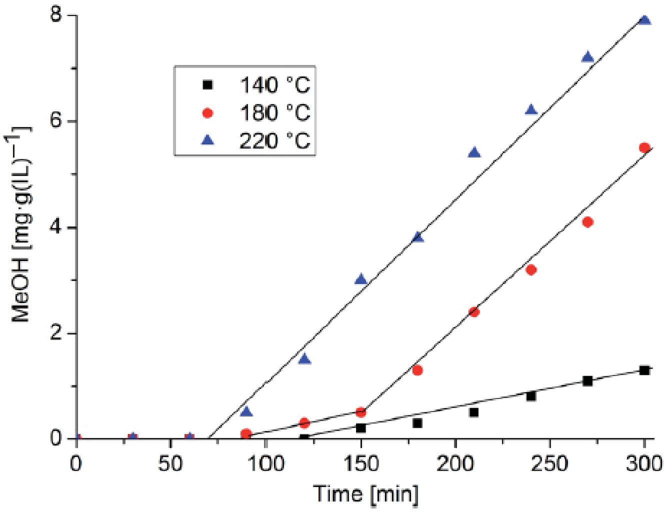

Abb. 4.1.12: Methanol-Synthese katalysiert durch β-CuZn-NPs in der IL [BMIm][BF$_4$] [25]-Published by the Royal Society of Chemistry.

4.2 Untersuchungen zur Katalyse mit mono – und bimetallischen Nanopartikeln in Ionischen Flüssigkeiten und Propylencarbonat

4.2.1 Darstellung von Ru-NPs@TRGO-400 in Propylencarbonat (PC) zur Katalyse von Lävulinsäure

Die Darstellung von Ru-NPs, geträgert auf thermisch reduziertem Graphitoxid (TRGO), wurde in Anlehnung an von Marcos-Esteban publizierte Reaktionsbedingungen durchgeführt [27]. Hierbei wurden $Ru_3(CO)_{12}$ mit TRGO-400 (hierbei gibt die Zahl die Reduktionstemperatur in °C an) zusammengegeben, 24 h in PC suspendiert und anschließend mittels Mikrowellenstrahlung für 10 min. bei 250 °C und 50 W zu Ru-NPs@TRGO-400 zersetzt (Schema 4.2.1.1). Anschließend wurde das, während der Reaktion, entstandene CO-Gas im HV abgezogen und die entstandenen Nanopartikel 6x mit je 5 mL Reinstwasser gefällt und gewaschen. Nach jedem Waschvorgang wurde die Partikel abzentrifugiert, bis das Lösemittel vollständig aus der Suspension entfernt war.

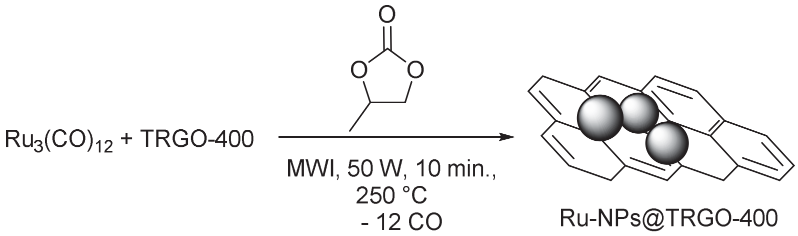

Schema. 4.2.1.1: Synthese von Ru-NPs@TRGO-400 mittels Mikrowellenstrahlung in PC.

Die Charakterisierung der geträgerten Ru-NPs erfolgte mittels PXRD und TEM-EDX. Die Größe der Partikel sowie der Erfolg der Trägerung auf TRGO-400 wurden mittels TEM-Aufnahmen überprüft.

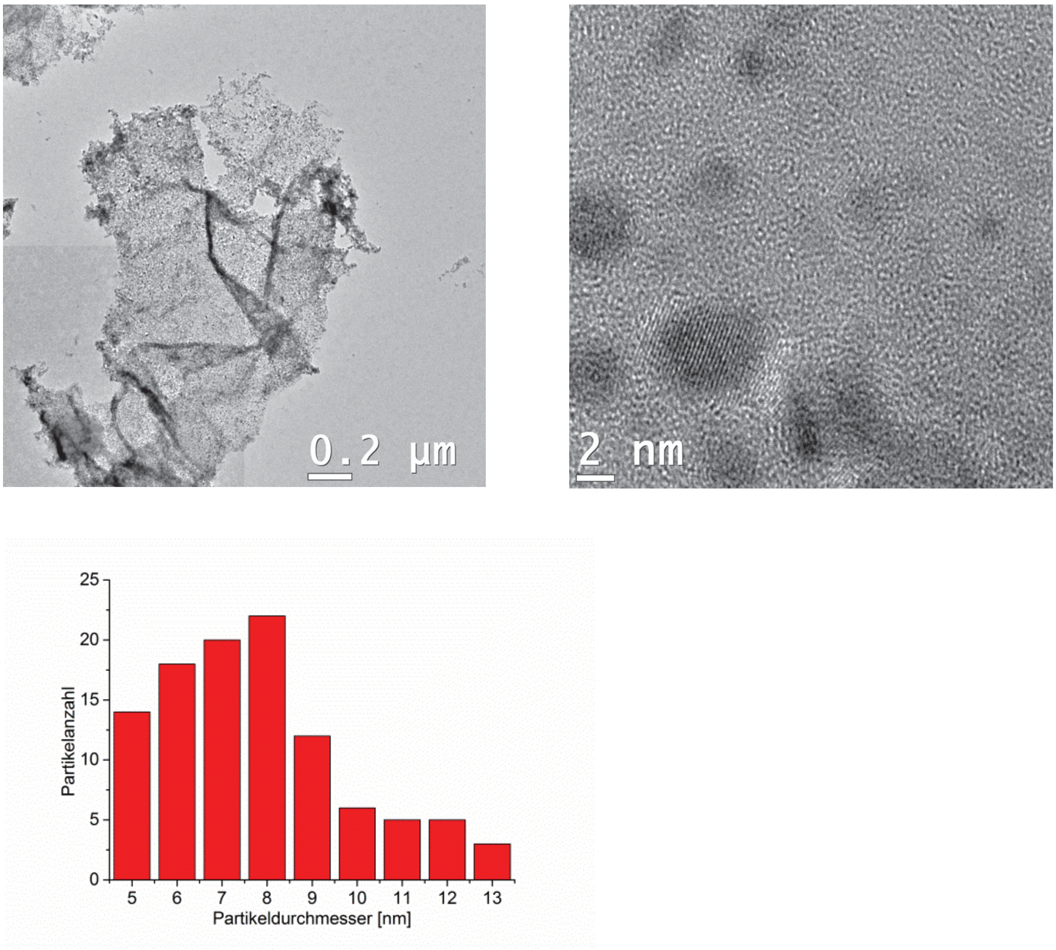

Abb. 4.2.1.1: TEM-Aufnahmen der Ru@TRGO-NPs vor Katalyse (aus 0.5 Gew.% Suspension in PC) Übersicht (oben links) und Nahaufnahme (oben rechts) sowie zugehörige Größenverteilung (unten). Mindestens 50 Partikel ausgezählt, 5-13 nm (Ø 9.0 ± 2.7 nm).

Anhand der TEM-Aufnahmen lässt sich erkennen, dass die Trägerung der Ru-NPs auf TRGO-400 erfolgreich war. Die Ru-NPs liegen in einer breiten Größenverteilung von 5-13 nm vor mit einer mittleren Größe von 9.0 ± 2.7 nm und sind als sphärische, isolierte Partikel erkennbar. Ebenfalls lässt sich die Schichtstruktur des TRGO-400 erkennen. Die Kristallinität der Partikel lässt sich anhand der Interferenzmuster in den Partikeln, gezeigt durch die TEM-Nahaufnahme, nachweisen.

Die Kristallinität der Partikel konnte zudem mittels PXRD nachgewiesen werden (Abb. 4.2.1.2, links). Ein weitere Charakterisierung der Ru@TRGO-400-NPs erfolgte mittels TEM-EDX (Abb. 4.2.1.2, rechts).

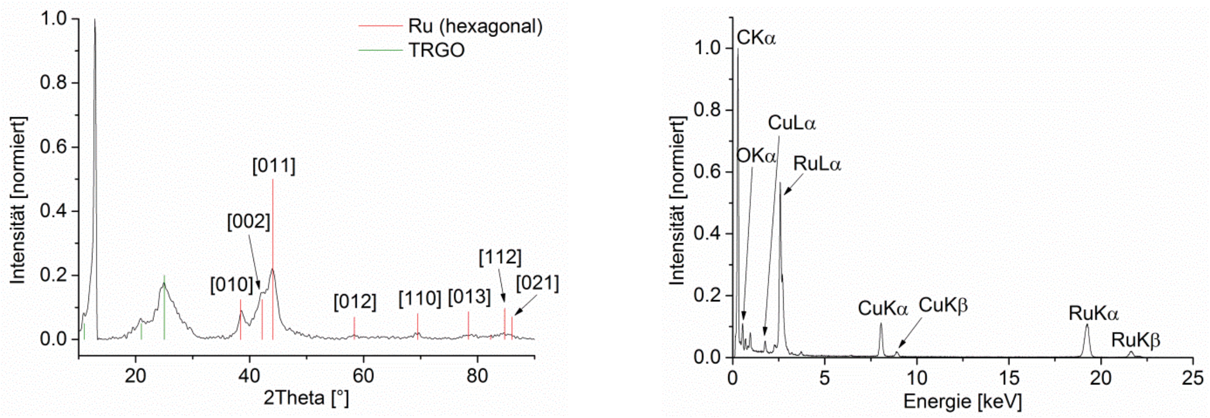

Abb. 4.2.1.2: PXRD der Ru@TRGO-NPs (aus 0.5 Gew.% Suspension in PC) (links, COD-Referenz Ru: 9008513, Referenz TRGO: Lit. [28]). EDX-Spektrum der Ru@TRGO-NPs (aus 0.5 Gew.% Suspension in PC) (rechts, das Kupfer-Signal ist durch das TEM-Grid begründet).

Anhand des PXR-Diffraktogramms lassen sich die Signale der Ru-NPs der hexagonalen Kristallphase zuordnen (rote Referenz). Ebenso treten bei ca. 23 ° 2Theta und 26 ° 2Theta die typischen Signale für das TRGO auf (grüne Referenz) [28]. Das EDX-Spektrum zeigt, dass es sich bei der Probe um Ru-NPs handelt. Die zusätzlichen Signale von Kupfer und Kohlenstoff lassen sich durch das TEM-Grid erklären, allerdings könnte die hohe Intensität des Kohlenstoffs zusätzlich ein Indiz auf vorhandenes TRGO-400 sein, welches durch die TEM-Aufnahmen ebenfalls bestätigt wurde (siehe Abb.4.2.1.1).

Nachdem sowohl die Synthese der Ru-NPs als auch die Trägerung dieser auf TRGO-400 erfolgreich durchgeführt wurde, wurden die Nanopartikel als Katalysator zur Hydrierung des Biostoffes Lävulinsäure zu *γ*-Valerolacton (GVL) eingesetzt. Lävulinsäure kann auf zwei Synthesewegen hergestellt werden (Abb. 4.2.1.3). Zum einen kann es über den Xylose-Weg aus Biomasse (Hemi-Cellulose, Cellulose und Lignin) hergestellt werden und zum anderen über den Glucose-Weg [29]. Der Vorteil an der Verwertung von Biomasse, wie Cellulose und Lignin besteht darin, dass es zu verschiedenen Zuckern, wie Xylose und Glucose umgewandelt und daraus zu verschiedenen Chemikalien weiter verwertet werden kann (Abb. 4.2.1.3). Aus diesen Chemikalien, wie z.B. Lävulinsäure, können für die Industrie sehr wichtige Vorläuferverbindungen (*γ*-Valerolacton) für Treibstoffe hergestellt werden [29].

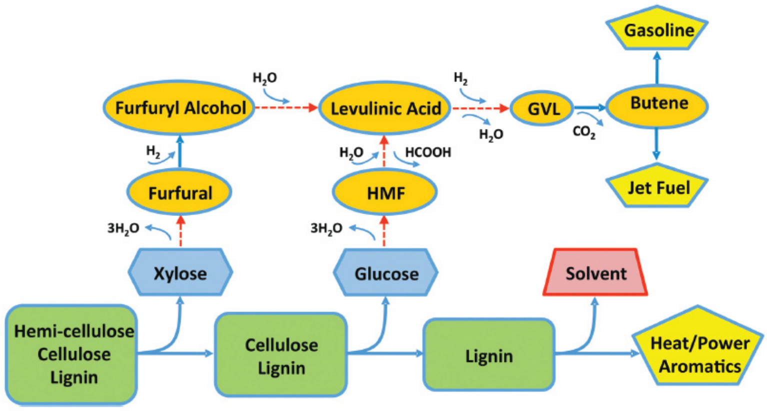

Abb. 4.2.1.3: Schema der Verwertung von Biomasse zu Lävulinsäure und γ-Valerolacton bis hin zu Treibstoffen. Adaptiert von [29] mit Erlaubnis von Royal Society of Chemistry.

Für die Katalyse von Lävulinsäure zu γ-Valerolacton wurden die ausgefällten Ru@TRGO-400-NPs unter Inertbedingungen (Glovebox) in einem Verhältnis von 1:1081 (genaue Einwaagen sind dem Experimentalteil, Abschnitt 6, zu entnehmen) mit dem Substrat Lävulinsäure in ein Glasinlet gefüllt und dieses in einen Stahlautoklaven gebracht. Der Autoklav wurde auf Dichtigkeit geprüft und 3x mit H_2 gespült. Nach Aufheizen des Autoklavs im Ölbad auf 100 °C, wurde das System mit 10 bar H_2 beschickt und der Katalysefortschritt mittels H_2-Aufnahmekurve über 3 h und für 5 Zyklen verfolgt (Abb. 4.2.1.4). Schema 4.2.1.2 zeigt eine vereinfachte Darstellung der Katalyse von Lävulinsäure zu γ-Valerolacton unter Einsatz der Ru@TRGO-400-NPs als Katalysator.

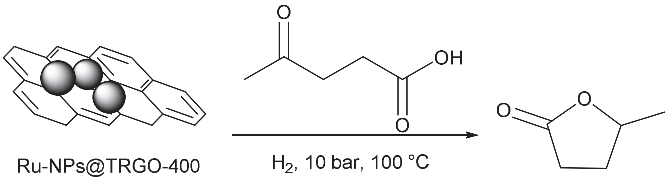

Schema 4.2.1.2: Vereinfachte Darstellung der Hydrierung von Lävulinsäure zu γ-Valerolacton, katalysiert durch Ru@TRGO-400-NPs.

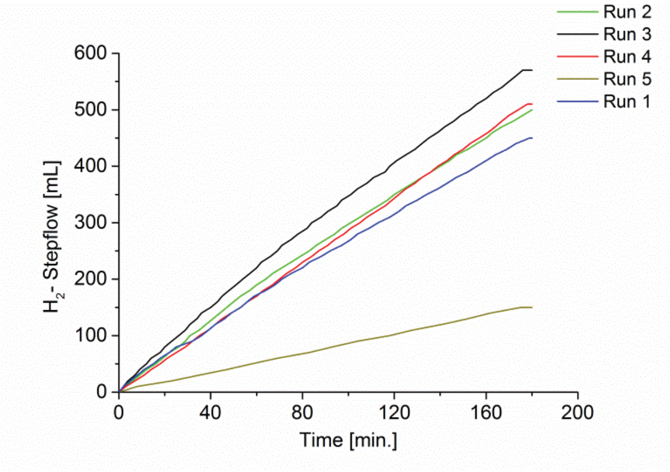

Abb. 4.2.1.4: H_2-Aufnahme in Abhängigkeit der Zeit für 5 Katalysezyklen der Hydrierung von Lävulinsäure zu *γ*-Valerolacton.

Nach dem ersten Katalysezyklus wurde der Katalysator per Ultrazentrifugation vom Produkt abgetrennt und 3x mit je 1 mL Methanol für weitere Katalysezyklen aufgereinigt und anschließend im HV getrocknet. Das Produkt wurde nach jedem Zyklus gesammelt und mittels Gaschromatographie (GC) auf seine Bestandteile überprüft. Tabelle 4.2.1.1 zeigt den jeweiligen Umsatz und die Produktselektivität der Hydrierung für 5 Zyklen.

Tab. 4.2.1.1: Umsätze und Selektivität der Hydrierung von Lävulinsäure zu *γ*-Valerolacton, katalysiert durch Ru@TRGO-400-NPs.

Zyklus	**Kat.**	**Edukt**	**Produkt**	**Umsatz [%]**	**Selektivität [%]**	**TOF[a] [h^{-1}]**
1	Ru@TRGO-400	Lävulinsäure	*γ*-Valerolacton	100	100	1156
2	Ru@TRGO-400	Lävulinsäure	*γ*-Valerolacton	100	100	1156
3	Ru@TRGO-400	Lävulinsäure	*γ*-Valerolacton	100	100	1156
4	Ru@TRGO-400	Lävulinsäure	*γ*-Valerolacton	17	89	197
			α-Angelicalacton	1	11	
5	Ru@TRGO-400	Lävulinsäure	γ-Valerolacton	81	82	936
			α-Angelicalacton	18	18	

[a] Turn over frequency (TOF) = mol (GVL) x (mol Ru)$^{-1}$ x h^{-1}

Der Vergleich zwischen der H_2-Aufnahme (Abb. 4.2.1.4) und den Umsatzraten in Tab. 4.2.1.1 zeigt, dass die katalytische Aktivität der Ru@TRGO-400-NPs vom ersten bis zum dritten Zyklus stetig zunimmt und die Reaktion nach ca. 170 min. beendet ist (siehe Plateau, Abb. 4.2.1.4). Der Grund hierfür besteht in den Oberflächenatomen der Nanopartikel, die grundlegend an der Katalyse beteiligt sind und einen großen Einfluss auf die katalytische Aktivität haben. So lässt sich hier anhand des Anstieges der H_2-Aufnahme vermuten, dass durch die Aufbereitung des Katalysators von Zyklus zu Zyklus mehr Oberflächenatome „aktiviert“ werden und somit höhere Umsätze in kürzerer Zeit erreicht werden (vgl. hierzu auch Lit. [27] und Abschnitt 3.1), da die Oberfläche von evtl. noch vorhandenem CO aus der Ausgangssynthese des Katalysators befreit wird. Ab dem vierten Zyklus sinkt die H_2-Aufnahmekurve und damit auch die katalytische Aktivität. Dieser Zusammenhang kann ebenfalls mit der Aufbereitung des Katalysators erklärt werden. Durch die Waschprozesse und eventuelle Edukt- und Produktrückstände kann es zu einer „Deaktivierung“ der Oberflächenatome kommen, die sich in der stetigen Abnahme der katalytischen Aktivität zeigt. Dies wird auch in den geringeren Umsatzraten in Tab. 4.2.1.1 deutlich, wobei die Selektivität immer noch auf Seiten des Hauptproduktes liegt und nur in geringen Anteilen auf Seiten des Nebenproduktes *α*-Angelicalacton. Eine Abnahme des Umsatzes wäre auch für den fünften Zyklus zu erwarten, jedoch steigt der Umsatz dort wieder an, wohingegen die H_2-Aufnahmekurve weiter abnimmt.

Die Bildung des Nebenproduktes *α*-Angelicalacton ab dem vierten Zyklus kann ebenfalls mit der Abnahme der katalytischen Aktivität erklärt werden. Ru-NPs sind bekannt dafür, dass sie als gute Katalysatoren für Hydrierungsreaktionen fungieren. Nimmt die katalytische Aktivität jedoch ab, kann es zur Bildung von Zwischenprodukten kommen und die Reaktion kann mittels Ru-Katalysator nicht mehr bis zum Endprodukt „durchhydriert“ werden. Schema 4.2.1.3 zeigt die Bildung des gewünschten Produktes *γ*-Valerolacton über zwei mögliche Zwischenprodukte.

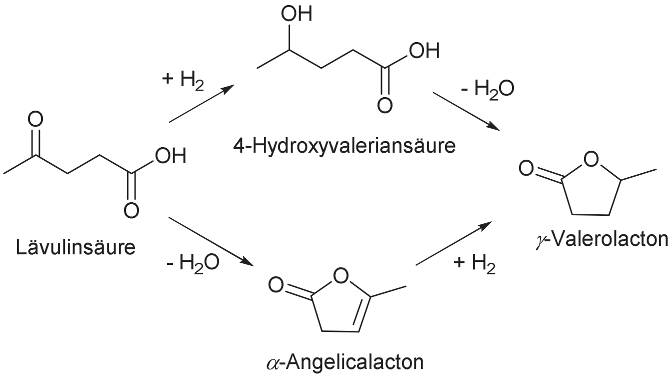

Schema 4.2.1.3: Synthese von Lävulinsäure zu γ-Valerolacton über die Zwischenprodukte 4-Hydroxyvaleriansäure oder α-Angelicalacton.

Die Bildung des Zwischenproduktes 4-Hydroxyvaleriansäure konnte mittels GC nicht nachgewiesen werden.

Eine Charakterisierung der Ru@TRGO-NPs über TEM-Aufnahmen und Größenverteilung erfolgte ebenfalls nach der Katalyse (Abb. 4.2.1.5).

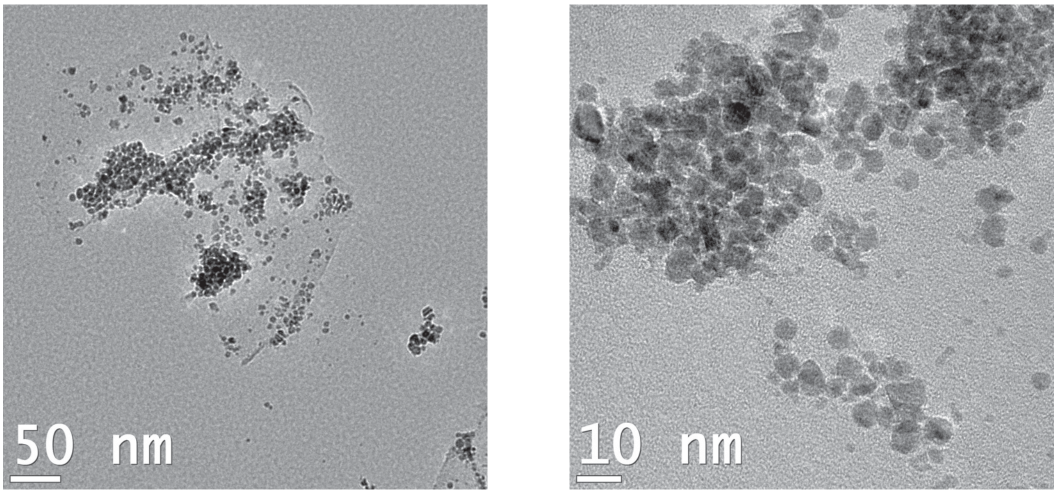

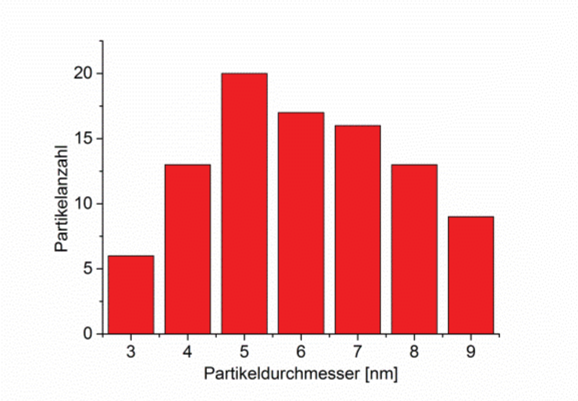

Abb. 4.2.1.5: TEM-Aufnahmen der Ru@TRGO-NPs nach Katalyse (aus 0.5 Gew.% Suspension in PC) Übersicht (oben links) und Nahaufnahme (oben rechts) sowie zugehörige Größenverteilung (unten). Mindestens 50 Partikel ausgezählt, 3-9 nm (Ø 6.0 ± 2.2 nm).

Anhand der TEM-Aufnahmen der Ru@TRGO-400-NPs nach der Katalyse (Abb. 4.2.1.5) lässt sich erkennen, dass diese nun deutlich agglomerierter vorliegen und ein Teil der Partikel nicht mehr auf dem TRGO-400 geträgert ist. Außerdem sind nicht mehr alle Partikel als sphärische Partikel zu erkennen sondern liegen zum Teil deformiert vor (siehe TEM-Nahaufnahme). Eine Aussage über die Kristallinität der Nanopartikel nach der Katalyse kann nicht getroffen werden, da aufgrund der geringen Partikelmenge kein PXRD nach der Katalyse aufgenommen werden konnte.

Die Ru@TRGO-400-NPs weisen auch nach der Katalyse eine breite Größenverteilung auf, sind jedoch mit einer mittleren Größe von 6.0 ± 2.2 nm nur um wenige nm kleiner als die Nanopartikel vor der Katalyse (vgl. Abb. 4.2.1.1).

4.2.2 Verwendung von Ru_2Sn-NPs in der IL [BMIm][BF_4] als Katalysator für die Semihydrierung von 1-Octin zu 1-Octen

Für die Semihydrierung des Alkins 1-Octin zum Alken 1-Octen wurden zur besseren Vergleichbarkeit im Vorfeld katalytische Studien mit reinen Ru-NPs in [BMIm][BF_4] durchgeführt und anschließend die Semihydrierung mit den Ru_2Sn-NPs (Darstellung und Charakterisierung siehe Abschnitt 3.2) vorgenommen. Da Ru-NPs als gute Katalysatoren sowohl für Hydrierungen als auch für Semihydrierungen bekannt sind, sollte hier überprüft werden, inwieweit eine „Vergiftung“ durch Sn Einfluss bzgl. der Umsätze und Alkenselektivitäten hat. Schütte *et al.* konnten dazu bereits für die Semihydrierung von 1-Octin zu 1-Octen mit einem durch Ga „vergifteten“ Ni-Katalysator gute Ergebnisse erzielen (siehe Abschnitt 4.1).

Zur Vorbereitung der katalytischen Studien wurden ausgehend von $Ru_3(CO)_{12}$ in der IL [BMIm][BF_4] durch Zersetzung mittels Mikrowellenstrahlung für 10 min., bei 250 °C und 50 W Ru-NPs erhalten, welche für die mögliche Hydrierung von 1-Octin zu n-Octan als Katalysator eingesetzt wurden (siehe Schema 4.2.2.1).

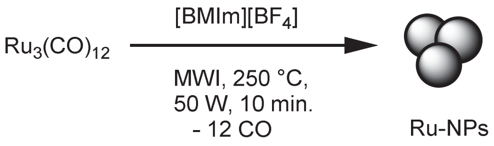

Schema 4.2.2.1: Synthese von Ru-NPs in [BMIm][BF_4] mittels Mikrowellenstrahlung.

Für die Hydrierung von 1-Octin zu n-Octan wurden die Ru-NPs in der IL unter Inertbedingungen (Glovebox) in einem Verhältnis von 1:837 (genaue Einwaagen sind dem Experimentalteil, Abschnitt 6, zu entnehmen) mit dem Substrat 1-Octin in ein Glasinlet gefüllt und dieses in einen Stahlautoklaven gebracht. Der Autoklav wurde auf Dichtigkeit geprüft und 3x mit H_2 gespült. Für den ersten Versuch der Hydrierung wurde der Autoklav im Ölbad auf 100 °C aufgeheizt, anschließend mit 5 bar H_2 beschickt und die Reaktion für 3 h gestartet. Nachdem nach 3 h kein H_2-Verbrauch zu beobachten war, wurde versucht, die Reaktionsbedingungen über die Temperatur– und Druckeinstellung nach nachfolgendem Schema 4.2.2.2 zu optimieren.

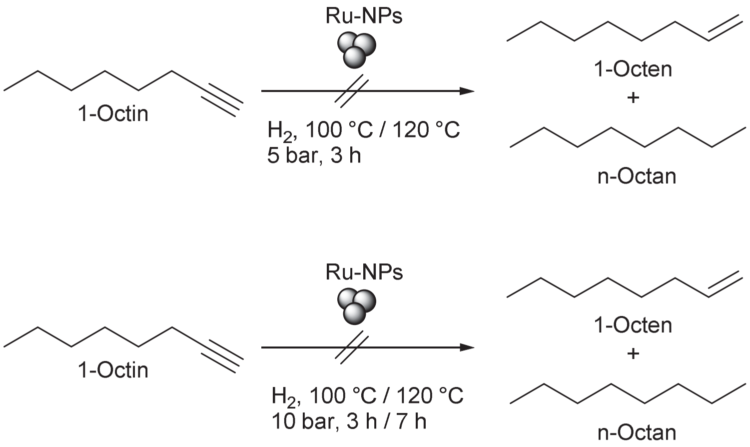

Schema 4.2.2.2: Veränderung der Reaktionsbedingungen für die Hydrierung von 1-Octin zu n-Octan mit Ru-NPs in [BMIm][BF_4].

Die Veränderung von Temperatur, Druck und Verlängerung der Reaktionszeit führte zu keinem Erfolg, sodass der Reaktionsdruck noch einmal auf 20 bar erhöht wurde, während die Badtemperatur bei 120 °C gehalten und die Reaktionszeit auf 7 h verlängert wurde. Durch die Druckerhöhung konnte ein H_2-Verbrauch während der Reaktion beobachtet werden und die Katalyse für 7 h und 3 Zyklen durchgeführt werden. Abb. 4.2.2.1 zeigt den Katalysefortschritt über die H_2-Aufnahme.

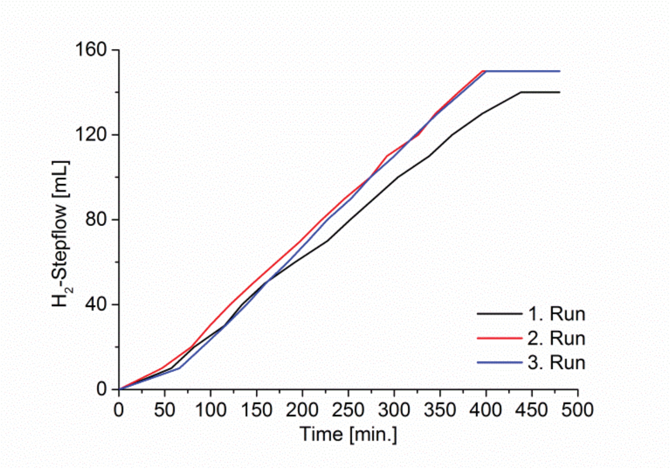

Abb. 4.2.2.1: H_2-Aufnahme in Abhängigkeit der Zeit für 3 Katalysezyklen der Hydrierung von 1-Octin zu n-Octan bzw. 1-Octen, katalysiert durch Ru-NPs in [BMIm][BF_4].

Nach jedem Katalysezyklus wurde das entstandene Produkt in eine Kühlfalle im HV bei 40 °C überführt, so vom Katalysator getrennt und mittels GC vermessen.

Für die weiteren Katalysezyklen wurde jeweils neues Substrat auf den Katalysator gegeben und die Hydrierung gestartet. Tab. 4.2.2.1 zeigt den Umsatz sowie die Produktselektivität für die Hydrierung über 3 Zyklen.

Tab. 4.2.2.1: Umsätze und Selektivität der Hydrierung von 1-Octin zu 1-Octen bzw. n-Octan, katalysiert durch Ru-NPs in [BMIm][BF_4].

Zyklus	**Katalysator**	**Edukt**	**Produkt 1**	**Produkt 2**	**Umsatz [%]**	**Alken-Selektivität [%]**	**TOF[a] [h^{-1}]**
1	Ru-NPs	1-Octin	1-Octen	n-Octan	36	45	31
2	Ru-NPs	1-Octin	1-Octen	n-Octan	23	57	19
3	Ru-NPs	1-Octin	1-Octen	n-Octan	26	61	25

[a] Turn over frequency (TOF) = mol (Produkt) x (mol Ru)$^{-1}$ x h^{-1}

Für alle drei Zyklen ist bei der H_2-Aufnahme bis ca. 60 min. ist eine Induktionszeit zu beobachten. Danach steigt der Kurvenverlauf in Abhängigkeit der Zeit stetig an, bis er bei ca. 460 min. für den ersten Zyklus und bei ca. 390 min. für die Zyklen 2 und 3 ein Plateau erreicht und die Reaktion beendet ist. Es lässt sich vermuten, dass der Katalysator innerhalb der Induktionszeit „aktiviert“ wird und die Reaktion anschließend von Zyklus zu Zyklus in kürzerer Zeit mit höherer Aktivität abläuft. Dabei sind die Umsatzraten vergleichsweise ähnlich (siehe Tab. 4.2.2.1), allerdings steigen die Alkenselektivitäten von Zyklus zu Zyklus an. Eine hohe Alkenselektivität bis zu 99% für 1-Octen ist ebenfalls von Niu *et al.* für die Semihydrierung von Alkinen zu Alkenen mit Poly(ethylen-glycol) (PEG_{2000})-stabilisierten (Ru-NPs beobachtet worden [30]. Allerdings wurden dort Umsätze bis zu 100% unter ähnlichen Reaktionsbedingungen erzielt. Der hier vorliegende deutlich geringere Umsatz könnte sich damit erklären lassen, dass die Ru-NPs direkt in der IL-Suspension für die Katalyse eingesetzt wurden und nicht als vorher gefällte Partikel. Die Stabilisierung von Nanopartikeln durch ILs erfolgt zwar über schwach koordinierende Wechselwirkungen, welche die Oberflächeneigenschaften der Nanopartikel erhalten sollen im Vergleich zur Stabilisierung mit klassischen Stabilisatoren (hier auch Vgl. zu Abschnitt 1.1). Dennoch wäre eine Diffusionsbarriere zwischen den Nanopartikeln und dem Substrat durch die IL möglich, welche eine vollständige Katalyse und das „Durchhydrieren“ zum n-Octan verhindert.

Für die sich anschließende Semihydrierung mit dem durch Sn „vergifteten“ Ru-Katalysator wurden die Ru_2Sn-Nanopartikel in [BMIm][BF_4] eingesetzt (vollständige Charakterisierung der Ru_2Sn-NPs erfolgte in Abschnitt 3.2).

Die mittels Mikrowellenstrahlung bei 220 °C und 50 W für 15 min. synthetisierten Nanopartikel wurden ebenfalls in der IL-Suspension in einem Verhältnis von 1:837 (bezogen auf Ru) mit dem Substrat 1-Octin eingesetzt und die Katalyse nach nachfolgendem Schema 4.2.2.3 durchgeführt.

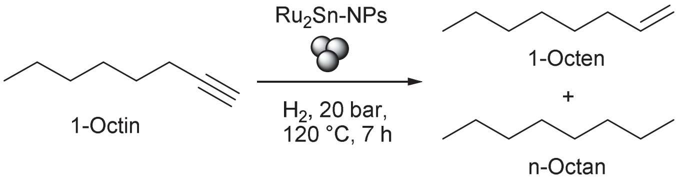

Schema 4.2.2.3: Hydrierung von 1-Octin zu 1-Octen bzw. n-Octan mit Ru_2Sn-NPs in [BMIm][BF_4].

Auch für diese Hydrierung lässt sich der Katalysefortschritt mittels H_2-Aufnahme nachverfolgen (Abb. 4.2.2.2).

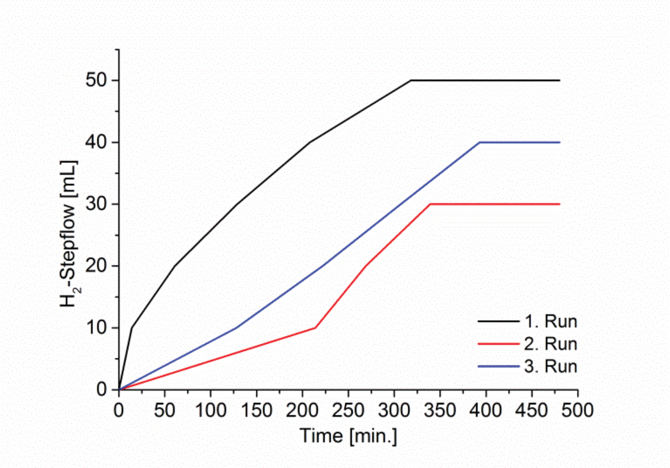

Abb. 4.2.2.2: H_2-Aufnahme in Abhängigkeit der Zeit für 3 Katalysezyklen der Hydrierung von 1-Octin zu 1-Octen bzw. n-Octan, katalysiert durch Ru_2Sn-NPs in [BMIm][BF_4].

Nach Überführen des Produktes in eine Kühlfalle bei 40 °C im HV, wurde erneut 1-Octin zu den Ru_2Sn-NPs gegeben und weitere Katalysezyklen durchgeführt. Die Umsätze und Alkenselektivitäten der drei Katalysezyklen sind Tab. 4.2.2.2 zu entnehmen.

Tab. 4.2.2.2: Umsätze und Selektivität der Hydrierung von 1-Octin zu 1-Octen bzw. n-Octan, katalysiert durch Ru-NPs in [BMIm][BF_4].

Zyklus	Katalysator	Edukt	Produkt 1	Produkt 2	Umsatz [%]	Alken-Selektivität [%]	TOF[a] [h^{-1}]
1	Ru_2Sn -NPs	1-Octin	1-Octen	n-Octan	7	32	3
2	Ru_2Sn -NPs	1-Octin	1-Octen	n-Octan	7	32	3
3	Ru_2Sn -NPs	1-Octin	1-Octen	n-Octan	7	49	4

[a] Turn over frequency (TOF) = mol (Produkt) x (mol Ru)$^{-1}$ x h^{-1}

Werden die H_2-Aufnahme und die Umsätze bzw. Alkenselektivitäten miteinander verglichen, wird deutlich, dass der Fehler bei der sehr geringen H_2-Aufnahmemenge sehr hoch sein muss. Es müsste für den ersten und zweiten Zyklus eine ähnliche H_2-Aufnahmemenge erkennbar sein, da die Alkenselektivitäten gleich hoch sind. Außerdem dürfte die Induktionsphase des zweiten Zyklus mit über 200 min. nicht so deutlich von den Induktionsphasen des ersten und dritten Zyklus abweichen. Der H_2-Verbrauch während der Hydrierungszyklen kann demnach nicht zum Vergleich herangezogen werden.

Vergleicht man die Umsätze und Alkenselektivitäten zwischen der Ru-NPs katalysierten Hydrierung (Tab. 4.2.2.1) und der Ru_2Sn-NPs katalysierten Hydrierung (Tab. 4.2.2.2), lässt sich dort keine genaue Aussage treffen, inwieweit die „Vergiftung“ des Katalysators durch Sn einen Einfluss auf die Umsätze bzw. Alkenselektivität der Reaktion hat. Da die Alkenselektivitäten bei beiden Katalysatoren in einem ähnlichen Bereich liegen, der Umsatz bei der, durch Ru_2Sn katalysierten, Hydrierung allerdings deutlich niedriger ist, besteht die Annahme, dass dies an der „Vergiftung“ des Katalysators durch Sn liegt. Allerdings könnten die niedrigen Umsätze auch durch die Diffusionsbarriere zwischen den Ru_2Sn-NPs und dem Substrat durch die IL begründet sein, so wie im Fall der Ru-NPs. Zu erwarten wäre für eine „Vergiftung“ des Systems durch Sn eine deutlich höhere Alkenselektivität im Vergleich zu einer Ru-NPs katalysierten Reaktion. Da für diese Hydrierungsreaktionen allerdings bei beiden Katalysatoren das Semihydrierungsprodukt 1-Octen entstanden ist und die Alkenselektivitäten ähnlich hoch sind, lässt sich keine Aussage darüber treffen, inwieweit die „Vergiftung“ durch Sn Einfluss auf die bevorzugte Bildung des Alkens 1-Octen nimmt.

4.3 Darstellung von Ru/Rh/Sn Nanopartikeln aus einem heterotrimetallischen (cod)Rh-Stannol-RuCp* Triple-Decker Komplex

Der folgende Abschnitt beinhaltet die Ergebnisse der Darstellung von Ru/Rh/Sn Nanopartikeln aus einem heterotrimetallischen (cod)Rh-Stannol-RuCp* Triple-Decker Komplex und entstand in Kooperation mit Prof. Dr. Masaichi Saito. Sowohl die hier vorliegenden Ergebnisse als auch der Triple-Decker Komplex sind unveröffentlicht.

Die Ergebnisse stehen mit eigenem Quellenverzeichnis für sich.

Anteil an den Ergebnissen:

- Synthese und Charakterisierung der Ru/Rh/Sn Nanopartikel.
- Konzipierung und Schreiben der Ergebnisse sowie zugehörige Literaturrecherche.
- Der heterotrimetallische (cod)Rh-Stannol-RuCp* Triple-Decker Komplex wurde von Herrn Prof. Dr. Masaichi Saito synthetisiert und zur Verfügung gestellt.
- Die TEM-, STEM- und SAED-Aufnahmen wurden mit der Unterstützung von Herrn Dr. Juri Barthel und Herrn Dr. Markus Heidelmann aufgenommen.
- Die Auswertung der STEM- und SAED-Aufnahmen erfolgte zum Teil über Herrn Dr. Juri Barthel.
- Die Korrekturen der Ergebnisse erfolgten über Herrn Prof. Dr. Christoph Janiak, ebenso wie die Koordination zwischen den Co-Autoren.

Metal nanoparticle results for (cod)Rh-stannole-RuCp* heterotrimetallic triple-decker complex

Susann Wegner,[a] Juri Barthel,[b] Christoph Janiak[a]
[a] Institut für Anorganische Chemie und Strukturchemie, Heinrich-Heine Universität Düsseldorf, Universitätsstr. 1, 40225 Düsseldorf, Germany.
Email: susann.wegner@hhu.de, janiak@hhu.de
[b] Gemeinschaftslabor für Elektronenmikroskopie RWTH-Aachen, Ernst Ruska-Centrum für Mikroskopie und Spektroskopie mit Elektronen D-52425 Jülich, Germany
Email: Ju.Barthel@fz-juelich.de

Introduction

In recent years, tin and its intermetallic compounds have gained increasing importance for industry and technology [1]. The application of these compounds is manifold and is reflected e.g. in the production of bronzes, superconductors and tinplate packaging [1].

Especially intermetallic phases with Ru, Rh with different phase compositions are frequent. Phases with different proportions of Rh and Sn are possible for the RhSn intermetallic phase [2]. Thus "Rh_3Sn_2" can be present in a composition range of 41 wt% Sn/59 wt% Rh (0.376 mol% Sn/ 0.624 mol% Rh) to 44 wt% Sn/56 wt% Rh (0.405 mol% Sn/ 0.594 mol% Rh) [3] or RhSn in a composition range of 56 wt% Sn/44 wt% Rh (0.524 mol% Sn/ 0.476 mol Rh) to 59 wt% Sn/41 wt% Rh (0.555 mol% Sn/ 0.445 mol% Rh) for Sn [4]. The metal composition changes with increasing temperature so that intermetallic phases like RhSn (475 °C) [5], $RhSn_2$ (temperatures above 500 °C) [6] and $RhSn_4$ (temperatures between 725 and 750 °C) could be obtained [7].

Intermetallic Ru/Sn alloys are also known and widely used as catalysts [8-11]. For the Ru/Sn system phases like Ru_2Sn_3 [12], $RuSn_2$ [12] und Ru_3Sn_7 [13] could be obtained. The phase Ru_3Sn_7 is found to be the most stable compound in the Ru-Sn system and to be in equilibrium with Sn [12].

For molecular trimetallic systems organometallic and coordination complexes with Pt/Ir/Sn [14], Ru_5PtSn [15] and Pt/Ru/Co [16] are known. Trimetallic complexes with Ru/Rh/Sn have not been reported yet.

Here we describe the use of the single-source triple-decker (cod)Rh-stannole-RuCp* bearing a stannole ligand as metal-organic precursors for the attempted synthesis of bi- or trimetallic rhodium-ruthenium-tin nanoparticles in the ionic liquids 1-butyl-3-methylimidazolium tetrafluoroborate ([BMIm][BF_4]) or 1-butyl-3-methylimidazolium bis(trifluoromethanesulfonyl)imide ([BMIm][NTf_2]) (Scheme 1).

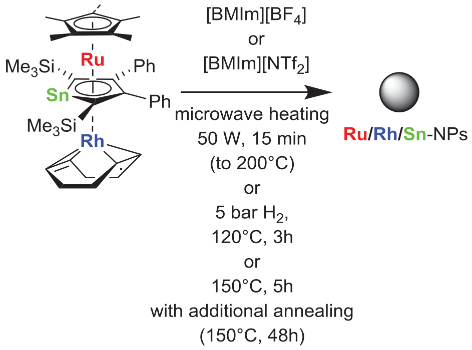

[BMIm][BF$_4$] = 1-*n*-butyl-3-methyl imidazolium tetrafluoroborate
[BMIm][NTf$_2$] = 1-*n*-butyl-3-methyl-imidazolium bis(trifluoromethanesulfonyl)imide

Scheme 1: Microwave-heating assisted thermal decomposition or hydrogenation-assisted thermal decomposition of the (cod)Rh-stannole-RuCp* heterotrimetallic triple-decker complex to intended trimetallic Ru/Rh/Sn-NPs in the ionic liquids [BMIm][BF$_4$] and [BMIm][NTf$_2$].

The precursor was given to us from the research group of Prof. M. Saito (Department of Chemistry, Graduate School of Science and Engineering, Saitama University, Shimo-okubo, Sakura-ku, Saitama 338-8570, Japan).

Experimental part

Materials and methods

All experimental manipulations were performed under an inert nitrogen or argon atmosphere by using standard Schlenk line and glove-box techniques.

The ionic liquid [BMIm][BF$_4$] was synthesized by treating 1-methylimidazole with 1-chlorobutane to yield first [BMIm][Cl] which was further reacted with HBF$_4$ to give [BMIm][BF$_4$] [13]. The IL [BMIm][NTf$_2$] was synthesized by treating 1-methylimidazole with 1-chlorobutane to yield first [BMIm][Cl] which was further reacted with lithium bis(trifluoromethansulfonyl)imide (Li(NTf$_2$)) to give [BMIm][NTf$_2$] [17].
Both ILs were dried under high vacuum (10^{-7} mbar) at 80°C for several days.
Quantitative anion exchange and, thus, IL anion purity of >99% was assessed by ion chromatography for [BMIm][BF$_4$] and >98% for [BMIm][NTf$_2$] (Dionex ICS-1100, with IonPac® AS14, 4 x 250 mm column). Water content was measured by coulometric Karl-Fischer titration (ECH/Analytik Jena AQUA 40.00) to below 10 ppm for [BMIm][BF$_4$] and below 30 ppm for [BMIm][NTf$_2$].

Transmission electron microscopy (TEM) and scanning transmission electron microscope (STEM) images were taken on a FEI Tecnai G20 (FZ Jülich) and on a JEOL JEM-2200FS (ICAN University Duisburg-Essen) operating at an accelerating voltage of 200 kV. Samples were prepared using 200 mm carbon-coated gold grids. A drop of the nanoparticle suspension obtained through microwave heating or hydrogenation-assisted thermal decomposition was placed on the carbon-coated gold grid. After immobilization, the grid was washed three times with 2 mL acetonitrile each to remove excess residues of the IL. Thereafter the grid was dried under vacuum and stored under inert conditions until TEM measurement. The size distribution was determined from a minimum of 50 nanoparticles. Energy dispersive X-ray (EDX) spectra were obtained on a FEI Tecnai f20 (FZ Jülich), at 136 kV; the exposure time for individual EDX spectra was 3 min, respectively 9 min for STEM measurements and on a SDD X-MaxN 80 with TLE detector (Interdisciplinary Center for Analytics on the Nanoscale (ICAN, University Duisburg-Essen) with the same parameters.

List of used *k*-factors:

	k (K-lines)	k (L-lines)
Ru	5.245	2.597
Rh	5.739	2.573
Sn	10.461	2.653

Nanoparticle Synthesis

The precursor (see Scheme 1) was suspended for 24 h under argon atmosphere (in a glove box) at room temperature in the ILs [BMIm][BF$_4$] and [BMIm][NTf$_2$]. To obtain a 1 wt% in total metal dispersion (Ru+Rh+Sn), a portion of 5 mg (0.005 mmol, M_W = 998.881 g/mol for $C_{46}H_{67}RhRuSi_2Sn$) was combined with 0.16 g of [BMIm][BF$_4$] or [BMIm][NTf$_2$].

The two mixtures were placed in vials in a microwave (CEM, Discover) and were thermally decomposed by microwave heating for 15 min at a power of 50 W reaching a temperature of 220 °C.

Two other mixtures of the precursor in [BMIm][BF$_4$] or [BMIm][NTf$_2$] were placed in a glass autoclave (Büchi miniclave) and the N_2 atmosphere was replaced by H_2. The autoclave was heated to 120 °C, charged with 5 bar H_2 and stirred (900 rpm) for 3 hours.

From the amount available for each decomposition experiment of the (cod)Rh-stannole-RuCp* triple-decker complex precursor (5 mg) only a small metal mass (32 wt% combined for RuRhSn, 1.76 mg) could be transformed into prospective Ru/Rh/Sn metal nanoparticles. The possibilities of analysis with such a small amount were limited.

Results and discussion

Analysis of nanoparticles obtained from (cod)Rh-stannole-RuCp heterotrimetallic triple-decker precursor in the ILs [BMIm][BF$_4$] and [BMIm][NTf$_2$] through microwave heating (50 W, 15 min, 220 °C) or through hydrogenation-assisted thermal decomposition (5 bar H$_2$, 120 °C, 3 h)*

- TEM images and nanoparticle distribution

The nanoparticle/ionic liquid dispersions were primarily analyzed by TEM methods in view of the small quantities available. The nanoparticle size and size dispersions were obtained from TEM images which are given in Fig. 1 together with their histogram size analysis.

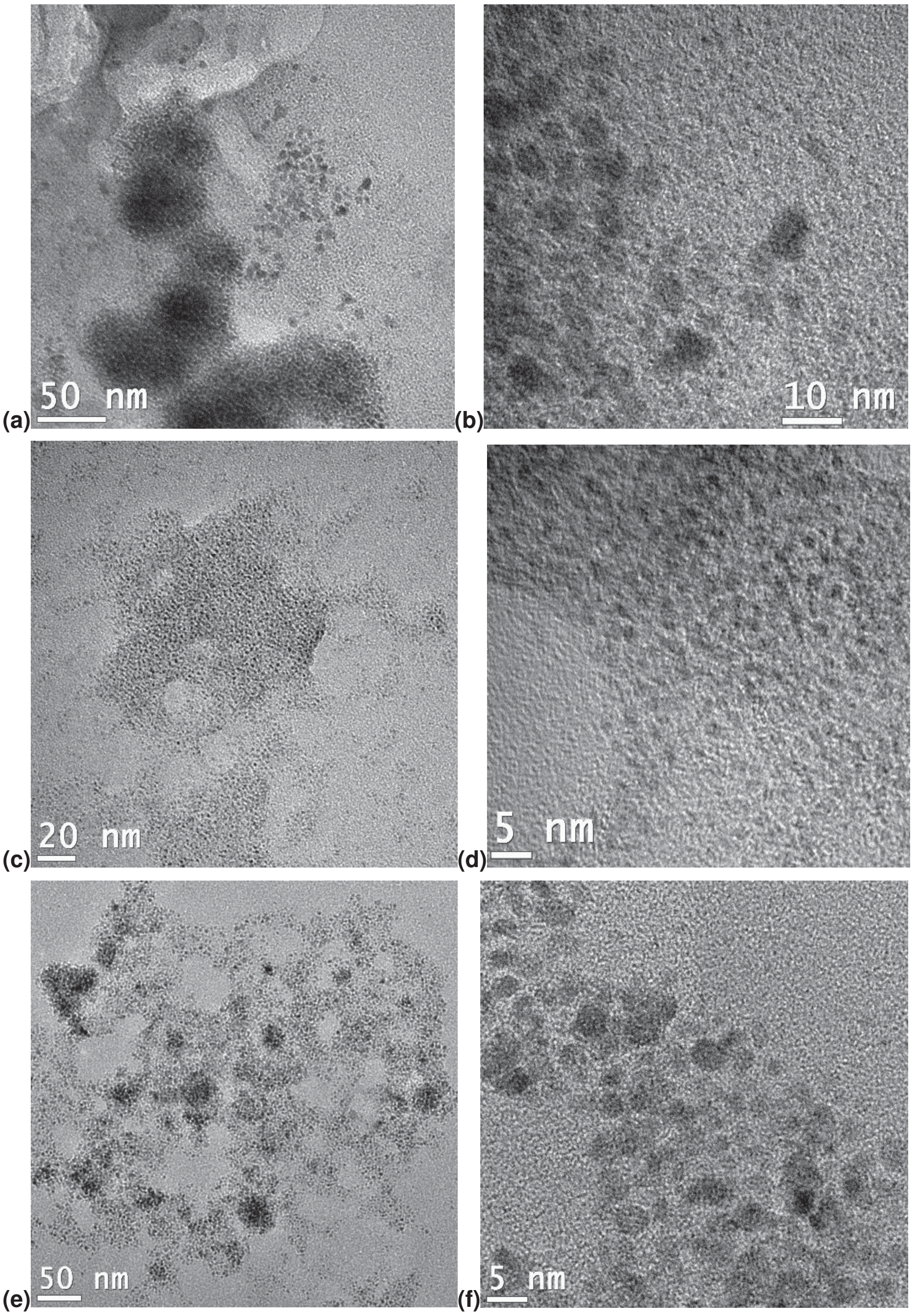

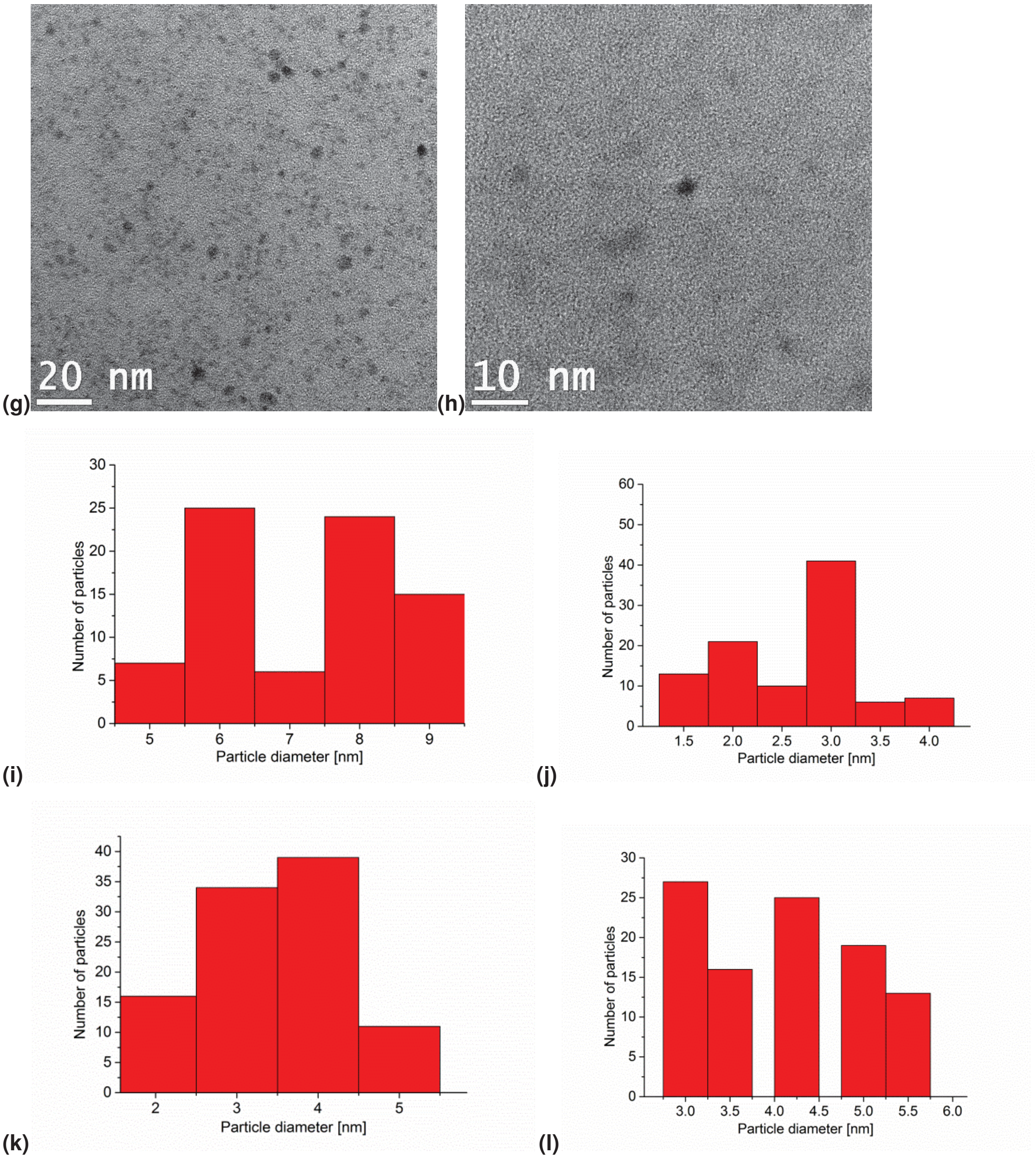

Fig. 1: TEM images of Rh/Ru/Sn-NPs in [BMIm][BF$_4$] ((a) and (b) with histogram (i)) and [BMIm][NTf$_2$] ((c) and (d) with histogram (j)) synthesized through microwave heating (50 W, 15 min, 220 °C). TEM images of Ru/Rh/Sn-NPs in [BMIm][BF$_4$] ((e) and (f) with histogram (k)) and [BMIm][NTf$_2$] ((g) and (h) with histogram (l)) synthesized through hydrogenation-assisted thermal decomposition (5 bar H_2, 120 °C, 3 h). (i)-(l) correspondent histograms of particle diameter measured on a minimum of 50 particles, each bar covers the range of ± 0.5 nm or 0.25 nm around its mid-point, respectively. TEM images were recorded on a FEI Tecnai G20 (FZ Jülich).

The TEM images in Fig. 1a-d show nanoparticles stabilized in [BMIm][BF$_4$] or [BMIm][NTf$_2$] and synthesized through microwave heating (50 W, 15 min., 220 °C) with a diameter from 5 to 9 nm (average 7 ± 2 nm in [BMIm][BF$_4$]) and from 1.5 to 4 nm (2.8 ± 0.9 nm in [BMIm][NTf$_2$]) (see also histogram of particle diameter (Fig. 1i and j)). The TEM images in Fig. 1e–h show nanoparticles synthesized through hydrogenation-assisted thermal decomposition (5 bar H_2, 120 °C, 3 h) with a diameter from 2 to 5 nm (3.5 ± 2 nm in [BMIm][BF$_4$]) and from 3 to 5.5 nm (4 ± 1 nm in [BMIm][NTf$_2$]) (see also histogram of particle diameter (Fig. 1k and l).

The nanoparticles, which were synthesized through microwave heating, appear more agglomerated while nanoparticles synthesized through hydrogenation-assisted thermal decomposition are better separated and less agglomerated. Nanoparticle size distribution shows a similar size ratio for both synthetic routes.

- Overview EDX and SAED analysis

The "macroscopic" nanoparticle element composition and phase analysis was based on energy-dispersive X-ray spectroscopy (EDX) and selected area electron diffraction (SAED) in combination with the TEM studies.

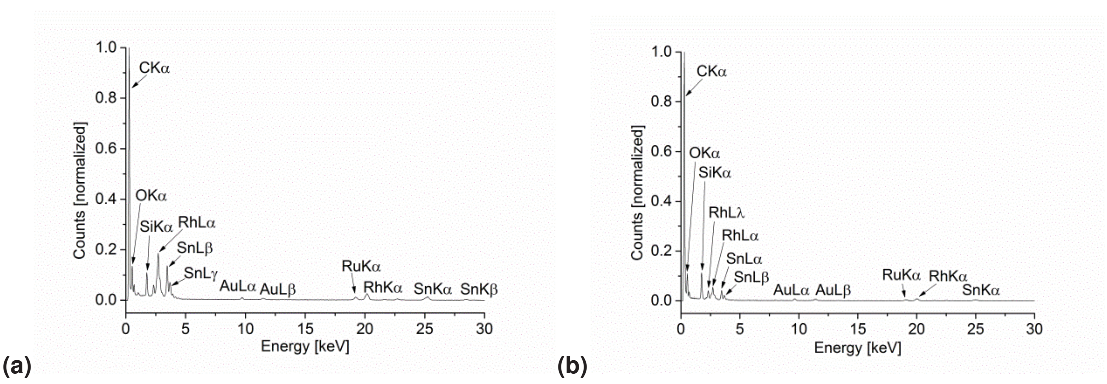

Fig. 2: EDX-spectra of nanoparticles in [BMIm][BF_4] (a) and [BMIm][NTf_2] (b) synthesized through microwave heating (50 W, 15 min., 220 °C). C and Au signals are due to the sample holder. EDX-spectra were recorded on the FEI Tecnai G20 (FZ Jülich).

The energy-dispersive X-ray spectrum (EDX) of the nanoparticles synthesized in [BMIm][BF_4] (Fig. 2a) shows all three metals in the nanoparticle suspension with a molar atom fraction of Ru, Rh and Sn as 15%:42%:43%. The EDX analysis is integrated over a large sample region and also a signal of silicon (Si) was found which is due to the precursor.

In both ILs (see Fig. 2b for [BMIm][NTf_2]) the metal ratio found by EDX matches nearly the average composition of "$Ru_{0.33}RhSn$". The 1:1 ratio of Rh and Sn is as given in the precursor. We note that the phases Rh_3Sn_2 and RhSn are the most stable Rh/Sn phases [34], while the most stable Ru/Sn phase is Ru_3Sn_7 [12].

Fig. 3 shows the SAED pattern of the nanoparticles synthesized in [BMIm][BF_4] and [BMIm][NTf_2] through hydrogenation-assisted thermal decomposition (5 bar H_2, 120 °C, 3h) together with the calculated diffraction rings of a cubic fcc crystal with lattice constant 4.19(5) Å which coincide with the observed nanoparticle reflections. The SAED patterns of the synthesized nanoparticles show reflections, which is a clear indication of crystallinity (Fig. 3). The crystallinity of the nanoparticles is also supported by the TEM close-view image in Fig. 1f, which shows the interference patterns within the particles. Interference patterns are only weakly recognizable due to the small size of the particles. The reflections in the SAED coincide with the lattice spacings of a face-centered cubic crystal packing, fcc. There are no additional diffraction rings, which could include a different phase than the fcc phase.

For the nanoparticles synthesized in [BMIm][NTf$_2$] the diffraction rings are rather broad, due to the very small size of the crystals (see Fig. 3c). The SAED pattern analysis of the nanoparticles in [BMIm][BF$_4$] (Fig. 3a) and [BMIm][NTf$_2$] (Fig. 3b,c) do not agree in the observed d-spacing for known bimetallic RuSn, RhRu or RhSn hcp or bcc phases. (Table 1)of the nanoparticles in [BMIm][BF$_4$].

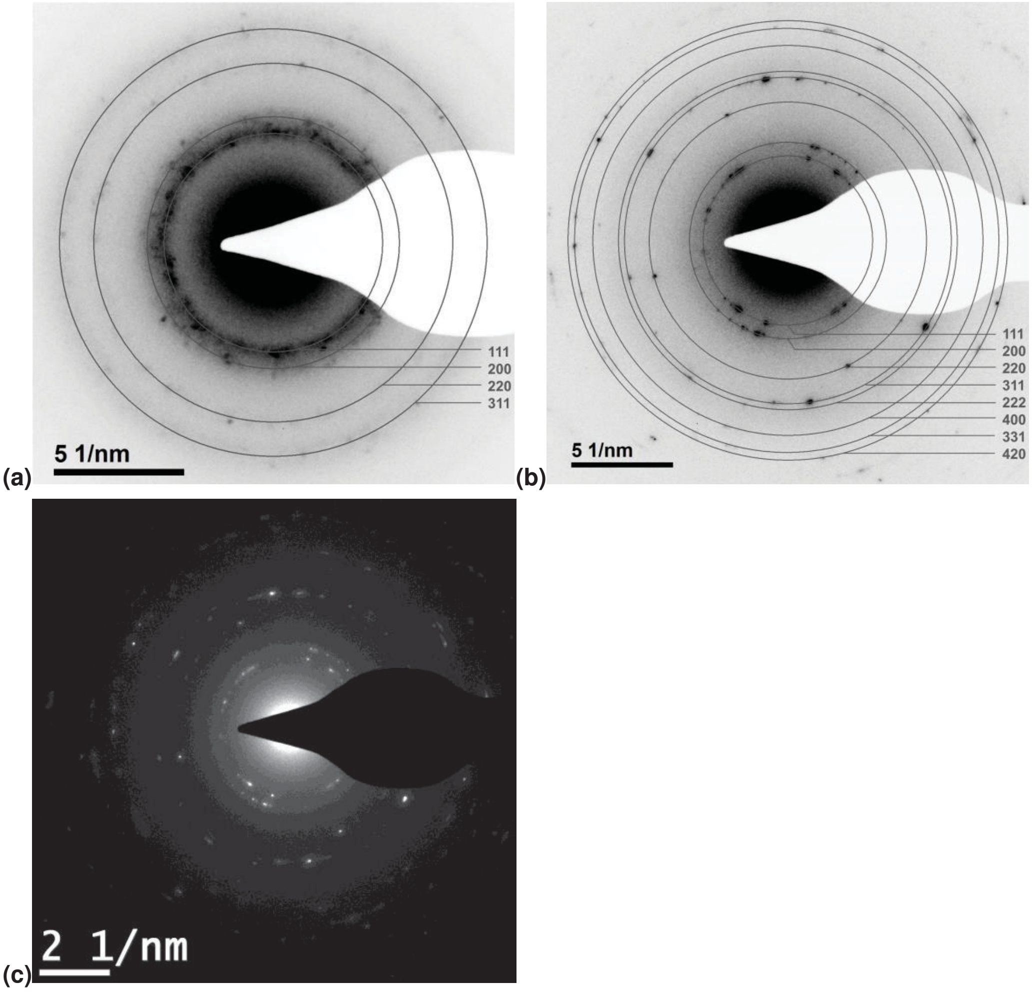

Fig. 3: Selected area diffraction pattern (SAED) pattern of the nanoparticles in (a) [BMIm][BF$_4$] and (b,c) [BMIm][NTf$_2$] synthesized through hydrogenation-assisted thermal decomposition (5 bar H_2, 120 °C, 3 h), superimposed with calculated diffraction rings of a simulated cubic fcc crystal with 4.19(5) Å lattice constant (and uni-atomic structure factor). SAED patterns of the nanoparticles were recorded on the FEI Tecnai G20 (FZ Jülich).

Table 1: Comparison of d-spacing from lattice spacings of synthesized nanoparticles and reference lattice spacings.

d-spacing measured (particles in [BMIm][BF$_4$]) [Å]	**d-spacing measured (particles in [BMIm][NTf$_2$]) [Å]**	**d-spacing (Ru_3Sn_7 (bcc)) [Å]**	**d-spacing (RhSn (bcc)) [Å]**	**d-spacing (RuRh (hcp)) [Å]**
1.56	1.55	2.20	2.29	2.06
1.34	1.39	2.49	2.09	1.14
0.93	0.84	2.70	1.37	1.35

- Small-range STEM-EDX analysis of the nanoparticles synthesized in [BMIm][BF$_4$] and [BMIm][NTf$_2$] through hydrogenation-assisted thermal decomposition (5 bar H$_2$, 120 °C, 3 h)

- in [BMIm][BF$_4$]

For analysis of the near-individual nanoparticle composition in [BMIm][BF$_4$] an EDX mapping over a small nanoparticle area was done (Fig. 4). The nanoparticle composition determined in this small area indicates mixed-metal nanoparticles. Qualitative analysis of the comparative L- and K-shells of three different metals (Ru-L, Rh-L, Sn-L and Ru-K, Rh-K and Sn-K) shows a superposition of three metals within the nanoparticles.

A rather approximate average composition of “Ru$_{0.1}$Rh$_{0.5}$Sn$_{0.4}$” (with an error for each element fraction of about ±0.1) is suggested from an area with sufficient particle concentration using the Cliff-Lorimer method for the respective K-Line intensities [18].

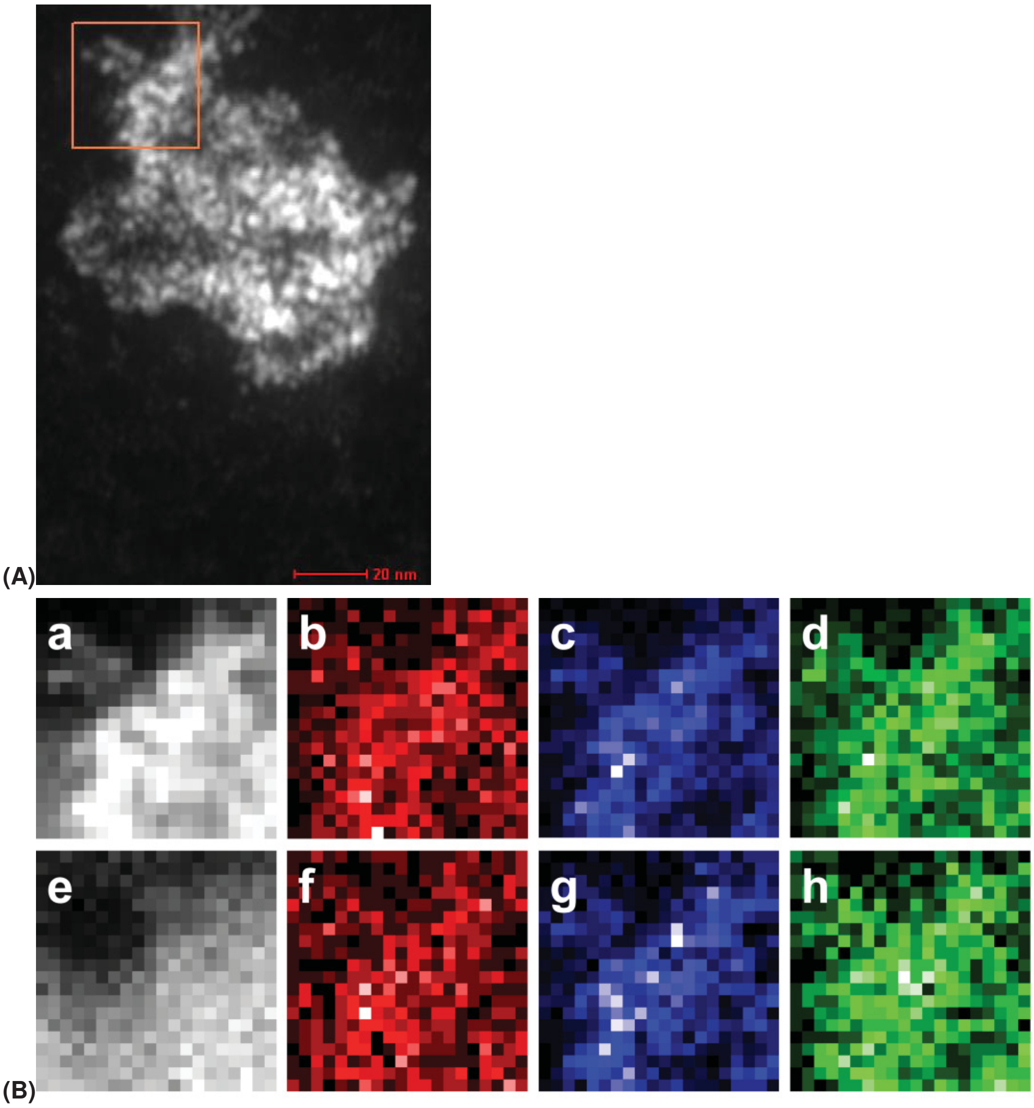

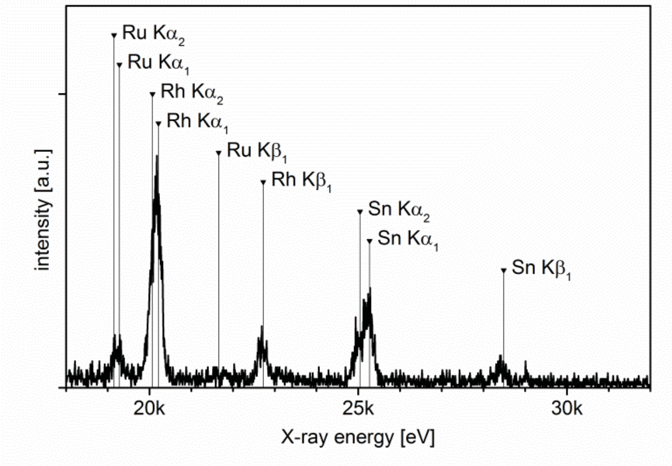

(C)

Fig. 4: (A) HAADF-STEM image with area for EDX mapping of Ru/Rh/Sn-NPs in [BMIm][BF$_4$] synthesized through hydrogenation-assisted thermal decomposition (5 bar H$_2$, 120 °C, 3 h) with individual nanoparticle composition analyzed from EDX mapping. (B) EDX element maps of a small sample area containing nanoparticles. (a) HAADF STEM image with white contrast indicates the presence of particles. (b), (c) and (d) are simultaneously recorded L$_\alpha$-line maps, while (f), (g) and (h) are K$_\alpha$-line maps of Ru (red), Rh (blue) and Sn (green), respectively. (e) Si-K$_\alpha$ map indicating an increasing Si contamination during the scanning acquisition from top to bottom. The width of the maps is 35 nm. Note that the intensity in the maps is not proportional to the element fraction. (C) Related EDX spectrum for K$_\alpha$-line maps of Ru, Rh and Sn. HAADF-STEM images and related EDX mapping were recorded on the FEI Tecnai G20 (FZ Jülich).

- in *[BMIm][NTf$_2$]*

For analysis of the nanoparticle composition in [BMIm][NTf$_2$] an EDX line scan over one larger nanoparticle was done (see Fig. 5). The element concentration measured on this nanoparticle indicates mixed-metal nanoparticles. Qualitative analysis of the comparative L- and K-shells of three different metals (Rh-L, Ru-L, Sn-L and Rh-K, Ru-K and Sn-K) shows a superposition of the three metals in this nanoparticle. For comparison, a HAADF figure has been added which only shows the contrast of the scanned particle (Fig. 5a).

A rather approximate average composition of “$Ru_{0.1}Rh_{0.75}Sn_{0.25}$” (with an error for each element fraction of about ±0.2) is suggested from an area with sufficient particle concentration using the Cliff-Lorimer method for the respective K-Line intensities [18].

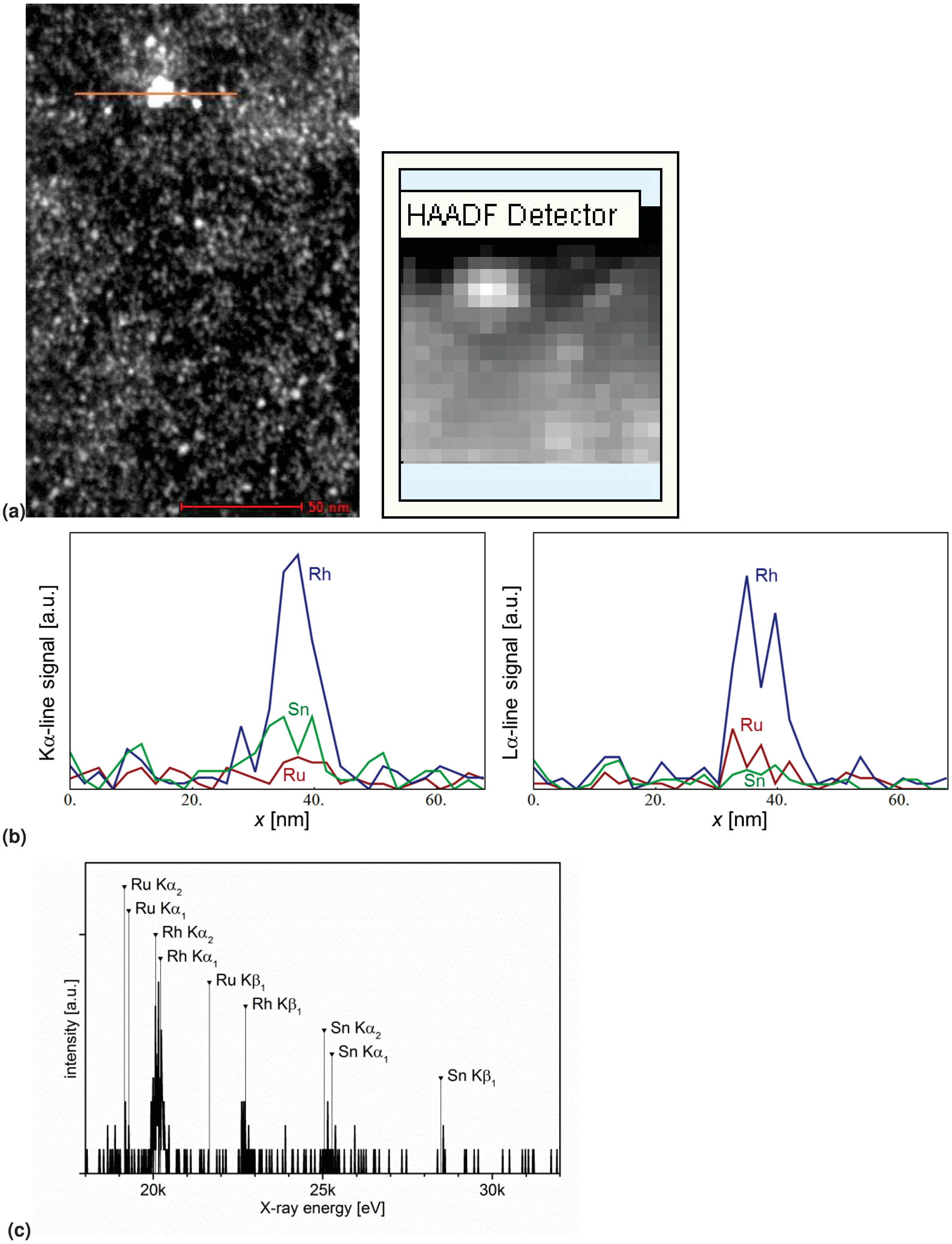

Fig. 5: (a) STEM image with line-scan for EDX mapping indicated for Ru/Rh/Sn-NPs in [BMIm][NTf$_2$] synthesized through hydrogenation-assisted thermal decomposition (5 bar H_2, 120 °C, 3 h) with correspondent HAADF figure. (b) Profiles of the X-ray K_α-line (left) and L_α-line (right) emission signals of Ru (red), Rh (blue) and Sn (green) recorded while scanning the electron probe over a particle of ca. 15 nm diameter. The profile intensities have been scaled to reflect approximately the relative concentration of the three metal components in the electron beam path. (c) Related EDX spectrum for the evaluation of K_α-line maps of Ru, Rh and Sn. STEM image and line-scan of EDX mapping were recorded on FEI Tecnai G20 (FZ Jülich).

Analysis of nanoparticles obtained from (cod)Rh-stannole-RuCp heterotrimetallic triple-decker precursor in the IL [BMIm][NTf$_2$] synthesized through hydrogenation-assisted thermal decomposition (5 bar H$_2$, 150 °C, 5 h) with additional annealing; 150 °C, 48 h)*

In an attempt to increase the very small nanoparticle sized for an clearer EDX elemental composition analysis on larger nanoparticles the nanoparticles were tried to grow by annealing at 150 °C for 48 h following their synthesis. Different from the expectation the size of the metal nanoparticles did not increase but decreased, as shown by their TEM images and histogram evaluation (Fig. 6a,c; compare to Fig. 1(l)).

- TEM images and EDX analysis

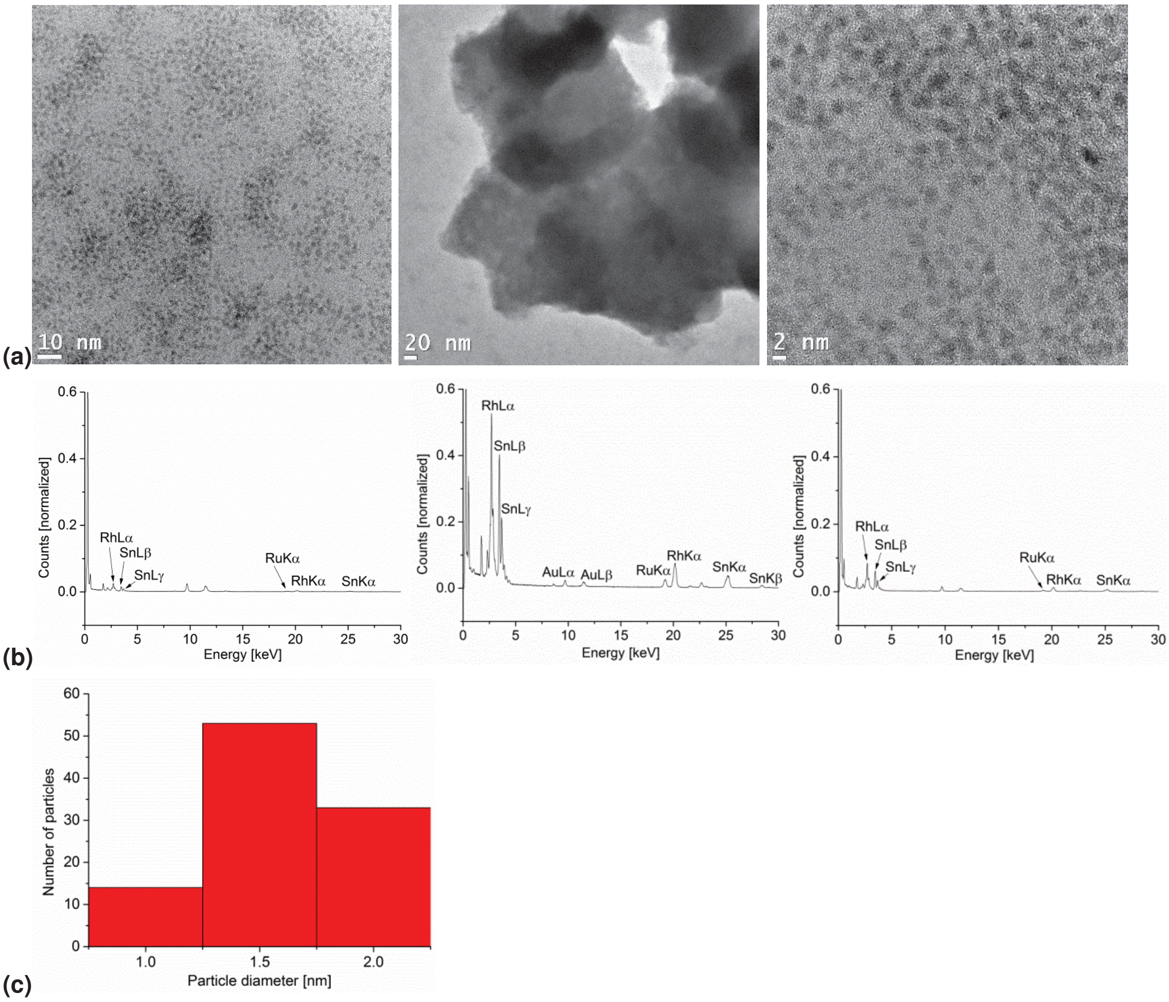

Fig. 6: TEM images of Ru/Rh/Sn nanoparticles in [BMIm][NTf$_2$] (a) synthesized trough hydrogenation-assisted thermal decomposition (5 bar, 150 °C, 5 h) with additional annealing (150 °C, 48 h) and (b) (top to bottom) corresponding EDX-spectra of the nanoparticles. (c) correspondent histogram of particle diameter measured on 100 particles, each bar covers the range of ± 0.25 nm. TEM images and EDX-spectra were recorded on FEI Tecnai G20 (FZ Jülich).

The energy-dispersive X-ray spectra (EDX) of the annealed nanoparticles synthesized in [BMIm][NTf$_2$] (Fig. 6b) show all three metals in the nanoparticle suspension (Table 2). The

EDX analysis is approximately integrated over the sample region shown in the corresponding TEM images (Fig. 6a). The metal ratio found by EDX matches nearly the average composition of "$Ru_{0.33}RhSn$". The 1:1 ratio of Rh and Sn is as given in the precursor. The ratio of Rh:Sn of ~1:1 and of Ru:Sn of ~1:3 agrees with the finding of Rh_3Sn_2 and RhSn as the most stable Rh/Sn phases [34], while the most stable Ru/Sn phase is Ru_3Sn_7 [12].

Table 2: EDX-quantification with the molar atom fraction.

EDX-quantification	Ru [K-shell]	Rh [K-shell]	Sn [K-shell]
EDX 1	0.13	0.43	0.44
EDX 2	0.12	0.44	0.44
EDX 3	0.13	0.45	0.42

Furthermore a localized point-EDX-spectrum was measured for a more accurate analysis of an individual nanoparticle composition (Fig. 7).

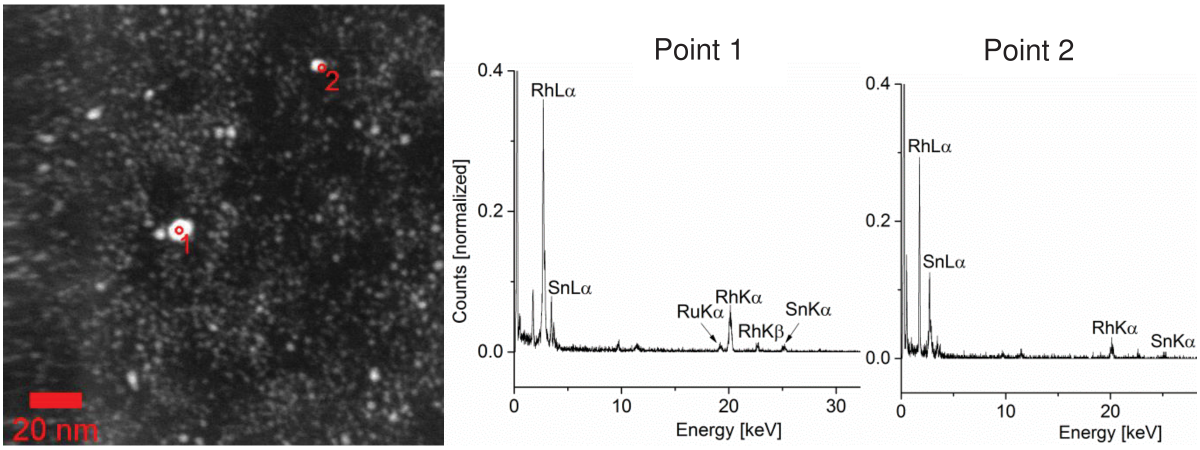

Fig. 7: HAADF-STEM image and point-EDX-spectra of an accumulation of several Ru/Rh/Sn nanoparticles. HAADF-STEM image and EDX-spectra were recorded on the FEI Tecnai G20 (FZ Jülich).

Measurement of a point-EDX-spectrum is only possible over an accumulation of several nanoparticles due to the nanoparticle size of 1-2 nm.

The metal ratio found at point 1 corresponds to the average composition of "$Ru_{0.08}Rh_{0.77}Sn_{0.15}$" and at point 2 to the average composition of "$Rh_{0.8}Sn_{0.2}$".

Further point-EDX-spectra show similar results (Fig. 8a, b). The metal ratio found by point-EDX-spectra given in Fig. 8a, b correspond to an average composition of "$Ru_{0.024}$ $Rh_{0.91}Sn_{0.067}$" (Fig. 8a) and "$Ru_{0.024}Rh_{0.88}Sn_{0.098}$" (Fig. 8b).

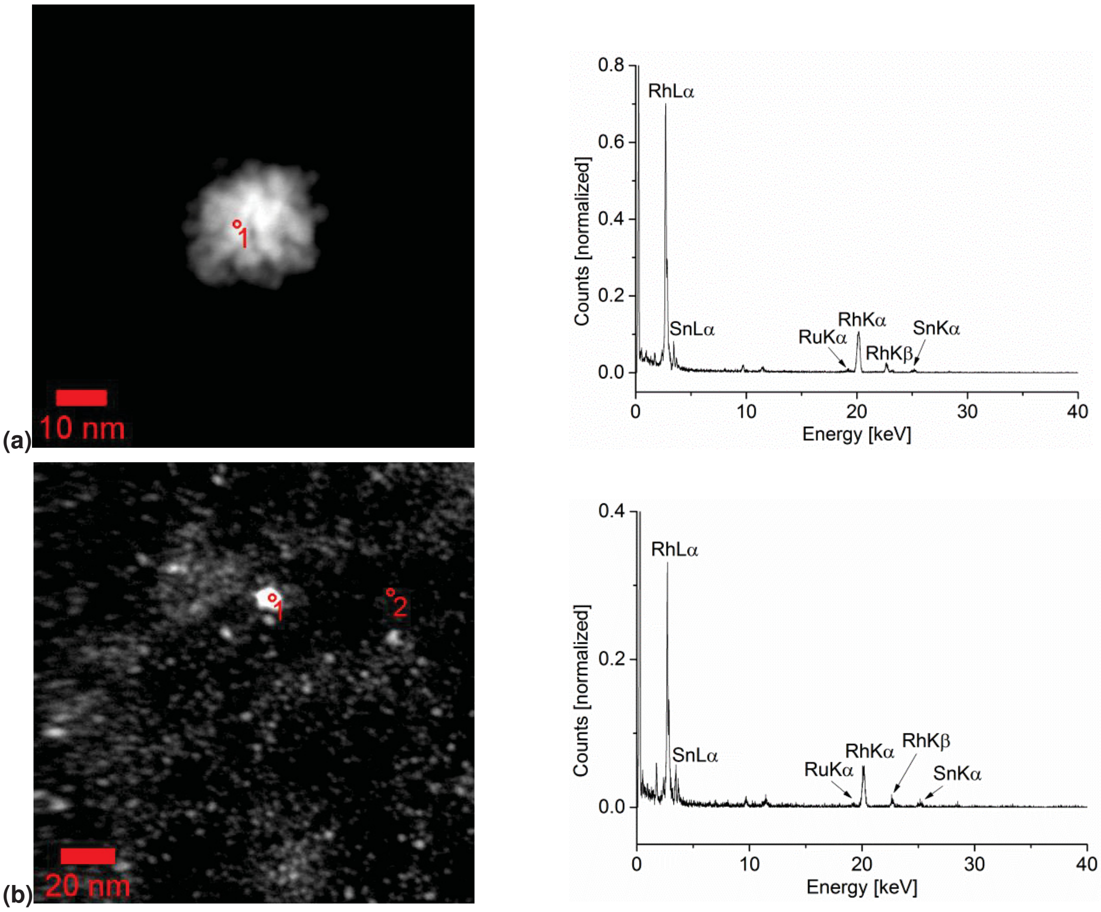

Fig. 8: HAADF-STEM images and point-EDX-spectra (a,b) of an accumulation of several Ru/Rh/Sn nanoparticles. HAADF-STEM images (left) and EDX-spectra (right) were recorded on FEI Tecnai G20 (FZ Jülich).

An additional EDX mapping was done on a SDD X-MaxN 80 with TLE detector (ICAN University Duisburg-Essen) (Fig. 9a, b).

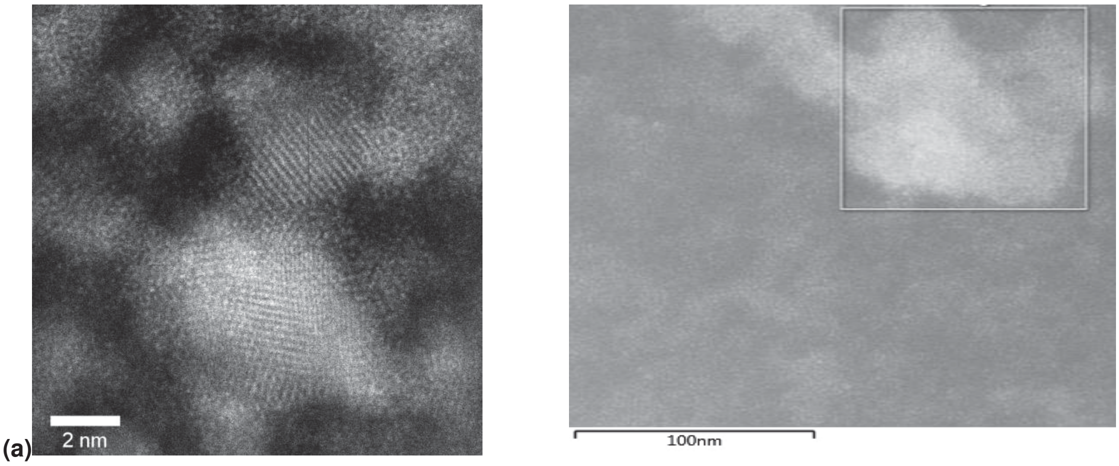

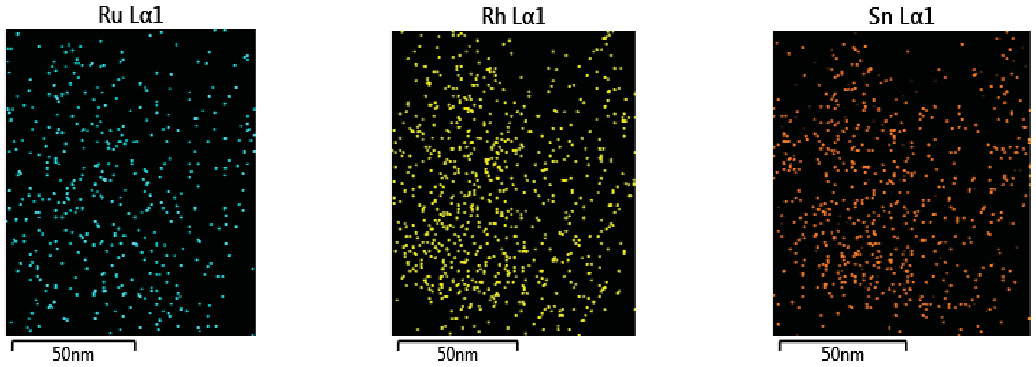

(b)

Fig. 9: (a): HR-TEM image of the Rh/Ru/Sn nanoparticles (left) and HAADF-STEM image corresponding to EDX mapping (right). (b): EDX mapping (qualitative) for the HAADF-STEM image area (a, right). HR-TEM image, HAADF-STEM image and EDX mapping were recorded on SDD X-MaxN 80 with TLE detector (ICAN, University Duisburg-Essen).

Qualitative analysis of the comparative L- shells of the three different metals (Ru-L, Rh-L Sn-L) shows a superposition of three metals within the nanoparticles with an average composition of "$Ru_{0.2}Rh_{0.6}Sn_{0.6}$". This ratio is identical to the "$Ru_{0.33}RhSn$" ratios obtained from the above EDX analyses on larger sample areas (cf. Fig. 2 and Fig. 6).

Conclusion

We described here the decomposition of a new heterotrimetallic (cod)Rh-stannole-RuCp* precursor (Scheme 1) to Rh/Ru/Sn nanoparticles in two different synthetic routes in the ionic liquids ([BMIm][BF_4] and [BMIm][NTf_2]) and without any other stabilizing agents. Route 1 had the precursor dispersed in [BMIm][BF_4] or [BMIm][NTf_2], respectively, and decomposed with microwave-induced heating. In route 2, the precursor was decomposed through hydrogenation-assisted thermal decomposition (5 bar H_2, 120 °C, 3 h) without and with additional annealing (150 °C, 48 h).

With both synthetic routes, similar results could be obtained for the synthesis of Rh/Ru/Sn nanoparticles. The nanoparticles were agglomerated and small (2-7 nm for decomposition through microwave induced heating and hydrogenation-assisted thermal decomposition without additional annealing and 1-2 nm for hydrogenation-assisted thermal decomposition with additional annealing).

The obtained nanoparticles appear to contain all three metals but the proportion of Ru was consistently the lowest.

SAED analysis showed that the nanoparticles reflections coincide with diffraction rings of a cubic fcc crystal. EDX mapping analysis showed commonly a composition of the metals Rh and Sn, frequently in a 1:1 ratio as given in the precursor, but also with a lower share of Sn.

RhSn compounds with cubic fcc structure are known. EDX-mapping on larger sample areas agreed on the composition "$Ru_{0.33}RhSn$" while EDX on smaller sample section gave "$Ru_{0.1}Rh_{0.75}Sn_{0.25}$" (line-scan)or "$Ru_{0.08}Rh_{0.77}Sn_{0.15}$" to "$Rh_{>0.8}Sn_{<0.2}$". (We note that the suggested element compositions of the nanoparticles are still approximate and qualitative with error margins of ± 0.2 for each element.).

In summary decomposition of the heterotrimetallic (cod)Rh-stannole-RuCp* precursor in ionic liquids leads to small metal nanoparticles with a small amount containing all three metals. For the most part, the nanoparticles consist, however, of Rh-richt Rh/Sn nanoparticles.
In other words it can also be assumed, that the obtained nanoparticles are RhSn-nanoparticles in a mixture with a small amount of RhRuSn nanoparticles and Ru nanoparticles.

From the precursor structure it is conceivable that the Rh(cod) moiety with the weakly bound cod ligand is most easily decomposed to Rh metal which explains the observed Rh-rich phases. Cyclooctadiene (cod) can generally be regarded as a good leaving group. Recently bimetallic NiGa and Ni_3Ga nanoparticles were readily obtained from from $[Ni(cod)_2]$ and GaCp* in mesitylene and $[BMIm][BF_4]$ as solvent [19].The Sn in the stannole ring is certainly more tightly bound. Also, the RuCp* appears to lead to a stable product other than Ru-metal nanoparticles. The deficiency of Ru in the metal nanoparticles is reasoned by the formation of a stable molecular species, possibly decamethylruthenocene, Cp^*_2Ru, which is removed with the ionic liquid during the TEM grid preparation.
It may also be of interest to follow the decomposition of heterotrimetallic (cod)Rh-stannole-RuCp* precursor in conventional organic solvents and in the presence of stabilizing capping agents to perhaps trap intermediate species or the ruthenium decomposition product.

References

---

[1] Pöttgen, R. (2006) Z. Naturforsch 61b, 677-698.
[2] Gmelin L. (1991) Handbook of inorganic and organometallic chemistry. Springer-Verlag, Heidelberg.
[3] Notwotny, H.; Schubert, K.; Dettinger, U. (1946) Metallforschung 1, 137-145.
[4] Schubert, K. (1947) Z. Naturforsch. 2a, 120.
[5] Nial O. (1947) Svensk Kern. Tidskr. 59, 172-183.
[6] Schubert, K.; Breimer, H.; Burkhardt, W.; Günzel, E.; Haufler, R.; Lukas, H.L.; Vetter, H.; Wegst, J.; Wilkens, M. (1957) Naturwissenschaften 44, 229-230.
[7] Miner, R.V.; Spencer, P.J.; Pool, M.J. (1968), Trans. Metall. Soc. 242, 1553-1554.
[8] Wettstein, S.G.; Bond, J.Q.; Alonso, D.M.; Pham, H.N; Datye, A.K.; Dumesic, J.A. (2012) Appl. Cat. B Environ. 117-118, 321-329.
[9] Han, J.; Sen, S.M.; Alonso, D.M.; Dumesic, J.A.; Maravelias, C.T. (2014) Green Chem. 16, 653-661.
[10] Akiyama, S.; Kakio, T.; Indou, S.; Oikawa, R.; Ugou, K.; Hiraki, R.; Sano, M.; Suzuki, T.; Miyake, T. (2014) J. Jpn. Pet. Inst. 57, 216-224.
[11] Sanchez, M.A.; Mazzieri, V.A.; Vicerich, M.A.; Vera,C.R.; Pieck, C.L. (2015) Ind. Eng. Chem. Res. 54, 6845-6854.
[12] Schwomma, O.; Nowotny, H. & Wittmann, A. (1964) Monatshefte für Chemie 95, 1538-1543.
[13] Wegner S.; Saito M.; Barthel J.; Janiak C. (2016) J. Organomet. Chem 821, 192-196.
[14] Tayal, J.; Rawat, B.; Basu, S. (2011) Int. J. Hydrog. Energy 36, 14884-14897.
[15] Hungria, A.B.; Raja R.; Adams, R.D.; Captain, B.; Thomas, J.M.; Midgley, P.A.; Golovko, V; Johnson, B.F.G. (2006) Angew. Chem. Int. Ed. 45, 4782-4785.
[16] Zhang, X.; Zhang, F.; Chan, K.-Y. (2004) Cat. Commun. 5, 749-753.
[17] Wegner, S.; Rutz, C.; Schütte, K.; Barthel, J.; Bushmelev, A.; Schmidt, A.; Dilchert, K.; Fischer, R.A.; Janiak, C. (2017) Chem. Eur. J. 23, 6330-6340.
[18] Cliff, G. & Lorimer, G.W. (1975) The quantitative analysis of thin specimens. J. Microsc. 103, 203–207.
[19] Schütte, K.; Doddi, A.; Kroll, C.; Meyer H.; Wiktor, C.; Gemel, C.; van Tendeloo, G.; Fischer, R.A.; Janiak, C. (2014) Nanoscale 6, 5532-5544.

5. Zusammenfassung und Ausblick

Die Ergebnisse dieser Dissertation werden in den folgenden Abschnitten zusammengefasst und jeweils ein kurzer Ausblick dazu gegeben.

Bei der Synthese der Ni-NPs war es möglich, sowohl aus dem $[Ni\{MeC(N\textit{i}Pr)_2\}_2]$ Precursor als auch aus dem $[Ni(COD)_2]$ Precursor Ni Nanopartikel in einer metastabilen hcp-Phase zu erhalten. Die mikrowellengestützte Synthese der Ni-NPs in den verschiedenen ILs lieferte kleine, einheitliche Partikel. Durch die Nutzung verschiedener Imidazolium-, Pyridinium- und Thiopheniumbasierten ILs mit unterschiedlich großen Anionen ($[BF_4]^-$,$[PF_6]^-$ und $[NTf_2]^-$) und unterschiedlichen Kettenlängen, war der Trend erkennbar, dass die Partikelgröße mit zunehmender Seitenkettenlänge und steigender Anionengröße ebenfalls zunimmt (vgl. Abschnitt 3.1). Im Vergleich der aus den beiden unterschiedlichen Precursoren hergestellten Ni-NPs, konnte kein signifikanter Unterschied in der Partikelgröße festgestellt werden. Die Wahl des Precursors für die mikrowellengestützte Synthese der Partikel scheint also keinen Einfluss auf die Partikelgröße zu haben. Sehr kleine kristalline Ni-NPs mit einer Größe von ≈ 2 nm konnten in den Pyridiniumbasierten ILs gefunden werden. Diese wurden auch für die magnetischen Messungen und den Vergleich der magnetischen Eigenschaften mit Ni-NPs aus $[LMIm][NTf_2]$ mit einer Größe von 10 ± 4 nm herangezogen. Hierbei wurden sehr ähnliche magnetische Eigenschaften zwischen den beiden Ni-NP Proben festgestellt. Ferner wurde die katalytische Aktivität der Ni-NPs in $[BMIm][NTf_2]$ und $[BPy][NTf_2]$ untersucht und es war möglich für die Hydrierung von Benzol und 1-Hexen Umsätze von > 90% zu erreichen, was für eine hohe katalytische Aktivität der Ni-NPs spricht.

Für die Darstellung von Ru/Sn-NPs (vgl. Abschnitt 3.2) war es möglich, durch Zersetzung der Single-Source Precursoren mittels Mikrowelle in der IL $[BMIm][BF_4]$ ohne Zusatz weiterer Stabilisatoren für den neutralen Triple-Decker Ruthenocen Precursor und den anionischen Ruthenocen Precursor, beide einen Stannolliganden beinhaltend, bimetallische Ru_2Sn Nanopartikel und Ru_3Sn_7 Nanopartikel mit α-Sn Nanopartikeln zu erhalten. Da die Ru_2Sn-NPs mit einer Größe von 4.3 ± 1.5 nm sehr klein waren und nur wenig Precursormaterial vorlag, konnte die Charakterisierung dieser Partikel ausschließlich über TEM-EDX- und SAED-Aufnahmen erfolgen. Eine Charakterisierung über PXRD war nicht möglich. Für die anionische Ruthenocen-Stannol Vorläuferverbindung konnten sphärische Ru_3Sn_7-NPs mit einer weiten Größenverteilung von 10-50 nm erhalten werden. Diese konnten daher über PXRD-Aufnahmen, TEM-EDX- und SAED-Aufnahmen vollständig charakterisiert werden.

Aufgrund der geringen Größenverteilung der Ru_2Sn-NPs, wurden diese in der IL [BMIm][BF_4] für katalytische Studien zur Semihydrierung von 1-Octin zu 1-Octen verwendet (siehe Abschnitt 4.2.2).

Hierfür wurden im Vorfeld zum besseren Vergleich reine Ru-NPs aus einem Carbonyl-Vorläufer als Katalysator zur Hydrierung verwendet. Die dazu erhaltenen Ergebnisse zeigten, dass auch bei Einsetzen der Ru-NPs eine Semihydrierung zum 1-Octen stattfand und keine vollständige Hydrierung zum n-Octan. Allerdings konnten bei der Semihydrierung keine, wie in der Literatur dazu bekannte, hohen Umsätze erzielt werden. Dies könnte mit einer möglichen Diffusionsbarriere zwischen der IL und den Nanopartikeln zusammenhängen, da die Partikel nach der Synthese nicht ausgefällt sondern in der IL-Suspension verbleibend für die Hydrierung eingesetzt wurden (siehe hier auch Auswertung in Abschnitt 4.2.2). Für die Semihydrierung von 1-Octin zu 1-Octen wurden für die, als Katalysator eingesetzten, Ru_2Sn-NPs noch geringere Umsätze erreicht. Inwieweit die geringe Umsatzrate mit einer möglichen „Vergiftung“ des Ru durch Sn zu erklären ist, oder ob diese geringen Umsätze ebenfalls mit der Diffusionsbarriere zwischen der IL und den Partikeln zustande kommen, konnte hier nicht eindeutig festgestellt werden. Ein Ansatz für einen besseren Vergleich könnte das Ausfällen der Partikel vor der Katalyse sein, sodass die Nanopartikel zwar noch durch die IL stabilisiert werden, eine Barriere zwischen dieser und den Partikeln aber weitgehend vermieden werden kann.

Zur Darstellung von Ru/Rh/Sn-NPs aus einer heterotrimetallischen (cod)Rh-Stannol-RuCp* Triple-Decker Komplex – Vorläuferverbindung, wurden zwei Zersetzungswege gewählt. Zum einen wurde der Precursor mittels Mikrowellenstrahlung in den ILs [BMIm][BF_4] und [BMIm][NTf_2] ohne Hinzugabe weiterer Stabilisatoren zersetzt und zum anderen wurde die Zersetzung durch Hydrierung bei milden Bedingungen durchgeführt (vgl. Abschnitt 4.3). Bei beiden Synthesewegen wurden kleine homogen verteilte Nanopartikel erhalten, die in kleinen Anteilen alle drei Metalle enthielten. Durch vollständige Analyse und Charakterisierung der Nanopartikel mittels TEM, TEM-EDX, STEM-EDX und SAED-Aufnahmen wurde im Ergebnis ein hoher Anteil an Rh- und RhSn-NPs gefunden und nur ein sehr geringer Anteil an Ru bzw. an Ru/Rh/Sn-NPs. Dies lässt sich mit der Struktur des Single-Source-Precursors begründen. Da der Rh(cod)-Ligand mit dem Cyclooctadien aufgrund der schwachen Bindung eine leicht abspaltbare Endgruppe enthält, liegt nach der Zersetzung des Precursors eine Rh-reiche Phase vor. Das Sn liegt in einem Stannolring und ist zwar im Vergleich zum Rh enger gebunden, lässt sich aber dennoch leicht zersetzen.

Der geringe Anteil an Ru in den Metallnanopartikeln rührt daher, dass sich das, im Precursor vorgegebene, RuCp* während der Zersetzung in eine stabile molekulare Form umwandeln könnte (siehe Auswertung in Abschnitt 4.3), die dann bei Fällung der Partikel und den anschließenden Waschvorgängen mit der IL entfernt wird. Eine Alternativsynthesemethode könnte die Darstellung der trimetallischen Partikel in organischen Lösemitteln und unter Zugabe von zusätzlichen Stabilisatoren sein, die eine Umwandlung des RuCp* in eine stabilere Molekülspezies unterbinden.

6. Experimentalteil

Sofern nicht anders beschrieben, wurden alle Synthesen unter Inertbedingungen (Glovebox, Schlenk-Technik) durchgeführt. Alle eingesetzten Lösemittel wurden vorher frisch destilliert, auf Molsieb (4 Å) gelagert und der Wassergehalt mittels KFT bestimmt.

Wassergehalt Propylencarbonat (PC): < 20 ppm

Wassergehalt 1-Octin: < 40 ppm

Zu Abschnitt 4.2.1: Darstellung von Ru-NPs@TRGO-400 in Propylencarbonat (PC) zur Katalyse von Lävulinsäure

Zur Darstellung von Ru-NPs geträgert auf TRGO-400 wurden 12.9 mg (0.5 wt%, 0.02018 mmol) $Ru_3(CO)_{12}$ mit 2.35 mg TRGO-400 (0.2 wt%) unter Inertbedingungen (Glovebox) in ein Mikrowellenröhrchen zusammengegeben und 24 h in 1 mL PC dispergiert. Anschließend wurde die Suspension in der Mikrowelle bei 250 °C und 50 W für 10 min. zersetzt und die schwarzen Ru@TRGO-400-NPs erhalten. Die während der Zersetzung entstandenen CO-Gase wurden im HV abgezogen und die Nanopartikel mit 5 mL Reinstwasser gefällt und weitere 5x mit derselben Menge gewaschen. Die geträgerten Nanopartikel wurden abschließend im HV getrocknet.

Zur Vorbereitung der Katalyse von Lävulinsäure zu γ-Valerolacton wurden 5 mg Ru@TRGO-400-NPs (3.5 wt% Ru, 1.73×10^{-3} mmol) und 0.22 g Lävulinsäure (191 µl, 1.89 mmol) in ein Glasinlet zusammengegeben und dieses in einen Stahlautoklaven gesetzt. Der Autoklav wurde auf Dichtigkeit geprüft und 3x mit H_2 gespült. Nach Aufheizen des Autoklavs im Ölbad auf 100 °C, wurde das System mit 10 bar H_2 beschickt und die Katalyse für 3 h durchgeführt. Nach dem Katalysezyklus wurden die Nanopartikel mittels Ultrazentrifugation (6000 U/min.) vom Produkt getrennt und für die nächsten Katalysezyklen aufgereinigt. Die Aufreinigung des Katalysators geschah über dreimaliges Waschen mit Methanol und anschließendem Trocknen im HV.

Zu Abschnitt 4.2.2: Verwendung von Ru_2Sn-NPs in der IL [BMIm][BF_4] als Katalysator für die Semihydrierung von 1-Octin zu 1-Octen

Für die katalytischen Vorstudien wurden 4.62 mg $Ru_3(CO)_{12}$ (1 wt%, $7.22x10^{-3}$ mmol) in 0.22 g [BMIm][BF_4] zusammengegeben und das Gemisch 24 h in der Glovebox suspensiert. Anschließend wurde der Precursor in der IL mittels Mikrowellenstrahlung für 10 min., bei 250 °C und 50 W zu Ru-NPs zersetzt.

Die entstandenen Nanopartikel wurden in der IL-Suspension für die Katalyse eingesetzt und vorher nicht gefällt. Zu der Suspension wurden 2.7 mL 1-Octin (0.018 mol) gegeben, das Gemisch in ein Glasinlet gegeben und dieses in einen Stahlautoklaven gebracht. Nach dreimaligem Spülen des Autoklaven mit H_2, wurde dieser im Ölbad auf 120 °C aufgeheizt, mit 20 bar H_2 beschickt und die Katalyse für 7 h durchgeführt. Nach dem Katalysezyklus wurde das Produkt bei 40 °C im HV in eine Kühlfalle überführt und erneut frisches 1-Octin zum Katalysator zugegeben.

Für die Katalyse mit Ru_2Sn-NPs wurden 1.64 mg (1 wt%, $5.12x10^{-3}$ mmol) Ru_2Sn-NP-IL-Suspension mit 1.35 mL 1-Octin in ein Glasinlet zusammengegeben und dieses in einen Stahlautoklaven überführt. Die Reaktionsbedingungen wurden analog zu den Vorstudien mit Ru-NPs als Katalysator gewählt.

7. Literaturverzeichnis

[1] Wegner S, Janiak C (2017) Top Curr Chem 375: 65. DOI: 10.1007/s41061-017-0148-1
[2] Wegner S, Rutz C, Schütte K, Barthel J, Bushmelev A, Schmidt A, Dilchert K, Fischer RA, Janiak C (2017) Chem Eur J 23: 6330-6340. DOI: 10.1002/chem.201605251
[3] Wegner S: Neue Synthesewege von ionischen Flüssigkeiten und deren Anwendung zur Stabilisierung von Nanopartikeln. Diplomarbeit, Heinrich-Heine-Universität Düsseldorf, 2014
[4] Wegner S, Saito M, Barthel J, Janiak C (2016) J Organomet Chem 821: 192-196. DOI: 1016/j.jorganchem.2016.05.010
[5] Prechtl MHG (2017) Nanocatalysis in Ionic Liquids, Wiley, Weinheim
[6] Yuan X, Yan N, Xiao C, Li C, Fei Z, Cai Z, Kou Y, Dyson PJ (2010) Green Chem 12: 228-233
[7] Borkowski T, Subik P, Trzeciak AM, Wolowiec S (2011) Molecules 16: 427-441
[8] Hayakawa K, Yoshimura T, Esumi K (2003) Langmuir 19: 5517-5521
[9] Gieshoff TN, Welther A, Kessler MT, Prechtl MHG, von Wangelin AJ (2014) Chem Commun 50: 2261
[10] Silva DO, Scholten JD, Gelesky MA, Teixeira SR, Dos Santos ACB, Souza-Aguiar EF, Dupont J (2008) Chem Sus Chem 1: 291-294
[11] Yu Y, Zhu W, Hua L, Yang H, Qiao Y, Zhang R, Guo L, Zhao X, Hou Z (2014) J Col Interf Sci 415: 117-126
[12] Rossi LM, Machado G, Fichtner PFP, Teixeira SR, Dupont J (2004) Cat Lett 92: 149-155
[13] Fonseca GS, Umpierre AP, Fichtner PFP, Teixeira SR, Dupont J (2003) Chem Eur J 9: 3263-3269
[14] Wu Z, Jiang H (2015) RSC Adv 5: 34622
[15] Leger B, Denicourt-Nowicki A, Roucoux A, Olivier-Bourbigou H (2008) Adv Synth Catal 350: 153-159
[16] Schwab F, Lucas M, Claus P (2011) Angew Chem Int Ed 50: 10453-10456
[17] Silveira ET, Umpierre AP, Rossi LM, Machado G, Morais J, Soares GV, Baumvol IJR, Teixeira SR, Fichtner PFP, Dupont J (2004) Chem Eur J 10: 3734-3740
[18] Vollmer C, Redel E, Abu-Shandi K, Thomann R, Manyar H, Hardacre C, Janiak C (2010) Chem Eur J 16: 3849-3858
[19] Esteban RM, Schütte K, Brandt P, Marquardt D, Meyer H, Beckert F, Mülhaupt R, Kölling H, Janiak C (2015) Nano-Structures&Nano-Objects 2: 11-18
[20] Tao FF, Zhang S, Nguyen L, Zhang X (2012) Chem Soc Rev 41: 7980-7993
[21] Armbrüster M, Kovnir K, Behrens M, Teschner D, Grin Y, Schlögl R (2010) JACS 132: 14745-14747
[22] Zea H, Lester K, Datye AK, Rightor E, Gulotty R, Waterman W, Smith M (2005) Appl Cat A 282: 237-245
[23] Armbrüster M, Kovnir K, Friedrich M, Teschner D, Wowsnick G, Hahne M, Gille P, Szentmiklosi L, Feuerbacher M, Heggen M, Girgsdies F, Rosenthal D, Schlögl R, Grin Y (2012) Nat Mat 11: 690-693
[24] Schütte K, Doddi A, Kroll C, Meyer H, Wiktor C, Gemel C, van Tendeloo G, Fischer RA, Janiak C (2014) Nanoscale 6: 5532-5544
[25] Schütte K, Meyer H, Gemel C, Barthel J, Fischer RA, Janiak C (2014) Nanoscale 6: 3116
[26] Vostrikov AA, Fedyaeva ON, Shishkin AV, Sokol MY (2009) J Supercrit Fluids 48: 161-166
[27] Esteban RM, Schütte K, Marquardt D, Barthel J, Beckert F, Mülhaupt R, Janiak C (2015) Nano-Structures&Nano-Objects 2: 28-34
[28] Wang Y, Liu H, Wang L, Wang H, Du X, Wang F, Qi T, Lee J-M, Wang X (2013) J Mater Chem A 1: 6839-6848
[29] Azadi P, Carrasquillo-Flores R, Pagan-Torres YJ, Gürbüz EI, Farnood R, Dumesic JA (2012) Green Chem 14: 1573-1576
[30] Niu M, Wang Y, Li W, Jiang J, Jin Z (2013) Cat Commun 38: 77-81